Quantum Control and Error Correction of Grid States in a Superconducting Oscillator

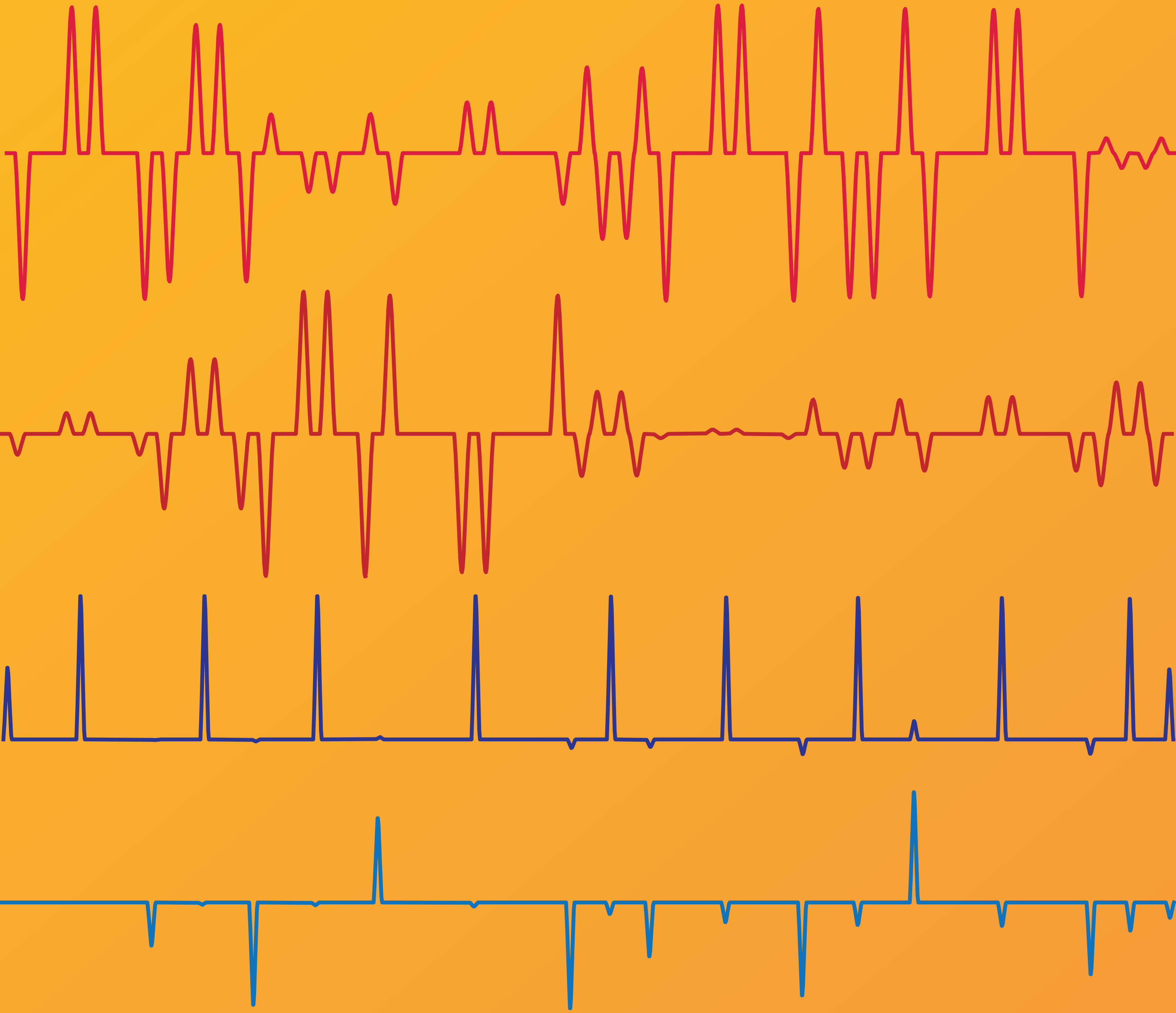

Alec Eickbusch

Abstract

Quantum Control and Error Correction of Grid States in a Superconducting Oscillator

Alec Eickbusch

2024

The potential of quantum systems for computation is challenged by decoherence, a process in which the system interacts with its noisy, uncontrolled environment. However, with quantum error correction (QEC), robust quantum computation in the presence of noise is possible. In a QEC encoding, information is stored as non-local correlations in an engineered multi-state, quantum many-body system. One promising encoding is the Gottesman-Kitaev-Preskill (GKP) code, in which logical states are encoded as oscillator grid states. However, ever since the code was envisioned in 2001, its experimental realization had remained out of reach. The most important barrier for realization was the code sensitivity to nonlinearity, an unfortunate requirement, given that a strong nonlinearity is in general favorable to control quantum systems. Whether it is possible to control a *linear* oscillator such that non-local correlations in phase space can be manipulated and stabilized is an open question. The goal of the PhD work reported in this dissertation is to answer this question. Our main result is the realization of universal control of a nearly-linear superconducting oscillator by weakly coupling it to a superconducting qubit in a many-drive-photon regime that previously was not controllable. Using this weak-coupling, large-displacement architecture, we demonstrate the first realization of stabilized quantum information encoded in grid states of an oscillator, ultimately leading in a follow-up experiment to a demonstration of qubit stabilized beyond break-even, i.e. in which the quantum coherence of the protected qubit is longer than that of all components of the system.

Quantum Control and Error Correction of Grid States in a Superconducting Oscillator

A Dissertation
Presented to the Faculty of the Graduate School
of
Yale University
in Candidacy for the Degree of
Doctor of Philosophy

by
Alec Eickbusch

Dissertation Director: Michel H. Devoret

May 2024

Dedicated to my parents, Wade and Celia Eickbusch,

and my brother, David Eickbusch.

Contents

List of Figures

List of Tables

List of Abbreviations and Symbols

Abbreviation	Phrase
QEC	quantum error correction
FTQC	fault-tolerant quantum computation
cQED	circuit quantum electrodynamics
GKP	Gottesman-Kitaev-Preskill (see: [1])
ECD	echoed conditional displacement
CD	conditional displacement
CNOT	controlled-not (gate)
CV	continuous-variable
DV	discrete-variable
+h.c.	plus hermitian conjugate
+c.c.	plus complex conjugate
∂_t	time derivative acting to the right $\partial_t f = \frac{\partial f}{\partial t}$
RWA	rotating-wave approximation
$\mathcal{O}$	big-O notation
ISA	instruction set architecture
SNAP	selective number-dependent arbitrary phase (gate)
NISQ	noisy intermediate-scale quantum

Abbreviation	**Phrase**
GRAPE	gradient ascent pulse engineering
OCT	optimal control theory
BS	beam-splitter
TMS	two-mode squeezing
JC	Jaynes-Cummings ($a^\dagger\sigma_- + a\sigma_+$)
AJC	anti-Jaynes-Cummings ($a^\dagger\sigma_+ + a\sigma_-$)
SQR	selective qubit rotation (gate)
qcMAP	qubit-cavity mapping protocol
VQE	variational quantum eigensolver
high-Q	high quality-factor
FPGA	Field-Programmable Gate Array
CPMG	Carr-Purcell-Meiboom-Gill
QSL	quantum speed limit
ST	sharpen-trim
sBs	small-Big-small
SNAIL	superconducting nonlinear asymmetric inductive element
JRM	Josephson Ring Modular
SPA	SNAIL parametric amplifier
HFSS	high frequency structure simulator
BCH	Baker-Campbell-Hausdorff

Name	**Symbol or Equation**
Qubit ground and excited states	$\{\|g\rangle, \|e\rangle\}$
Oscillator Fock states	$\{\|0\rangle, \|1\rangle, \|2\rangle, ...\}$
inductance	L (henries)
capacitance	C (farads)
characteristic impedance	$Z = \sqrt{L/C}$ (ohms)
temperature	T (kelvin)
Boltzmann constant	$k_B = 1.380\,649 \times 10^{-23}\,\mathrm{J\,K^{-1}}$
Planck constant	$h = 6.626\,070\,15 \times 10^{-34}\,\mathrm{J\,Hz^{-1}}$
Reduced Planck constant	$\hbar = h/2\pi$
angular frequency	ω (radians per second)
position	$\hat{X}$ (meters)
momentum	$\hat{P}$ (kilogram meters per second)
position zero-point fluctuations	$X_{\mathrm{ZPF}} = \sqrt{\hbar Z/2}$ (meters)
momentum zero-point fluctuations	$P_{\mathrm{ZPF}} = \sqrt{\hbar/2Z}$ (kilogram meters per second)
Reduced position	$\hat{q} = \hat{X}/\sqrt{2}X_{ZPF}$
Reduced momentum	$\hat{p} = \hat{P}/\sqrt{2}P_{ZPF}$
imaginary unit	$i = \sqrt{-1}$
position probability distribution	$\mathcal{P}(q)$
momentum probability distribution	$\mathcal{P}(p)$
Wigner quasiprobability distribution	$W(\alpha)$
Standard deviation	$\Delta\hat{O} = \sqrt{\langle\hat{O}^2\rangle - \langle\hat{O}\rangle^2}$
displacement operator	$D(\alpha) = \exp\left(\alpha a^\dagger - \alpha^* a\right)$
translation operator	$T(\beta) = D\left(\frac{\beta}{\sqrt{2}}\right)$

Name	**Symbol or Equation**
GKP logical Pauli operators	$\{X, Y, Z\}$
GKP position and momentum stabilizers	$\{S_q, S_p\}$
Speed of light in vacuum	$c = 2.997\,924\,58 \times 10^{8}\,\mathrm{m\,s^{-1}}$
Superconducting magnetic flux quantum	$\Phi_0 = h/2e = 2.067\,833\,848 \times 10^{-15}\,\mathrm{Wb}$
elementary charge	$e = 1.602\,176\,63 \times 10^{-19}\,\mathrm{C}$
energy decay time constant	T_1 (seconds)
energy decay rate	$\kappa = 1/T_1$ (inverse seconds)
quality factor	$Q = \omega T_1$
oscillator drive	$\varepsilon(t) \in \mathbb{C}$ (radians per second)
qubit Rabi drive	$\Omega(t) \in \mathbb{C}$ (radians per second)
ECD gate	$\mathrm{ECD}\left(\beta\right) = D\left(\beta/2\right)\left\|e\right\rangle\left\langle g\right\| + D\left(-\beta/2\right)\left\|g\right\rangle\left\langle e\right\|$
CD gate	$\mathrm{CD}\left(\beta\right) = D\left(\beta/2\right)\left\|g\right\rangle\left\langle g\right\| + D\left(-\beta/2\right)\left\|e\right\rangle\left\langle e\right\|$
Kerr coefficient K	$H/\hbar = K a^{\dagger 2} a^{2}$ (radians per second)
qubit rotation gate	$R_{\varphi}(\theta) = \exp\left[-i(\theta/2)\left(\sigma_x \cos\varphi + \sigma_y \sin\varphi\right)\right]$
channel fidelity	$\bar{\mathcal{F}}$
state fidelity	$\mathcal{F}$
vector of control signals	$\mathbf{u}(t)$
qubit Pauli operators	$\{\sigma_x, \sigma_y, \sigma_z\}$
gate time	T
quantum channel	$\mathcal{E}(\rho)$
Error or Kraus operators	$\{E_n\}$ or $\{K_n\}$
circuit depth	N
oscillator annihilation operator	$\hat{a}$ or a
transmon annihilation operator	$\hat{b}$ or b

Name	Symbol or Equation
qubit lowering operator	$\sigma_- = \sigma_x + i\sigma_y$
qubit raising operator	$\sigma_+ = \sigma_-^\dagger$
bare qubit-oscillator detuning	$\Delta = \tilde{\omega}_q - \tilde{\omega}_o$
linear coupling rate	g (radians per second)
bare qubit frequency	$\tilde{\omega}_q$ (radians per second)
bare oscillator frequency	$\tilde{\omega}_a$ (radians per second)
dispersive shift χ	$H/\hbar = \chi a^\dagger a \sigma_z/2$ (radians per second)
conditional parity gate	$C\Pi = \exp\left(-i\pi a^\dagger a \sigma_z/2\right)$
time-ordered exponential	$\mathcal{T}\exp\left(.\right)$
finite-energy GKP operator	$\hat{O}_\Delta = E_\Delta \hat{O} E_\Delta^{-1}$
offset gate charge	N_g (units of $2e$)
Cooper-pair number operator	$\hat{N}$
Josephson phase operator	$\hat{\varphi}$
second-order dispersive shift (χ')	$H/\hbar = \chi' a^{\dagger 2} a^2 b^{\dagger 2} b^2$ (radians per second)
thermal occupation number	n_{th} (photons)
non-Lindblad superoperator	$\mathcal{S}\left[X, Y\right]\rho = X\rho Y^\dagger - \left\{Y^\dagger X, \rho\right\}$
oscillator pure dephasing rate	κ_ϕ (inverse seconds)
displaced frame trajectory	$\alpha(t)$
large displacement magnitude	α_0
cost function	C
Characteristic function	$\mathcal{C}\left(\beta\right) = \mathrm{Tr}\left(\hat{O}D(\beta)\right)$ (see appendix A.3)

Name	**Symbol or Equation**
charging energy	$E_C = e^2/2C_\Sigma$ (joules)
Josephson critical current	I_0 (amperes)
Josephson energy	$E_J = \Phi_0 I_0/2\pi$ (joules)
Ramsey coherence time	T_{2R} (seconds)
echoed coherence time	T_{2E} (seconds)
homodyne expectation value	$\hat{O}_H$
perpendicular quadrature	$q_\perp = \cos(\Theta)\hat{p} - \sin(\Theta)\hat{q}$
QEC Gain	$G = \Gamma_{\text{physical}}/\Gamma_{\text{logical}}$

Acknowledgments

The past six years in New Haven have proven to be the most rewarding period of my life. I owe this to several extremely talented, supportive, and compassionate people, each of whom has played pivotal roles in shaping my journey as a scientist, especially my thesis committee: Michel Devoret, Rob Schoelkopf, Steve Girvin, and Shruti Puri.

My advisor, Michel Devoret, has shown unwavering support throughout the peaks and valleys of my graduate school journey. Michel's profound knowledge, scientific stamina, and passion for learning the truth still astound me and shape my approach to research. Above all else, Michel has cultivated an environment in Qulab that fosters genuine scientific exploration, with the support needed for projects to grow, fail, change, and adapt at the rapid pace required for cutting-edge research. Michel has instilled in me a desire to approach physics intuitively without sacrificing crucial details, and for this, I am profoundly indebted.

The collaborative environment on Becton's fourth floor would not exist without Rob Schoelkopf. Rob graciously spent many hours in his office discussing my projects. He always gives constructive feedback, intuition, and historical context that perfectly complements Michel's perspective. Rob's innovative vision and leadership perfectly blend with all the Yale Quantum Institute's groups, creating an environment at Yale where new ideas thrive. For this, I cannot thank Rob enough.

This thesis would be nothing without the collaboration and mentorship of Steve Girvin and Shruti Puri. Steve's ability to quickly grasp new concepts astounds me, and his physics intuition is unparalleled. Collaborating on various theory projects under Steve's guidance has been transformative, and I'm grateful for the many hours Steve spent with me in his office working on these ideas. Equally instrumental is Shruti Puri, whose early mentorship shaped my exploration of bosonic codes and error correction. Shruti's diligence and pursuit of the truth have been invaluable in shaping my career.

Of course, the fourth floor of Becton would be nothing without Luigi Frunzio. Luigi is the glue that has held my PhD together, and I'm so grateful for Luigi's help with this dissertation. Luigi's unwavering support, wealth of knowledge, patient mentoring, and tireless efforts keep the lab running. Luigi provided crucial feedback in the writing of this thesis that was, put simply, invaluable. Luigi is one of the kindest and most intelligent people I've had the pleasure to know.

In the early years of my PhD, mentorship from my first post-doc, Philippe Campagne-Ibarcq, was instrumental; without him, I would not have accomplished this PhD. Philippe always embodied a great deal of patience while teaching me new concepts, and for this, I am profoundly grateful. Philippe also encouraged the pursuit of grand and impactful ideas, and this shapes my research even today. Beyond science, Philippe has become a close and cherished friend, and I look forward to continuing our friendship and collaboration into the future.

During my later years at Yale, the collaboration and mentorship from my second post-doc, Benjamin Brock, have significantly advanced GKP research beyond the scope of this thesis. Ben brought novel ideas on bosonic codes, error correction, measurement, and electronics to our projects, and this has broadened my perspective. Above all, Ben has gone out of his way to help me graciously whenever I have asked for support, no matter how small or large a request. I cherish Ben as both a friend, a colleague, and a mentor.

I've also had the great pleasure to mentor and work with Andy Z. Ding, and for this, I am incredibly grateful. It has been a prized experience to know Andy as both a colleague and a friend, and Andy's positive attitude has been a constant source of upliftment in the lab. These days, I'm learning more from Andy than he's learning from me. I can't wait to follow the research Andy produces in the coming years, and I hope to stay close to Andy for many more years to come.

During the pandemic, I started to collaborate with Volodymyr Sivak, and this blossomed into one of the most rewarding collaborations and friendships of my time in New Haven. I've spent many hours sitting in Vlad's office, having deep conversations about physics, machine learning, error correction, and life. Vlad's contributions have been integral to the completion of this research, and I'm glad to have the opportunity to continue our collaboration and friendship into the future.

I'm also grateful to several other colleagues and postdocs who made significant contributions to this dissertation. During the early stages of GKP research, I collaborated closely with Steven Touzard, dedicating many hours to constructing the GKP experiment, taking data in the lab, and having great conversations about science and life. Steven's work laid the foundation for the rest of my PhD research, and I owe him a great deal for that. I extend my thanks to Ioannis Tsioutsios for patiently teaching me fabrication techniques and for always being available to discuss any scientific topic. Shraddha Singh has been a valuable collaborator, teaching me about error correction and quantum computing, and I look forward to continuing our friendship. Baptiste Royer's guidance has significantly shaped my understanding of bosonic codes, and I owe him a great deal for his collaboration. Additionally, Aniket Maiti's scientific intuition, collaboration, and friendship have made a lasting impact on my career.

I've had the pleasure to work with many colleagues who have become great friends, and their support has been invaluable. Spencer Diamond has been a close friend and colleague, always answering my scientific questions with intuition, and I'm grateful for our many squash matches, soccer games, basketball watching, and years of friendship. Jacob Curtis, who I am happy to call a close friend, has always been there for me. I've learned a great deal about quantum control from Jacob, and I have enjoyed the many hours we've spent smoking brisket and watching college football together. I'm indebted to Suhas Ganjam, whose home-cooked meals helped our cohort make it through our PhDs, and Suhas has taught me much about fabrication and coherence. Also, I have had many great scientific discussions with James Teoh, and our jam-sessions have always been filled with fun.

It has also been a pleasure to mentor and collaborate with two former Yale undergraduates, Shantanu Jha and Gabrielle Roberts, who have both become excellent physicists. I hope to carry our friendships and collaboration into the future and continue to learn from both Shantanu and Gabrielle.

I would also like to thank the many other wonderful colleagues whom I've worked with and learned from in Qulab over the past several years, including Tom Connolly, Rodrigo Cortiñas, Wei Dai, Valla Fatemi, Nick Frattini, Alex Grimm, Max Hays, Sumeru Hazra, Vidul Joshi, Akshay Koottandavida, Pavel Kurilovich, Alessandro Miano, Zlatko Minev, Mazyar Mirrahimi, Shantanu Mundhada, Anirudh Narla, Heekun Nho, Max Schäfer, Kyle Serniak, Shyam Shankar, Clarke Smith, Cassady Smith, Gautham Umasankar, Jayameenakshi Venkatraman, Uri Vool, Zhixin Wang, Xu Xiao, and Evan Zalys-Geller. I owe you all a great deal and cherish our time together.

Of course, the Becton fourth-floor environment is nothing without RSL. I am especially grateful for the collaboration and discussions with Luke Burkhart, Benjamin Chapman, Nathanael Cottet, Stijn de Graaf, Sal Elder, Christa Flühmann, Yvonne Gao, John Garmon, William Kalfus, Lev Krayzman, Chan U Lei, Alexander Read, Philip Reinhold, Serge Rosenblum, Neel Thakur, Takahiro Tsunoda, Christopher Wang, Patrick Winkel, Sophia Xue, Nico Zani, and many more.

I've been fortunate to also collaborate with researchers from many other groups, both at Yale and at other institutions, including Anthony Brady, Jahan Claes, Ondřej Černotík, Eleanor Crane, Michael Austin DeMarco, Radim Filip, Florian Hopfmueller, Liang Jiang, Valentin Kasper, Dany Lachance-Quirion, Marc-Antoine Lemonde, Julien Camirand Lemyre, Yuan Li, Kyungjoo Noh, Iivari Pietikäinen, Philippe St-Jean, and Quntao Zhuang. For each of you, our interactions have shaped my perspective as a physicist, and for this, I am thankful.

My gratitude also extends to the administrative staff, including Alexander Bozzi, Florian Carle, Theresa Evangeliste, Nuch Graves, Giselle Maillet, and Racquel Miller for their critical support. And to my external dissertation reader, Alexandre Blais, thank you for taking the time to provide crucial support to this thesis; your feedback is invaluable.

Finally, to my parents Wade and Celia Eickbusch, and my brother David Eickbusch, along with many other close family members who have always been there for me, I give heartfelt thanks for your unwavering support over the past six years. Although I've left Texas, I'm grateful that you have provided a home where I will always be warmly welcomed.

I'm proud to have called Yale and New Haven my home for the past six years. Although leaving the East Coast is bittersweet, the relationships and support of the people mentioned here, as well as many others, will always be cherished.

Chapter 1

Introduction

1.1 Motivation and summary

In quantum science, the fundamental unit of information is called the *qubit* - a quantum state $|\psi\rangle = a\,|g\rangle + b\,|e\rangle$ where $\{|g\rangle\,, |e\rangle\}$ are labels for two possible discrete outcomes of a measurement, while the values a and b are continuous (complex) numbers satisfying $|a|^2 + |b|^2 = 1$ [2]. The goal of quantum computation is to perform accurate calculations using qubits that are intractable for classical computers, which instead perform calculations on classical bits[1]. The most promising examples of potential applications of quantum computation include the simulation of quantum systems [3] and the factoring of large numbers into primes [4].

Modern classical bits have an extremely low probability of failure [5]. Modern qubits, on the other hand, fail with a high probability; state-of-the-art multi-qubit chips have gate failure probabilities on the order of one failure per every one-thousand two-qubit gates [6]. This failure probability is far too high to solve useful problems using a quantum computer. For example, it is estimated that a useful quantum simulation that is intractable for a classical computer would require, at a minimum, a failure probability of less than one per ten-million two-qubit gates [7].[2] Even more practical problems, such as simulating molecular physics or

---

[1] consisting of two possible discrete values: $\{0, 1\}$

[2] The example problem cited here is the quantum simulation of the time evolution for a spin-1/2 Heisen-

factoring a 1024-digit number, will require orders-of-magnitude lower failure probabilities.

The main limitation causing high error rates in current hardware is the uncontrolled entanglement of a quantum system with its environment, a process known as decoherence. Thankfully, there is a path forward to realizing robust quantum computation even in the presence of decoherence, called quantum error correction (QEC) [8]. The central goal of QEC is to realize fault-tolerant quantum computation (FTQC), where the result of a quantum computation can be accurate even in the presence of a small amount of local noise [9]. In a QEC encoding, logical qubits are stored as non-local correlations in an engineered multi-state, quantum many-body system. Remarkably, with QEC it is possible in principle to perform accurate quantum computation, as long as the physical error rate per gate or per time step is below a threshold [10]. However, such error correction requires a hardware overhead, where many physical components must be engineered for each logical qubit encoded.

A few promising technologies exist for the potential realization of FTQC, including trapped-ions, quantum photonics, and superconducting circuits, the latter of which is the focus of this work. In several proposals for FTQC using superconducting circuits, logical qubits are embedded in the Hilbert space of many physical qubits, each realized as the lowest-two energy levels of a nonlinear superconducting circuit. A popular encoding example is QEC using the stabilizer formalism [11], such as the surface code [12–14], in which logical qubits are stored as non-local quantum correlations of many physical qubits on a planar lattice. As an encouraging example of this, a recent experiment [6] demonstrated an error-corrected surface code memory in which the logical error rate slightly decreased as the number of physical components was increased, showing errors can in principle be reduced as the system is scaled.

An alternative to the many-qubit approach is the many-oscillator approach. In these bosonic encodings, logical qubits are embedded into the non-local quantum correlations of a system consisting of many physical harmonic oscillators [15]. In contrast to a physical

---

berg chain with 100 spins.

qubit, each physical oscillator consists of many quantum levels, $\{|0\rangle, |1\rangle, |2\rangle, ...\}$, called Fock states. In superconducting circuits, such oscillators can be realized as linear superconducting resonators in either a planar geometry [16] or as three-dimensional microwave cavities [17]. It is possible that using oscillators instead of qubits can lead to a lower physical overhead due to the additional quantum levels in each oscillator. Intuitively, these additional levels could hopefully be used to encode quantum information more redundantly, requiring less physical components.

There are a few proposals for robustly encoding quantum information in oscillators [18]. Among these, one of the most promising candidates is called the Gottesman-Kitaev-Preskill (GKP) code, named after the three authors who introduced the code in 2001 [1]. The GKP code is of great interest because, among many nice properties, it is optimal for correcting photon loss, one of the most important decoherence mechanics in superconducting oscillators [19–22]. In the single-oscillator GKP code, quantum information is stored as quantum correlations in the oscillator's position and momentum. Errors can be measured and corrected without disturbing the logical information encoded in these correlations. The GKP code could also be concatenated in a multi-oscillator encoding, such as a GKP surface code [15, 23, 24].

However, ever since the GKP code was envisioned in 2001, its experimental realization had remained out of reach. The most important barrier for realization was the code's sensitivity to nonlinearity, an unfortunate requirement, given that a strong nonlinearity is in general favorable to control quantum systems. In superconducting circuits, the control methods developed over the past thirty years have by-and-large pushed towards realizing strong nonlinear interactions so that gates can be performed quickly; this is inherently incompatible with quantum states of the oscillator that are highly squeezed, such as the GKP code.

Given that nonlinearity is both a blessing and a curse, a natural question arises: **can the quantum state of a nearly-linear oscillator be controlled coherently?** Here, by 'nearly-linear', we mean that the oscillator nonlinearity should be weak enough as to not become a limiting factor for the preparation and stabilization of finite-energy GKP states when compared with other decoherence mechanisms.

As I will show in the following chapters, the primary result of this thesis is an affirmative answer to the question posed above, namely, that a nearly-linear oscillator can be controlled coherently. **Our main result is the realization of universal control of a nearly-linear superconducting oscillator by weakly coupling it to a superconducting qubit in a many-drive-photon regime that previously was not controllable [25]. Using this, we demonstrate the first quantum error correction of GKP states encoded in an oscillator [26, 27].** The techniques developed for this error correction and the weak-coupling architecture should be seen as the building blocks needed to eventually scale up to a multi-oscillator GKP encoding.

Besides error correction, it is likely that using bosonic modes and encodings can aid in realizing efficient near-team quantum simulation [28], quantum communication [29], and quantum sensing, including the search for dark matter axions [30]. The architecture, control, and measurement methods developed in this PhD thesis could be directly applicable in these domains, allowing control in situations where minimizing oscillator nonlinearity is crucial.

With these motivations in mind, in order to be pedagogical, research results in this thesis are presented in logical order, rather than chronological order. First, in the remainder of this chapter, I will outline the main ideas of this dissertation in more detail, including some preliminaries.

In chapter 2, I give a thorough introduction to bosonic quantum control, focusing on a gate-based approach to control an oscillator. This leads into a description of the phase-space instruction set architecture (ISA) in section 2.4.5, one of the principal results of this thesis. As one application, I demonstrate the numerical optimization of gates on the finite-energy GKP code using the phase-space ISA.

Next, in chapter 3, I outline the weak-coupling dispersive architecture, consisting of a superconducting qubit with a weak coupling to a high quality-factor superconducting oscillator. This description includes calibration, characterization, and oscillator tomography methods, developed here in a regime where previous approaches fail. I also discuss pitfalls of this approach, and the analysis of oscillator loss and dephasing in this setting.

In chapter 4, I demonstrate the phase-space ISA using the weak-coupling architecture. In particular, we measure preparation of Fock states (Fock $|1\rangle$ with fidelity $\mathcal{F} = 98 \pm 1\%$), oscillator squeezing at 11.1 dB - the largest achieved to date in the microwave domain[3] - and unitary state preparation of finite-energy GKP states.

In chapter 5, we apply these ideas to the quantum error correction of the single-mode GKP states. Our demonstrations include the stabilization using a measurement-based and semi-autonomous protocol, ultimately leading to the stabilization of a quantum memory beyond break-even, meaning the quantum coherence of the protected qubit is longer than that of all components of the system.

Lastly, in chapter 6, I discuss proposals for future research directions, with a focus on the GKP code.

1.2 Preliminaries

1.2.1 Quantum oscillators

A physical oscillator can be realized in many ways, such as a mass on a spring, an electrical circuit consisting of an inductor and capacitor in parallel (often called an L-C oscillator), or an electromagnetic mode confined by two mirrors. For a closed system, these oscillators can be described by two properties: angular frequency ω and characteristic impedance Z.[4] The mass on a spring example is easy to visualize, and classically its state is described by two dynamical variables, its instantaneous position X and momentum P; other physical

---

[3] to the best of my knowledge.

[4] For a mass m on a spring, the impedance is given by $Z = 1/\sqrt{km}$, where k is the spring constant. For an L-C (inductor-capacitor) electrical circuit oscillator, the impedance is given by $Z = \sqrt{L/C}$.

oscillators can be mathematically mapped onto this system. For instance, in an L-C oscillator circuit, the flux through the inductor Φ is analogous to position, and the charge difference on the capacitor Q is analogous to momentum [31]. For this reason, I will use the language of position (represented by the variable X) and momentum (represented by the variable P) to describe a general oscillator, even if is not a physical mass-on-spring system.

When an oscillator is cooled such that $k_B T \ll \hbar\omega$, where k_B is the Boltzmann constant and $\hbar = h/2\pi$ is the reduced Planck constant, the thermal fluctuations are suppressed, and quantum effects become important. In such a regime, the position and momentum (or analogous variables) are promoted to quantum operators, $X \rightarrow \hat{X}$ and $P \rightarrow \hat{P}$ that obey a commutation relation, $\left[\hat{X}, \hat{P}\right] = i\hbar$ where $\left[\hat{A}, \hat{B}\right] = \hat{A}\hat{B} - \hat{B}\hat{A}$ is the commutator[5] of two operators[6] [32].

As a result of the Heisenberg uncertainty relation, a quantum oscillator cooled to its ground state will still have small fluctuations of position and momentum. For an oscillator with characteristic impedance Z, the standard deviation of ground-state fluctuations is given by $\Delta\hat{X} = \sqrt{\hbar Z/2} \equiv X_{\mathrm{ZPF}}$ in position and $\Delta\hat{P} = \sqrt{\hbar/2Z} \equiv P_{\mathrm{ZPF}}$ in momentum, where the subscript ZPF stands for zero-point fluctuations. Notice that these ground-state fluctuations satisfy $X_{\mathrm{ZPF}} P_{\mathrm{ZPF}} = \hbar/2$. For an L-C circuit oscillator in the microwave regime with a typical frequency of $\omega/2\pi = 10\,\mathrm{GHz}$ and impedance of $Z = 100\,\mathrm{Ohms}$, ground state voltage fluctuations are on the order of $0.3\,\mu\mathrm{V}$ [33], allowing for strong coupling between quantum electromagnetic circuits [34].

It is often convenient to work with position and momentum operators that are scaled by the zero-point-fluctuations, so position and momentum are set on equal footing. Here, we write the scaled versions as $\hat{q} = \hat{X}/\sqrt{2}X_{\mathrm{ZPF}}$ and $\hat{p} = \hat{P}/\sqrt{2}P_{\mathrm{ZPF}}$. In these reduced coordinates, the phase-space trajectory of a harmonic oscillator that is usually an oval in

---

[5] We will say operators commute if $\left[\hat{A}, \hat{B}\right] = 0$

[6] Throughout this work, I will use hats for operators that could be misconstrued as variables. In many cases, I will omit hats when it is obvious what is being represented.

$X-P$ phase-space is transformed into a circle in $q-p$ phase space, and the position-momentum commutator becomes $[\hat{q},\hat{p}]=i$. These operators are also called quadratures, and they form an orthonormal basis for oscillator wave functions, $\psi(q)=\langle q|\psi\rangle$ and $\psi(p)=\langle p|\psi\rangle$ with

$$|\psi\rangle=\int dq\,\psi(q)\,|q\rangle=\int dp\,\psi(p)\,|p\rangle \tag{1.1}$$

related by the Fourier transform $|q\rangle=\frac{1}{\sqrt{2\pi}}\int dq\,e^{-ipq}\,|p\rangle$ under the convention $\delta(x-x')=\int dke^{i(x-x')k}/2\pi$.

The quantum state of an oscillator is quantized using an infinite number of discrete levels called Fock states, $\{|0\rangle,|1\rangle,|2\rangle,..\}$. When the oscillator is an electromagnetic mode, these excitations are called photons. Translations in the Fock state basis can be generated by the creation operator $a^\dagger$ and annihilation operator a according to

$$a^\dagger\,|n\rangle=\sqrt{n+1}\,|n+1\rangle \tag{1.2}$$

$$a\,|n\rangle=\sqrt{n}\,|n-1\rangle\,. \tag{1.3}$$

These are related to the quadrature operators by

$$\hat{q}=\left(a+a^\dagger\right)/\sqrt{2} \tag{1.4}$$

$$\hat{p}=-i\left(a-a^\dagger\right)/\sqrt{2}, \tag{1.5}$$

and the photon number operator is given by $\hat{n}=a^\dagger a$ such that $\hat{n}\,|n\rangle=n\,|n\rangle$.

The quadrature operators are the generators of displacements in phase-space. Specifically, a translation in the position-momentum phase space of an oscillator is performed by the translation operator,

$$\hat{T}(\alpha)=\exp\left(-i\mathrm{Re}(\alpha)\hat{p}+i\mathrm{Im}(\alpha)\hat{q}\right), \tag{1.6}$$

where α is a complex number. Such operators are also called Weyl operators [35], and they were first used by Weyl, Wigner, Moyal, and others to develop what we now call the phase-space formulation of quantum mechanics [36]. The translation operator is related to the displacement operator $D(\alpha) = \exp\left(\alpha a^\dagger - \alpha^* a\right)$ by a scale factor, $T(\alpha) = D\left(\alpha/\sqrt{2}\right)$. When the translation operator is applied to a state, $|\tilde{\psi}\rangle = \hat{T}\,|\psi\rangle$, the resulting state $|\tilde{\psi}\rangle$ is a shifted copy of $|\psi\rangle$ in position-momentum phase-space by an amount $\mathrm{Re}\,(\alpha)$ in position and $\mathrm{Im}\,(\alpha)$ in momentum, along with an additional phase factor. This phase factor can be found by evaluating the group commutator[7], given by

$$T(\gamma)T(\delta) = e^{(\gamma\delta^* - \gamma^*\delta)/2}T(\delta)T(\gamma) = e^{iA}T(\delta)T(\gamma), \tag{1.7}$$

where A is the signed area of the parallelogram formed by the translation operators in phase-space (see appendix A.1). This is an example of geometric phase (also called Berry phase) in the phase-space of the oscillator [37]. From this, we see that two translation operators commute if they enclose an area in phase space that is an even-integer multiple of π, and they will anti-commute[8] if the area enclosed is an odd-integer multiple of π.

The phase space of the oscillator is described by a quasi-probability distribution called the Wigner function, $W(\alpha) \in \mathbb{R}$, where negative values indicate non-classical effects. The Fourier transform of the Wigner function is called the characteristic function, defining the reciprocal space of the oscillator. Given an oscillator density matrix ρ, the characteristic function is given by

$$\mathcal{C}\left(\beta\right) = \langle D(\beta)\rangle = \mathrm{Tr}\left(\rho D(\beta)\right). \tag{1.8}$$

The characteristic function is further developed in appendix A.3. The relationship between

---

[7] The group commutator of $\hat{A}, \hat{B}$ is $\hat{A}\hat{B}\hat{A}^\dagger\hat{B}^\dagger$.

[8] two operators anti-commute if $\left\{\hat{A}, \hat{B}\right\} = 0$ where $\left\{\hat{A}, \hat{B}\right\} = \hat{A}\hat{B} + \hat{B}\hat{A}$ is called the anti-commutator.

the displacement operator (or translation operator) and the reciprocal space of the oscillator can be seen by writing the translation operator in terms of sines and cosines. We can write

$$\langle T(\alpha = k_p + ik_q)\rangle = \langle \cos\left(k_q\hat{q} - k_p\hat{p}\right)\rangle + i\left\langle \sin\left(k_q\hat{q} - k_p\hat{p}\right)\right\rangle, \tag{1.9}$$

and hence a measurement of the translation operator is sensitive to the Fourier component of the state at angular frequency $2\pi/|\alpha|$ along the cut $k_q\hat{q} - k_p\hat{p}$ in phase-space. Since the operator is non-Hermitian, the real and imaginary parts must be measured separately.

1.2.2 The Gottesman-Kitaev-Preskill Code

Error channels such as photon-loss and heating of an oscillator can be thought of as small, unknown translations of position and momentum [1], leading to a diffusion in phase-space [38]. This type of diffusion will suppress high-frequency components in the reciprocal space of the oscillator more quickly than lower-frequency components, effectively applying a Gaussian filter to the characteristic function. A description of this model is given in appendix A.3.

With this type of noise in mind, it would be advantageous to encode logical qubit information in an oscillator as low-frequency correlations of position and momentum, since diffusion noise will suppress the high-frequency components in reciprocal space more quickly. Furthermore, we would like to be able to measure and correct small translations of the oscillator without corrupting the logical information encoded in these low-frequency correlations.

A code with these properties was first introduced by Daniel Gottesman, Alexei Kitaev, and John Preskill (GKP) in their seminal 2001 work [1]. Their code can be generalized to multiple oscillators, however here we will focus on the most straightforward example of a qubit-into-oscillator GKP code. In the position basis, the infinite-energy logical states are

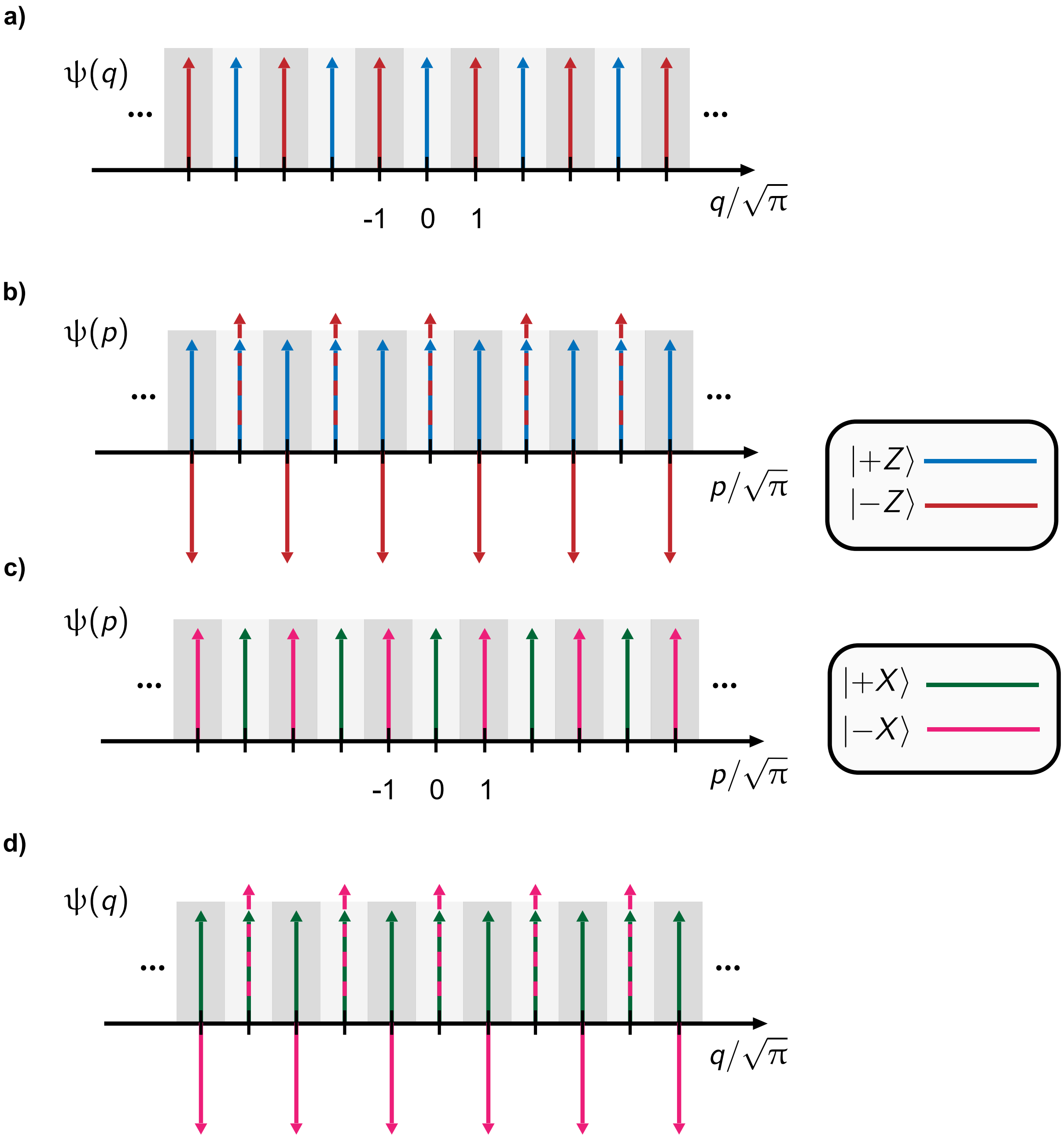

Figure 1.1: **Infinite-energy GKP wavefunctions. (a.)** Position and **(b.)** momentum wavefunctions of the square infinite-energy GKP code states $|{+Z}\rangle$ and $|{-Z}\rangle$. **(c.)** Momentum and **(d.)** position wavefunctions of $|{+X}\rangle$ and $|{-X}\rangle$. Shaded regions represent the $+1$ (light) and -1 (dark) results of an error-corrected readout of the corresponding logical operators. Arrows in the wavefunction represent Dirac delta-functions.

given by

$$|+Z\rangle = \sum_{s=-\infty}^{\infty} |q = 2s\sqrt{\pi}\rangle \tag{1.10}$$

$$|-Z\rangle = \sum_{s=-\infty}^{\infty} |q = (2s+1)\sqrt{\pi}\rangle\,, \tag{1.11}$$

as is shown in fig. 1.1a. These states are superpositions of infinitely-squeezed position eigenstates (a Dirac comb). They cannot be normalized, and are thus unphysical. Realistic code words have a finite variance for the modular position and momentum, these states will be discussed later in section 5.1.2, as for the purposes of introducing the GKP code, it is best to first understand the infinite-energy code, then later modify the description to account for a finite squeezing.

The Fourier transform of these states can be taken to find the wavefunctions in the momentum representation; since they are Dirac combs, their Fourier transforms will also be Dirac combs. As shown in fig. 1.1b, in the momentum representation, logical information is stored as the winding of the wavefunction phase around the momentum axis. Forming their superpositions, the logical X eigenstates[9] are shown in fig. 1.1c, are given in the momentum basis by

$$|+X\rangle = \sum_{s=-\infty}^{\infty} |p = 2s\sqrt{\pi}\rangle \tag{1.12}$$

$$|-X\rangle = \sum_{s=-\infty}^{\infty} |p = (2s+1)\sqrt{\pi}\rangle\,. \tag{1.13}$$

As is evident from these wave functions, the Z logical information (the ‘bit’) and the X logical information (the ‘phase’) encoded in these states have some protection against small translations in position and momentum. To see this, we can define an error-robust logical Z

---

[9] $|+X\rangle \propto |+Z\rangle + |-Z\rangle$, $|-X\rangle \propto |+Z\rangle - |-Z\rangle$.

and X operators for the code as the square-waves [39, 40]

$$Z_{C+E} = \operatorname{sgn}\left(\cos\left(\sqrt{\pi}\hat{q}\right)\right), \tag{1.14}$$

$$X_{C+E} = \operatorname{sgn}\left(\cos\left(\sqrt{\pi}\hat{p}\right)\right). \tag{1.15}$$

Here, $C+E$ stands for 'code plus error space', meaning the logical operators are robust to small displacements. These error-robust logical operators are shown as the light ($=+1$) and dark ($=-1$) regions behind the wavefunctions in fig. 1.1. It is clear from these operators that the value of Z_{C+E} or X_{C+E} will be unchanged under a small unknown translation of the position or momentum, $\hat{T}(\delta)$, as long as $|\delta| < \sqrt{\pi}/2$. This defines the distance of the code (the maximum size of correctable errors) in the translation basis.[10] We can now define the logical operators for the code as

$$X_L = \hat{T}\left(\sqrt{\pi}\right) \tag{1.16}$$

$$Y_L = \hat{T}\left((1+i)\sqrt{\pi}\right) \tag{1.17}$$

$$Z_L = \hat{T}\left(i\sqrt{\pi}\right), \tag{1.18}$$

where code words satisfy $Z_L\left|\pm Z\right\rangle = \pm\left|\pm Z\right\rangle$ (with a similar relation for X_L and Y_L).[11]

In order to measure and correct small displacements without revealing the logical information, we can define measurement operators that commute with the logical operators.

---

[10] Technically, all translations such that $\operatorname{sgn}\left(\cos\left(\sqrt{\pi}|\delta|\right)\right) = +1$ are correctable. However, diffusion in phase space is a local process, and we would like to correct errors before they become large translations.

[11] Some authors define the $C+E$ operators as the logical operators. However, unlike the translation operators, the ideal logical states are not the unique $+1$ eigenstates of the $C+E$ operators.

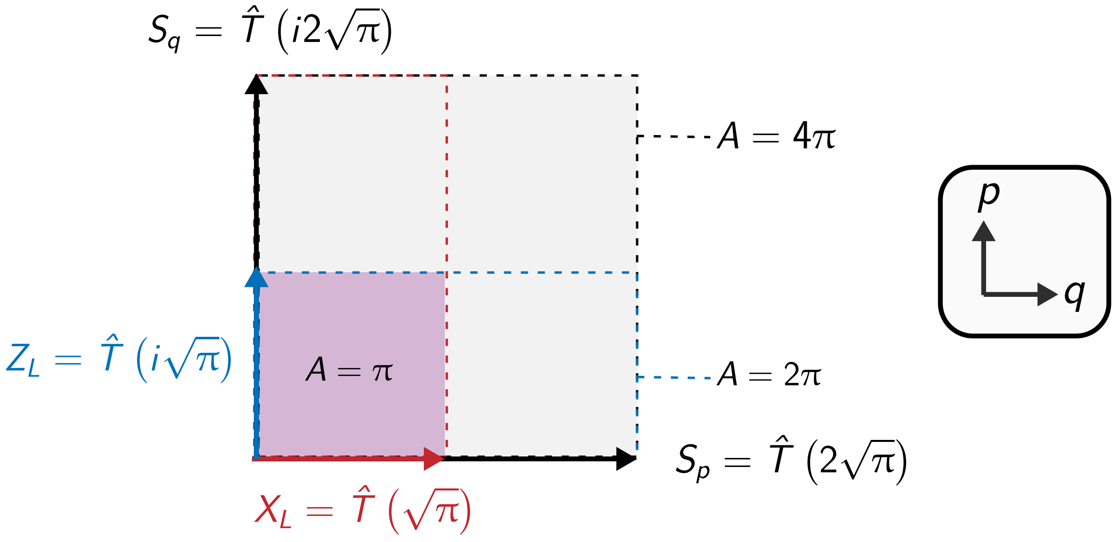

Figure 1.2: **GKP logical operators and stabilizers.** Phase-space representation of the logical translation operators. According to the translation commutation area law (eq. (A.16), the areas enclosed by the logical and stabilizer translations satisfy the commutation relations required for a valid QEC code (eq. (1.21)).

Such operators are called the stabilizers, and for the GKP code they are given by[12]

$$\hat{S}_q = \hat{Z}^2 = \hat{T}\left(i2\sqrt{\pi}\right), \tag{1.19}$$

$$\hat{S}_p = \hat{X}^2 = \hat{T}\left(2\sqrt{\pi}\right). \tag{1.20}$$

As is shown in fig. 1.2, using the geometric-phase area law introduced in eq. (A.12), the logical operators and stabilizers satisfy the required commutation and anti-commutation relations for a valid QEC qubit code,

$$[S_q, S_p] = 0 \tag{1.21}$$

$$[S_{q,p}, \mathcal{P}] = 0 \tag{1.22}$$

$$\{X_L, Z_L\} = 0, \tag{1.23}$$

where $\mathcal{P}$ is one of X_L, Y_L, Z_L.

---

[12] The full stabilizer group is generated by all products of these two operators.

Furthermore, it is easy to see from the wavefunctions of the logical states in fig. 1.1 that translations of $2\sqrt{\pi}$ (the stabilizers) will leave the states unchanged, and translations of $\sqrt{\pi}$ (the logicals) along position or momentum will apply the correct bit-flip or phase-flip operation.

Using the area commutation law, we can derive how the stabilizers can be used to measure small translations. Defining a GKP state that has undergone a small, erroneous translation as $|\psi_\delta\rangle = \hat{T}(\delta)|\psi\rangle$, we see that[13]

$$S_q |\psi_\delta\rangle = e^{i2\sqrt{\pi}\mathrm{Re}(\delta)} |\psi_\delta\rangle , \tag{1.24}$$

$$S_p |\psi_\delta\rangle = e^{-i2\sqrt{\pi}\mathrm{Im}(\delta)} |\psi_\delta\rangle . \tag{1.25}$$

By measuring $\mathrm{Re}(S_q) = \cos(2\sqrt{\pi}\hat{q})$ and $\mathrm{Im}(S_q) = \sin(2\sqrt{\pi}\hat{q})$ (and the real and imaginary parts of S_p), the value of δ can be extracted and corrected without corrupting the logical information, as long as $|\delta| \leq \sqrt{\pi}/2$.

If we expect $|\delta|$ to be small, a measurement of the imaginary part of the stabilizers will be more sensitive to δ than the real part, since the sine function is first-order sensitive while the cosine is second-order sensitive to changes of small values of the argument near 0. The experimental quantum error correction of the GKP code performed in this PhD dissertation can be thought of as first performing measurements that extract some information about $\mathrm{Im}(S_q)$ and $\mathrm{Im}(S_p)$, using a decoder given the noise model to guess the value of δ, and applying a small displacement of $-\delta$ to correct in real time. If this process is repeated faster than diffusion in phase space can accumulate, the GKP code logical information can be stabilized longer than an uncorrected code.

I will return to the GKP code in chapter 5 to describe the finite-energy GKP code and the details of our error correction and control protocols. For a complete overview, see our recent review article [22], as well as the other reviews, perspectives, and theses related to

---

[13] I encourage the reader to try this exercise.

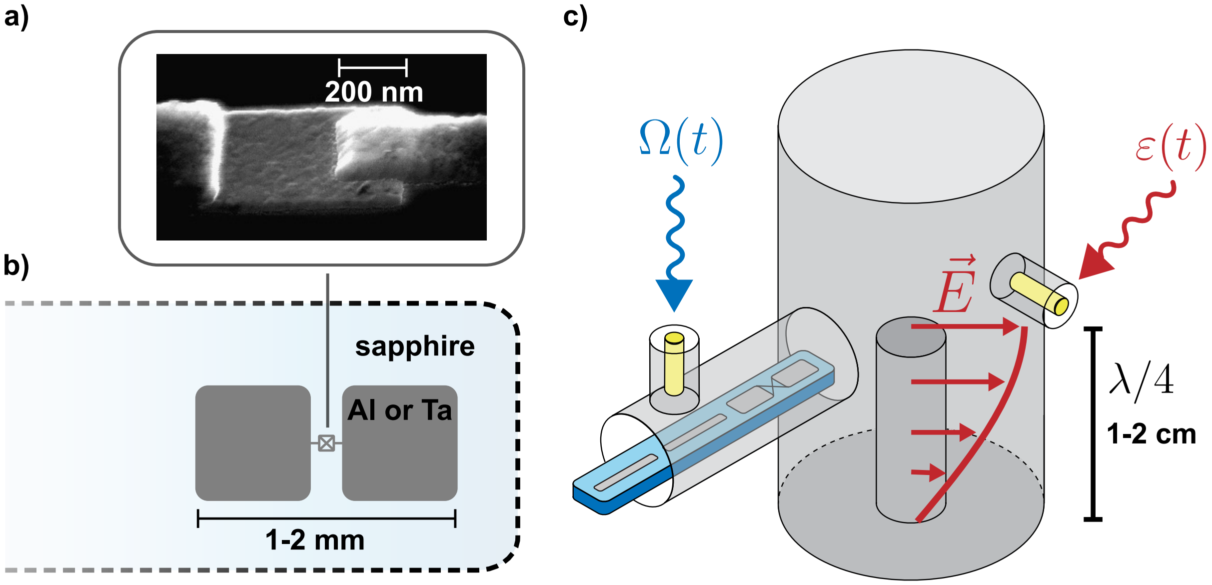

Figure 1.3: **Transmon coupled to a 3D high-Q microwave cavity a.)** Scanning electron microscope (SEM) image of a Josephson junction fabricated using the Dolan bridge technique [46] with an approximate scale bar shown. The JJ consists of Aluminum(Al)-Aluminum Oxide ($\mathrm{AlO_x}$)-Aluminum(Al) structure, with a typical oxide thickness on the order of $\sim 1\,\mathrm{nm}$ (SEM image courtesy of Luigi Frunzio). **b.)** A 3D transmon, consisting of superconducting thin-film forming capacitor pads (aluminum or tantalum) connected with a JJ. The pads couple to the electric field of the 3D microwave cavity. **c.)** A 3D high-quality-factor superconducting post cavity coupled to a transmon qubit. The transmon chip also includes a low-Q readout resonator and a Purcell filter. The cavity resonator is formed as a $\lambda/4$ resonator at the bottom of a terminated waveguide, with electric field shown [17]. Microwave drives $\varepsilon(t)$ and $\Omega(t)$ are applied through the copper pins coupled to the cavity and transmon.

the GKP code and its experimental realization [14, 18, 41–45].

1.2.3 Superconducting qubits and cavities

Although the GKP code was proposed in 2001, it was initially too complex for direct realization in a physical system, as the quantum control needed was far out of reach at the time. The GKP code was first designed with optics in mind - the experimental physics of light with frequencies at and near the visible regime. However, as will be discussed in depth in section 2.2.2, the realization of non-Gaussian oscillator states requires strong non-linear interactions. Such nonlinearities are weak in the optical domain [47], making the realization of optical GKP states quite difficult. To date, and to the best of my knowledge, only one experiment in the optical domain has achieved GKP-like states, with a low squeezing parameter [48].

Superconducting circuits, on the other hand, are an easier platform for realizing GKP states and error correction with current technology, since a strong and coherent nonlinearity can be utilized. Operating in the microwave frequency regime ($\omega/2\pi \sim 1\,\mathrm{GHz}$ to $20\,\mathrm{GHz}$), cooling these circuits such that $\hbar\omega << k_b T$ will require $T \sim 20\,\mathrm{mK}$.[14]. These circuits can be thought of as collective excitations of a superconducting condensate of Cooper-pairs defined by some physical circuit geometry. These collective modes have excitations that are bosonic in nature called photons (even in the case of modes that only have a small electric field participation in free space) and are described by the quantum mathematics of oscillators introduced in the previous section and in appendix A. Unlike classical circuits, in the quantum case these oscillators have quantized (discrete) energy levels.

The central building block needed for quantum experiments with microwave photons is a low-dissipation source of nonlinearity. The Josephson junction, shown in fig. 1.3a, plays this role. The Josephson junction is a superconductor-insulator-superconductor structure, and it can be thought of as a nonlinear inductor shunted by a small capacitance, where the nonlinear inductor has a current (I) -voltage (V) relation of $I(t) = I_0 \sin(\varphi)$ where I_0 is the critical current parameter and $\varphi(t) = (2\pi/\Phi_0) \int d\tau\, V(\tau) \,\mathrm{mod} 2\pi$ is the phase difference of superconducting condensates on either side of the junction [50] and $\Phi_0 = h/2e = 2.067\,833\,848 \times 10^{-15}\,\mathrm{Wb}$ is the superconducting magnetic flux quantum. Crucially, the critical current I_0 can be controlled in a reproducible way by the area of the junction ang/or the oxide thickness.

To build a simple nonlinear superconducting oscillator in the $\sim 1\,\mathrm{GHz}$ to $\sim 10\,\mathrm{GHz}$ range, we can shunt the Josephson junction with a large capacitance, as shown in fig. 1.3b. The first two levels of this nonlinear oscillator can be used as a qubit. We design and operate

---

[14] This cooling is performed by a dilution refrigerator, making use of a phase transition between superfluid and normal states of a helium 3 and helium 4 mixture [49].

the circuit in a parameter regime where the charging energy $E_c = e^2/2C_\Sigma$ is small compared to the Josephson energy $E_J = \Phi_0 I_c/2\pi$. In this regime, the transition frequency of the qubit is exponentially insensitive to charge noise, and we call this circuit a transmon [51]. Specifically, the transmon shown in fig. 1.3b and used in this work is called a fixed-frequency 3D-transmon [52].

For the realization of the GKP code, a nearly linear oscillator is needed with a high quality factor, $Q = \omega T_1$, where T_1 is the timescale at which energy stored in the oscillator will decay. Although research is progressing quickly on high-Q planar superconducting oscillators with quality factors in the tens of million [16], in this work we will use the fundamental mode of a three-dimensional superconducting cavity [53], as shown in fig. 1.3c. Although these cavities are likely not practical to scale beyond hundreds of modes, they are currently the highest quality-factor microwave cavities, and serve as a good testing ground for quantum information experiments that could eventually be realized in a more scalable technology. In 3D aluminum post-cavities (such as is shown in the figure), typical quality factors can be on the order of thirty million (energy decay times are on the order of $T_1 \sim 1\,\mathrm{ms}$ at $5\,\mathrm{GHz}$) [17]. Recent advancements in niobium cavities have demonstrated quality factors on the order of one billion or higher, with lifetimes of $T_1 \sim 30\,\mathrm{ms}$ [54] to even $T_1 \sim 1\,\mathrm{s}$ [55].

To control and measure the quantum state of a linear oscillator, it is often coupled to a nonlinear superconducting circuit, such as a transmon, as shown in fig. 1.3. Such a system was first studied in the context of measuring the transmon - if the oscillator is also strongly coupled to a microwave transmission line (not shown), the energy level of the nonlinear circuit can be read out in a non-destructive manner [56, 57]. However, with the advent of high-quality-factor 3D cavities, focus has shifted to using these cavities to store quantum information in bosonic error correcting codes such as the GKP code.

The quantum state of the oscillator and transmon is controlled by applying shaped microwave drives, $\varepsilon(t)$ and $\Omega(t)$, at frequencies resonant with the oscillator and transmon respectively. Here, the nonlinearity of the junction is essential for quantum control. The topic of quantum control of this type of system is a central part of this work, and is discussed in depth in chapter 2. Finally, the setup also contains a low-Q oscillator, fabricated as a distributed-element superconducting resonator on the same chip as the transmon. This second resonator is strongly coupled to a transmission line and used to measure the energy level of the transmon, a process called readout. This is the only element in the setup that is used for measurement, and the quantum state of the high-Q oscillator is only measured through its interaction with the transmon.

The architecture shown in fig. 1.3c - a transmon strongly coupled to a high-coherence storage oscillator - was first developed for the realization of a different type of bosonic code, called cat codes, where a logical qubit is encoded as superpositions of coherent states in the phase-space of an oscillator [23]. To realize the cat encoding, a control operation called the conditional-rotation (CR) gate is needed. The CR gate is an entangling gate between the storage oscillator and auxiliary qubit in which the state of the storage state rotates in phase-space by an angle that depends on the state of the qubit. This gate is, in some sense, natural to realize in this architecture, for reasons that will be elucidated in section 2.4.3.

The GKP code, on the other hand, is arguably more difficult to realize in cQED than the cat code (without taking fault tolerance into account). A few reasons for this are:

- As mentioned in the introduction, the GKP code states are very sensitive to a small amount of oscillator nonlinearity. For GKP code realization using the methods outlined in this work, we require $K/\kappa \lesssim 10^{-2}$, where K is the self-Kerr coefficient given the Hamiltonian $H/\hbar = K a^{\dagger 2} a^2$ and $\kappa = 1/T_1$ [19, 26]. Note that for the oscillators used in typical cat code experiments [58], $K/\kappa \sim 1$, and for a transmon, $K/\kappa \sim 10^5$.

- The entangling operation needed for measurement of displacement operators is called the conditional displacement interaction[15] [59], and this operation is not native in the transmon-oscillator architecture. The conditional displacement needs to be engineered

---

[15] Also called the conditional-translation or the state-dependent-force.

out of the native operations that are available, and it should be fast relative to the rate of photon loss of the oscillator.

- The photon-number probability distribution of the GKP code is a thermal distribution (a geometric distribution) with a long tail [19]. Because of this, GKP states with typical squeezing require coherent manipulation of wave-function coefficients up to one-hundred or more photons in the oscillator. However, in superconducting circuits, it has been shown in a number of experiments that populating an oscillator coupled to a transmon with a large photon number leads to un-recoverable errors of the transmon [60–63]. In typical coupling regimes, these effects emerge when populating the oscillator with tens of photons, and previous to this work, coherent quantum manipulation of oscillator states with distributions up to hundreds of photons had not been achieved.

1.3 Main results

The first main result of this dissertation is the experimental and theoretical development of a novel cQED architecture for the universal quantum control and measurement of an oscillator with a Kerr coefficient of $K/2\pi \sim 1\,\mathrm{Hz}$ and relative control rate of $T_{\mathrm{gate}}/T_1 \lesssim 10^{-2}$, where T_{gate} is the typical time for operations. Our results demonstrate quantum control of an oscillator in a linear regime that, to the best of my knowledge, had not previously been achieved [25, 26]. The theory for this development is introduced in chapter 2, and the experimental demonstration and technical details are discussed in chapter 4. The architecture we developed consists of a few essential components,

- A superconducting qubit weakly coupled to a high-quality-factor ($Q = \omega\tau \approx 10^7$) oscillator with a small relative-nonlinearity of $K/\kappa \sim 5 \times 10^{-3}$, allowing occupation of ~ 1000 photons in the oscillator without major issues (section 4.2.1).

- A fast, microwave-activated qubit-oscillator entangling operation - the echoed conditional displacement (ECD) gate - that can be turned on and off to achieve sufficient

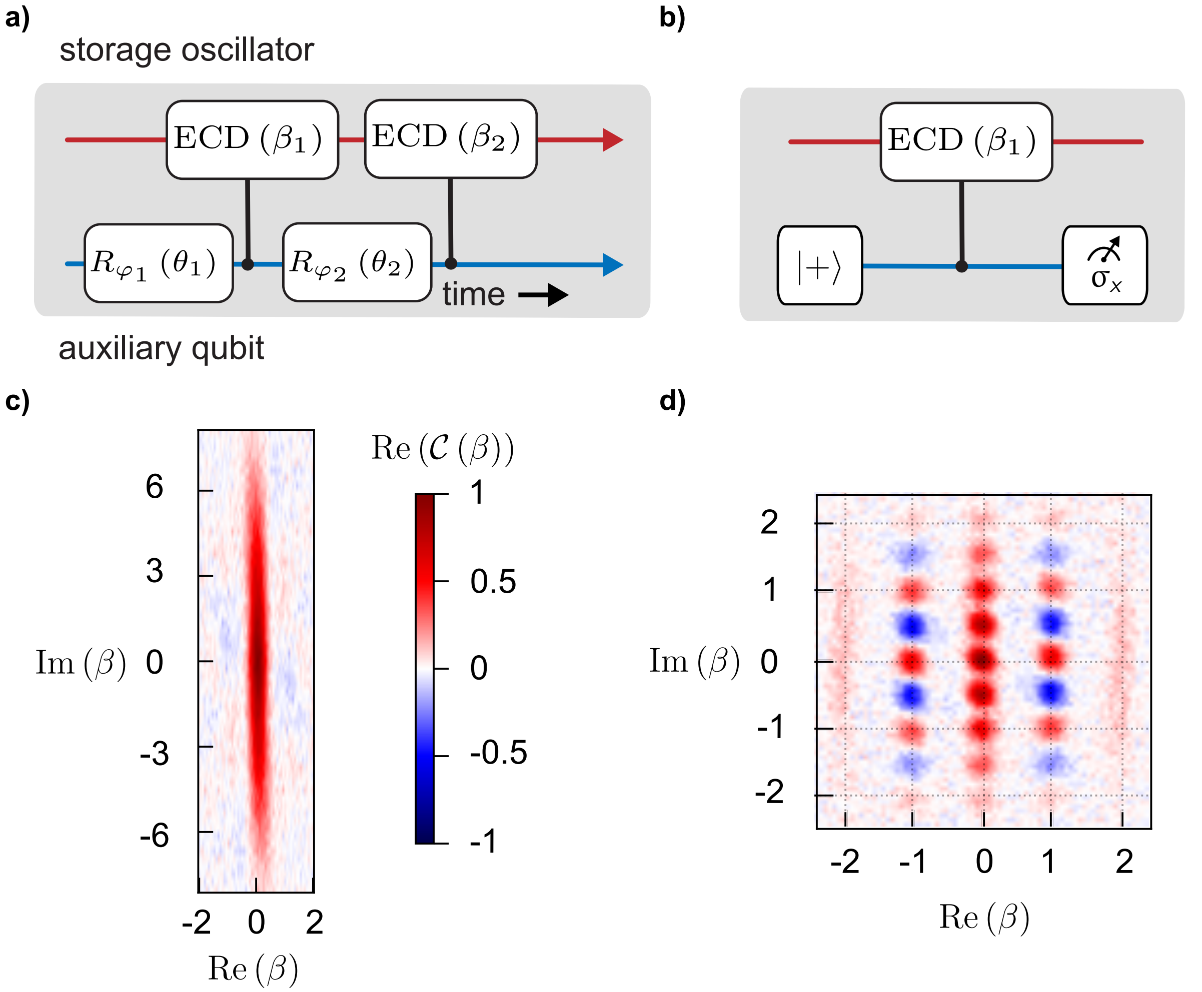

Figure 1.4: **Control of a nearly-linear oscillator. a)** A unitary circuit constructed with the phase-space instruction set architecture. The top rail (red) represents the oscillator, while the bottom rail (blue) represents the auxiliary qubit. ECD gates (eq. (1.26)) and qubit rotation gates are interleaved, and this general construction allows for the realization of arbitrary unitaries, where the number of gates required depends on the target unitary and the circuit parameters are found through numerical optimization. **b)** Measurement circuit for the real part of a displacement operator, $\langle\sigma_x\rangle = \langle D(\beta)\rangle$, giving the characteristic function. **c) and d)** Measured characteristic functions for state preparation of position-squeezed state **(c.)** and a finite-energy GKP $|+Z\rangle$ logical state **(d.)**, using the same colorbar. Data taken from [25].

isolation in the ‘off’ state (section 3.3).

- A set of calibration, characterization, and measurement routines in this novel coupling regime where previous methods fail, including a fast open-quantum-system simulation technique (section 3.2).
- An instruction-set-architecture (ISA) for realizing universal control and measurement of an oscillator and qubit based on the ECD gate, and an algorithm for numerical unitary gate synthesis (section 2.4.5).

A central result of these developments is the engineering of the echoed-conditional-displacement (ECD) gate, first introduced in [26, 45] and further developed in [25], which enacts the qubit-oscillator entangling operation

$$\mathrm{ECD}\left(\beta\right) = D\left(\frac{\beta}{2}\right)\left|e\right\rangle\left\langle g\right| + D\left(\frac{-\beta}{2}\right)\left|g\right\rangle\left\langle e\right|. \tag{1.26}$$

As shown in fig. 1.4a, when the ECD gate is interleaved with rotations of the auxiliary qubit, $R_{\varphi}(\theta) = \exp\left[-i(\theta/2)\left(\sigma_x\cos\varphi + \sigma_y\sin\varphi\right)\right]$, this forms a universal gate set called the phase-space instruction set architecture. Using this type of control, arbitrary unitaries on the storage oscillator and auxiliary qubit can be performed.

The ECD gate can also be used to measure displacement operators through the phase estimation circuit shown in fig. 1.4b. These measurements are used to measure the characteristic function in experiment, $\mathcal{C}\left(\beta\right)$.

To demonstrate this control and measurement, we have used the phase-space ISA to prepare a squeezed state and a finite-energy GKP logical $\left|+Z\right\rangle$ state in the oscillator and measured their characteristic functions, as shown in fig. 1.4c and fig. 1.4d. To the best of my knowledge, the squeezed state shown is the most-well-resolved position distribution (the largest squeezing) state that has been prepared in measured in the microwave regime. These results and others are detailed more in section 3.3.

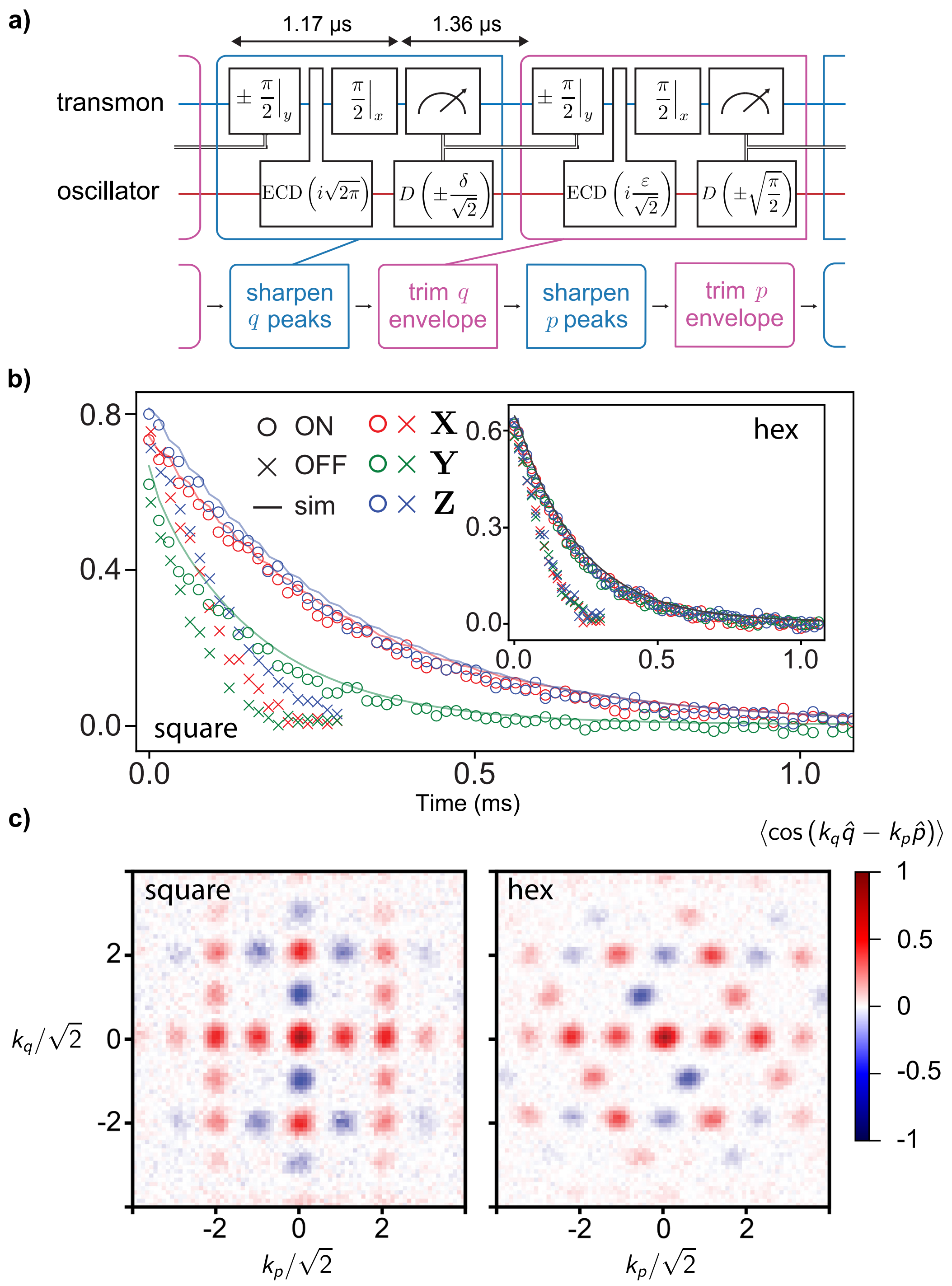

Figure 1.5: **Quantum error correction of the GKP code.** **a.)** The sharpen-trim quantum error correction protocol for the finite-energy GKP code. Double lines represent the flow of classical information, used for real-time feedback displacements. **b.)** Results of the uncorrected (crosses) and corrected (open circles) square and hexagonal GKP codes using the sharpen-trim protocol. The hexagonal code is shown in the inset. **c.)** Measured characteristic functions for the finite-energy $\pi/8$ states (eq. (1.27)) in the square code (left) and hexagonal code (right) using a measurement-based gate teleportation protocol. Data taken from [26].

The second main result of this PhD work is the development and experimental demonstration of real-time quantum error correction for the finite-energy GKP code [26]. This development was enabled by the architecture introduced in the previous section. The protocol introduced in this experiment has led to more optimal protocols [64, 65]. By combining these with model-free reinforcement learning, we have achieved stabilization of a quantum memory with coherence beyond break-even, meaning the logical qubit stabilized in the quantum memory lives longer than the bare decay rate of the oscillator [27, 44].

The first QEC protocol used in 2020, called the sharpen-trim protocol, is shown in fig. 1.5a. Consisting of two parts, the 'sharpen' step is a one-bit measurement of the imaginary part of the stabilizers. As introduced in section 1.2.2, this measurement is sensitive to small displacements. After each measurement, a small 'kick' is applied to the oscillator, stabilizing the GKP grid. The second part of the protocol, the 'trim' step, is used to confine the energy of the GKP code, leading to stabilization of a code with finite squeezing. As shown in the figure, the four-round protocol consists of sharpen-trim rounds for both position and momentum. Each round is about 2.5 µs and includes a fast classical feedback displacement depending on the result of each measurement using a field-programmable gate array (FPGA) with latency of about 200 ns.

To measure the performance of this QEC protocol, the logical $\{\left|+X\right\rangle, \left|+Y\right\rangle, \left|+Z\right\rangle\}$ states of the GKP qubit are prepared using measurement and feedback. As shown in fig. 1.5b, after a time t (shown on the x-axis), the expectation values $\{\langle X\rangle(t), \langle Y\rangle(t), \langle Z\rangle(t)\}$ are measured without performing QEC - the results are shown as the crosses. The same measurement is then performed when turning on the QEC sharpen-trim protocol, the results of which are shown as the open circles. As a result of the QEC protocol, the lifetime of the corrected GKP logical qubit is about twice as long as the uncorrected GKP qubit.

As introduced in section 1.2.2, the area-law commutation relation of translation operators allows other grids in phase space to be defined and used as logical qubits. The code discussed so far is called the square GKP code, where the logical X and Z operators are corners of a square. An alternative GKP code is called the hexagonal GKP code, where the logical X,Y, and Z operators define a hexagonal unit cell in the characteristic function. The hexagonal GKP code can also be stabilized using a six-round sharpen-trim protocol, with lifetime results shown in the inset of fig. 1.5b. In the hexagonal code, the lifetimes of all Pauli operators are equal.

Finally, using the ECD gates and measurements, arbitrary control of the finite-energy GKP qubit can be performed with a measurement-based gate-teleportation protocol [26,66]. As an example of this, we prepared the logical $\pi/8$ state, given by

$$|\psi\rangle = \cos\left(\frac{\pi}{8}\right)|{+X}\rangle - \sin\left(\frac{\pi}{8}\right)|{-X}\rangle\,. \tag{1.27}$$

The measured characteristic functions of the $\pi/8$ states in both the square GKP code and the hexagonal GKP code are shown in fig. 1.5c.

It is clear that grid states hold promise in realizing a quantum advantage for FTQC, sensing, and communication [22]. The remainder of this thesis introduces and reviews the experimental and theoretical results that could hopefully be used to eventually scale up to a multi-oscillator GKP encoding.

Chapter 2

Bosonic quantum control

2.1 The goal of quantum control

Any transformation that a quantum system can physically undergo is described by a completely-positive trace-preserving map $\mathcal{E} : \rho \to \mathcal{E}(\rho)$ called a *quantum channel* [2]. The goal of quantum control, from an experimentally-motivated point of view, is to realize a quantum channel $\mathcal{E}$ in the presence of noise that is as close as possible to a target channel $\mathcal{E}_{\text{target}}$ under a relevant metric.

In many contexts, the target channel is unitary, $\mathcal{E}_{\text{target}}(\rho) = U\rho U^\dagger$. Here, the closeness is quantified by the average channel fidelity,[1]

$$\bar{\mathcal{F}}(\mathcal{E}, U) = \int d\psi \, \langle\psi| U^\dagger \mathcal{E}(\psi) U |\psi\rangle \,, \tag{2.1}$$

where the integral is taken over the uniform measure in state space called the Harr measure. Nielsen gives a simple formula for measuring the average channel fidelity for a qudit [67], and we use this formula later in this dissertation for measuring the performance of QEC against the target identity channel.

---

[1] Also called the gate fidelity.

In many cases, we are instead interested in preparing an engineered quantum system in some target density matrix, σ. Given that we actually prepare our system in state ρ, the quantity of interest is the state fidelity,

$$\mathcal{F}\left(\sigma,\rho\right)=\left(\mathrm{Tr}\left(\sqrt{\sqrt{\rho}\sigma\sqrt{\rho}}\right)\right)^2. \tag{2.2}$$

In the case where the target state is pure, $\sigma = \left|\psi_t\right\rangle\left\langle\psi_t\right|$, the state fidelity reduces to the overlap,

$$\mathcal{F}\left(\left|\psi_t\right\rangle\left\langle\psi_t\right|,\rho\right)=\left\langle\psi_t|\rho|\psi_t\right\rangle. \tag{2.3}$$

One simple interpretation of this formula is: if you prepare a classical mixture of the target state $\left|\psi_t\right\rangle$ with probability p, and some other orthogonal state $\left|\psi_\perp\right\rangle$ with probability $1-p$ such that $\rho = p\left|\psi_t\right\rangle\left\langle\psi_t\right| + (1-p)\left|\psi_\perp\right\rangle\left\langle\psi_\perp\right|$, the state fidelity will be $\mathcal{F}=p$. Finally, if the state you prepare is pure, $\rho = \left|\psi\right\rangle\left\langle\psi\right|$, then the fidelity reduces to the overlap squared, $\mathcal{F} = \left|\left\langle\psi_t|\psi\right\rangle\right|^2$. In all these cases, the goal of quantum control is to maximize the fidelity in experiment in the presence of systematic and stochastic noise.

2.2 Universality

The concept of universality originates from classical computer science, and it is best first understood in that context; I will first cover classical computational universality in section 2.2.1. Next, in section 2.2.2, I will discuss universality in discrete-variable and continuous-variable systems.

2.2.1 Classical computational universality

In the circuit model of classical computation, primitive operations called gates (OR, NOT, AND, etc...) act on bits and are strung together to realize a computation. A classical set of gates is said to be universal if a circuit exists using only gates from that set to perform any desired boolean function[2]. For example, the NAND gate on its own is universal, and so is the NOR gate[3].

If a classical gate set is universal, we may wonder how many gates it takes to compute a given boolean function? This is the question of classical circuit complexity. Interestingly, as shown using a simple counting argument by Claude Shannon in 1949, almost all Boolean functions on n bits require exponentially large circuits of at least $\sim 2^n/n$ gates to compute [68]. Only a minority of boolean functions require polynomaly many gates, and these are said to be 'feasible' or 'efficient'.[4]

To compare with the quantum case, it is also worth mentioning an alternative model of classical computation, called the artificial neural network. In a neural network, primitive units called neurons are strung together in a tree-like fashion acting on continuously-valued inputs as opposed to bits, and each neuron specified by a set of values called weights and biases. The neural network is also universal in the sense that it can approximate any function acting on those input values [71]. Importantly, however, there often exists efficient training algorithms to find the proper weights and biases needed to realize a given function, and in this sense neural networks can be programmed efficiently.

At their core, each neuron in a neural network is a primitive nonlinear function acting on inputs to produce an output. Such nonlinearity is essential for the neural network to be a universal function approximator. This is closely related to quantum universality; as we will see in the case of quantum control of continuous-variable systems, nonlinearity is also essential to realize all operations. Interestingly, in the neural network, the specific nonlinear

---

[2] This property is also called functional completeness.

[3] Assuming the FANOUT operation is also available.

[4] An interesting property of classical computation is universal gate sets exist which consist of only reversible gates. As an example, the Toffoli gate on its own is universal and reversible. Given this, classical computation can, in principle, be performed in a reversible way [69]. However, it takes energy to erase information; Landauer's principle states that the erasure of one bit of information necessarily requires an energy of at least $k_b T \ln 2$, where T is the temperature of the environment of the computer [70].

function used in each neuron is not important, and in some sense it is not difficult to build a universal classical model of computation by stringing together nonlinear primitive gates. A similar situation is true for quantum bosonic systems, where in principle any nonlinear interaction can be used to realize universality. However, some nonlinear interactions are easier to implement than others in superconducting circuits.

2.2.2 Quantum universality

Preliminaries

In the next two subsections, I will focus on quantum control of both finite-dimensional and continuous-variable[5] systems, using the language of either Hamiltonian-level control or gate-level control. Hamiltonian-level control (sometimes called pulse-level control) can be thought of as the problem of realizing a target quantum operation by manipulating time-dependent parameters in the Hamiltonian of an engineered quantum system. Gate-level control, on the other hand, is the problem of realizing a quantum operation from a set of well-defined quantum gates. One of the central messages of this dissertation is that designing a well-parameterized gate-set in a continuous-variable quantum system, where each gate is realized by pulse-level optimization, is essential for scaling up control of bosonic modes.

In the case of Hamiltonian control, we are interested in closed quantum systems that obey the Schrödinger equation[6]. That is, working in units such that the Hamiltonian is expressed in multiples of $\hbar$, the Schrödinger equation in operator form is

$$i\partial_t U(t) = H(t)U(t), \tag{2.4}$$

---

[5] Continuous-variable, or CV for short, is referencing the position and momentum of an oscillator, which are continuous. We will often refer to bosonic modes as continuous-variable quantum systems, even though they can also be expressed in a basis with a countably infinite number of discrete energy levels (Fock states).

[6] It's a bit paradoxical to even discuss control of closed quantum systems, since the ability to control the system necessarily exposes it to an external environment. However, for now, we will consider the influence of this environment to be negligible. Later, we will extend our discussion to open quantum systems, focusing on control in the presence of decoherence.

with initial condition $U(0) = I$ and system Hamiltonian $H(t)$. For engineered pulse-level control of a quantum system, we have $H(t) = H(\mathbf{u}(t))$ where $\mathbf{u}(t) = (u_1(t), u_2(t), ..., u_N(t))$, $\{u_i(t) \in \mathbb{R}\}$ is the set of control signals.

To understand quantum universality, it is useful to first note the following two product formulas (also called Trotter formulas) [72]: given two Hamiltonians, $\{H_A, H_B\}$, the identities

$$e^{-iH_A\delta t}e^{-iH_B\delta t}e^{iH_A\delta t}e^{iH_B\delta t} = e^{[H_A,H_B]\delta t^2} + O(\delta t^3), \tag{2.5}$$

$$e^{iH_A\delta t/2}e^{iH_B\delta t/2}e^{iH_B\delta t/2}e^{iH_A\delta t} = e^{i(H_A+H_B)\delta t} + O(\delta t^3), \tag{2.6}$$

can be used to generate the action of the Hamiltonian $-i[H_A, H_B]$ and the Hamiltonian $H_A + H_B$ in the limit $\delta t^3 \to 0$ with finite δt^2 and δt [73]. [7] By repeated application of the identities above, we can generate evolution which is any superposition of nested commutators of the original set of generators. This relation is the key to gaining an intuition about quantum control - the more steps in a control process, the higher and higher order nested commutators we can generate. In the language of nonlinear bosonic systems, the longer a control pulse (or the stronger a control pulse), the higher-order nonlinear interactions we can generate from nested commutators of the control Hamiltonians. This is quite similar to the problem of realizing time-dependent quantum simulation with Trotter techniques [75].

In the next three sections, I will discuss quantum universality in three different cases: finite-dimensional systems, continuous-variable systems, and the realization of arbitrary quantum channels on an oscillator.

Finite-dimensional universality

Before moving to control of continuous-variable systems, I will discuss control of a finite-dimensional system. Examples include a qubit, high-dimensional spin, or set of many qubits. Understanding quantum control in this context is important to contrast it with continuous

---

[7] The first of these identities is sometimes called the parallel parking theorem with analogy to the classical task of parallel parking a car [74].

variable systems in the next subsection. For readers unfamiliar with basic single-qubit and two-qubit gates (such as T,S,$CNOT$,...), I recommend the introduction in [76]. In the finite-dimensional case, we define Hamiltonian-level universality in the following way:

> An $n \times n$ Hamiltonian $H(\mathbf{u}(t))$ is universal if for every $n \times n$ unitary matrix U with $\det(U) = 1$ there exists a set of control pulses $\mathbf{u}(t)$ for which the solution of eq. (2.4) at some time $t = T > 0$ is U.[8]

Given a finite-dimensional Hamiltonian, a procedure called the Lie algebra rank condition can be used to determine if it is universal [77]. This procedure is carried out in the following way: we first find set of operators $S_0 = \{A_1, A_2, ...\}$ that form a basis for the space spanned by $-iH(\mathbf{u})$, where the control fields $\mathbf{u}$ take on all possible values[9]. Next, we use a iterative process: at each step k, we find a new set S_k consisting of all linearly independent operators formed by commutators $[X, Y]$ where $X, Y \in S_{k-1}$. In this way, we build up all possible linearly independent operators that can be generated with nested commutators ($[A,[B,[...,[C,D]]]]$) of the original set $A, B, C, ..., D \in S_0$. Once we find that $S_k = S_{k-1}$, the procedure stops. If $\dim(S_k) = n^2$ or $\dim(S_k) = n^2 - 1$, the set generated is equivalent to the Lie algebra $u(n)$ (or $su(n)$), and the Hamiltonian is universal [77].

As a simple pedagogical example, consider the case of a qubit described by the Hamiltonian $H_q = \omega\sigma_z/2 + \Omega(t)\sigma_x/2$, where we can control $\Omega(t) \in \mathcal{R}$. A basis set for the control is $S_0 = \{-i\sigma_z, -i\sigma_x\}$. Clearly, $S_1 = \{-i\sigma_z, -i\sigma_x, -i\sigma_y\}$. Since $\dim(S_1) = 3 = n^2 - 1$, the Hamiltonian is universal; any state on the qubit Bloch sphere can be reached, and any unitary can be performed. However, in this case the time it takes to perform a given unitary on the qubit will be limited by ω and the maximum value of Ω. This type of limit on evolution

---

[8] H is said to be *operator-controllable* if all $n \times n$ unitaries can be performed. The Hamiltonian is said to be *state-controllable* for unitaries with determinant unity (the special unitary group). Operator-controllable Hamiltonians can perform any pure state transformation $|\psi_i\rangle \rightarrow e^{i\phi}|\psi_f\rangle$, where the phase ϕ can be controlled. State-controllable Hamiltonians can not control this global phase. For this dissertation, the distinction is not important (see [77]).

[9] Here we're interested in Lie algebras of Skew-Hermitian operators, hence the $-i$.

is often called the quantum speed limit [78–81]. Furthermore, note that the universality condition does not mean we can have full control of the state for all times t, it instead means we can find the pulse to generate a desired unitary after some time T. For example, in the case of the qubit H_q, realizing the identity operation $U = I$ could be performed by $\Omega(t) = 0$ for a time $T = 2\pi/\omega$,[10] however we cannot 'stop' the evolution.

Instead of working with Hamiltonian control directly, we often define a set of quantum gates and use those to build up unitaries, similar to the case of classical computation. Such a gate set can be either a continuously-parameterized family of gates (a set which includes at least one gate parameterized by a real number) or a discrete set. For example, for a single qubit, the set $\{\exp\left(-i\theta_z\sigma_z/2\right), \exp\left(-i\theta_x\sigma_x/2\right)\}$ is a continuous family while $\{H, T\}$ is a discrete family. Compared to Hamiltonian-level control, in an experimental context, a gate set is easier to calibrate, optimize, and error-budget than full Hamiltonian control, and it is of course needed to scale up to multiple qubits. Although the discussion here is focused on control of physical qubits, it should be noted that for logical qubits in quantum error correction, we instead work with a discrete set of logical gates; the discreteness of the gate set is important for fault-tolerant constructions [2, 11], and the same concept of universality also applies.

A continuously-parameterized finite-dimensional gate set can be universal in a similar sense as Hamiltonian control: if the gates can be strung together to realize any unitary on the space exactly, we call the set universal. For a set of qubits, the first universal gate set given by Deutsch in 1989 with the controlled-controlled-rotation gate, which was also the introduction of the circuit model of quantum computation [82]. Later, in 1995, it was shown that arbitrary single-qubit rotations along with the CNOT gate is universal in this sense [83, 84]. It is not hard to find a universal gate set; in 1995 it was shown that almost all quantum gates involving two or more qubits are universal [85, 86].

The case of a finite-dimensional discrete gate set is slightly different. Since there are an

---

[10] This would give a global phase of -1. We could also use $4\pi/\omega$ for a true identity.

uncountable number of possible $n \times n$ unitaries, and a countable number of possible circuits from a discrete gate set, the best we can do is hope to realize every unitary approximately. In this case, a discrete $n \times n$ quantum gate set is said to be universal if gates from the set can be strung together to approximate any $n \times n$ unitary operation U with $\det(U) = 1$ to within a desired accuracy ϵ. Here, the accuracy of the unitary implemented by the approximate circuit U' is quantified by the *operator norm*[11], $\epsilon = \max_{|\psi\rangle} ||(U - U') |\psi\rangle ||_2$.[12]

An important example of a discrete gate set acting on qubits that is *not* universal is the *Clifford* group, generated by $\mathcal{C} = \{H, S, CNOT\}$. Quantum circuits generated using the Clifford group (along with state preparation and measurements in the computational basis) are called *stabilizer circuits*, and these circuits are important for quantum error correction as discussed in [11]. Importantly, the Gottesman-Knill theorem states that these circuits can be simulated efficiently using classical computation [88, 89]. Thus, circuits made using only the Clifford group can not be used for a quantum computational advantage. Interestingly, any single non-Clifford gate can be added to the Clifford group for a universal gate set. Out of these, an discrete gate set that is important for QEC is the set $\mathcal{C} \cup \{T\}$ (the Clifford group along with the T gate) [90].

Besides the Gottesman-Knill theorem, there is another important theorem related to quantum control called the Solovay-Kitaev theorem. Given that a discrete universal gate set acting on n qubits, the Solovay-Kitaev theorem states that an arbitrary unitary can be realized up to an error ϵ (in the operator norm) using $O\left(4^n \text{polylog}\left(1/\epsilon\right)\right)$ gates [91, 92], and an explicit algorithm is given to realize this approximation. This is quite useful for low-dimensional cases, such as a single qubit or a few qubits, however it still requires an exponential number of gates in the number of qubits to realize a general unitary. In section 2.2.1 it was pointed out that, for classical computation, most boolean functions

---

[11] the operator norm is useful because any measurement performed after applying U or U' has probabilities that differ by at most 2ϵ [2]

[12] If we wish to perform a circuit $U_k U_{k-1} ... U_1$ and approximate each unitary U_k with error ϵ, the errors add linearly, with a total error bounded by $k\epsilon$ [87].

require an exponential number of gates. Perhaps unsurprisingly, the same holds for quantum circuits as well: almost all $2^n \times 2^n$ unitaries acting on n qubits require an exponential number ($\sim 2^n$) of gates [93]. The circuits that require a number of gates that is polynomial in the number of qubits are said to be efficient, and finding these is the topic of quantum algorithms [2, 94].

Continuous-variable universality

We are now in a position to discuss universality in continuous-variable (CV) bosonic systems. A basic understanding of quantum oscillators (bosonic modes) is needed for this section; for readers unfamiliar with these concepts, please see the introduction in section 1.2.3 and the more detailed description in appendix A. In these systems, we will often call a description of a specific gate set along with an associated list of possible measurements an instruction-set-architecture (ISA); it contains all the fundamental operations available in a hardware platform needed to communicate between quantum hardware engineers and computer scientists [95].

For oscillators, we must modify our notion of universality, as their continuous-variable nature makes the notion of universality different from the finite-dimensional spaces discussed in the previous section [73,96]. For both Hamiltonian-level control and gate-level control, we have two options to define CV universality. In a first definition, a CV gate set is universal if the set can approximately[13] generate all unitaries on a subspace defined by the first N Fock states, where N can be as large as desired. This is the type of universality taken by a gate-set called the SNAP and displacement gate set [97] (also called the Fock-space ISA), and it will be discussed in more depth in section 2.4.3. A second approach to defining universality for CV systems is to show that a Hamiltonian or gate set can approximately generate unitary

---

[13] In the sense of the operator norm.

transformations of the type

$$U = \exp\left(-i\left(\sum_{m,n=0}^{k} c_{mn} a^{\dagger m} a^{n} + \text{h.c.}\right)\right), \tag{2.7}$$

that is, unitaries generated by polynomial Hamiltonians up to order k where $c_{mn} \in \mathbb{C}$. If k can be as large as desired, the control scheme is universal.

The polynomial-Hamiltonian definition of universality (the latter definition in the previous paragraph) can also be expanded to universality over multiple modes, including hybrid bosonic-qubit systems. For example, universality in a two-mode bosonic system can be defined as the ability to realize arbitrary unitaries of the type

$$U = \exp\left(-i\left(\sum_{m,n,u,v=0}^{k} c_{mnuv} a^{\dagger m} a^{n} b^{\dagger u} b^{v} + \text{h.c.}\right)\right), \tag{2.8}$$

and universality in a hybrid bosonic-qubit system is the ability to realize all unitaries of the type

$$U = \exp\left(-i\left(\sum_{\sigma_i \in \{I, \sigma_-, \sigma_+\}} \sum_{m,n=0}^{k} c_{mni} a^{\dagger m} a^{n} \sigma_i + \text{h.c.}\right)\right). \tag{2.9}$$

This is the approach to universality taken by the ECD gate set [25] (also called the phase-space ISA) introduced as part of this dissertation work and discussed in section 2.4.5.

In both definitions of CV universality, proving that a Hamiltonian or gate-set is universal follows the same procedure as outlined in section 2.2.2: nested commutators can be used to find the Lie algebra associated with a control scheme. In the Fock-space definition of universality, if the Lie algebra spans $su(N)$,[14] and N can be chosen as large as needed, the scheme is universal. In the phase-space case, if the Lie algebra can be used to generate Hamiltonians polynomial in a and $a^\dagger$ up to order k, and k can be chosen as large as needed,

---

[14] The special unitary algebra of dimension N, given by the set of traceless anti-Hermitian $n \times n$ complex matrices.

the scheme is universal.

Channel universality

There is one final notion of universality, and that is *quantum channel universality*, defined as the ability to realize any completely-positive trace-preserving map $\mathcal{E} : \rho \to \mathcal{E}(\rho)$ (including those which are non-unitary). Any quantum channel can be written in the operator sum representation,

$$\mathcal{E}(\rho) = \sum_{k}^{N} E_k \rho E_k^\dagger, \tag{2.10}$$

where the operators E_k are sometimes called Kraus operators, and the number of Kraus operators, N, is called the rank of the channel.

In the setting of a hybrid qubit-oscillator system, it was shown in [98] that any channel acting on the oscillator with rank N can be realized in $\log_2 N$ steps by using an auxiliary qubit. This scheme requires a universal hybrid qubit-oscillator gate set, measurement, and feed-forward. For example, the phase-space ISA in section 2.4.5 could be used with measurement and feed-forward to realize any arbitrary quantum channel on the oscillator. When the target channel is non-unitary, this construction is an example of quantum dissipation-engineering. The experimental quantum error correction of the GKP code demonstrated later in this dissertation (chapter 5) can be thought of as a realization of dissipation-engineering with the phase-space ISA using rank-2 quantum channels [26, 64, 99].

2.3 Gate-based quantum control of oscillators

In an eventual FTQC using oscillators, a discrete and fault-tolerant gate set acting on the error-corrected logical qubits (encoded in the quantum correlations across multiple oscillators) will be used to perform quantum algorithms. However, for near-term NISQ applications, it is likely that using the bosonic nature of oscillators will lead to some advantage for quantum simulation compared with the case of using multiple qubits [95]. In both cases, a model for control will be needed that extrapolates between the desired quantum algorithm/application and the actual pulse sequences played on the hardware.

Often when dealing with control of a single oscillator (or a small number of oscillators), full Hamiltonian-level control is used to realize all desired unitary operations and state preparation. In these cases, a model of the system Hamiltonian is produced, and optimal control theory (OCT) [100] (including GRadient Ascent Pulse Engineering (GRAPE)) or other related optimization techniques are used to find the desired pulse sequence [101–105]. However, full pulse-level control will be difficult to scale up to multiple oscillators, especially when practical experimental considerations are taken into account. A central message of this dissertation is that it is best to define a CV gate-set (either continuously parameterized or discretely parameterized), and such a gate-set will be helpful when scaling, especially in a NISQ setting.

The gate-set for continuous-variable systems should be chosen in a well-parameterized way such that it is expressive enough to realize complex unitaries, however it should not over-parameterized. Furthermore, it is advantageous to pick a set of fundamental gate operations that have some symmetries built in, such as the dynamical decoupling of low-frequency noise in the hardware. As discussed later in chapter 4, this is the case for the ECD gate set. Once the gate set is well-defined, the experimental pulses used for each gate can be optimized at the hardware level, and individually for each module in a multi-oscillator system. For this, an attractive choice is closed-loop model-free optimization [103]. Here, pulse-level controls for each gate can be routinely adjusted to account for small drifts in system parameters over time and account other hardware-level nonidealities that cannot be easily included in a model.

In the following sections, I will discuss the primitive gate operations for continuous-variable systems. These include Gaussian operations (section 2.3.1), non-Gaussian operations (section 2.3.2), and hybrid qubit-oscillator entangling operations (section 2.4). Although our experimental work is focused on the realization of the phase-space ISA, a basic understanding of these other operations is needed to put our work in context and for the realization of logical gates on GKP codes. With that in mind, throughout the following sections I will give context of how operations are related to the GKP encoding.

2.3.1 Gaussian operations

Single- and multi-mode bosonic Hamiltonian terms that are polynomial in the annihilation and creation operators can be grouped into two categories: those which are quadratic order or lower (such as $H \propto a^2 + a^{\dagger 2}$), called Gaussian, and those which are degree three or higher (such as $H \propto a^3 + a^{\dagger 3}$), called non-linear or non-Gaussian[15]. The reason for this distinction is that all Gaussian Hamiltonians lead to linear equations of motion for the annihilation operator in the Heisenberg picture, $\hat{a}(t)$. For two oscillators A and B, with annihilation operators $\hat{a}$ and $\hat{b}$, the common Gaussian Hamiltonians that have names are:

- **'linear drive' or 'displacement':** $H \propto g^* a + g a^\dagger$;
- **'rotation' or 'detuning':** $H \propto a^\dagger a$;
- **'single-mode squeezing':** $H \propto g^* a^2 + g a^{\dagger 2}$;
- **'beam-splitting', 'conversion' or 'linear coupling':** $H \propto g^* a b^\dagger + g a^\dagger b$
- **'two-mode squeezing':** $H \propto g^* a b + g a^\dagger b^\dagger$
- **'quadrature-quadrature coupling':** $H \propto (g_a^* a + g_a a^\dagger)(g_b^* b + g_b b^\dagger)$

As indicated by eq. (2.5) and the discussion in previous sections, the control associated with a given Hamiltonian is the Lie algebra spanned by nested commutators of those control

---

[15] Gaussian Hamiltonians are sometimes called linear Hamiltonians (even though they could be quadratic in the creation and annihilation operators) because the Hamilton equations of motion corresponding to Gaussian Hamiltonians are linear. They are also sometimes called classical since they represent transformations for which the equations governing classical physics and quantum physics are the same [106].

operations. By evaluating nested commutators of Gaussian bosonic Hamiltonians, it is easily seen that the Lie algebra generated is closed, and no polynomial Hamiltonians of higher than quadratic order can be generated. For this reason, Gaussian transformations alone are not universal. The set of operations given above is also overcomplete for realizing Gaussian evolution; by evaluating nested commutators, it is easy to show that the single-mode Gaussians (displacement, rotation, single-mode squeezing) along with only one of either beam-splitting or two-mode squeezing is enough to realize all Gaussian operations on a multi-mode bosonic system.

The unitary transformations generated by Gaussian Hamiltonians also have a special property: they transform Gaussian quasi-probability distributions (characteristic functions and Wigner functions) into other Gaussians (hence the name). For bosonic modes initialized in a Gaussian state[16], evolution under Gaussian Hamiltonians can be simulated efficiently with classical computation by tracking how the mean and variance of each mode changes [107]. Additionally, Gaussian operations cannot introduce negativity into positive-valued Wigner functions.

There are also non-unitary transformations that preserve Gaussianity. The general class of quantum transformations $\mathcal{E}(\rho)$ that preserve the Gaussian nature of the (possibly multi-mode) characteristic and Wigner function are called Gaussian channels, and these include photon loss and amplification. For more info, I recommend the useful 2012 review article from Weedbrook *et al.* [107], our review on recent progress in GKP codes [22], or Kyungjoo Noh's thesis [43]. A few of these Gaussian channels are described in appendix A.3, and their effect on the characteristic function is analyzed.

If we represent the position and momentum of an N-mode bosonic system by the vector

---

[16] Note that the vacuum state, $|0\rangle$, is a Gaussian with zero mean $\langle\hat{q}\rangle = \langle\hat{p}\rangle = 0$ and variance governed by the Heisenberg uncertainty relation, $(\Delta\hat{q})^2 = (\Delta\hat{p})^2 = 1/2$.

Name	Definition	$\hat{a}, \hat{b}$ transformation
Displacement	$D(\alpha) = \exp\left(\alpha a^\dagger - \alpha^* a\right)$, $\alpha \in \mathbb{C}$	$D^\dagger(\alpha) a D(\alpha) = a + \alpha$
Rotation	$R(\theta) = \exp\left(-i\theta a^\dagger a\right)$, $\theta \in \mathbb{R}$	$R^\dagger(\theta) a R(\theta) = e^{-i\theta} a$
Single-Mode Squeezing	$S(\zeta) = \exp\left(\left(\zeta^* a^2 - \zeta a^{\dagger 2}\right)/2\right)$, $\zeta = re^{i\theta} \in \mathbb{C}$	$S^\dagger(\zeta) a S(\zeta) = a\cosh(\zeta) - e^{i\theta} a^\dagger \sinh(\zeta)$
Beam-Splitter	$\mathrm{BS}(\theta, \varphi) = \exp\left(-i\frac{\theta}{2}\left(e^{i\varphi} a^\dagger b + e^{-i\varphi} a b^\dagger\right)\right)$	$\mathrm{BS}^\dagger(\theta, \varphi)\, a\, \mathrm{BS}(\theta, \varphi) = \cos\frac{\theta}{2} a - i \sin\frac{\theta}{2} e^{+i\varphi} b$ $\mathrm{BS}^\dagger(\theta, \varphi)\, b\, \mathrm{BS}(\theta, \varphi) = \cos\frac{\theta}{2} b - i \sin\frac{\theta}{2} e^{-i\varphi} a$
Two-Mode Squeezing	$\mathrm{TMS}(r, \varphi) = \exp\left(\left(re^{i\varphi} a^\dagger b^\dagger - re^{-i\varphi} ab\right)\right)$	$\mathrm{TMS}^\dagger(r, \varphi) a \mathrm{TMS}(r, \varphi) = \cosh(r) a + e^{i\varphi} \sinh(r) b^\dagger$ $\mathrm{TMS}^\dagger(r, \varphi) b \mathrm{TMS}(r, \varphi) = \cosh(r) b + e^{i\varphi} \sinh(r) a^\dagger$
Two-Mode SUM	$\mathrm{SUM}(\lambda) = e^{-i\lambda \hat{x}_a \hat{p}_b}$	$\hat{q}_a \to \hat{q}_a \qquad \hat{p}_a \to \hat{p}_a - \lambda \hat{p}_b$ $\hat{q}_b \to \hat{q}_b + \lambda \hat{q}_a \qquad \hat{p}_b \to \hat{p}_b$

Table 2.1: **Single-mode and two-mode Gaussian unitary transformations** The gate definitions, parameters, and transformations acting on one (a) or two (a and b) mode annihilation operators are shown.

$\mathbf{x} = (\hat{q}_1, \hat{p}_1, \hat{q}_2, \hat{p}_2, ..., \hat{q}_N, \hat{p}_N)$, then all Gaussian channels apply a transformation of the form

$$\mathbf{x} \to \mathbf{S}\mathbf{x} + \mathbf{d} \tag{2.11}$$

where $\mathbf{S}$ is a symplectic matrix, and $\mathbf{d}$ is a vector representing the change of the mean value [107]. This description is powerful, as it allows us to write a unitary transformation (such as $U^\dagger a U$) in the form of a simple matrix multiplication. For the case of two bosonic modes, a fundamental generating set of parameterized Gaussian unitaries is given in table 2.1, along with their transformations on the mode operators, which are realizations of eq. (2.11) cast into the language of the annihilation and creation operators.

Figure 2.1 shows the action of the single-mode Gaussian transformations on the phase-space representations of the oscillator. The two-mode operations such as the beam-splitter and two-mode squeezing are more difficult to visualize. The (possibly detuned) beam-splitter is well represented by its action on the so-called operator-valued Bloch sphere, with more details found in [108]. The two-mode squeezing transformation, on the other hand, reduces the variance in the $\hat{q}_a - \hat{q}_b$ and $\hat{p}_a + \hat{p}_b$ plane of the four-dimensional, two-mode Wigner function. In particular, the variance in these two operators is reduced by the two mode squeezing factor e^{-2r}.

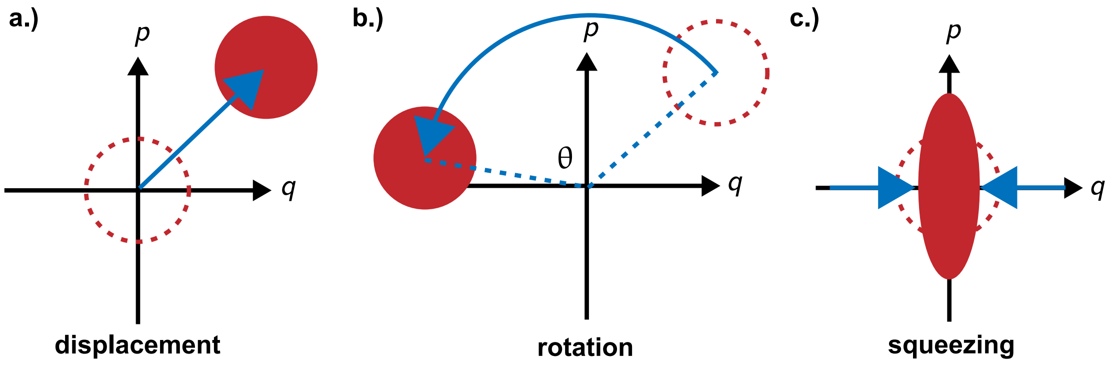

Figure 2.1: **Single-mode Gaussian operations acting on vacuum Wigner functions** **a)** Displacement operation shifts the state in phase space. **b)** Rotation operation rotates phase space by an angle θ. **c)** Squeezing reduces the variance in one quadrature at the expense of an increased variance in the orthogonal quadrature.

Finally, it should be noted that in the infinite-dimensional GKP code, the Gaussian unitary operations realize the Clifford group operations [1]. Compilation of general Gaussian unitaries into these primitive operations can be done efficiently by means of the Bloch-Messiah decomposition and other standard techniques [107]. As an example, the two-mode SUM gate $\text{SUM}(\lambda) = e^{-i\lambda\hat{x}_a\hat{p}_b}$ with $\lambda = 1$ acts as the infinite-dimensional CNOT on the square-lattice qubit-into-oscillator GKP code. These gates must be modified when realized on finite-energy GKP encodings (section 5.1.2).

The Gaussian operations of displacement, squeezing, and two-mode-squeezing can be combined with nonlinear interactions to enhance the effective nonlinear coupling rate, a procedure called Hamiltonian amplification. This effect is essential to realizing control of an oscillator in the weak-coupling regime, and it is covered in detail in section 2.4.4.

2.3.2 Non-Gaussian operations

As shown in the previous section, Gaussian Hamiltonians and unitaries on their own are not sufficient for universal control. However, as first shown by Lloyd in 1999 [96], the addition of a single non-linear Hamiltonian is enough for continuous-variable universality, even in a multi-mode setting! For example, the unitary generated by the Kerr Hamiltonian $H_K = Ka^{\dagger 2}a^2$

Name	Parameters	Definition
Cubic phase	$r \in \mathbb{R}$	$C(r) = \exp\left(-ir\hat{x}^3\right)$
Self-Kerr	$\theta \in \mathbb{R}$	$K(\theta) = \exp\left(-i\theta a^{\dagger 2} a^2\right)$
Cross-Kerr	$\theta \in \mathbb{R}$	$\chi(\theta) = \exp\left(-i\theta a^\dagger a b^\dagger b\right)$
Generalized squeezing	$z \in \mathbb{C}, N \geq 3$	$U_N(z) = \exp\left(z a^{\dagger N} - z^* a^N\right)$
SNAP	$\vec{\varphi} = \{\varphi_n\}, \varphi_n \in [0, 2\pi)$	$\mathrm{SNAP}(\vec{\varphi}) = \sum_n e^{-i\varphi_n} \lvert n\rangle \langle n\rvert$

Table 2.2: **Common nonlinear oscillator operations.** All operations listed require an external nonlinearity to be coupled to an otherwise linear oscillator for their realization. In addition, SNAP explicitly requires an auxiliary qubit.

(Kerr gate $U_K(\theta) = \exp\left(-i\theta a^{\dagger 2} a^2\right)$), together with the Gaussian operations, is sufficient for universal control, so the gateset $\mathcal{K} = \mathcal{G} \cup \{U_K(\theta)\}$ could be used alone for realizing arbitrary unitaries on the oscillator. In table 2.2, I have listed some of the most common oscillator-only non-Gaussian operations. The lowest order nonlinearity that can be used to realize a non-Gaussian gate is a cubic nonlinearity, $H \propto \hat{q}^3$, and the operation associated with this Hamiltonian is called the cubic-phase gate. This particular gate is important because it can be used, along with a SUM interaction, to realize a non-Clifford logical T gate on the infinite-energy GKP code [1].

In order to perform these gates, a source of nonlinearity is required, however such nonlinearity does not necessarily need to be an auxiliary qubit (this case is treated explicitly in the next section). For example, it was recently shown that by flux-pumping a SNAIL [109] (superconducting nonlinear asymmetric inductive element) coupled to an oscillator, a cubic-phase interaction can be generated, without Kerr nonlinearity [110, 111]. In the case of the Selective Number-dependent Arbitrary Phase (SNAP) gate [97], defined in table 2.2 and discussed in section 2.4.3, an auxiliary qubit is required.

Finally, an alternative approach to realizing non-Gaussian operations is to use non-Gaussian resource states instead of non-linear Hamiltonians. As an example, the cubic phase state, defined as $\lvert\gamma\rangle = \int dq e^{i\gamma q^2} \lvert q\rangle$, can be used along with Gaussian operations to realize a logical T gate in the GKP encoding using gate teleportation [1].

2.4 Qubit-oscillator entangling gates

The most common way to realize a nonlinear interaction and control the quantum state of a superconducting high-quality-factor oscillator is to couple it to a superconducting qubit (see section 1.2.3 for an introduction). For the sake of brevity, I will not discuss the detailed modeling of superconducting qubits here, as those details can be found in a number reviews [34, 76]. I will instead treat the auxiliary qubit as a two-level-system. In later chapters focused on the experimental realization, and where necessary throughout this chapter, I will discuss the implications of this assumption, and where it breaks down. Note that as of writing, the methods I will discuss and propose here have been demonstrated experimentally to different degrees; I will include experimental references where applicable.

Additionally, I will keep the discussion as general as possible, without specifying the exact qubit-oscillator system. This is because many hybrid bosonic systems share the same control mathematics and principles, with slight adjustments of each for various other effects. For example, in addition to their use in superconducting circuits, the conditional displacement and sideband interactions can be realized to control the motional state of a trapped ion [66, 112].

I will also discuss ISAs for realizing universal control of an oscillator and qubit, each consisting of a set of gates. A summary of the named gates in these ISAs is discussed is given in table 2.3. For each gate set, a desired unitary operation can be realized by interleaving the gates in the set, and optimizing the parameters of the circuit. Examples of these circuit constructions are shown in fig. 2.2. Additionally, the optimization of circuit parameters will be discussed in section 2.6.

Many physical systems consisting of a two-level-system (such as a superconducting qubit or Rydberg atom) coupled to a bosonic mode are described by the Rabi model [113]. This is a good starting point to discuss hybrid qubit-oscillator control. In the lab frame, and

Name	Parameters	Definition
Conditional rotation	$\theta \in \mathbb{R}$	$\mathrm{CR}(\theta) = \exp\left(-i\frac{\theta}{2}\sigma_z a^\dagger a\right)$
Selective Qubit Rotation	$\varphi_n, \theta_n \in \mathbb{R}$	$\mathrm{SQR}(\vec{\theta}, \vec{\varphi}) = \sum_n R_{\varphi_n}(\theta_n) \otimes \lvert n\rangle \langle n\rvert$
Jaynes-Cummings	$\theta, \varphi \in \mathbb{R}$	$\mathrm{JC}\left(\theta, \varphi\right) = \exp\left(-i\theta\left(a^\dagger \sigma_- e^{i\varphi} + a\sigma_+ e^{-i\varphi}\right)\right)$
Anti-Jaynes-Cummings	$\theta, \varphi \in \mathbb{R}$	$\mathrm{AJC}\left(\theta, \varphi\right) = \exp\left(-i\theta\left(a^\dagger \sigma_+ e^{i\varphi} + a\sigma_- e^{-i\varphi}\right)\right)$
Conditional displacement	$\alpha \in \mathbb{C}$	$\mathrm{CD}(\alpha) = \exp\left[\left(\alpha a^\dagger - \alpha^* a\right)\sigma_z\right]$
Rabi interaction	$\theta \in \mathbb{R}$	$\mathrm{RB}(\theta) = \exp\left[-i(\theta a^\dagger + \theta^* a)\sigma_x\right]$
Conditional squeezing	$\zeta \in \mathbb{C}$	$\mathrm{CS}\left(\zeta\right) = \exp\left[\frac{1}{2}(\zeta^* a^2 - \zeta a^{\dagger 2})\sigma_z\right]$

Table 2.3: **Hybrid Qubit-Oscillator entangling gates**

ignoring constant terms, the driven Rabi Hamiltonian is given by

$$H = H_{\mathrm{Rabi}} + H_{\mathrm{drive}}, \tag{2.12}$$

$$H_{\mathrm{Rabi}}/\hbar = \omega_a a^\dagger a - \omega_q \frac{\sigma_z}{2} + g\left(a + a^\dagger\right)\sigma_x, \tag{2.13}$$

$$H_{\mathrm{drive}}/\hbar = \varepsilon_{\mathrm{lab}}(t)(a + a^\dagger) + \Omega_{\mathrm{lab}}(t)\sigma_x. \tag{2.14}$$

The derivation of the Rabi Hamiltonian for the case of a superconducting qubit (approximated as a two level system) coupled to an oscillator can be found in [34]. Here, $\varepsilon_{\mathrm{lab}}(t) \in \mathbb{R}$ and $\Omega_{\mathrm{lab}}(t) \in \mathbb{R}$ are the lab-frame oscillator and qubit drives, respectively. I will denote the detuning between oscillator and qubit as $\Delta = \omega_a - \omega_q$. Also, by coupling the Rabi drive to σ_x, I am assuming a qubit with '$x - y$' control, and not 'z' control. This is motivated by the experiments using fixed-frequency transmons (see section 1.2.3), where there is no flux tunablility of the frequency. Some flux-tunable qubits have the additional ability of a σ_z drive, $\omega_q(t)\sigma_z$, which could be included in the gate set if desired [6].

As shown in appendix D, the classical oscillator and Rabi drives can be written as $\varepsilon_{\mathrm{lab}}(t) = \varepsilon^*(t)e^{i\omega_a t} + \varepsilon(t)e^{-i\omega_a t}$ and $\Omega_{\mathrm{lab}}(t) = \Omega^*(t)e^{i\omega_q t} + \Omega(t)e^{-i\omega_\Omega t}$ where $\{\varepsilon(t), \Omega(t)\} \in \mathbb{C}$ are the baseband envelopes modulating the carrier frequencies. Here, we have assumed the oscillator and qubit drive frequencies are near resonant with the the oscillator and qubit, respectively. Any additional drive detunings can be captured in the time-dependence of the phasors $\varepsilon(t)$ and $\Omega(t)$.

In the regime where $\omega_a + \omega_q \gg g$, which is typical in cQED, the rotating-wave approximation (RWA) can be invoked. In this approximation, fast rotating terms in the Hamiltonian are dropped. In this regime the Rabi Hamiltonian is reduced to the Jaynes-Cummings (JC) Hamiltonian,[17]

$$H_{\mathrm{JC}}/\hbar = \omega_a a^\dagger a - \omega_q \frac{\sigma_z}{2} + g(a^\dagger \sigma_- + a\sigma_+). \tag{2.15}$$

We note that the interaction term $(a^\dagger \sigma_- + a\sigma_+)$ is often called the Jaynes-Cummings interaction, while the term that was dropped $(a^\dagger \sigma_+ + a\sigma_-)$ is called the anti-Jaynes-Cummings interaction. A similar RWA can be performed on the drive terms, as shown in appendix D. Under these approximations, and applying a rotating-frame transformation at the oscillator and qubit frequencies, the model Hamiltonian in the rotating-frame can be written as

$$\tilde{H}/\hbar = g\left(a^\dagger \sigma_- e^{i\Delta t} + a\sigma_+ e^{-i\Delta t}\right) + \varepsilon^*(t)a + \varepsilon(t)a^\dagger + \Omega^*(t)\sigma_- + \Omega(t)\sigma_+. \tag{2.16}$$

This Hamiltonian is the starting point for a general discussion of control of an oscillator using an auxiliary qubit. In the following sections, I will focus on using $\tilde{H}$ in different regimes to realize quantum control with a gate-based approach. These gates can be can be performed by modulating $\varepsilon(t)$ and $\Omega(t)$.

For the qubit, by modulating $\Omega(t)$, we can realize a qubit rotation gate by angle θ around the $\cos(\varphi)\sigma_x + \sin(\varphi)\sigma_y$ axis of the Bloch sphere, with a unitary given by

$$R_\varphi(\theta) = \exp\left(-i\frac{\theta}{2}\left(\cos(\varphi)\sigma_x + \sin(\varphi)\sigma_y\right)\right). \tag{2.17}$$

Such a gate can be realized with the qubit drive term in eq. (2.16) by letting $\Omega(t) = \tilde{\Omega}(t)e^{i\varphi}$ with constant φ and real-valued envelope $\tilde{\Omega}(t)$ such that $\theta = 2\int_0^{T_{\mathrm{gate}}} d\tau\, \tilde{\Omega}(t)$. Often, the envelope is chosen to be a truncated-Gaussian or cosine waveform. Each qubit rotation gate should be performed quickly relative to the other effective Hamiltonian terms, with

---

[17] $\sigma_- = (\sigma_x + i\sigma_y)/2$,$\sigma_+ = (\sigma_x - i\sigma_y)/2$ are the qubit raising and lowering operators.

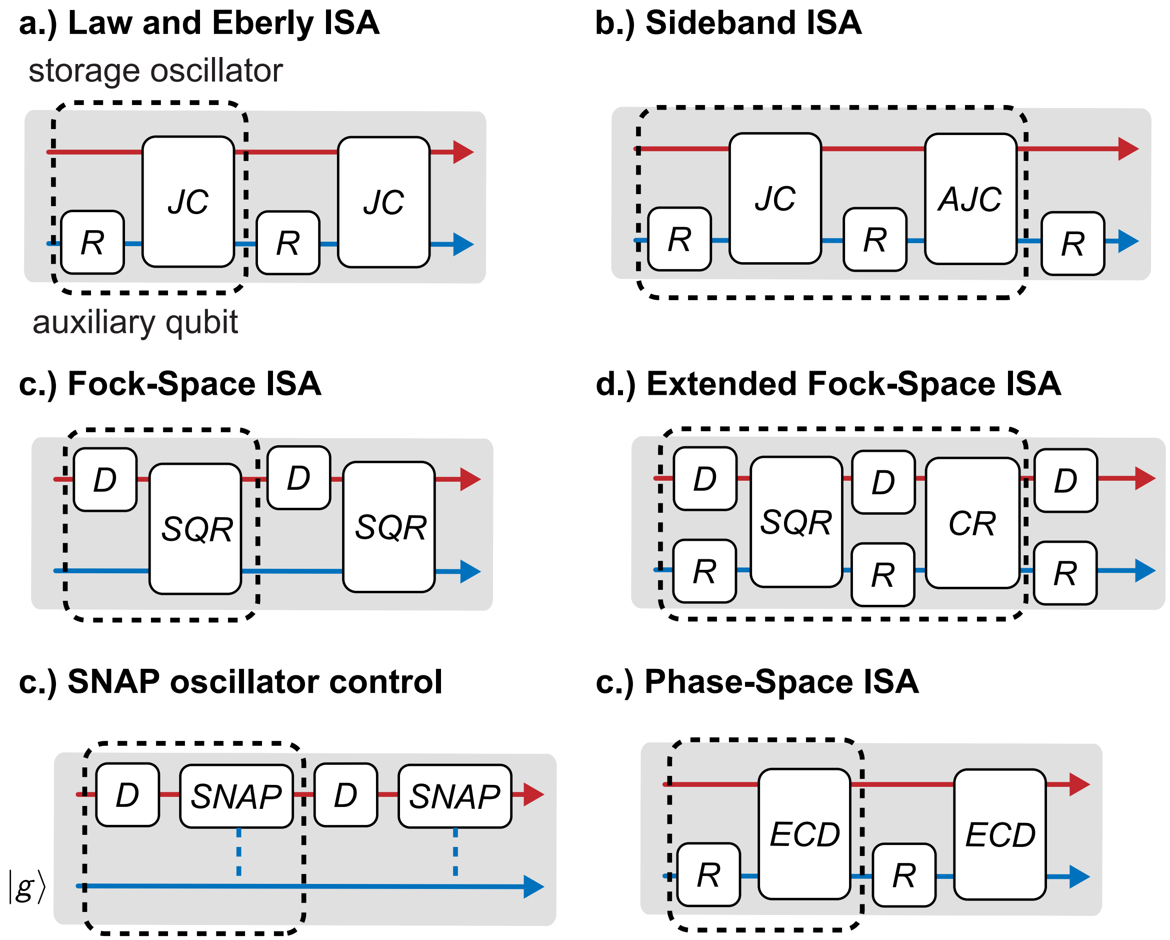

Figure 2.2: **Hybrid gate sets.** For each gate set shown, a single 'layer' of a circuit constructed using the gate set is outlined with a dotted line. The extended Fock-space gate set (part **d**) is an example of an overcomplete construction, where additional gates available in the hardware are included in a layer definition to aid in circuit optimization (see section 2.6)

different specific conditions discussed below. Note that the $R_\varphi(\theta)$ gate alone is sufficient for universal control of a single qubit.

2.4.1 Control in the resonant regime (Law and Eberly)

I will first consider the resonant regime, $\Delta = 0$. Specifically, I will consider the case where the JC interaction strength can be tuned or turned on and off in the resonant regime, with

Name	Gates	Comments
Gaussian	$\mathcal{G} = \{D(\alpha), S(\zeta), \mathrm{BS}(\theta,\varphi), \mathrm{TMS}(r,\varphi)\}$	Not universal
Cubic	$\mathcal{G} + \{C(r)\}$	Implemented in [111]
Quartic	$\mathcal{G} + \{K(\theta)\}$	Used in [114]
SNAP	$\{D(\alpha), \mathrm{SNAP}\left(\vec{\varphi}\right)\}$	Implemented in [115]
Law and Eberly	$LE = \{R_\varphi\left(\theta\right), \mathrm{JC}\left(\right)\}$	Implemented in [116]
Sideband	$SB = LE + \{\mathrm{AJC}\left(\theta\right)\}$	Implemented in [117]
Dispersive	$\mathcal{D} = \{D(\alpha), R_\varphi(\theta), \mathrm{CR}(\theta), \}$	Related to [118]
Fock-Space	$\mathcal{FS} = \{\mathrm{SQR}\left(\theta\right), D(\alpha)\}$	related to [119]
Phase-Space	$\mathcal{PS} = \{\mathrm{ECD}\left(\beta\right), R_\varphi\left(\theta\right)\}$	Theory and implementation in [25]
Hamiltonian	$\mathcal{H} = \left\{\mathcal{T}\exp\left(-i\int_0^{T_{\mathrm{step}}} \hat{H}\left(\mathbf{u}\left(\tau\right)\right)d\tau\right)\right\}$	similar to GRAPE

Table 2.4: **Universal hybrid qubit-oscillator gate sets discussed in this thesis.** with references to implementations given. Any gateset defined here for a qubit and oscillator can be combined with a beam-splitter operation to realize universal multi-mode control.

an additional controllable phase, such that $g(t) \in \mathbb{R} \rightarrow g(t) \in \mathbb{C}$.[18] Here, the Hamiltonian in the rotating frame of the qubit and oscillator takes the form

$$\tilde{H}_{LE}/\hbar = \left(g(t)a^\dagger\sigma_- + g^*(t)a\sigma_+\right) + \Omega^*(t)\sigma_- + \Omega(t)\sigma_+, \tag{2.18}$$

where I have purposefully omitted the oscillator drive[19], and LE stands for 'Law and Eberly' after their seminal 1996 article [120]. In superconducting circuits, this Hamiltonian could be achieved in a few ways:

- A tunable coupler between the qubit and oscillator, driven to realize a parametric beam-splitting interaction with either four-wave (such as in [121]) or three-wave (such as in [122]) mixing. The strength and phase of the parametric drive allow a controllable $g(t)$.

- A flux-tunable superconducting qubit or oscillator where low-frequency (DC) flux control can be used to quickly bring the two systems on-resonance ($\Delta = 0$) or off-resonance

---

[18] Even in situations where $g \in \mathbb{R}$, if the oscillator rotation gate is available $R(\theta)$, then a phase can be realized since $R^\dagger(\theta)aR(\theta) = e^{-i\theta}a$.

[19] A cavity drive could of course be used to aid with control, but is unneeded in this model for universality.

($\Delta >> |g|$) quickly relative to $1/|g|$ (see [6] and references therein).

- An effective resonant Jaynes-Cummings interaction realized in the dispersive regime ($g \ll \Delta$) using sideband driving, such as in [123, 124]. I will cover this method in section 2.5.3. The sideband method can also be used to realize an anti-Jaynes-Cummings type interaction and conditional displacements.

In this setting, a controllable Jaynes-Cummings unitary gate can be realized, defined as

$$\mathrm{JC}\left(\theta, \varphi\right) = \exp\left(-i\theta\left(a^\dagger \sigma_- e^{i\varphi} + a\sigma_+ e^{-i\varphi}\right)\right), \tag{2.19}$$

where $\theta = \int_0^T d\tau \, |g(\tau)|$, $\varphi = \text{angle}\left(g(t)\right)$,[20] assuming the phase is constant throughout the pulse.

In [120], Law and Eberly proposed a method to prepare arbitrary quantum states of an oscillator starting from vacuum using the gate set $LE = \{\mathrm{JC}\left(\theta, \varphi\right), R_\varphi\left(\theta\right)\}$. Their particular method can roughly be thought of as shuffling quanta, one-by-one, between the qubit and oscillator, such that the qubit is disentangled after each step. Remarkably, they were able to derive the speed limit at which this state preparation can be done given a maximum JC interaction strength and qubit drive amplitude.[21] In 2009, the Law and Eberly method was first used for a demonstration of arbitrary control of a superconducting oscillator by Hofheinz *et al.* [125]. [22]

However, the Law and Eberly method can be extended beyond state preparation. As is shown in appendix E.1, by evaluating nested commutators, the LE gate set is universal for

---

[20] defined as $\text{angle}\left(ae^{i\varphi}\right) = \varphi$.

[21] the total state preparation time is bounded by $T > \frac{M\pi}{2\Omega_{\max}} + \frac{\pi}{2g_{\max}} \sum_{j=1}^{M} \frac{1}{\sqrt{j}}$ where M is the maximum photon number in the oscillator state to be prepared [120]. It is interesting to note the *bosonic enhancement factor* $\sum_{j=1}^{M} \frac{1}{\sqrt{j}}$, which comes from the matrix elements associated with the JC interaction which scale like $\sqrt{a^\dagger a}$.

[22] Also see the 2007 paper from Houck *et al.* [116], demonstrating control of the $|0\rangle$,$|1\rangle$ subspace of a superconducting oscillator.

hybrid oscillator and qubit control. An example circuit construction using this gate set is shown in fig. 2.2a. Since the qubit rotation gates R can be performed when the effective $g(t) = 0$, there is no restriction on the bandwidth or speed of $\Omega(t)$.

2.4.2 Sideband instruction set

In some settings, a tunable on-resonance anti-Jaynes-Cummings interaction $\tilde{H} = \left(g(t)a^\dagger\sigma_+ + g^*(t)a\sigma_-\right)$ can be realized (here written in the rotating frame of the qubit and oscillator). I will discuss how this Hamiltonian can be accomplished in the dispersive regime in section 2.5.3. This corresponds to the unitary operation

$$\mathrm{AJC}\left(\theta,\varphi\right) = \exp\left(-i\theta\left(a^\dagger\sigma_+e^{i\varphi} + a\sigma_-e^{-i\varphi}\right)\right). \tag{2.20}$$

Since this gate along with the $\mathrm{JC}\left(\theta\right)$ can be realized in trapped-ions [66,112] or superconducting circuits (see section 2.5.3) using sideband interactions, the set $SB = \{R_\varphi(\theta), \mathrm{JC}\left(\theta\right), \mathrm{AJC}\left(\theta\right)\}$ is called the sideband ISA. Clearly $LE \subset SB$, so the sideband ISA is universal, and the inclusion of the AJC gate can help realize certain unitaries and states using circuits with fewer layers than LE alone. The circuit construction is shown in fig. 2.2b.

2.4.3 Control in the dispersive regime

As can be found in [34, 57, 76], in the dispersive regime the oscillator and qubit weakly hybridize, and eq. (2.15) can be approximated to realize the effective Hamiltonian

$$H_{\text{dispersive}}/\hbar = \tilde{\omega}_a a^\dagger a - \tilde{\omega}_q\frac{\sigma_z}{2} + \chi a^\dagger a\frac{\sigma_z}{2} + O\left(\left(\frac{g^2}{\Delta}\right)^2\right), \tag{2.21}$$

with dispersive shift $\chi = 2g^2/\Delta$ and renormalized frequencies $\tilde{\omega}_a = \omega_a + g^2/\Delta$ and $\tilde{\omega}_q = \omega_q - g^2/\Delta$ to first order in g^2/Δ. Note that for a transmon (or other superconducting circuit) coupled to an oscillator, these formulas must be modified to account for the finite anharmonicity and other effects [34]; the resulting terms can differ by a large percentage from the values predicted by the two-level-system approximation.

The dispersive approximation also results in higher-order nonlinear interactions that scale with $(g^2/\Delta)^2$ or and higher powers. For the present discussion, we will ignore this higher order terms. However, they become quite important for realization of the GKP code and other highly-squeezed states with a large photon-number distribution. This will be discussed explicitly in chapter 4 and chapter 5. Ignoring these terms, and including the oscillator and qubit drive, here we will be considering this Hamiltonian in the rotating frame of the qubit and oscillator at their renormalized frequencies,

$$\tilde{H}_{\text{dispersive}}/\hbar = \chi a^\dagger a \frac{\sigma_z}{2} + \varepsilon^*(t)a + \varepsilon(t)a^\dagger + \Omega^*(t)\sigma_- + \Omega(t)\sigma_+. \tag{2.22}$$

The dispersive interaction ($H_{\text{int}}/\hbar = \chi a^\dagger a \sigma_z/2$) can be thought of in two ways. Written in the basis of qubit eigenstates, $H_{\text{int}}/\hbar = \frac{\chi}{2} a^\dagger a \left|g\right\rangle\left\langle g\right| - \frac{\chi}{2} a^\dagger a \left|e\right\rangle\left\langle e\right|$, the coupling is interpreted as a shift in the oscillator's frequency depending on the state of the qubit by an amount χ. Similarly, written in the oscillator number basis, $H_{\text{int}}/\hbar = \chi \sum_{n=0}^{\infty} \left|n\right\rangle\left\langle n\right| \frac{\sigma_z}{2}$, we see the frequency of the qubit will be shifted according to the photon-number distribution of the cavity. As a result of the interaction, the oscillator and qubit will entangle if they are not in states that are eigenstates of σ_z or $\hat{n} = a^\dagger a$.

The driven dispersive Hamiltonian eq. (2.22) is universal for the oscillator and qubit, using the Hamiltonian definition of universality as defined in section 2.2.2. This has been exploited, using optimal control theory, to control the oscillator in a number of cQED experiments, most notably [101]. Here, I will focus on gate-based control using the dispersive Hamiltonian, with a short discussion of OCT methods in section 2.6. Using a gate approach, there are a few gates that are, in some sense, natural to realize in the dispersive regime.

The first question we can ask is: what happens if we do nothing ($\Omega(t) = \varepsilon(t) = 0$)? Importantly, we do not realize the identity operation. Instead, we realize an entangling gate called the conditional-rotation[23] gate, given by

$$\mathrm{CR}\left(\theta\right) = \left(-i\frac{\theta}{2}\sigma_z a^\dagger a\right), \tag{2.23}$$

which causes the oscillator to rotate by $\pm\theta/2$ conditioned on the qubit state $|g\rangle$ or $|e\rangle$ where $\theta = \chi T$.

If the qubit is not in an eigenstate of σ_z, this gate will entangle the qubit and oscillator for $\theta \neq 2\pi m, m \in \mathbb{Z}$. The special case of $\theta = \pi$ is called the conditional-parity gate, $\mathrm{C}\Pi = \exp\left(-i\pi a^\dagger a \sigma_z/2\right)$. This gate (and other controlled-rotation gates) is important in the context of rotationally-symmetric bosonic codes [23], as it can be used to measure the error syndrome (parity) [126].

Given evolution under eq. (2.21), the controlled-parity gate requires a wait time of $\tau_{\text{parity}} = \pi/\chi$, and a full 2π controlled-rotation takes a time $\tau = 2\pi/\chi$. It is for this reason that we sometimes say that the *typical gate time* of the dispersive gate set (and related operations) is $\tau \sim 2\pi/\chi$ or longer. This typical speed limit has also been found to be held when using pulse-level optimal control theory for realizing unitaries [101, 104]. For this reason, typical dispersive control, including the gate sets described in this section, are performed in a regime where χ is engineered to be as large as possible (often on the order of $\chi \sim 1\,\mathrm{MHz}$) before other unwanted effects become important. In our work, this regime is called the strong-coupling regime.

Finding the quantum speed limit of a bosonic operation can be difficult, due to the unbounded Hilbert space. For example, using the dispersive Hamiltonian, control solutions for state preparation of a state with maximum Fock level N_{state} exist that utilize the higher Fock levels $N_{\text{control}} > N_{\text{state}}$. These solutions are often aided by the so-called bosonic-enhancement

---

[23] Note that some authors will write this gate as $\tilde{\mathrm{CR}}\left(\theta\right) = \exp\left(-i\theta a^\dagger a \left|e\right\rangle\left\langle e\right|\right)$, which is equivalent to $\mathrm{CR}\left(\theta\right)$ by a oscillator rotation. I find it useful to call $\mathrm{CR}\left(\theta\right)$ the conditional-rotation and $\tilde{\mathrm{CR}}\left(\theta\right)$ the controlled-rotation, where the word 'conditional' vs 'controlled' indicates if the operation is conditioned on σ_z directly, or if it is controlled on the qubit being in state $|e\rangle$. Note that in multi-qubit algorithms, we often work with controlled-gates, however in bosonic systems, it is often useful to instead use conditional gates, as they are more symmetric. This designation also applies for controlled vs. conditional displacements.

factor, a name given to the fact that the operators a and $a^\dagger$ have matrix elements in the Fock basis that scale with $\sqrt{n}$, and control schemes that utilize the higher Fock states can be enhanced by this factor. This bosonic enhancement is often not fully exploited in numerical optimization solutions, since the numerics will often impose an unphysical Fock level cutoff in the simulation, hence why previous studies have found optimal control solutions to follow the same scaling of $2\pi/\chi$ for typical gate times. In our work, we fully exploit this bosonic enhancement for faster gates using an effect called Hamiltonian amplification, discussed in section 2.4.4. This will be expanded on in later sections.

An interesting question we can ask is: if the dispersive coupling is always on, how can we avoid entanglement between the qubit and oscillator? By analyzing the interaction term in eq. (2.21), we can intuit that if the value of σ_z were rapidly changed from $+1$ to -1, the interaction would cancel when evaluating the time-ordered unitary. In particular, the Hamiltonian

$$H/\hbar = \chi a^\dagger a \frac{\sigma_z}{2} + \Omega \frac{\sigma_x}{2} \tag{2.24}$$

will result in the identity operation after a time T when $\Omega \gg \chi \langle a^\dagger a \rangle$ and $\Omega T = 2\pi m, m \in \mathbb{Z}$. This is a form of dynamical decoupling [127]; other dynamical decoupling techniques could also be used, such as a sequence of equally spaced qubit $R_0(\pi)$ pulses.

The controlled parity gate, along with displacements and qubit rotations should be thought of as the most fundamental gate set arising from the dispersive Hamiltonian, ($\mathcal{D} = \{\mathrm{CR}(\theta), D(\alpha), R_\varphi(\theta)\}$), and this forms a minimum universal gate set (proof in appendix E.2) called the dispersive gate set. The echoed conditional displacement gate discussed in section 2.4.5 is built from these fundamental operations.

However, a more powerful entangling gate can be activated by driving the system. By driving the qubit with a frequency comb of Rabi drives $\Omega(t)$ at detuned frequencies $\omega_q - k\chi$ where $k \in \mathbb{Z}$, qubit rotations can be performed conditioned on oscillator Fock state $|k\rangle$.

This gate is called a number-Selective Qubit Rotation (SQR). With a derivation given in appendix B, the unitary is given by

$$\mathrm{SQR}(\vec{\theta}, \vec{\varphi}) = \sum_n R_{\varphi_n}(\theta_n) \otimes |n\rangle \langle n| \tag{2.25}$$

parameterized by a vector of rotation angles $\vec{\theta} = (\theta_0, \theta_1, ..., \theta_k)$ and phases $\vec{\varphi} = (\varphi_0, \varphi_1, ..., \theta_k)$ corresponding to the rotation applied to each independent qubit Bloch sphere entangled with each qubit Fock level $|n\rangle$ up to level k, chosen by the extent of the frequency comb. The bandwidth of the pulse must be small compared to χ, requiring the drive to be sufficiently slow, typically on the order of $T > 2\pi/\chi$ or slower. Effects of faster pulses and mitigation strategies when this condition breaks down are discussed in [99, 128, 129].[24]

The SQR gate can be used to define a powerful gate set called the Fock-Space ISA, the name indicating that the control operations are generally best understood in the Fock basis, given by $\mathcal{FS} = \{\mathrm{SQR}\,(\theta)\,, D(\alpha)\}$. The unselective qubit rotation $R_\varphi(\theta)$ could also be explicitly included in $\mathcal{FS}$, however in the strong-coupling regime, these unconditional rotations must be performed with a bandwidth that is large compared to $\chi \langle a^\dagger a\rangle$. This can be difficult in some situations where the oscillator states have a large photon-number extent. In such situations, the unselective qubit rotation can be realized by using the SQR gate.

Finally, in cases where $\theta = m\pi, m \in \mathbb{Z}$, the qubit and oscillator are disentangled after the SQR gate. In this special case, the SQR gate reduces to the Selective Number-dependent Arbitrary Phase (SNAP) gate [97, 115]. Parameterized by the phases $\vec{\varphi}$, the SNAP gate can be used to apply phases to each Fock state,

$$\mathrm{SNAP}\,(\vec{\varphi}) = \sum_{n=0}^{k} e^{-i\varphi} |n\rangle \langle n|\,. \tag{2.26}$$

The SNAP gate, together with an oscillator displacement, is universal for control of the

---

[24] Discussed in these references in the context of SNAP.

oscillator [97], defining the SNAP ISA, given in table 2.4.[25]

2.4.4 Hamiltonian amplification

In bosonic systems, Gaussian operations can be combined with non-linear operations to achieve faster control than the rate of the native nonlinear coupling alone. This technique is called Hamiltonian amplification, and the two most basic examples use the displacement and squeezing operations. In particular, notice that the displacement and squeezing operations transform the annihilation and quadrature operators according to

$$D^\dagger(\alpha)\hat{a}D(\alpha) = a + \alpha \tag{2.27}$$

$$D^\dagger(\alpha)\hat{a}^\dagger D(\alpha) = a^\dagger + \alpha^* \tag{2.28}$$

$$S^\dagger(r)\hat{q}S(r) = qe^{-r} \tag{2.29}$$

$$S^\dagger(r)\hat{p}S(r) = qe^{r}. \tag{2.30}$$

These transformations allows terms in a Hamiltonian to be amplified (or suppressed) when that Hamiltonian is conjugated with displacement or squeezing, as shown in as shown in fig. 2.3. The phase of the squeezing can be varied to amplify/suppress the desired quadratures.

As a relevant example, when a displacement of α and $-\alpha$ is applied before and after the dispersive interaction Hamiltonian $H_\chi = \chi a^\dagger a\sigma_z/2$, it is transformed to the displaced-dispersive Hamiltonian,

$$\tilde{H}_\chi = D^\dagger(\alpha)H_\chi D(\alpha) = \chi\left(\alpha a^\dagger + \alpha^* a\right)\frac{\sigma_z}{2} + \chi a^\dagger a\frac{\sigma_z}{2} + \chi|\alpha(t)|^2\frac{\sigma_z}{2}, \tag{2.31}$$

corresponding to a conditional displacement term, a dispersive term, and a qubit stark-shift

---

[25] Unlike the full Dispersive, Fock-Space, or Phase-Space ISA, the SNAP ISA does not allow for entangling operations between the qubit and oscillator. It is universal for unitaries on the oscillator, but not entangling unitaries between the oscillator and qubit.

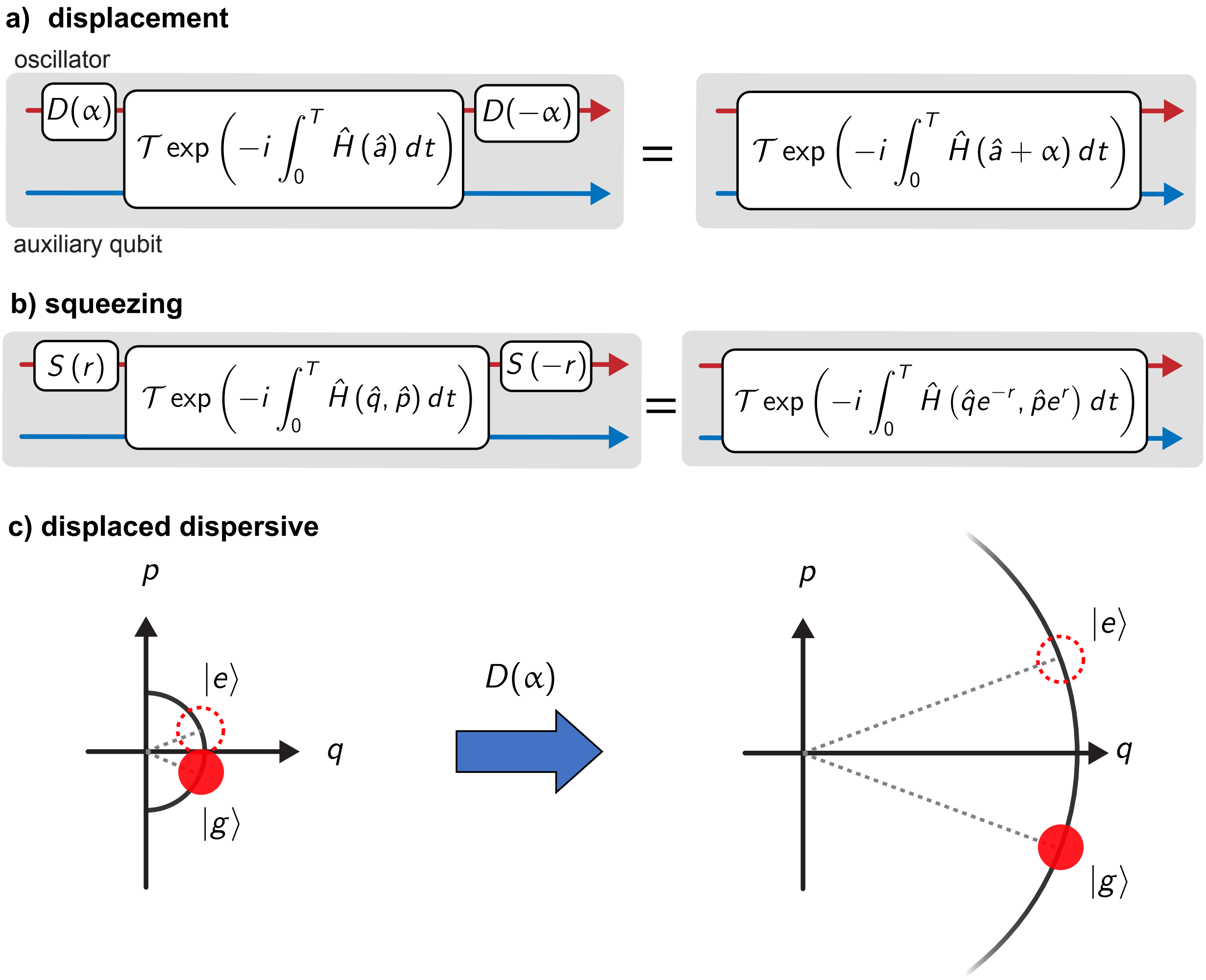

Figure 2.3: **Hamiltonian amplification** using **a)** displacement transformation and **b)** single-mode-squeezing. In **c)**, an example of Hamiltonian amplification using a large displacement is shown, acting on the dispersive interaction. The usual dispersive interaction (a rotation of the oscillator depending on the state of the qubit) shown on the left is transformed by the large displacement to a conditional displacement, as shown on the right. The large displacement can be thought of as a lever arm, amplifying the effect of the conditional rotation.

term. Importantly, the rate of the conditional displacement term is amplified by $|\alpha|$. The action of the displacement on the dispersive interaction is shown in fig. 2.3c. It is important to notice that the displacement operation $\hat{a} \to \hat{a}+\alpha$ will take a polynomial Hamiltonian in the annihilation and creation operators $H \propto a^{\dagger m} a^n$ and generate an effective Hamiltonian where the amplified terms are of one order lower, $\tilde{H} = D^\dagger(\alpha) H D(\alpha) \propto \alpha^* a^{\dagger(m-1)} a^n + \alpha a^\dagger a^{(n-1)} + \ldots$. This means that the generation of amplified non-linear terms will require starting with, at a minimum, a Hamiltonian that is at least fourth-order polynomial in a and $a^\dagger$ for a single mode. A similar statement holds for multi-mode nonlinear couplings, where a fourth order polynomial is required.[26] Squeezing Hamiltonian amplification [130], on the other hand, does not have this requirement; a cubic nonlinearity such as $H \propto \hat{q}^3$ can be amplified with the squeezing transformation to $\tilde{H} = S^\dagger(-r) H S(-r) \propto e^{3r}\hat{q}^3$, resulting in an amplified nonlinear interaction that could be used for faster universal control within the cubic ISA.

It should be noted that when Hamiltonian amplification is performed, noise can also be amplified. Fortunately, Hamiltonian amplification with displacements does not increase photon loss or photon gain. However, dephasing-type noise can be amplified, and other higher-than-linear order (in a and $a^\dagger$) Lindbladians. This is covered explicitly in section 3.2.1.

2.4.5 Echoed conditional displacement and the phase-space ISA

Since displacements can be used to amplify the dispersive Hamiltonian (eq. (2.31)), a natural question arises: can this effect be incorporated into a gate-based approach to control the oscillator?

The answer to this question is subtle, since in theory, the Hamiltonian amplification effect could be included already in the dispersive gate set, $\mathcal{D}$, as defined in table 2.4. In particular, by incorporating large displacements into the compilation of a target unitary using $\mathcal{D}$, gate-

---

[26] Note that when the qubit is realized as the first two levels of a bosonic mode (such as a transmon), $\sigma_z = 1 - 2\hat{b}^\dagger\hat{b}$, where $\hat{b}$ is the annihilation operator of the transmon mode. In this sense, the dispersive coupling $a^\dagger a \sigma_z/2 \propto a^\dagger a b^\dagger b$ is fourth order (four-wave mixing), and the conditional-displacement coupling $(\alpha a^\dagger + \alpha^* a)\sigma_z \propto (\alpha a^\dagger + \alpha^* a)\hat{b}^\dagger\hat{b}$ is third-order (three-wave mixing).

speed enhancement using Hamiltonian amplification could be used. However, this method is sub-optimal for two important reasons:

- Attempting to compile an operation using Hamiltonian amplification at the level of $\mathcal{D}$ would require the compiler to have intricate knowledge about the time it takes to perform gates and limitations of the physical system.
- Using Hamiltonian amplification requires large displacements. However, in practice these displacements are not instantaneous; the rate of change of $|\langle a \rangle|$ is limited by the maximum drive strength through the equation $\partial_t |\langle \hat{a} \rangle (t)| = |\epsilon(t)|$. The non-instantaneous nature of the displacements means that the always-on dispersive interaction causes curved trajectories through phase-space, along with controlled-rotations, causing an unwanted oscillator-qubit entanglement to occur during an otherwise ideal displacement operation.[27]

Clearly, what is needed is a clever primitive gate that has Hamiltonian amplification built in, such that a higher-level compiler can abstract away these hardware-level details, and all compiled circuits can be performed at the maximum speed possible. One potential option for this primitive is a unitary gate defined as the displaced dispersive Hamiltonian $\tilde{H}_\chi$ (eq. (2.31)) acting for some time T. However, the full $\tilde{H}_\chi$ is a complicated operation, and it would be difficult to design algorithms using it.

A more clever primitive gate that makes use of Hamiltonian amplification and is simple enough to be used in a compilation is called the Echoed Conditional Displacement (ECD) gate, shown in fig. 2.4. We first introduced this gate as the 'Swiss-army-knife' for stabilizing and measuring GKP codes [26] (chapter 5), and we later extended its use for universal control [25], both of which are central results of this dissertation.

First, in the present section, I will discuss the ideal ECD gate, assuming instantaneous displacements, and a lossless quantum system. However, as mentioned above, the effects of

---

[27] See fig. 3.6 for trajectories with an example of this effect.

finite-duration displacements are important, as are the effects of loss and dephasing; these details are included in the pulse-level optimization of the ECD gate and are covered in section 3.3.2. In particular, the finite duration of the displacements leads to a geometric phase imparted on the qubit during the ECD gate, and the loss must be transformed into the displaced frame; both these effects are taken into account in the next chapter.

The goal of the ECD gate is to perform a conditional displacement using Hamiltonian amplification. The ECD gate is best visualized in terms of the oscillator's phase-space trajectories coupled to qubit states $|g\rangle$ and $|e\rangle$, as shown in fig. 2.4b. By inspecting the displaced-dispersive Hamiltonian $\tilde{H}_\chi$ in eq. (2.31), it's clear that the conditional displacement term is included in the displaced frame, however the other two terms (the dispersive interaction and qubit stark-shift) are unwanted. These terms can be echoed away by a pulse sequence for the ECD gate that includes a qubit π pulse at time $T/2$, flipping $\sigma_z \to -\sigma_z$ and canceling these unwanted terms. To keep the desired conditional displacement term, we can perform a phase-space echo, and simultaneously flip the value of $\alpha \to -\alpha$ half way through the gate, such that the product $\sigma_z \alpha$ in $\tilde{H}_\chi$ has the same phase throughout the gate. With this description in mind, the ideal ECD gate unitary is defined as

$$\mathrm{ECD}\left(\beta\right) = D(\beta/2)\left|e\right\rangle\left\langle g\right| + D(-\beta/2)\left|g\right\rangle\left\langle e\right| = \sigma_x \mathrm{CD}\left(\beta\right), \tag{2.32}$$

$$\mathrm{CD}\left(\beta\right) = \exp\left(\left(\beta a^\dagger - \beta^* a\right)\frac{\sigma_z}{2}\right). \tag{2.33}$$

ECD applies a displacement of the oscillator by $+\beta/2$ or $-\beta/2$ conditioned on qubit state $|g\rangle$ or $|e\rangle$ respectively, followed by an additional qubit σ_x rotation. In particular, as shown in fig. 2.4a, the ECD gate is a sequence of displacement, qubit rotation, and controlled-rotation gates compiled from the dispersive gate set ($\mathcal{D}$) as:

$$\mathrm{ECD}\left(\beta\right) = D(\alpha_3)\mathrm{CR}\left(\chi T/2\right) D(-\alpha_2)R_0\left(\pi\right) D(-\alpha_2)\mathrm{CR}\left(\chi T/2\right) D(\alpha_1), \tag{2.34}$$

$$\alpha_1 = \alpha_0 \tag{2.35}$$

$$\alpha_2 = \alpha_0 \cos\left(\chi T/4\right) \tag{2.36}$$

$$\alpha_3 = \alpha_0 \cos\left(\chi T/2\right), \tag{2.37}$$

$$\beta = 2i\alpha_0 \sin\left(\chi T/2\right). \tag{2.38}$$

The specific displacements are chosen such that the trajectory of the oscillator's center-of-mass in phase space lies on a uniform circle during the conditional rotations as shown in fig. 2.4b. Inverting the equation for β, the total gate time is

$$T = \frac{2\arcsin\left(\frac{|\beta|}{2|\alpha_0|}\right)}{2\chi} \approx \frac{|\beta|}{\chi|\alpha_0|}, \tag{2.39}$$

the second equation holding in the small-angle approximation, $|\alpha_0| \gg |\beta|$. The speed of the gate is enhanced by the bosonic enhancement factor $|\alpha_0|$ due to Hamiltonian amplification via displacements.

The ECD gate, along with the qubit rotation $R_\varphi\left(\theta\right)$ forms a universal gate set, with a proof given in appendix E.3. The name given to this gate set is the phase-space ISA, $\mathcal{PS} = \{\mathrm{ECD}\left(\beta\right), R_\varphi\left(\theta\right)\}$, since the operations are best understood in the phase-space basis (the Wigner function).[28]

For experimental reasons that will be discussed in depth in the next chapter, the ECD gate with large displacements is best performed in systems where the dispersive shift χ is relatively small, on the order of $\chi/2\pi \sim 20\,\mathrm{kHz}$ to $\sim 100\,\mathrm{kHz}$. However, for hybrid qubit-oscillator systems in the strong-coupling regime, there is a simple way to realize the

---

[28] The gate set can be written in terms of (non-echoed) conditional-displacements $\mathcal{PS} = \{\mathrm{CD}\left(\beta\right), R_\varphi\left(\theta\right)\}$, which is equivalent.

conditional displacement. Recall that the conditional-parity operation is given by $\mathrm{C\Pi} = \mathrm{CR}\left(\pi\right)$. Using this operation, it can be shown that

$$\left(\mathrm{C\Pi}\right)\hat{a}\left(\mathrm{C\Pi}\right)^{\dagger} = i\sigma_z\hat{a} \tag{2.40}$$

which is sometimes called the exponentiation gadget. This is powerful when combined with Gaussian operations. For example, Chapman *et al.* used the exponentiation gadget to realize a controlled beamsplitter operation [131]. When used with a displacement operator,

$$\left(\mathrm{C\Pi}\right)D\left(\frac{i\alpha}{2}\right)\left(\mathrm{C\Pi}\right)^{\dagger} = \mathrm{CD}\left(\alpha\right), \tag{2.41}$$

providing a simple path to realize the phase-space ISA in strong-coupling architectures. Such a gate sequence is the essential element in an earlier protocol, called the qubit cavity mapping protocol (qcMAP), used to prepare oscillator cat states and other coherent-state superpositions [118]. However, unlike the ECD gate, the conditional-parity approach to conditional displacement is limited to $T_{\text{gate}} = 2\pi/\chi$, assuming instantaneous displacements.

Besides the ECD gate, two other implementations of conditional displacements have been performed in cQED, to the best of my knowledge. The first was used for readout by Touzard *et al.* [132] in 2019 by driving a transmon at the readout resonator frequency and applying a simultaneous cancellation drive to the readout. In chapter 6, I discuss how this protocol could be applied using a high-quality-factor oscillator, as additional echoing is required than what is needed for readout. Finally, Wang *et al.* recently demonstrated conditional displacements using sideband driving in [117], adapting an earlier protocol first demonstrated for dissipation engineering in [123]. In section 2.5.3, I expand upon this method.

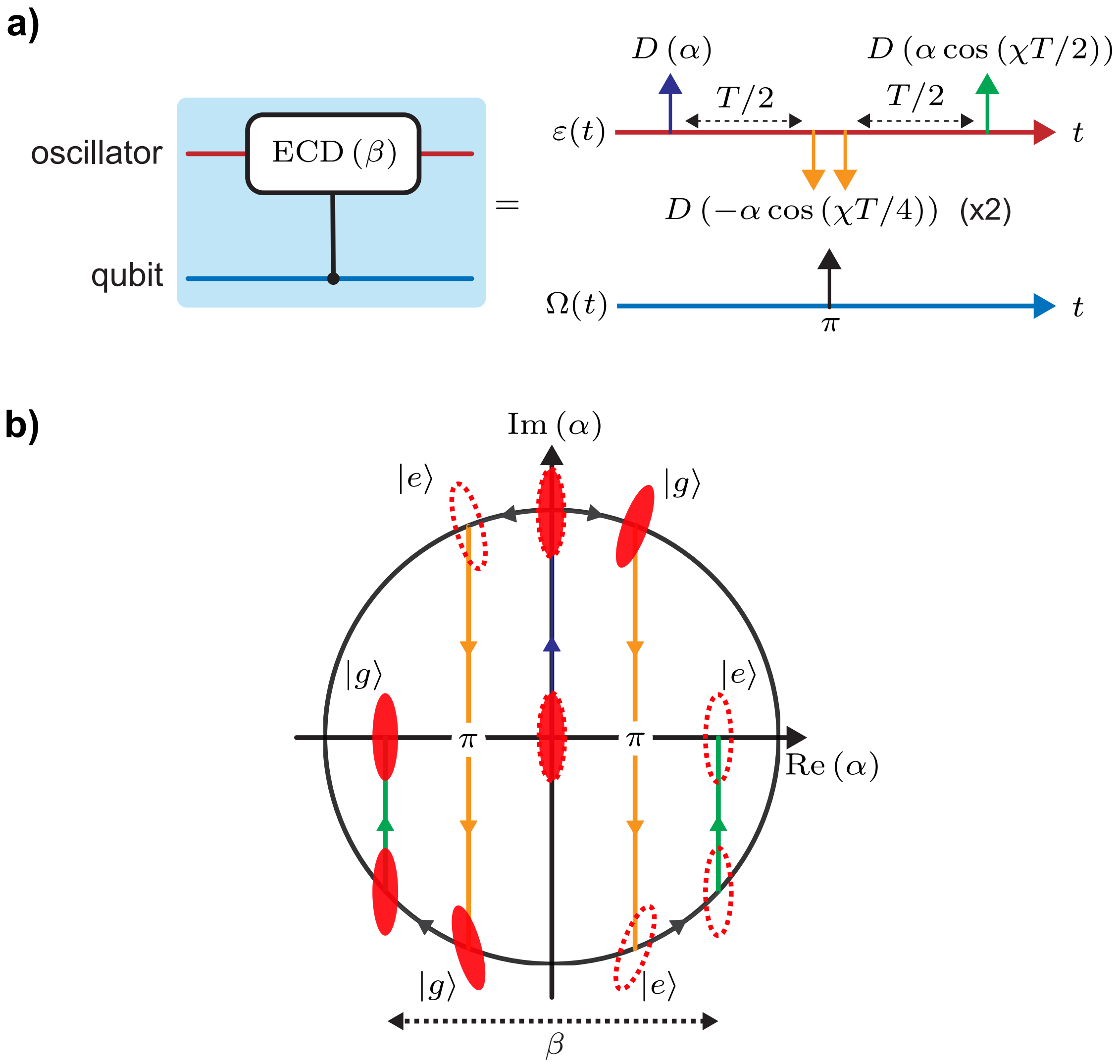

Figure 2.4: **Ideal Echoed Conditional Displacement (ECD) gate sequence a)** The ECD unitary acting on the oscillator and qubit (left) is realized in the ideal limit as the pulse sequence shown on the right, where the instantaneous oscillator displacement ($\varepsilon(t)$) and qubit rotation ($\Omega(t)$) pulses are represented as delta functions. **b.)** The phase-space trajectory (in Wigner units) of the ideal ECD gate, represented as the gate's action on a squeezed state initialized at the origin and qubit initialized in state $|+\rangle$. The oscillator state entangled with $|g\rangle$ and $|e\rangle$ is shown as the solid and dotted distributions, respectively.

2.5 Hamiltonian-level bosonic quantum control

The dispersive Hamiltonian eq. (2.21) is universal in the sense introduced in section 2.2.2. With this in mind, and alternative approach to controlling the hybrid qubit-oscillator system is to use optimal control theory (OCT) to find the drives $\varepsilon(t)$ and $\Omega(t)$ needed to perform a desired quantum operation [101, 102].

In reality, the model Hamiltonian of the system is not typically accurate enough to reach decoherence-limited fidelities with model-based OCT alone. However, if OCT is used in combination with model-free closed-loop optimization, it can be a powerful tool. That is, the pulses optimized with a model can be used as a seed for closed-loop optimization in experiment. This is another reason why a gate-based approach is powerful; each well-parameterized gate can be optimized individually in an experiment with closed-loop techniques, and the optimization can occur routinely between shots of an experiment.

In the next two sections, I outline two pulse-level Hamiltonian optimization techniques developed during the research for this dissertation. First, in section 2.5.1, I discuss how Hamiltonian amplification with large displacements can be used for pulse-level optimization of arbitrary unitaries using the dispersive Hamiltonian. Next, in section 2.5.2, I simplify this method by requiring that the oscillator's phase-space trajectory live on a circle. This is later connected to previously developed sideband control techniques, rounding out the pedagogical chapter on hybrid bosonic control.

2.5.1 Displaced-frame optimal control

Using the driven dispersive Hamiltonian (eq. (2.22)), $\varepsilon(t)$ and $\Omega(t)$ are usually optimized directly (I will outline some techniques in section 2.6). However, the model can break down given restrictions placed on the simulation. In particular, if the oscillator is simulated with a finite-dimensional Fock space with some cutoff $N_{\max}$, the optimizer will not be able to explore solutions that use large photon numbers than $N_{\max}$. This is of particular relevance in the weak-coupling regime, where large photon numbers are useful for speeding up control.

The solution to the problem of a finite Hilbert space cutoff is to instead perform the pulse-level optimization in the time-dependent displaced frame of the oscillator. The time-dependent displaced frame transformation is derived in section C.2.1 in the time-dependent displaced frame the dispersive Hamiltonian in eq. (2.21) takes the form

$$\tilde{H}/\hbar = \chi a^\dagger a \frac{\sigma_z}{2} + \chi(\alpha(t) a^\dagger + \alpha^*(t) a)\frac{\sigma_z}{2} + \chi|\alpha(t)|^2 \frac{\sigma_z}{2} + \Omega^*(t)\sigma_- + \Omega(t)\sigma_+, \tag{2.42}$$

$$\partial_t \alpha(t) = -i\varepsilon(t) - (\kappa/2)\,\alpha(t). \tag{2.43}$$

Note that this is similar to the displaced-dispersive Hamiltonian, $\tilde{H}_\chi$ in eq. (2.31), however now $\alpha(t)$ is time-dependent. In particular, in eq. (2.43), the complex-valued center-of-mass[29] $\alpha(t) = \langle a(t) \rangle = (\langle \hat{q} \rangle (t) + i \langle \hat{p} \rangle (t)) / \sqrt{2}$ is related to the baseband drive $\varepsilon(t)$, here including oscillator photon loss at rate κ. Other effects, such has higher order nonlinearities like self-Kerr, can also be accounted for in this frame, as shown in section C.2.1.

By tracking the center of mass, governed by eq. (2.43), we have effectively eliminated all classical (Gaussian) dynamics from the problem, and the photon number required for the simulation and optimization is minimized. This procedure of a time-dependent frame transformation can also be carried out for other Gaussian Hamiltonian terms, such as detuning or squeezing, with the general idea that eliminating classical dynamics by solving coupled differential equations leads to more efficient quantum simulation. This method is useful even if large displacements are not used during the control, such as is often the case in strong-coupling architectures.

To perform optimal control, the center of mass trajectory $\alpha(t)$ can be optimized using standard techniques (see section 2.6) under the constraint $\alpha(0) = \alpha(T) = 0$ and $\partial_t|\alpha(t)| < \varepsilon_{\max}$ (and other possible constraints such as a maximum α if desired). Once $\alpha(t)$ and $\Omega(t)$

---

[29] If the initial oscillator state has a $\langle \hat{a} \rangle = 0$. Otherwise, $\alpha(t)$ is the change of the center-of-mass relative to the initial state. Also, note that here 'center-of-mass' is a misnomer for obvious reasons.

have been optimized, the pulse $\varepsilon(t)$ can be found from solving eq. (2.43) with finite-difference methods.

2.5.2 Circle-trajectory optimal control

In a 2012 experiment, Murch *et al.* used a clever method of sideband driving to cool and stabilize a superconducting qubit in the $|+\rangle = (|g\rangle + |e\rangle)/\sqrt{2}$ state by driving a readout cavity with a detuned drive (a 'sideband') and simultaneously Rabi-driving the qubit with a Rabi rate equal to the drive detuning. In the Murch work, the oscillator was strongly coupled to a transmission line (a readout cavity). Here, and in the next section, we use intuition from this work to derive a similar method for high-quality-factor universal oscillator control with optimization (this section) and sideband driving (next section) [95].

This circle-trajectory introduced here can be seen as a simplification to the displaced-frame optimal control method of section 2.5.1. Starting from the time-dependent displaced-frame Hamiltonian, eq. (2.42), instead of optimizing the center of mass trajectory $\alpha(t)$, we can pick a circle trajectory,

$$\alpha(t) = \alpha_0(t)e^{-i\tilde{\Delta}t} \tag{2.44}$$

where $\alpha_0(t)$ is a real-valued envelope function with a ring-up and ring-down satisfying $\alpha_0(0) = \alpha_0(T) = 0$ (for example, a smoothed-trapezoidal envelope). The drive $\varepsilon(t)$ is found according to eq. (2.43) to be $\varepsilon(t) = \exp\left(-i\tilde{\Delta}t + \pi/2\right)\left(\partial_t\alpha_0(t) + \alpha_0(t)\left(-i\tilde{\Delta} + \kappa/2\right)\right)$, a detuned sideband with in-quadrature ring-up and ring-down component. The linear component of higher-order nonlinearities in the displaced-frame could be included as in section C.2.1.

Under such a condition, the displaced-frame Hamiltonian is written as

$$\tilde{H}/\hbar = \chi a^\dagger a\frac{\sigma_z}{2} + \chi\alpha_0(t)(e^{-i\tilde{\Delta}t}a^\dagger + e^{i\tilde{\Delta}t}a)\frac{\sigma_z}{2} + \chi\alpha_0(t)^2\frac{\sigma_z}{2} + \Omega^*(t)\sigma_+ + \Omega(t)\sigma_+. \tag{2.45}$$

Two additional frame transformations can be applied - an oscillator rotating frame transformation at frequency $\tilde{\Delta}$ and a time-dependent qubit rotating frame at frequency $\chi|\alpha(t)|^2$ to eliminate the Stark-shift term[30]. In this new frame,

$$\tilde{H}/\hbar = \chi a^\dagger a \frac{\sigma_z}{2} + \tilde{\Delta} a^\dagger a + \chi \alpha_0(t)(a^\dagger + a)\frac{\sigma_z}{2} + \Omega^*(t)\sigma_+ + \Omega(t)\sigma_+. \tag{2.46}$$

Equation (2.46) gives universal control, as is shown in the next section. With this 'circle trajectory' simplification, the drive $\Omega(t)$ can be optimized without optimizing $\alpha(t)$. The circle drive on the oscillator can be calibrated in experiment independent of the specific problem in mind. For example, when using a transmon as the auxiliary qubit, effects such as photon-induced state transitions of the transmon as discussed in the next chapter could be navigated by picking the envelope $\alpha_0(t)$ wisely.

2.5.3 Effective resonant regime (sideband driving)

An additional and powerful simplification can be made to eq. (2.46). With a detailed derivation given in the supplement of [123] and [117], if the qubit is driven with a Rabi drive with Rabi rate equal to the detuning of the oscillator drive $\Omega(t) = \pm\tilde{\Delta}$, an effective tunable Jaynes-Cummings or Anti-Jaynes-Cummings Hamiltonian can be engineered,

$$\tilde{H}_{\text{sideband}} = \chi \alpha_0(t) \left(g^*_{\text{JC}}(t)\tilde{\sigma}_- a^\dagger + g_{\text{JC}}(t)\tilde{\sigma}_+ a + g^*_{\text{AJC}}(t)\tilde{\sigma}_+ a^\dagger + g_{\text{AJC}}(t)\tilde{\sigma}_- a \right). \tag{2.47}$$

Here, the raising and lowering operators are in the Hadamard frame[31]: $\tilde{\sigma}_- = |-\rangle\langle+|$ and $\tilde{\sigma}_+ = |+\rangle|-\rangle$. Importantly, the strength of the interaction is amplified by the large displacement α_0. The JC or AJC terms correspond to the Rabi driving with a positive or negative Rabi rate. Alternatively, they can be engineered by picking either a red- or blue-sideband drive on the oscillator ($\pm\tilde{\Delta}$). This Hamiltonian can be used to engineer the sideband ISA.

---

[30] These additional transformations are not strictly necessary but can be helpful for optimization

[31] The Hadamard frame is found by applying a Hadamard unitary transformation to the Hamiltonian.

If both the red- and blue- sideband are played together, the resonant Rabi interaction is realized, given by

$$\tilde{H}/\hbar = \chi\alpha_0(t)g(t)\left(e^{i\varphi}a + e^{-i\varphi}a^\dagger\right)\sigma_x. \tag{2.48}$$

The phase factor φ that can be tuned using the phase between the sideband interactions.

Similar to the goal of the ECD construction, this simultaneous red- and blue- sideband driving realizes a conditional displacement, here conditioned on σ_x. It is thus an alternative way to engineer conditional displacements in cQED, as shown in [117].

2.6 Numerical compilation

A target algorithm or quantum simulation running on bosonic modes must be compiled down to a sequence of gates using an ISA. In most useful cases, this will mean running an algorithm on many bosonic modes and qubits on a hybrid CV-DV processor with some connectivity defined by the hardware. Similar to algorithms with multiple qubits (such as Shor's algorithm [4]), this will often be engineered by a human using intuition. Other techniques, such as a variational quantum eigensolver (VQE) [133] can be used in conjunction with a bosonic ISA for quantum simulation. These techniques are needed because a full quantum algorithm acting on N bosonic modes cannot typically be 'optimized' since, the whole point of the algorithm, is that it is difficult to simulate with a classical computer. In these cases, each gate needed should be optimized on each module in the physical system using closed-loop model-free optimization techniques, such as in Sivak *et al.* [99].

With that in mind, the present section will instead focus on numerical compilation of a target unitary operation into a bosonic ISA in cases where the full dynamics can be simulated. This is the case with one or a few oscillators, such as the experimental demonstrations of the phase-space ISA shown in chapter 4. For this, it is advantageous to make use of methods and tools developed by the computer science community, particularly in the field of machine learning, to efficiently solve these non-convex problems.

One may wonder, if we have a numerical technique for compilation of a target unitary into a specified gate-set, can we use the same techniques for realizing a unitary with Hamiltonian-level control? Thankfully, the answer is yes, and the method is somewhat simple. First, notice that a universal Hamiltonian itself defines a gate set. That is, we can define a gate set $\mathcal{H}$ where each gate is defined as action under a universal Hamiltonian H for some time T_{step},

$$\mathcal{H} = \{U = \mathcal{T}\exp(.)\}\,, \tag{2.49}$$

parameterized by the control signal values $\mathbf{u}$ acting for some time τ.[32] The control signals do not necessarily need to be constant during this time, allowing additional freedom in their parameterization[33]. In this sense, the only difference between usual Hamiltonian-level control optimization (for example, using GRAPE [101, 102]) and an ISA is that in Hamiltonian-level control, we typically impose some smoothness condition on the control values $\mathbf{u}(\tau)$ when stringing gates together to make a circuit due to the finite-bandwidth constraints in experiment; such a constraint is not necessary when using the other gate sets such as the phase-space or Fock-space ISA. Given that Hamiltonian-level control can be cast in the language of an ISA, we now proceed to discuss general numerical compilation of a target operation using a desired gate set.

In [25], methods were developed for numerical compilation of a target unitary that make use of parallel processing, automatic differentiation, back-propagation, graphical-processing-units, and efficient calculation of parameterized bosonic operations to find the gate parameters for a given target operation. Here, we extend these methods to any ISA, and give

---

[32] $\mathcal{T}\exp\left(-i\int_0^{T_{\text{step}}}\hat{H}\left(\mathbf{u}(\tau)\right)d\tau\right)$ is the time-ordered exponential, meaning it's the solution to the time-dependent Schrödinger equation. It can be solved in a number of ways, however the *Magnus expansion* is useful for control applications, as the solution is unitary at all levels of approximation.

[33] For example, the control signals could be parameterized in frequency space, allowing easy implementation of bandwidth constraints.

example operations.

Constructing a circuit layer

To define the optimization problem, we first define the fundamental unit of each hybrid bosonic circuit called a *layer*. In fig. 2.2, each layer is outlined in a dotted box. The *circuit depth* N is the number of layers in the total circuit. Each layer, at a minimum, should consist of at least one application of each gate in the ISA on every qubit and oscillator. This ensures that the circuit is expressive enough to perfectly compile any target unitary with enough layers.

Assuming each layer consists of k unitary gates U_i from the gate set, let $b\left(\vec{\theta}\right) = U_k U_{k-1} ... U_2 U_1$ be the unitary operation defined by a single layer, parameterized by all the parameters entering into the gates in the unitaries $\left(\vec{\theta}\right)$.

Parallel cost function

The phenomenon of barren plateaus, in which the gradient of the fidelity vanishes, makes numerical optimization difficult. This is studied using the phase-space ISA with ECD gates in [134]. To help optimize circuits in the case of a vanishing gradient, we realize a parallel optimization of a batch of B circuits.

Let b_{jk} denote the k^{th} layer of the j^{th} circuit in the parallel optimization. We can write the unitary generated by the jth circuit as

$$U_j = b_{jN} \ldots b_{j1} b_{j0}. \tag{2.50}$$

Given a target quantum operation (such as state preparation, or a full unitary), the relevant fidelity metric can be used (defined in chapter 2). Let $\mathcal{F}_j$ denote the fidelity of the

j^{th} circuit. To optimize B circuits in parallel, we construct the total cost function

$$\mathrm{C} = \sum_{j=1}^{B} \log(1 - \mathcal{F}_j). \tag{2.51}$$

Since C function is a simple sum of independent logarithmic cost functions, gradient descent of C realizes independent gradient descent of each circuit realization in parallel. The logarithm of $1 - \mathcal{F}_j$ is taken to aid with the problem of vanishing gradients as the solution infidelity approaches 0.

Once the parameterized cost function is defined, it is optimized using gradient-descent with back-propagation. These techniques are well established, and numerical solvers from the field of machine learning can be used. The optimization is stopped when any $\mathcal{F}_j$ reaches the target fidelity, and the parameters from the j^{th} circuit are selected.

In the following two sections, I give two relevant examples of this type of optimization taken from [25]. In section 2.7.1, I give the example of optimizing Fock state preparation using the phase-space gate set. Finally, in section 2.7.2, I give examples of optimizing logical gates on finite-energy GKP codes.

2.7 Optimization of ECD circuit parameters

2.7.1 Fock State preparation

For state preparation using ECD control, the quantum control problem we aim to solve is

$$U_{\mathrm{ECD}} = D(\beta_{N+1}/2) R_{\varphi_{N+1}}(\theta_{N+1})\, \mathrm{ECD}(\beta_N) R_{\varphi_N}(\theta_N) \ldots \mathrm{ECD}(\beta_2) R_{\varphi_2}(\theta_2)\, \mathrm{ECD}(\beta_1) R_{\varphi_1}(\theta_1) \tag{2.52}$$

$$\mathcal{F} = |\langle\psi_t|U_{\mathrm{ECD}}|\psi_i\rangle|^2 \tag{2.53}$$

$$\left\{\vec{\beta}, \vec{\varphi}, \vec{\theta}\right\} = \operatorname{argmax}_{\left\{\vec{\beta}, \vec{\varphi}, \vec{\theta}\right\}}(\mathcal{F}) \tag{2.54}$$

with initial state $|\psi_i\rangle$ and target state $|\psi_t\rangle$. The circuit depth N should be chosen such that $\mathcal{F}$ at its maximum is above an acceptable value with experimental considerations in mind. Although we focus on state preparation in this section, the optimization method described can also be used to realize a general unitary U_{target} by replacing the Fidelity function with $\mathcal{F} = \left|\frac{1}{\text{Tr}(P)}\text{Tr}\left(PU^{\dagger}_{\text{target}}U_{\text{ECD}}\right)\right|^2$, where P is a projector onto a possible subspace of interest [105]; this is the approach taken in the next section. Here, we include a final qubit rotation $R_{\varphi_{N+1}}(\theta_{N+1})$ and displacement $D(\beta_{N+1}/2)$ after the last ECD gate in the optimizer. Often, the optimizer converges to protocols with $\beta_{N+1} = 0$. These gates are implemented quickly with respect to typical ECD gates and are not included in the quoted circuit depths N which only counts the total number of ECD gates.

We realize a multi-start method to solve this non-convex problem by optimizing B independent variations of U_{ECD} in a parallel manner. Denoting the j^{th} variation of the ECD unitary as $U_{\text{ECD},j}$ with circuit parameters $\left\{\vec{\beta}_j, \vec{\varphi}_j, \vec{\theta}_j\right\}$ and fidelity $\mathcal{F}_j = |\langle\psi_t|U_{\text{ECD},j}|\psi_i\rangle|^2$, we perform gradient descent on all $4BN$ real parameters using the total cost function $\text{C} = \sum_{j=1}^{B}\log(1-\mathcal{F}_j)$.

We realize gradient descent of the cost function using *Adam* [135] implemented in TensorFlow. To construct this cost function and its gradient, we represent the batch of circuit parameters by the tensors $\boldsymbol{\beta}$, $\boldsymbol{\varphi}$ and $\boldsymbol{\theta}$ of dimensions $B \times N$ such that $\boldsymbol{\beta}_{ji}$ is the i^{th} parameter appearing in circuit j. Given a tensor-product structure of $\mathcal{H} = \mathbb{C}^2 \otimes \mathbb{C}^{N_o}$ where N_o is the truncation of the oscillator's Hilbert space, the ECD unitaries and cost function are represented in the block-matrix form

$$U_{\text{ECD},j} = \boldsymbol{b}_{jN}...\boldsymbol{b}_{j2}\boldsymbol{b}_{j1} \tag{2.55}$$

$$\boldsymbol{b}_{ji} = \text{ECD}(\boldsymbol{\beta}_{ji})R_{\boldsymbol{\varphi}_{ji}}(\boldsymbol{\theta}_{ji}) = \begin{pmatrix} D^{\dagger}(\boldsymbol{B}_{ji})e^{i\boldsymbol{\Phi}_{ji}}\sin\boldsymbol{\Theta}_{ji} & D^{\dagger}(\boldsymbol{B}_{ji})\cos\boldsymbol{\Theta}_{ji} \\ D(\boldsymbol{B}_{ji})\cos\boldsymbol{\Theta}_{ji} & -D(\boldsymbol{B}_{ji})e^{-i\boldsymbol{\Phi}_{ji}}\sin\boldsymbol{\Theta}_{ji} \end{pmatrix} \tag{2.56}$$

$$\text{C} = \sum_{j=1}^{N}\log\left(1 - |\langle\psi_t|\,\boldsymbol{b}_{jN}...\boldsymbol{b}_{j2}\boldsymbol{b}_{j1}\,|\psi_i\rangle|^2\right) \tag{2.57}$$

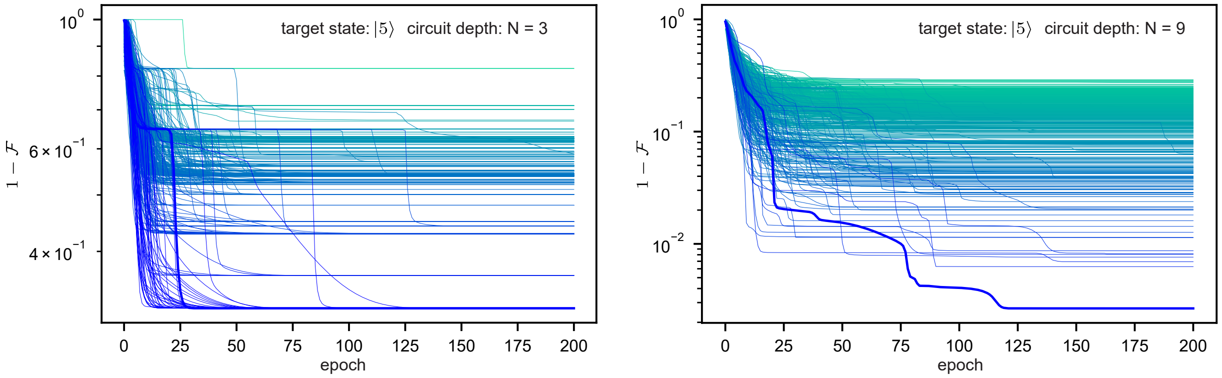

Figure 2.5: **Numerical circuit optimization using backpropagation** Examples of optimization curves for Fock 5 state preparation. Each line represents a circuit fidelity F_j, and 500 randomly initialized circuits are optimized in parallel. In the case of small circuit depth $N = 3$ (left panel), the best infidelity reached is ~ 0.3. With a larger circuit depth $N = 9$ (right panel), one circuit out of the 500 reaches an infidelity of ~ 0.003, demonstrating the need for multi-start optimization.

with reduced parameters $\boldsymbol{B} = \frac{\boldsymbol{\beta}}{2}$, $\boldsymbol{\Theta} = \frac{\boldsymbol{\theta}}{2}$ and $\boldsymbol{\Phi} = \boldsymbol{\varphi} - \frac{\pi}{2}$, and D is the displacement operator defined on the oscillator's Hilbert space truncated to N_o. To construct each block operator $\boldsymbol{b}_{ji}$, we first compute the displacement operators. For this, we use the batched displacement operator implementation in [99], which uses pre-diagonalization of the truncated position and momentum operators to efficiently construct the displacement matrices. With this, we compute all $B \times N$ displacement operators $D(\boldsymbol{B})$ in parallel, then build the block matrices b_{ji} block-by-block while reusing computed functions to minimize the total number of computations. Once these blocks are computed, the cost function is implemented by contracting along the i index, taking the logarithm, then contracting along the j index. To compute the gradient of the cost function with respect to $\boldsymbol{\beta}$, $\boldsymbol{\varphi}$, and $\boldsymbol{\theta}$, we use TensorFlow to realize reverse-accumulation automatic differentiation.

In fig. 2.6 we show an example by plotting the infidelities of each circuit in the batch as a function of optimization epoch for Fock $|5\rangle$ state preparation ($|0\rangle |g\rangle \rightarrow |5\rangle |g\rangle$) using two different circuit depths, $N = 3$ and $N = 9$. For these examples, we use a batch size of $B = 500$ circuits, with each epoch representing 100 steps of gradient descent using Adam with a learning rate of 0.001 carried out using an Nvidia Tesla v100 GPU. The typical wall

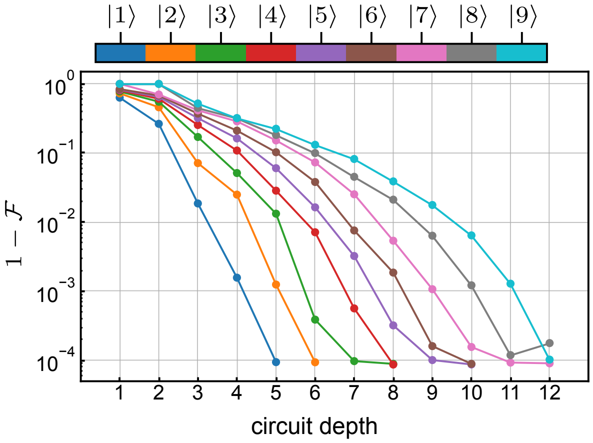

Figure 2.6: **Fock state optimization results.** Best state transfer infidelity found when optimizing ECD circuit parameters to prepare oscillator Fock state $|n\rangle$ from vacuum as a function of circuit depth N. Here, $\mathcal{F} = |\langle g| \langle n| U_{\text{ECD}} |0\rangle |g\rangle|^2$. Note that this figure has been slightly updated with respect to [25], here using an updated optimizer.

clock time for circuit optimization with a batch size of $B \sim 500$ is in the range of 10 to 100 seconds, depending on circuit depth and Hilbert space size.

In fig. 4.8, we show an example of the pulse parameters found using this procedure for state preparation of the GKP $|+Z\rangle$ logical state. The magnitude of the echoed conditional displacements found in this example is typical of most demonstrations in this work - the largest $|\beta|$ found is $|\beta| \approx 2.75$. We note the optimization procedure does not include a constraint on $|\beta|$, but generally the scale of $|\beta|$s found is set by the phase-space extent of the target state. As shown in this example, the optimizer often converges to pulses with interpretable values of qubit rotation angles and phases: values in that pulse are close to $\pi/4$, $\pi/2$, etc, and this is a common feature for the demonstrations in this work.

2.7.2 Optimization of logical gates on a finite energy GKP code

As mentioned previously, Gaussian unitaries can be used to realize Clifford gates on the GKP code. However, any logical gate (Clifford or non-Clifford) that does not commute with the number operator $\hat{n} = a^\dagger a$ must be modified to account for finite-squeezing effects. This modification is introduced and described in section 5.1.2.

In this section, we focus on the implementation of finite-energy GKP logical gates using ECD control. In particular, we demonstrate numerical optimization of the phase and T gates for a finite-energy square GKP encoding. For these gates, the target state maps $\{|\psi_i\rangle\} \to \{|\psi_t\rangle\}$ acting on the finite energy logical subspace are given by

$$\begin{aligned} S &: \{|{+Z}\rangle_\Delta |g\rangle, |{-Z}\rangle_\Delta |g\rangle\} \to \{|{+Z}\rangle_\Delta |g\rangle, e^{i\pi/2} |{-Z}\rangle_\Delta |g\rangle\} \\ T &: \{|{+Z}\rangle_\Delta |g\rangle, |{-Z}\rangle_\Delta |g\rangle\} \to \{|{+Z}\rangle_\Delta |g\rangle, e^{i\pi/4} |{-Z}\rangle_\Delta |g\rangle\} \end{aligned} \tag{2.58}$$

where we have also included the condition that the ancilla qubit starts and ends in $|g\rangle$. To optimize these logical gates, we modify the cost function in section 3.3.2 to be

$$C = -\sum_j \mathrm{Re}\left(\langle\psi_{t,j}| U_{\mathrm{ECD}} |\psi_{i,j}\rangle\right) \tag{2.59}$$

where the sum is carried out over a logical state map, such as the state map for the S and T gates given in eq. (2.58). Here, we only optimize the gate over the logical subspace, and in future work, the optimization could be modified to focus on error transparent gates [136].

To quantify the quality of the optimized logical gates, we numerically calculate their average fidelity [67], defined as

$$\overline{\mathcal{F}} = \frac{1}{6}\mathrm{Tr}\left(R^T[\mathcal{U}_{\mathrm{target}}]R[\mathcal{E}]\right) + \frac{1}{3} \tag{2.60}$$

where $R_{ij}[\mathcal{E}] = \frac{1}{2}\mathrm{Tr}\left(\sigma_i \mathcal{E}\left[\sigma_j\right]\right)$ is the Pauli transfer matrix (PTM) associated to a quantum channel $\mathcal{E}$. Here, we define the finite energy logical Pauli operators using the numerically computed logical states as described in section 4.5.2 to be $X_\Delta = \left(|{+Z}\rangle_\Delta \langle{-Z}|_\Delta + |{-Z}\rangle_\Delta \langle{+Z}|_\Delta\right)|g\rangle\langle g|$ and analogous definitions for I_Δ, Y_Δ, and Z_Δ. For these operations, the target unitary channel is defined as $\mathcal{U}_{\mathrm{target}}\left[\rho\right] = U_{\mathrm{target}}\rho U_{\mathrm{target}}^\dagger$ and the applied channel is $\mathcal{E}\left[\rho\right] = U_{\mathrm{ECD}}\rho U_{\mathrm{ECD}}^\dagger$, where U_{ECD} is the result of the optimization.

The optimization results for the finite energy S and T gates are shown in fig. 2.7 at

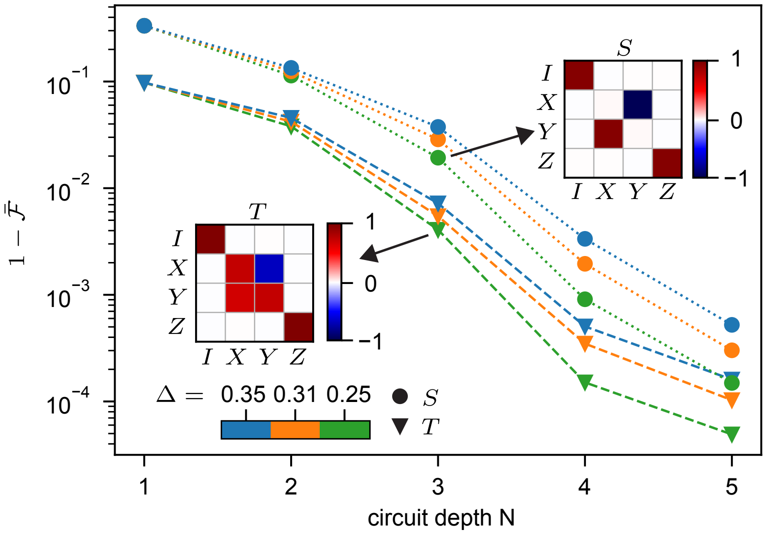

Figure 2.7: **Optimized finite-energy GKP S and T logical gates.** Plotted is the average fidelity for optimized ECD circuits at different values of Δ and circuit depth N. S gate results are shown with circles, T gate results are indicated with triangles, and the color indicates the squeezing. Also shown (insets) are the Pauli transfer matrices for the ECD S and T gates optimized at $N = 3, \Delta = 0.25$. Differences in Fidelity at different values of Δ are likely caused by the small finite overlap of the finite-energy logical states.

three different squeezing values $\Delta = \{0.25, 0.31, 0.35\}$. Remarkably, these gates can be performed with a low circuit depth, only requiring $N = 3$ ECD gates to reach a channel fidelity $\overline{\mathcal{F}} \approx 0.99$ for the T gate and $N = 4$ for the S gate. These results indicate that the ECD gate set is especially well-suited for control over the GKP code, however we note that these gate implementations are not fault tolerant with respect to ancilla qubit errors.

Chapter 3

The weak-coupling dispersive architecture

A number of previous experiments involving bosonic control and error correction of a high-quality-factor oscillator have been carried out in a regime where the dispersive shift was on the order of or larger than $\chi/2\pi \sim 1\,\mathrm{MHz}$ (for example, [58, 101]). In our work, we are instead interested in using a dispersive coupling that is over an order-of-magnitude weaker, on the order of $\chi/2\pi \sim 30\,\mathrm{kHz}$. As discussed in the introduction of this dissertation, this weak coupling can minimize the inherited nonlinearity of the oscillator, allowing for the preparation and control of highly squeezed states that are sensitive to nonlinearity such as GKP states. However, while the coupling is weak, the effective operation speed can remain decent by using large displacements.

In this chapter, I will discuss the technical details of the so-called weak-coupling dispersive architecture developed as part of this PhD work. This consists of:

- A transmon coupled to a high-Q oscillator with dispersive coupling on the order of $\chi/2\pi \sim 30\,\mathrm{kHz}$, discussed in section 3.1. The transmon is also coupled to a readout resonator with possible Purcell filter as in fig. 1.3c.

- A set of calibration and characterization techniques for tuning up the system, where previous approaches designed for a strong coupling would fail. This is discussed in section 3.2.

- An efficient entangling gate between the transmon and oscillator, called the Echoed Conditional Displacement (ECD) gate, discussed in section 3.3. The ECD gate, together with transmon rotations, forms a universal gate set, as discussed previously in section 2.4.5.
- A method for performing efficient tomography of the oscillator, called the Characteristic function, in a regime where the widely-used Wigner function would give low contrast. This is discussed in section 3.4.

The control and error correction results, covered in chapter 4 and chapter 5, can be seen as applications of this architecture. In a few places in this chapter, I will include some experimental data as an example. The experimental parameters for the data shown can be found in table 4.2.

Besides the reduced oscillator nonlinearity, the weak-coupling architecture is motivated for two other important reasons. First, the limit of the oscillator lifetime due to its coupling to the transmon (called the reverse Purcell effect) is increased. Second, the transmon Stark-shift associated with oscillator states that have large photon distributions (often with long tails in photon number) is reduced. This, along with the reduced nonlinearity, allows the preparation of oscillator states with large photon numbers without Stark shifting the transmon into unwanted effects in frequency space, such as two-level systems. To better motivate these ideas, in the next section I review the details of a transmon with dispersive coupling to an oscillator, including a few unwanted side-effects of such a coupling.

3.1 Coupling a transmon to an oscillator

Here we will focus on the specific platform shown in fig. 1.3c, consisting of a fixed-frequency 3D transmon [51,52] coupled to a superconducting high-quality-factor post-cavity [17]. However, recent advancements in the materials science and fabrication have led to similarly high-quality-factor planar superconducting oscillators [16]; it is likely that a planar architecture is more feasible for scaling up to many modes, and the results of this section can also apply in that setting. It is for this reason that I will often refer to the ‘cavity’ by the more generic name ‘oscillator’. The typical frequency of this mode is around 5 GHz.

In such a setting, the model Hamiltonian of the transmon (charging energy E_C and Josephson energy E_J) with capacitive coupling to the oscillator can be written as

$$H = 4E_c(\hat{N} - N_g)^2 - E_J \cos(\hat{\varphi}) + \hbar\omega_a^{\text{bare}}\tilde{a}^\dagger\tilde{a} + \hbar g(\hat{N} - N_g)\left(\tilde{a} + \tilde{a}^\dagger\right) \tag{3.1}$$

where $2g$ is the vacuum Rabi rate, $\hat{N}$ is the Cooper-pair number operator, $\hat{\varphi}$ is the conjugate Josephson phase, N_g is the offset charge in units of $2e$, and $\tilde{a}$ ($\tilde{a}^\dagger$) is the bare cavity mode annihilation (creation) operator. For a derivation of this model, please see [34, 51]. By applying the dispersive transformation, and moving to the rotating frame at the oscillator and transmon Lamb-shifted (hybridized) frequencies, we arrive at the effective Hamiltonian in the dispersive regime ($g \ll \Delta = \omega_b - \omega_a$),

$$H_{\text{dispersive}}/\hbar = \tilde{\Delta}a^\dagger a - \chi a^\dagger a b^\dagger b - \chi' a^{\dagger 2}a^2 b^{\dagger 2}b^2 - K_a a^{\dagger 2}a^2 - K_b b^{\dagger 2}b^2 + H_d/\hbar \tag{3.2}$$

$$H_d/\hbar = \varepsilon^*(t)a + \varepsilon(t)a^\dagger + \Omega^*(t)\sigma_- + \Omega(t)\sigma_+ \tag{3.3}$$

In the hybridized frame, a is now the annihilation operator of the oscillator-like mode, and b is the annihilation operator of the transmon-like mode. Unlike the previous chapter, where the transmon is treated as a two-level-system, it is here treated as a nonlinear bosonic mode (a more accurate description). The Hamiltonian is written in the frame of the oscillator and transmon drives, detuned by $-\tilde{\Delta}$ from the $|g\rangle$ frequency at low power. $\tilde{\Delta}$ can be chosen arbitrarily, and for experiments involving conditional displacements, we often use $\tilde{\Delta} = \chi/2$.

The coefficients are approximately[1] given by

$$\chi \approx \frac{g^2 E_C/\hbar}{\Delta\left(\Delta - E_C/\hbar\right)} \tag{3.4}$$

$$K_a \approx \frac{E_C/\hbar}{4}\left(\frac{g}{\Delta}\right)^4 \tag{3.5}$$

$$K_b \approx \frac{E_C/\hbar}{2} \tag{3.6}$$

$$\chi' \approx \chi\left(\frac{g}{\Delta}\right)^2 \tag{3.7}$$

with more accurate expressions given in [137]. To get a sense for the order-of-magnitude of these coefficients, I've included typical values for both the strong-coupling regime and weak-coupling regime in table 3.1. Note that the transmon anharmonicity $\approx E_C$ sets the speed of transmon rotations; it is bounded from below by the need to do fast transmon gates (typically $E_C/2\pi > 100\,\mathrm{MHz}$), and it is bounded from above from the need to remain in the transmon regime, $E_J/E_C \gtrapprox 50$, where E_J is set by the design parameters including the transmon frequency, $\omega_b \approx \sqrt{8E_JE_C} - E_C$.[2] As shown in the table, reducing the value of g by an order-of-magnitude leads to a three-order-of-magnitude reduction in K_a.

When the oscillator and transmon hybridize, they also inherit loss from one another. In the dispersive regime, if the uncoupled transmon and oscillator have photon-loss rates $\tilde{\gamma}$ and $\tilde{\kappa}$, the hybridized transmon-like and oscillator-like modes will have modified loss rates γ, κ approximately given by

$$\kappa \approx \tilde{\kappa} + \left(\frac{g}{\Delta}\right)^2 \tilde{\gamma} \tag{3.8}$$

$$\gamma \approx \tilde{\gamma} + \left(\frac{g}{\Delta}\right)^2 \tilde{\kappa} \tag{3.9}$$

where the approximation holds to second order in $\left(\frac{g}{\Delta}\right)$, and assumes the transmon and oscillator are coupled to independent white baths [138]. The additional loss inherited due

---

[1] The expression for χ' here is within the two-level system approximation. See [137].

[2] Typical transmon frequency is around 6 GHz.

Parameter	**Strong-coupling**	**Weak-coupling**
Coupling rate	$g/2\pi \approx 100\,\text{MHz}$	$g/2\pi \approx 10\,\text{MHz}$
Transmon-oscillator detuning	$\Delta/2\pi \approx 1\,\text{GHz}$	$\Delta/2\pi \approx 1\,\text{GHz}$
Transmon anharmonicity	$E_C/2\pi \approx 200\,\text{MHz}$	$E_C/2\pi \approx 200\,\text{MHz}$
Dispersive shift	$\chi/2\pi \approx 2.5\,\text{MHz}$	$\chi/2\pi \approx 25\,\text{kHz}$
Oscillator Kerr	$K_a/2\pi \approx 5\,\text{kHz}$	$K_a/2\pi \approx 0.5\,\text{Hz}$
Second-order shift	$\chi'/2\pi \approx 25\,\text{kHz}$	$\chi'/2\pi \approx 2.5\,\text{Hz}$
Reverse Purcell limit	$T_{1a} \lesssim 10\,\text{ms}$	$T_{1a} \lesssim 1\,\text{s}$

Table 3.1: **Typical values for the strong and weak coupling regimes.** The Purcell limits are calculated assuming a transmon with $T_1 = 100\,\mu\text{s}$. The reduction of coupling rate g by an order of magnitude results in a two orders-of-magnitude reduction in χ with a favorable four orders-of-magnitude reduction in K_a and χ'. The increase in reverse Purcell limit has enabled the control of an ultra-high quality-factor oscillator in [54]. Note that the Kerr coefficient is sometimes read as an oscillator frequency shift of $K_a/2\pi \approx 0.5\,\text{Hz}$ *per photon*, emphasizing that the effect can be amplified and measured by displacing the oscillator.

to the hybridization is called the Purcell effect [139]. Usually, this effect is discussed in the context of a transmon coupled to a readout resonator where $\tilde{\kappa} \gg \tilde{\gamma}$. In this setting, the transmon's spontaneous emission rate will increase when it is coupled to a lossy readout resonator; it can be mitigated by engineering a Purcell filters [60, 140, 141]. However, in the context of a transmon coupled to a high-quality-factor superconducting oscillator, it is typically in the opposite regime, where $\tilde{\kappa} \ll \tilde{\gamma}$. In this case, the cavity effective loss rate κ will increase due to its coupling to the transmon. This is sometimes called the reverse Purcell effect.

Besides the reduced nonlinearity, a secondary motivation for the weak-coupling architecture is a lowering of the reverse Purcell effect. As shown in table 3.1, the limit on oscillator T_1 assuming a state-of-the-art transmon with $T_1 = 100\,\mu\text{s}$ is increased from $\sim 30\,\text{ms}$ to $\sim 1\,\text{s}$ in the weak coupling regime. This can be important for the control of ultra-high-quality-factor cavities, such as the SRF (superconducting radio frequency) cavities recently demonstrated by Fermilab to have a single photon lifetime on the order of $\sim 1\,\text{s}$ [55]. The weak coupling architecture has been used, for example, to control a cavity with a single photon lifetime of $30\,\text{ms}$ [54]. Using the weak coupling, we can also reduce the participation of the oscillator field in the lossy interfaces associated with the transmon chip. In other words, in a weak-coupling architecture, the transmon 'dips' into the cavity tunnel less. This can also help to avoid cross-talk between modes with driving the system.

In practice, these approximations for evaluating effective Hamiltonian coefficients and the Purcell rate are only used as a first order approximation for designing an experiment. To predict more accurate values, finite-element microwave simulations are used to evaluate the effective Hamiltonian of the system, often with the High Frequency Structure Simulator (HFSS) software from Ansys. Using the energy-participation ratio approach [142], which is a modification of the earlier black-box quantization approach [143], the effective Hamiltonian and loss can be predicted with higher accuracy. However, for a full description of the coupled system, numerical diagonalization can be used; I discuss this approach and give an example using our experimental parameters in section 3.2.3. Once an experiment is built and measured, the simulation can be slightly modified to better model other non-idealities in the experiment.

Besides inherited loss, a few other effects should be taken into account when coupling the transmon and oscillator, especially when we intend to populate the oscillator with large photon numbers.

- **Thermal shot-noise dephasing**

  Thermal fluctuations of any mode dispersively coupled to the oscillator will cause frequency fluctuations of the oscillator. In the case of a bosonic mode (such as a transmon) at frequency ω_b and in thermal equilibrium with a bath at T, the average occupation will be determined by the Bose-Einstein distribution,

$$n_{\text{th}} = \langle b^\dagger b \rangle = \frac{1}{e^{\frac{\hbar\omega_q}{k_B T}} - 1}. \tag{3.10}$$

  Typically, the filtering of the microwave lines between room-temperature and the device-under-test anchored at 20 mK is designed so that the effective thermal population of the transmon mode will be on the order of $n_{\mathrm{th}} \lesssim 10^{-3}$. However, the transmon is sometimes measured to have a larger n_{th}, on the order of $n_{\mathrm{th}} \sim 10^{-2}$ to 10^{-1}, due to poor thermal anchoring through the substrate, and anomalous excitation from quasiparticle poisoning [144–146]. If this mode has dispersive coupling χ to the high-quality-factor oscillator, the oscillator will dephase at an effective rate [17]

$$\kappa_{\varphi} = \frac{\gamma}{2}\mathrm{Re}\left(\sqrt{\left(1+\frac{2i\chi}{\gamma}\right)^{2}+\frac{8i\chi n_{\mathrm{th}}}{\gamma}}-1\right). \tag{3.11}$$

When $\chi \gg \gamma$, this can be approximated as $\kappa_{\varphi} \approx n_{\mathrm{th}}\gamma$. In other words, every time the transmon state jumps (at rate γ), the oscillator is completely dephased.

- **Dressed dephasing**

  Transmon dephasing will be dominated by noise coupled to $b^{\dagger}b$ at low frequency, $\gamma_{\varphi}(\omega \to 0)$ [76]. However, noise coupled to $b^{\dagger}b$ with spectral components at the difference frequency between the oscillator and qubit, $\pm\Delta$, will be up-converted, causing correlated loss and gain of the oscillator and transmon [138]. In the dispersive limit, this can be written as an effective master equation

  $$\partial_t \rho = \gamma_{\Delta}\mathcal{D}\left[a^{\dagger}b\right]\rho + \gamma_{-\Delta}\mathcal{D}\left[ab^{\dagger}\right]\rho \tag{3.12}$$

  where $\gamma_{\pm\Delta} = 2\left(g/\Delta\right)^{2}\gamma_{\varphi}\left(\pm\Delta\right)$ is the transmon's dephasing rate due to noise coupled to $b^{\dagger}b$ with spectral density components around $\pm\Delta$. This effect has been measured explicitly using noise injection in [147]. However, for fixed-frequency 3D transmons with typical difference frequencies on the order of $\Delta \gtrsim 1\,\mathrm{GHz}$, it is likely that noise coupled to the transmon at Δ is strongly suppressed. For example, in [148], it was shown that by proper filtering and thermalization of the readout resonator, a 3D fixed-frequency transmon can reach $T_{2E} = 2T_1$.

- **Breakdown of the dispersive approximation**

  The approximations leading to the effective dispersive Hamiltonian no longer hold when $\langle a^\dagger a\rangle \gtrsim n_{\text{crit}}$, where n_{crit} is called the critical photon number of the oscillator. This critical number depends on the state of the transmon. From [34] the critical oscillator photon number for the j^{th} transmon state is

  $$n^j_{\text{crit}} = \frac{1}{2j+1}\left(\frac{|\Delta - jE_C|^2}{4g^2} - j\right). \tag{3.13}$$

  In the case where $\Delta \gg E_C$, the critical photon number for $|g\rangle, |e\rangle$ is roughly the photon number point at which the transmon Stark-shifts by one-half and one-sixth of its anharmonicity $n_{\text{crit}} \approx \left\{\frac{E_C}{2\chi}, \frac{E_C}{6\chi}\right\}$, respectively.

  The critical photon number should be thought of as a rule-of-thumb for when higher-order nonlinearities become important. However, for high-fidelity control of the oscillator with large displacements, they must be accounted for at values much lower than n_{crit}, see section 3.2.3 for an example. Additionally, because of effects such as multi-photon nonlinear resonances and two-level systems (discussed below), the photon number at which bad effects occur can be quite different (lower and higher) than the critical photon number.

- **Multi-photon nonlinear resonances**

  When populating an oscillator with dispersive coupling to a transmon, the transmon will sometimes be excited outside of the $\{|g\rangle, |e\rangle\}$ manifold. This is commonly observed for transmon readout, and has been shown to occur due to both non-RWA [61] and RWA [63] terms, depending on the frequencies of the transmon and oscillator. The most extreme example of this is called transmon ionization[3], when the oscillator is driven with so many photons that the transmon is excited outside of the cosine

---

[3] Sometimes called 'bright-stating'

potential well [37, 149, 150]. At lower drive powers, the transmon will be excited to higher states, and sometimes these transitions are well-resolved at particular oscillator photon numbers. These effects can fluctuate with the transmon's offset gate charge, since the higher excited states of the transmon can have a large dispersion with offset charge. It is possible that adding an inductive shut to the transmon can help mitigate this effect [151]. Research is ongoing to better understand this problem for transmon readout, and developments made on that front should also be applicable to the case of a high-quality-factor oscillator coupled to a transmon.

- **Two-level systems**

  In superconducting circuits, anomalous two-level systems (TLS) are believed to be a dominant source of loss. The TLS heuristic model can be used to explain the power-dependence and temperature-dependence of the quality-factor of superconducting oscillators [16, 152]. It is believed that TLSs may be localized in insulating materials and oxides on the surface, including amorphous aluminum oxide (used in the junction[4]) and silicon oxide [153, 155–159]. When TLSs are resonant with the transmon, they can couple strongly, and manifest as discrete effects in the frequency spectrum. The defects can fluctuate in time [160], and some redistribution of TLSs are believed to occur with background ionizing radiation, such as γ-rays and cosmic ray muons that cannot easily be shielded [161].

  In the case of an oscillator[5] coupled to a transmon, when the oscillator is driven, it can Stark-shift the transmon into resonance with these defects, causing a change of the transmon's T_1 [25, 99]. The transmon can also be broadened due to the photon-number distribution in the oscillator, or it can be broadened due to measurement-induced dephasing in the case of readout, modifying the TLS noise it's coupled to. We believe

---

[4] The TLS density has been measured to be around $0.5\,\mathrm{um}^{-2}\mathrm{GHz}^{-1}$ [153, 154] in Josephson junctions. However, this is likely highly dependent on fabrication details.

[5] High-Q or readout.

these effects are one of the main limiting factors in realizing high-fidelity control and error correction using large displacements of the oscillator, with a supporting measurement shown in fig. 3.4 and [25, 27]. The use of an in-situ frequency-tunable transmon could help to better navigate the unpredictable landscape of TLSs in frequency space, however, this can also introduce other unwanted noise sources such as low-frequency flux noise. Additionally, if flux-tunable transmon gates require the flux-tuning over a large frequency range, it becomes likely the transmon must be tuned through TLSs, resulting in loss.

With the weak-coupling dispersive architecture discussed in this chapter, the transmon Stark shift associated with a large photon-number state idling in the oscillator (not when displaced) is reduced. This lowers the probability that the transmon is resonant with a discrete two-level-system defect when the oscillator is populated with a GKP or highly-squeezed state. Note that this argument does not hold when driving the system; the transmon will Stark shift by roughly the same amount in both the strong coupling and weak coupling regime when performing gates. The weak coupling regime, however, allows a larger ON-OFF ratio, measured in units of transmon Stark shift when performing gates and when idling.

- **Readout and reset induced dephasing of the high-Q oscillator**

  In addition to the transmon and high-Q oscillator, an additional low-Q oscillator called the readout is needed to measure and reset the transmon. The readout and high-Q storage will couple due to their individual couplings to the transmon, leading to a dispersive coupling term $\chi_{rs} r^\dagger r a^\dagger a$.

  When the readout is populated with photons to measure or reset the transmon, the storage oscillator may be dephased. This effect is discussed in more detail and measured in [126].

- **Coupling to other modes**

> Finally, the transmon can also be coupled to other, uncontrolled degrees of freedom. As an example, the cavity will have higher harmonics that also couple to the transmon (and hence couple to the fundamental high-Q storage mode) dispersively. These modes, if not thermalized properly, can dephase the transmon, and cause other unwanted couplings and transitions when driving the system. Simulation and proper design can help to avoid these couplings.

Finally, besides the motivations for weak coupling given above, I note one additional motivation: it is an interesting physics question, in itself, if it is even possible in principle to control a nearly-linear oscillator. The results of the next chapter show that it is indeed possible, with many nuances that lower the fidelity.

3.2 Simulation, calibration, and characterization

In this section, we outline techniques to characterize an oscillator and qubit coupled with $\chi/2\pi$ on the order of or smaller than qubit decoherence rates. In this regime, methods for calibration of control and Hamiltonian parameters which rely on large number-splitting are inefficient. For these calibrations, we rely on semi-classical phase-space trajectories as derived in section 3.2.2. In section 3.2.3, we describe the *out-and-back* method, which uses large displacements of the oscillator mode to realize a measurement of Hamiltonian parameters. Finally in section 3.2.6 we describe a simple geometric phase measurement which is used to calibrate the oscillator drive strength $|\varepsilon|$.

3.2.1 Oscillator relaxation and dephasing in the displaced frame

When large oscillator displacements are used to enhance the effective rate of control, we are also populating the oscillator with many more photons. Given this, one may wonder: won't the likelihood to lose a photon be much greater, effectively canceling the gain we might achieve by using a large displacement? Fortunately, this is not the case. As is shown

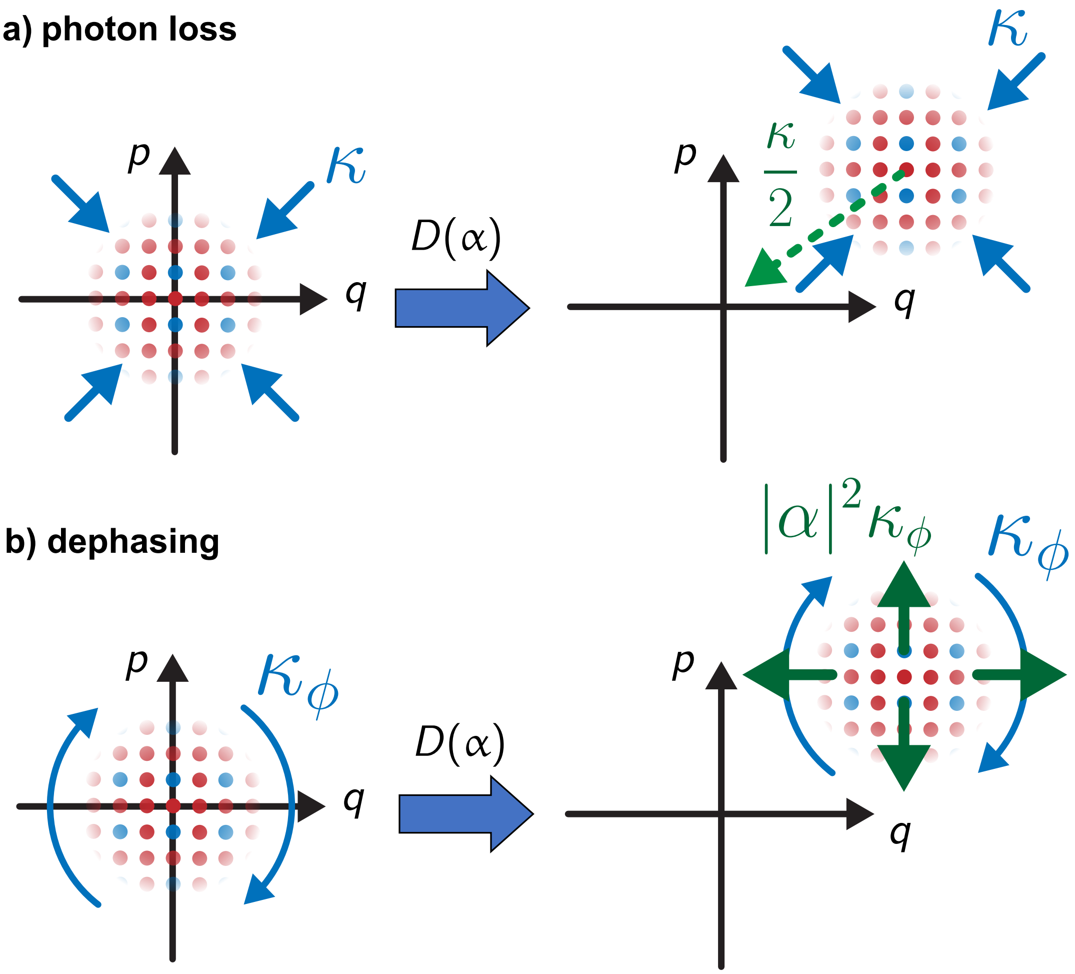

Figure 3.1: **Loss and dephasing in the displaced frame.** Here, the effect is depicted as acting on a $|+Z\rangle$ GKP state, however the results apply to any oscillator state. **a)** Photon loss at rate κ acts as a drift and diffusion in phase-space, as indicated with the blue arrows acting on a state centered at the origin (left). When a displaced-frame transformation is made ($D(\alpha)$), (right), photon loss is transformed into two components: loss at rate κ, equivalent to when the state is at the center of phase-space, as well as a deterministic force at rate $\kappa/2$ towards the origin (green arrow). This deterministic force can be accounted for in the drive equation for $\varepsilon(t)$, so photon loss does not lead to additional noise in the displaced frame. **b)** Dephasing, on the other hand, acts as random rotations in phase space, as shown by the blue arrows on a centered state (left). When the state is displaced, the dephasing noise is amplified, and is converted to diffusion-like noise at an enhanced rate $|\alpha|^2\kappa_\phi$.

below, when the oscillator is displaced, linear error channels (such as loss and gain) do not cause enhanced noise, as long as the deterministic part of the evolution is accounted for. Higher order error channels however, such as dephasing, do lead to enhanced noise under a displacement.

With photon loss at a rate κ, the oscillator's density matrix evolves according to the quantum master equation in Lindblad form

$$\partial_t\rho = -i\left[H,\, \rho\right] + \kappa\mathcal{D}\left[a\right]\rho, \tag{3.14}$$

$$H = H_s + \varepsilon a^\dagger + \text{h.c.}, \tag{3.15}$$

were $\mathcal{D}[L] = L\rho L^\dagger - (1/2)\left\{L^\dagger L, \rho\right\}$, H_s is the system Hamiltonian (given in eq. (3.2) for the dispersive case), and we have included a time-dependent oscillator drive $\varepsilon(t)$, working in units such that $\hbar = 1$. Evolution of the density matrix in a time-dependent displaced frame $\tilde{\rho} = D^\dagger\left(\alpha\right)\rho D\left(\alpha\right)$ is given by the equivalent master equation

$$\partial_t\tilde{\rho} = -i\left[\tilde{H}, \tilde{\rho}\right] + \kappa\mathcal{D}\left[a+\alpha\right]\tilde{\rho} \tag{3.16}$$

$$\tilde{H} = D^\dagger\left(\alpha\right)H_s D\left(\alpha\right) + \left(-i\partial_t\alpha + \varepsilon\right)a^\dagger + \text{h.c.} \tag{3.17}$$

In particular, the displaced frame Lindbladian can be recast as

$$\kappa\mathcal{D}\left[a+\alpha\right]\tilde{\rho} = \kappa\mathcal{D}\left[a\right]\tilde{\rho} - i\left[i\frac{\kappa}{2}\left(\alpha^* a - \alpha a^\dagger\right), \tilde{\rho}\right], \tag{3.18}$$

corresponding to photon loss at a rate κ, and a Hermitian re-centering force at a rate $\frac{\kappa}{2}|\alpha|$. This deterministic force can be lumped into the effective displaced-frame Hamiltonian, giving

$$\partial_t\tilde{\rho} = -i\left[\tilde{\tilde{H}}, \tilde{\rho}\right] + \kappa\mathcal{D}\left[a\right]\tilde{\rho} \tag{3.19}$$

$$\tilde{\tilde{H}} = D^\dagger\left(\alpha\right)H_s D\left(\alpha\right) + \left(-i\partial_t\alpha - i\frac{\kappa}{2}\alpha + \varepsilon\right)a^\dagger + \text{h.c.} \tag{3.20}$$

Given a desired $\alpha(t)$, $\varepsilon(t)$ can be chosen such that the term in parentheses is zero, satisfying the equation $\partial_t\alpha(t) = -i\varepsilon(t) - (\kappa/2)\,\alpha(t)$ and counteracting the re-centering force. Higher-order nonlinear terms such as Kerr can also result in linear Hamiltonians in the displaced frame and can be included in this equation, as is done in section 3.2.2. For photon loss, the state dynamics under a displacement is depicted in fig. 3.1a. With this choice of drive, the deterministic evolution is accounted for, and relaxation in the displaced frame is not enhanced compared to relaxation at the origin of phase space. The same procedure can be carried out for photon gain at rate $\kappa_\uparrow$, described by the dissipator $\partial_t\rho = \kappa_\uparrow\mathcal{D}\left[a^\dagger\right]\rho$.

White-noise oscillator dephasing is given by the master equation $\partial_t\rho = 2\kappa_\phi\mathcal{D}\left[a^\dagger a\right]\rho$. Defining the superoperator $\mathcal{S}\left[X,Y\right]\rho = X\rho Y^\dagger - \left\{Y^\dagger X,\rho\right\}$, oscillator dephasing is transformed in the displaced frame to

$$
\begin{aligned}
&\partial_t\tilde{\rho} = 2\kappa_\phi\mathcal{D}[(a^\dagger+\alpha^*)(a+\alpha)]\tilde{\rho}\\
&= 2\kappa_\phi\left\{\mathcal{D}[a^\dagger a]\tilde{\rho} + |\alpha|^2\left(\mathcal{D}[a]\tilde{\rho}+\mathcal{D}[a^\dagger]\tilde{\rho}\right)\right.\\
&+\alpha^2\mathcal{S}\left[a^\dagger,a\right]\tilde{\rho}+\alpha^{*2}\mathcal{S}\left[a,a^\dagger\right]\tilde{\rho}\\
&+\alpha\left(\mathcal{S}\left[a^\dagger a,a\right]\tilde{\rho}+\mathcal{S}\left[a^\dagger,a^\dagger a\right]\tilde{\rho}\right)\\
&\left.+\alpha^*\left(\mathcal{S}\left[a^\dagger a,a^\dagger\right]\tilde{\rho}+\mathcal{S}\left[a,a^\dagger a\right]\tilde{\rho}\right)\right\}.
\end{aligned}
\tag{3.21}
$$

In the displaced frame, the noise is dominated by diffusion-like terms at rate $2\kappa_\phi|\alpha|^2$, and unlike the relaxation case, there is no deterministic part that can be counteracted with a simple displacement. This effect is depicted in fig. 3.1b. However, this master equation is only valid in the Markovian regime; the spectral density of oscillator frequency fluctuations can instead be non-uniform due to effects such as two-level-system defects [162]. In such a colored noise case, it is possible that part of the enhanced dephasing noise could be echoed away using symmetric pulse constructions [105], including ECD. Finally, it is possible that an alternative ECD gate could be implemented that does not have amplified dephasing noise; this is proposed in chapter 6.

The enhanced dephasing noise leads to a trade-off between faster gates and enhanced diffusion in phase-space. This trade-off is analyzed explicitly for state preparation in section 4.6.4, and a model for the fidelity of a single ECD gate including this effect is derived in section 3.3.3.

3.2.2 Dynamics of a lossy displaced oscillator with dispersive coupling to a transmon

Here we apply the results of the previous section to the case of the dispersive Hamiltonian in eq. (3.2). The resulting equations are used for simulation, characterization, and pulse optimization, as outlined in the later sections.

Starting from $H_{\text{dispersive}}$ in eq. (4.1), we perform a time-dependent displaced frame transformation using the unitary $U = D^\dagger(\alpha(t)) = \exp\left\{\alpha^*(t)a - \alpha(t)a^\dagger\right\}$. This modifies the state according to $\tilde{\rho}(t) = D^\dagger(\alpha(t))\rho(t)D(\alpha(t))$, and the Hamiltonian according to $H \to \tilde{H} = UHU^\dagger + (i\hbar)\left(\partial_t U\right)U^\dagger = D^\dagger\left(\alpha(t)\right)HD\left(\alpha(t)\right) + (i\hbar)\left(a\partial_t\alpha^*(t) - a^\dagger\partial_t\alpha(t)\right)$, giving

$$\begin{aligned}\frac{\tilde{H}}{\hbar} &= \tilde{\Delta}a^\dagger a - (\chi + 4\chi'|\alpha|^2)a^\dagger a q^\dagger q - \chi' a^{\dagger 2}a^2 q^\dagger q - K_c a^{\dagger 2}a^2 - K_q q^{\dagger 2}q^2 - (\chi + 2|\alpha|^2\chi')(\alpha^* a + \alpha a^\dagger)q^\dagger q \\ &- (\chi|\alpha|^2 + \chi'|\alpha|^4)q^\dagger q - 4K_c|\alpha|^2 a^\dagger a + \left(\tilde{\Delta}\alpha^* - 2K_c|\alpha|^2\alpha^* + i(\partial_t\alpha^*) + i\frac{\kappa}{2}\alpha^* + \varepsilon^*\right)a + \text{h.c.} \\ &- K_c\left(2\alpha a^{\dagger 2}a + \alpha^2 a^{\dagger 2} + \text{h.c.}\right) - \chi'\left(2\alpha a^{\dagger 2}a + \alpha^2 a^{\dagger 2} + \text{h.c.}\right)q^\dagger q + \Omega^*(t)q + \text{h.c.}\end{aligned} \tag{3.22}$$

We have also included the deterministic part of oscillator relaxation at a rate $\kappa/2$ as described in the section 3.2.1.

Simulating in the displaced frame

Given an oscillator drive $\varepsilon(t)$, it is numerically advantageous to cancel the classical part of the oscillator's phase-space trajectory by picking a time-dependent frame $\alpha(t)$ which cancels the displacement term in $\tilde{H}$. This is done by solving

$$\begin{aligned} \partial_t \alpha(t) &= -i\tilde{\Delta}\alpha(t) + 2iK_c|\alpha(t)|^2\alpha(t) - \frac{\kappa}{2}\alpha(t) - i\varepsilon(t) \\ \alpha(0) &= 0, \end{aligned} \tag{3.23}$$

for $\alpha(t)$. In practice, we first pick a desired $\alpha(t)$, and solve eq. (3.23) for the $\varepsilon(t)$ that produces it. The trajectory must be picked such that bandwidth and amplitude constraints on $\varepsilon(t)$ are satisfied, meaning $\alpha(t)$ should not rise or fall too quickly. Once this is known, $\tilde{H}$ without the linear terms in a and $a^\dagger$ is used to efficiently simulate a cavity and transmon evolution in the displaced frame using a truncated Hilbert space. This displaced frame Hamiltonian is used for master equation simulations in section 4.6.

Semiclassical trajectories

During a period where the qubit populations stay constant ($\Omega(t) = 0$), we can instead determine the oscillator's phase-space trajectories conditioned on the qubit's ground or excited state. This semiclassical approximation is done by replacing $q^\dagger q$ in $\tilde{H}$ with $\{0, 1\}$ for transmon states $\{|g\rangle, |e\rangle\}$. This replacement gives the two Hamiltonian sectors

$$\begin{aligned} \frac{\tilde{H}_g}{\hbar} &= (\tilde{\Delta} - 4K_c|\alpha|^2)a^\dagger a - K_c a^{\dagger 2}a^2 + \left(\tilde{\Delta}\alpha^* - 2K_c|\alpha|^2\alpha^* + i(\partial_t\alpha^*) + i\frac{\kappa}{2}\alpha^* + \varepsilon^*\right) a + \text{h.c.} \\ &\quad - K_c\left(2\alpha a^{\dagger 2}a + \alpha^2 a^{\dagger 2} + \text{h.c.}\right), \\ \frac{\tilde{H}_e}{\hbar} &= (\tilde{\Delta} - \chi - 4\chi'|\alpha|^2 - 4K_c|\alpha|^2)a^\dagger a - (\chi' + K_c)a^{\dagger 2}a^2 \\ &\quad + \left(\tilde{\Delta}\alpha^* - 2K_c|\alpha|^2\alpha^* + i(\partial_t\alpha^*) + i\frac{\kappa}{2}\alpha^* + \varepsilon^* - (\chi + 2|\alpha|^2\chi')\alpha^*\right) a + \text{h.c.} \\ &\quad - (K_c + \chi')\left(2\alpha a^{\dagger 2}a + \alpha^2 a^{\dagger 2} + \text{h.c.}\right) \end{aligned} \tag{3.24}$$

describing the dynamics of the driven oscillator when the transmon is in the ground or excited state. Similar to the displaced-frame simulation, the linear part of these Hamiltonians can be individually cancelled, resulting in the two equations

$$\begin{aligned}\partial_t \alpha_g(t) &= -i\tilde{\Delta}\alpha_g(t) + 2iK_c|\alpha_g(t)|^2\alpha_g(t) - \frac{\kappa}{2}\alpha_g(t) - i\varepsilon(t)\\ \partial_t \alpha_e(t) &= -i\tilde{\Delta}\alpha_e(t) + 2iK_c|\alpha_e(t)|^2\alpha_e(t) - \frac{\kappa}{2}\alpha_e(t) - i\varepsilon(t) + i(\chi + 2\chi'|\alpha_e(t)|^2)\alpha_e(t)\end{aligned} \tag{3.25}$$

which can be used to calculate the semiclassical trajectories for the ground or excited states during periods when $\Omega(t) = 0$. In the case of a conditional displacement, after each π pulse, the Hamiltonians are swapped, and the result from the previous part of the trajectory is used to seed the next initial value problem. In our simulations, we solve these nonlinear initial value problems using a central-difference method with trajectories sampled at 1 ns. These trajectories are used in section 3.2.3 for Hamiltonian parameter calibration and in section 3.3.2 for optimization of the cavity and qubit drives to produce ECD gates.

3.2.3 Effective Hamiltonian characterization: out-and-back measurement

In a typical strong-dispersive coupling system, the Hamiltonian can be characterized by displacing the oscillator and performing spectroscopy of the transmon. The strong number-split peaks can be fit to find the effective dispersion. However, in a system where the dispersive shift is weak, these number-split peaks can be difficult to resolve, with a low contrast. In this section, we apply the semiclassical trajectories derived in the previous section in order to characterize the oscillator in the weak-dispersive regime, using a measurement called ‘out-and-back’, developed as part of this PhD work.

Although many of the Hamiltonian terms are small relative to the rate of transmon decoherence, they can be estimated in experiment using large displacements to enhance their effective strength, similar to Hamiltonian amplification used to derive the ECD gate. Here, we make use of this enhancement through the measurement sequence shown in fig. 3.2a. We first prepare the qubit in the ground or excited state then displace the oscillator out by

α_0. After a time t, the oscillator is displaced back by $-e^{i\phi}\alpha_0$, where ϕ is swept. The second displacement serves as an attempt to displace the oscillator's state back to the origin of phase-space. If the attempt is successful, ϕ encodes the oscillator's coherent-state phase accumulation at a displacement α_0 after a time t. A narrow-bandwidth π pulse ($\sigma = 200\,\mathrm{ns}$) is then used as a probe, only flipping the transmon's state measured by m_2 if the oscillator's state is close to the origin of phase space. Finally, we post-select the results of m_2 on the condition $m_1 = |\psi_i\rangle$, where $|\psi_i\rangle$ is the initial transmon state, in order to remove the influence of transmon relaxation or heating.

In fig. 3.2b, we show the results of this experiment with $t = 1\,\mu\mathrm{s}$ and $N = 5$ repetitions of out and back, used to enhance the sensitivity. In initial state $|e\rangle$, the signal is lost above $\langle n\rangle \gtrsim 2500$ photons, and in initial state $|g\rangle$, the signal is lost above $\langle n\rangle \gtrsim 7500$ photons. These values represent the oscillator photon numbers at which the qubit is excited outside of the $|g\rangle, |e\rangle$ manifold due to higher-order nonlinear transitions, a process sometimes referred to as transmon ionization that has been observed in previous experiments using readout resonators [61,62,149]. Such an effect could potentially be suppressed by using an inductive shunt, proving a path forward to engineering faster gates [151]. Figure 3.2b also indicates the critical photon number for which the effective Hamiltonian, calculated using the dispersive approximation expressions from section 3.1, begins to deviate from the exact calculation of these terms. In this system, $n^g_{\mathrm{crit}} \approx 2740$ and $n^e_{\mathrm{crit}} \approx 910$.

To extract the effective Hamiltonian values, we fit the frequency shift of the oscillator as a function of oscillator photon number, determined by the return angle and the wait time. At each $\langle n\rangle$ below the bright-stating point, the relative oscillator frequency when the transmon is in the ground or excited state is obtained by fitting $\langle\sigma_z\rangle$ to a Gaussian function and dividing its mean phase accumulation by the wait time t. The resulting relative frequency dispersion as a function of average cavity photon number $\langle n\rangle = \alpha_0^2$ for transmon states $|g\rangle$ and $|e\rangle$ is shown in fig. 3.3 by the open circles. Note that the finite duration of the displacement pulses will also influence the result, and as a secondary check, the experiment can be repeated at

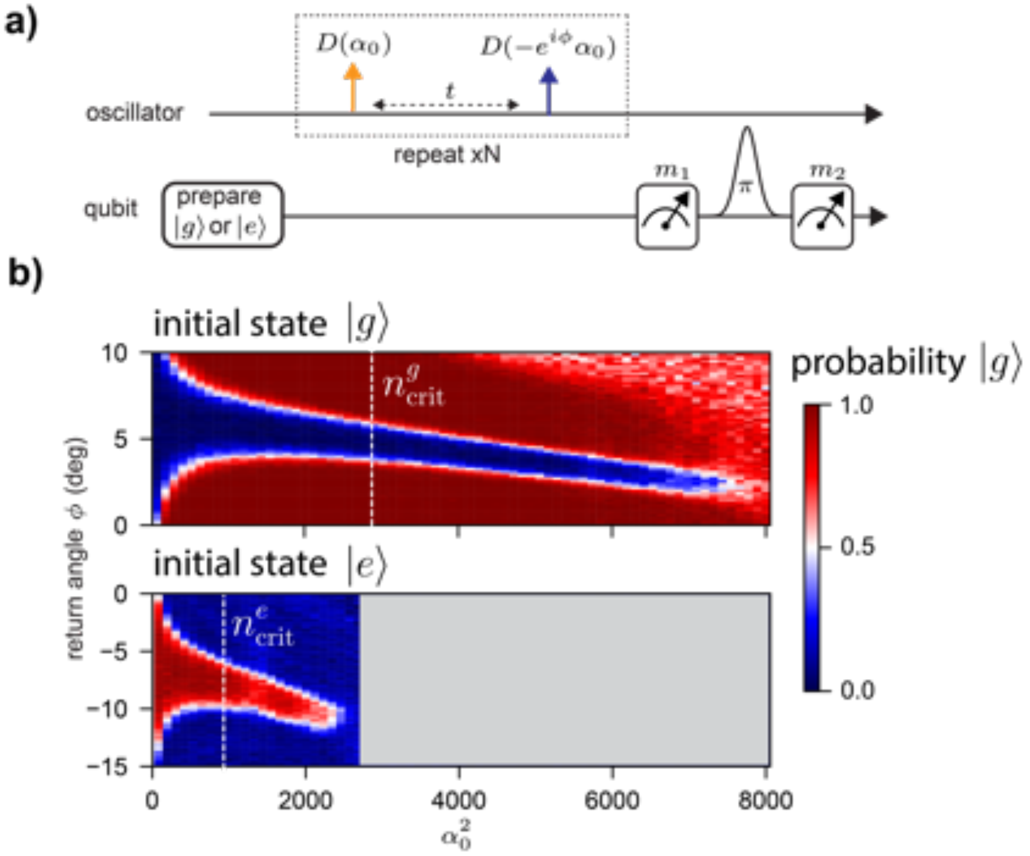

Figure 3.2: **Out-and-back measurement.** **a)** Experimental sequence to measure the phase accumulation of a coherent state with radius α_0 after a time t when the transmon is in the ground or excited state. **b)** Measurement result with initial transmon state $|g\rangle$ (top panel) and $|e\rangle$ (bottom panel) with a fixed wait time of $t = 1\,\mu\text{s}$ and $N = 5$ repetitions post-selected on measurement m_1 matching the prepared state. Colored data shown is the probability of the readout signal indicating $|g\rangle$. Also shown is the critical photon number for transmon states $|g\rangle$ and $|e\rangle$ (white dotted lines).

different wait times t.

We fit the measured dispersion (open circles in fig. 3.3) to that expected from $H_{\text{dispersive}}$ in eq. (3.2). In particular, the semiclassical trajectories in eq. (3.25) which govern the evolution of coherent states predict the effective cavity rotation frequencies to be

$$\Delta_g = \tilde{\Delta} - 2K_c\alpha_0^2 \tag{3.26}$$

$$\Delta_e = \tilde{\Delta} - \chi - (2K_c + 2\chi')\alpha_0^2 \tag{3.27}$$

as a function of the average number of photons in the cavity α_0^2 when the transmon is in the ground and excited states respectively. By fitting the sum and difference of two dispersion curves to the sum and difference of these linear functions, we can extract the four unknown Hamiltonian parameters χ, χ', K, and $\tilde{\Delta}$. The dispersion fits well to a linear function in the range of interest for control, for photon numbers up to $\alpha_0^2 < 2000$, with results given in table 4.2. For experiments using echoed conditional displacements, we use this experiment to calibrate the cavity drive frequency such that it is driven half-way between the $|g\rangle$ and $|e\rangle$ frequencies at low power, $\tilde{\Delta} = \chi/2$.

3.2.4 Predicting the effective Hamiltonian with numerical diagonalization

When using large displacements for high-fidelity control, the ability to predict the Hamiltonian before device fabrication is essential. In this section, I show that brute-force numerical diagonalization of the coupled transmon-oscillator system can predict the measured Hamiltonian with accuracy up to thousands of photons. Additionally, the transmon ionization point can be predicted, matching measurements. These methods can be compared to the analysis shown in [150] and [163]. Higher-order perturbation theory can also be used to predict an analytic effective Hamiltonian at large photon numbers in the cavity, as shown in [164].

Here, we perform numerical diagonalization of the coupled transmon-oscillator Hamilto-

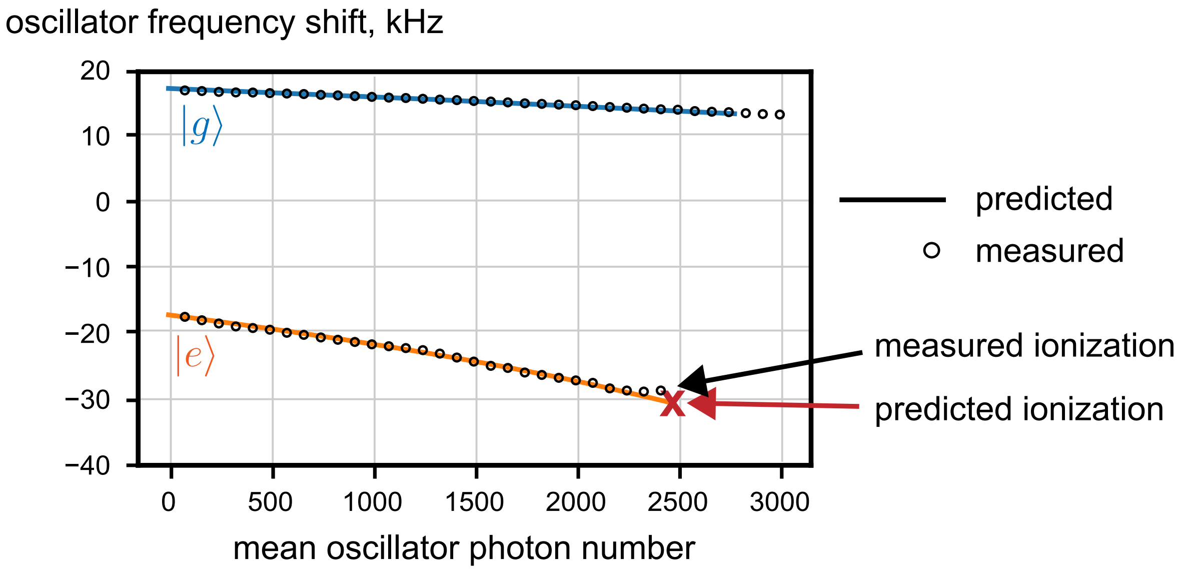

Figure 3.3: **Effective Hamiltonian prediction and measurement.** Measured relative cavity frequency shift (open circles) compared to numerical diagonalization prediction (solid lines). The open circles is a fit of the data shown in fig. 3.2. The red X indicates the predicted ionization in $|e\rangle$ using diagonalization. The measured ionization point is indicated as the last open circle fit to the data (note that the ionization point can slightly fluctuate with changing offset gate charge). The diagonalization was performed at $N_g = 0$, however other values could be used. The ground state ionizes around 7000 photons (fig. 3.2), beyond the maximum Fock number used in the diagonalization.

nian

$$\frac{H}{\hbar} = 4E_c(\hat{N} - N_g)^2 - E_J \cos(\hat{\varphi}) + \omega_c^{\text{bare}} a^\dagger a + g(\hat{N} - N_g)\left(a + a^\dagger\right) \tag{3.28}$$

where $\hat{N}$ is the Cooper-pair number operator, $\hat{\varphi}$ is the conjugate Josephson phase, N_g is the offset charge in units of $2e$, and $\hat{a}$ is the bare cavity mode annihilation operator [51].

The numerical diagonalization is carried out in two steps. First, we diagonalize the transmon in the charge basis, using 40 charge states. The transmon-oscillator coupling term is then transformed into the basis of transmon eigenstates, after which it is truncated to the first 12 transmon eigenstates. The full Hamiltonian is then diagonalized, keeping 12 transmon eigenstates and 2800 bare oscillator Fock states, following the method outlined in [165].

For photon numbers up to $\langle n\rangle \approx 1000$, we have confirmed that the oscillator's dispersion for qubit states $|g\rangle$ and $|e\rangle$ does not depend on offset charge, so we set $N_g = 0$. With this choice, we use second-order perturbation theory to find the bare Hamiltonian parameters which fit the measured hybridized mode frequencies, transmon anharmonicity, and dispersion at low $\langle n \rangle \approx 0$, resulting in the bare parameters $g/2\pi = 9.12\,\mathrm{MHz}$, $E_j/2\pi = 32.33\,\mathrm{GHz}$, $E_c/2\pi = 181\,\mathrm{MHz}$ and $\omega_c^{\mathrm{bare}} = 5.26\,\mathrm{GHz}$. Using these parameters, we numerically diagonalize eq. (3.28) using the method outlined above. The resulting dispersion is shown by the solid lines in fig. 3.3, which have excellent agreement with the measured dispersion.

When performing this diagonalization, each eigenstate in the hybridized basis should be matched to an eigenstate in the bare basis that would adiabatically transform into it under a slow ramp of the oscillator photon number. Such a mapping is sometimes called quantum number assignment, and it is needed to produce the solid lines in fig. 3.3. However, it is sometimes difficult to assign a unique bare state to a given hybridized state since the hybridized state has amplitudes spread across many different bare states. In the setting studied here, this is evidence that the transmon state has left the manifold of well-defined states in the cosine potential ($|g\rangle, |e\rangle, |f\rangle, \ldots$), and we call this process ionization. In our system, the diagonalization algorithm predicts a breakdown of quantum number assignment for transmon state $|e\rangle$ at 2500 photons in the oscillator, closely matching the measured transmon ionization, as is shown in fig. 3.3.

Finally, the effective Hamiltonian can also be predicted using higher-order RWA methods. As an example, the Stark-shift data shown in fig. 3.3 is explicitly compared with a recursive higher-order RWA perturbation theory in [164], showing an excellent agreement. This method is more efficient than the brute force diagonalization shown here.

3.2.5 Characterizing transmon relaxation with large oscillator displacements

As discussed in section 3.1, effects such as two-level-system defects cause the transmon relaxation rate to increase due to the Purcell effect when the transmon is Stark-shifted onto resonance with them. Here, we probe this effect using large displacements.

We use a similar out-and-back measurement to probe the transmon relaxation and heating rate while the cavity is displaced to a large coherent state, since a reduction in transmon lifetime has been observed when displacing readout resonators [166]. For this, we use the out-and-back sequence in fig. 3.2a, except we sweep t, and fix $\phi(t)$ close to phases that displace the oscillator's state back to the origin of phase-space at each $\langle n \rangle$ given the measured dispersion. In this case, we focus on the result of m_1. We find that, up to 2000 oscillator photons, there is no appreciable heating out of $|g\rangle$ when displacing the cavity state, indicating that the dressed dephasing rate is small [138]. However, when preparing the transmon in $|e\rangle$, we measure that the transmon's relaxation rate shows a dependence on cavity photon number. In fig. 3.4 we plot the measured probability of the transmon remaining in $|e\rangle$ after a wait time t up to 4 µs when displacing the cavity to $\langle n \rangle = \alpha_0^2$, with experiments run on three consecutive days.

We suspect this time-dependent $\tilde{T}_{1,q}$ vs $\bar{n}_{\text{cav}}$ effect is caused by fluctuating two-level-systems (TLS) which come into resonance with the transmon as it is Stark-shifted by cavity photons [160, 167, 168]. Although the T_1 vs $\bar{n}$ changes with time, we find an average value of $\tilde{T}_{1,q} \approx 30\,\mu\text{s}$ for $\bar{n} = 900$ over the data plotted in fig. 3.4, and we use this value when performing master equation simulations in section 4.6.

3.2.6 Oscillator drive strength calibration with geometric phase

In this section, we discuss a simple experiment which can be used to calibrate a linear oscillator drive amplitude in the weak-χ regime. Starting with the qubit prepared in $|\psi_i\rangle = \frac{1}{\sqrt{2}}\left(|g\rangle + |e\rangle\right)$, we construct an oscillator drive sequence which encloses an area in phase space for both $|g\rangle$ and $|e\rangle$ trajectories. By disentangling the qubit and oscillator at the end of the sequence, the qubit will be left in the state $|\psi_f\rangle = \frac{1}{\sqrt{2}}\left(|g\rangle + e^{i\phi}|e\rangle\right)$ where ϕ encodes the enclosed area [169–172]. Given an arbitrary displacement pulse shape $g(t)$ with a length t_p,

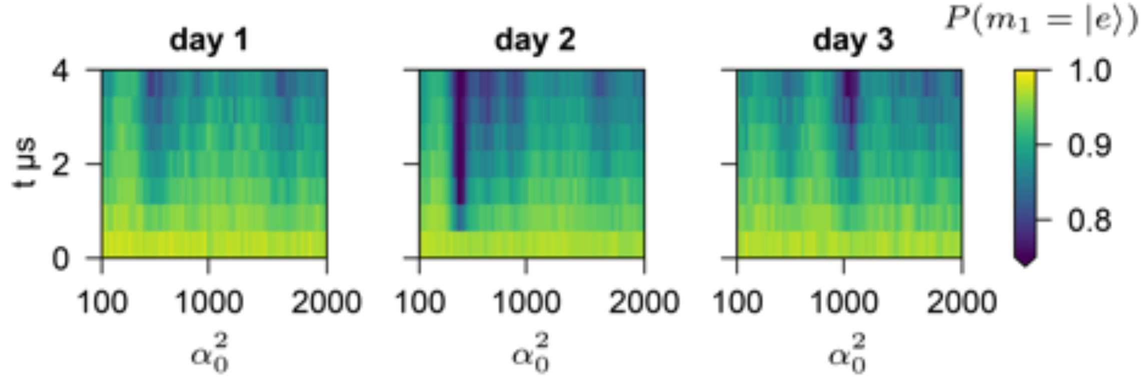

Figure 3.4: **Fluctuating transmon relaxation when populating the cavity.** Measured transmon relaxation as a function of $\alpha_0^2 = \langle n \rangle$ found by analyzing m_1 measurement results in an out-and-back measurement similar to fig. 3.2 with initial transmon state $|e\rangle$ and sweeping t. For this measurement, the transmon is initialized in $|e\rangle$, and the oscillator is displaced. After a time t (y-axis), the oscillator is displaced back to the origin, assuming the transmon was in $|e\rangle$ throughout the delay. The resulting transmon state is then measured. Measurement results shown for three consecutive days with each experiment averaging for around 1 hour. It is possible that the observed fluctuations of T1 when displacing the oscillator are caused by the transmon Stark-shifting into fluctuating two-level-systems, as here we do not observe excitations outside the $|g\rangle$,$|e\rangle$ manifold, so it is unlikely that the effect is caused by nonlinear photon-induced transitions outside the ground and excited state manifold. These effects need further investigation as they are likely a limiting factor in GKP error correction and control using large displacements.

a simple pulse sequence that accomplishes this is

$$\varepsilon(t) = \varepsilon_0 \left[g(t) - rg(t-(t_p+t_w)) - rg(t-(2t_p+t_w)) + g(t-(2t_p+2t_w))\right] \tag{3.29}$$

as shown in fig. 3.5a with a phase-space trajectory shown in fig. 3.5b. This drive is similar to a conditional displacement without a qubit π pulse, and the goal here is to calibrate the pulse scale ε_0.

To analyze this sequence, we note that for low photon numbers, the Hamiltonian is well described by only the dispersive term. With this approximation, the semiclassical trajectories in eq. (3.25) can be solved with initial value $\alpha_{\substack{g\\e}}(0) = 0$ giving

$$\alpha_{\substack{g\\e}}(t) = e^{-\frac{1}{2}(\pm i\chi+\kappa)t}\left(e^{\frac{1}{2}(\pm i\chi+\kappa)t_0}\alpha_{\substack{g\\e}}(t_0) - i\int_{t_0}^{t} e^{\frac{1}{2}(\pm i\chi+\kappa)\tau}\varepsilon(\tau)d\tau\right). \tag{3.30}$$

Substituting $\varepsilon(t)$ into eq. (3.30), we solve for the ratio of the middle-two pulses, r, such that the condition $\alpha_{\substack{g\\e}} = 0$ is satisfied at the end of the entire sequence, and the qubit and oscillator are disentangled. Remarkably, this ratio is independent of the shape of the displacement pulse $g(t)$, and is found to be

$$r = \frac{1 + e^{\frac{1}{2}(\pm i\chi+\kappa)(3t_p+2t_w)}}{e^{\frac{1}{2}(\pm i\chi+\kappa)(t_p+t_w)} + e^{\frac{1}{2}(\pm i\chi+\kappa)(2t_p+t_w)}} \tag{3.31}$$

where t_p is the length of the displacement pulses $g(t)$ and t_w is the wait time. By Taylor expanding this ratio in orders of κ, we find in the limit $(t_p + t_w) << 1/\kappa$,

$$r = \cos\left(\frac{\chi}{4}(3t_p + 2t_w)\right)\sec\left(\frac{\chi}{4}t_p\right) \tag{3.32}$$

independent of the qubit state. In the high-Q oscillator limit, this sequence disentangles the oscillator and qubit and can be used to measure the geometric area enclosed by the trajectory.

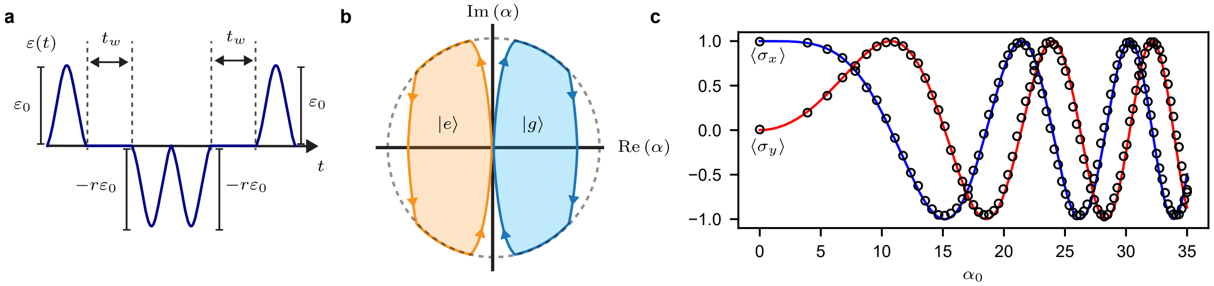

Figure 3.5: **Geometric phase measurement. a.** Geometric phase measurement drive sequence and drive parameterization. **b.** Phase space trajectories for α_g and α_e. **c** Measured $\langle\sigma_x\rangle$ and $\langle\sigma_y\rangle$ compared to expected phase found by solving the semiclassical trajectories in eq. (3.25) (solid lines) as a function of phase space radius α_0.

Using eq. (3.30), we numerically integrate the sequence with displacement pulses $g(t)$ chosen as truncated Gaussians with standard deviation $\sigma = 11\,\mathrm{ns}$ and total pulse duration $t_p = 44\,\mathrm{ns}$ to find the phase-space trajectories for $\alpha_{\substack{g\\e}}$, including the maximum phase-space radius α_0, and the associated geometric phase difference. By measuring $\langle\sigma_x\rangle$ and $\langle\sigma_y\rangle$ while sweeping the drive scale, this phase difference is fit to the experiment, allowing a calibration of ε_0 in terms of DAC amplitude. In fig. 3.5c we show an example of the measured phase accumulation as ε_0 is linearly scaled ($t_w = 200\,\mathrm{ns}$), along with the phase predicted using the integrated geometric area. If desired, nonlinear effects can be included by using eq. (3.25) when calculating the trajectories, however in this case it is no longer guaranteed that r given by eq. (3.31) will exactly disentangle the oscillator and qubit. Using this, we find a maximum drive amplitude of $|\varepsilon|_{\max}/2\pi \approx 400\,\mathrm{MHz}$ before saturating our room-temperature amplification chain.

3.3 Realizing the echoed conditional displacement gate

In section 3.3.1 we derive the echoed conditional displacement unitary assuming an ideal dispersive Hamiltonian. Next, in section 3.3.2, we optimize the ECD gate considering drive constraints and higher-order nonlinearities.

3.3.1 Derivation of the ECD gate

Here, $\varepsilon(t)$ is a complex-valued function representing the envelope of an I-Q modulated drive with a carrier frequency $(\omega_g + \omega_e)/2$, where ω_g (ω_e) is the oscillator's frequency when the qubit is in the ground (excited) state. In the co-rotating frame at the drive frequency and qubit frequency, the ideal Hamiltonian is

$$\frac{H}{\hbar} = \chi a^\dagger a \frac{\sigma_z}{2} + \varepsilon^*(t)a + \varepsilon(t)a^\dagger \tag{3.33}$$

where we have neglected terms rotating at twice the drive frequency.

The echoed conditional displacement gate consists of two driving steps with a qubit π pulse between, here assumed instantaneous. In this case, the general solution to the time-dependent Schrödinger equation $i\hbar\partial_t U = HU$ is

$$U = \mathcal{T}e^{-\frac{i}{\hbar}\int_{t_1}^{T} H(\tau)d\tau}\sigma_x \mathcal{T}e^{-\frac{i}{\hbar}\int_{0}^{t_1} H(\tau)d\tau} \tag{3.34}$$

where t_1 is the time of the π pulse, T is the total time of the gate, and $\mathcal{T}$ is the time-ordering operator.

To represent the action of the π pulse flipping the sign of σ_z between the two trajectories, we instead modify the dispersive Hamiltonian to include a function $z(t) = \pm 1$ which represents the sign of σ_z, giving

$$\frac{H}{\hbar} = \chi a^\dagger a \frac{\sigma_z z(t)}{2} + \varepsilon^*(t)a + \varepsilon(t)a^\dagger. \tag{3.35}$$

Using this modified Hamiltonian, we take as an ansatz for the solution of the Schrödinger equation

$$U = e^{i\theta\frac{\sigma_z}{2}} e^{a^\dagger(\gamma + \delta\sigma_z) - a(\gamma^* + \delta^*\sigma_z)} e^{i\phi a^\dagger a \sigma_z} \tag{3.36}$$

where θ represents an ancilla qubit phase, γ and δ represent a displacement and conditional displacement, ϕ represents a qubit state-dependent rotation of the oscillator, and these variables are time-dependent.

Ignoring a global phase, the Schrödinger equation gives

$$\partial_t \theta = -2\mathrm{Re}\left[\delta \varepsilon^*\right] \tag{3.37}$$

$$\partial_t \gamma = -i\frac{\chi}{2} z(t)\delta - i\varepsilon \tag{3.38}$$

$$\partial_t \delta = -i\frac{\chi}{2} z(t)\gamma \tag{3.39}$$

$$\partial_t \phi = -\frac{\chi}{2} z(t). \tag{3.40}$$

These equations can be solved, giving

$$\theta(t) = -2\int_0^t d\tau \mathrm{Re}\left[\varepsilon^*(\tau)\delta(\tau)\right] \tag{3.41}$$

$$\gamma(t) = -i\int_0^t d\tau \cos\left[\phi(\tau) - \phi(t)\right]\varepsilon(\tau) \tag{3.42}$$

$$\delta(t) = -\int_0^t d\tau \sin\left[\phi(\tau) - \phi(t)\right]\varepsilon(\tau) \tag{3.43}$$

$$\phi(t) = -\frac{\chi}{2}\int_0^t d\tau z(\tau). \tag{3.44}$$

The state-dependent rotation of the oscillator can be canceled by setting $\phi(T) = 0$. For the echoed conditional displacements in this work, this is done by applying a single qubit π pulse at time $T/2$. If desired, more qubit echoes can be included, subject to the condition $\int_0^T d\tau z(\tau) = 0$.

Using the Baker-Campbell-Hausdorff formula, the conditional displacement and displacement can be separated, giving the overall unitary

$$U = \sigma_x e^{i\theta' \frac{\sigma_z}{2}} D(\lambda) CD(\beta) \tag{3.45}$$

corresponding to a conditional displacement $CD(\beta) = D(\beta/2)\left|g\right\rangle\left\langle g\right| + D(-\beta/2)\left|e\right\rangle\left\langle e\right|$, a displacement, and an additional qubit phase with the parameters $\beta = 2\delta(T)$, $\lambda = \gamma(T)$, and $\theta' = \theta(T) + 2\mathrm{Im}\left[\gamma(T)\delta(T)\right]$. We have also explicitly included a σ_x operator to represent the action of the single π pulse (here $\mathrm{ECD}\left(\beta\right) = \sigma_x CD(\beta)$).

To realize an ECD gate, we aim to null the qubit phase and oscillator displacement. In the limit of instantaneous displacements and motivated by the geometry of rotating phase-space, this can be perfectly achieved by choosing the drive

$$\varepsilon(t) = \alpha\left[\delta(t) - 2\delta(t - T/2)\cos\left(\chi T/4\right) + \delta(t - T)\cos\left(\chi T/2\right)\right] \tag{3.46}$$

where $\delta(t)$ is the Dirac delta function. This drive corresponds to the displacement sequence described in fig. 2.4 of the previous chapter with $\beta = 2i\alpha e^{i\phi}\sin\left(\chi T/2\right)$ and $|\alpha| = \alpha_0$.

The drive in eq. (3.46) cannot be realized in experiment due to bandwidth and amplitude limits of a realistic microwave drive. Also, effects such as photon loss, higher-order nonlinearities, and the finite duration of the qubit π pulse are not taken into account in Equations (3.41) to (3.44). To realize a high-fidelity ECD gate in the presence of these effects, we optimize $\varepsilon(t)$ using semiclassical trajectories as described in the next section 3.3.2.

3.3.2 Optimization of the ECD gate

In our experiment, the dynamics can slightly differ from those described by eqs. (3.41) to (3.44) due to the second-order dispersive shift χ' and the oscillator Kerr K_c which become relevant at large phase-space displacements. These effects can be studied by examining the displaced-frame Hamiltonian in eq. (3.22). In $\tilde{H}$, nonlinear terms proportional to χ' or K_c can generally cause distortions to the state. However, simulations indicate that these terms do not significantly decrease the fidelity of ECD control protocols given our system parameters in table 4.2. This is partially because the deleterious effect of terms which are proportional to $\mathrm{sign}(\alpha)$ or $\mathrm{sign}(\sigma_z)$ are significantly reduced due to the phase-space echo $\alpha \rightarrow -\alpha$ and qubit echo $|g\rangle \leftrightarrow |e\rangle$ at time $T/2$ during the ECD gate, which cancels part of their on-average effect to the state distortion in the same way the qubit-state dependent oscillator rotation is canceled during the ideal ECD gate.

With this in mind, we optimize ECD gates using semiclassical trajectories (section 3.2.2) which account for the linear displaced-frame terms (proportional to a), including those caused by the second-order disperse shift, Kerr, and photon loss. We assume a form of the unitary still given by eq. (3.45), with the values of β, λ and θ' calculated using the trajectories $\alpha_{\substack{g\\e}}(t)$ for the ground and excited qubit states. We note that ECD(β) can be generated with any α_0 or χ as long as $\chi T < 2\pi$ and the qubit rotation pulse bandwidth is sufficiently large compared to χ. In particular, a large α_0 is not required.

To construct each ECD gate, we start by imposing the drive to be of the form shown in fig. 3.6a, which replaces the Dirac δ-functions in eq. (3.46) with fixed-length Gaussian waveforms, chosen in our experiment with a standard deviation of $\sigma = 11\,\text{ns}$ and a total length of $4\sigma = 44\,\text{ns}$. This simplification is chosen so that the drive strength required to realize the large displacements used in this work remains in the linear regime of our room temperature amplification chain, and so the displacements take the exact same form as those used to calibrate the drive amplitude using the geometric phase measurement shown in section 3.2.6. The amplitude ratio of the second, third, and fourth Gaussian to the first are given by r_2, r_3, and r_4, and the wait time between the displacements is given by t_w.

Using a simple optimization strategy, we find the values of $\{\varepsilon_0, r_2, r_3, r_4\}$ which realize a target conditional displacement β with intermediate phase-space radius α_0 in the shortest time t_w. Starting with a large guess time t_w, the parameters are optimized with a Nelder-Mead method using the cost function

$$\mathrm{C} = |\alpha_g(T/2) + \alpha_e(T/2)|^2 + |\alpha_g(T) + \alpha_e(T)|^2 + \tag{3.47}$$

$$\left(\frac{|\alpha_g(T/4) + \alpha_e(T/4)|}{2} - \alpha_0\right)^2 + \left(\frac{|\alpha_g(3T/4) + \alpha_e(3T/4)|}{2} - \alpha_0\right)^2 \tag{3.48}$$

where $\alpha_{\substack{g\\e}}(t)$ is calculated using eq. (3.25) including the second-order dispersive shift, Kerr, and photon loss. This cost function minimizes the final and midpoint net displacement, and ensures an intermediate phase space radius of α_0 for the first and third displacements. Once $\{\varepsilon_0, r_2, r_3, r_4\}$ have converged at a given t_w, β is calculated as $\alpha_e(T) - \alpha_g(T)$, and t_w is stepped down until the target β is realized. If t_w reaches 0, and the target β has not been reached, then α_0 is reduced until the target β is realized. We note that shorter pulses could instead be used in this small-β case, however in our proof of principle example, we keep the displacement duration fixed such that the pulses do not occupy a larger bandwidth than those used in the calibration.

The form of the resulting conditional displacement strongly depends on β and the choice of α_0. In fig. 3.6b and fig. 3.6c we illustrate the result of this optimization using our system parameters for $\beta = 1$ in two different regimes, $\alpha_0 = 10$ and $\alpha_0 = 50$. In the first case, a majority of the conditional displacement is accumulated during the wait times t_w. In the second case, t_w is reduced to 0, resulting in α_0 being further lowered to ≈ 45 to realize the gate. In this regime, the conditional displacement is accumulated during the driving periods, and increasing the target α_0 does not result in a faster gate after optimization. This is the reason for the drive-constraint limit shown in fig. 4.1a in the next chapter.

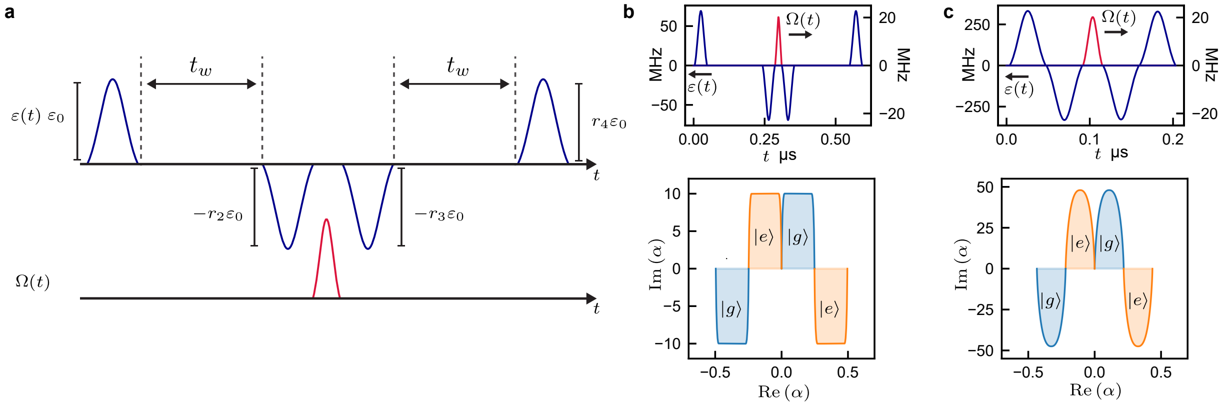

Figure 3.6: **Echoed conditional displacement optimization and trajectories. a.** Parameterization of the drive $\varepsilon(t)$ for the echoed conditional displacement. **b. and c.** Echoed conditional displacement gate for $\beta = 1$ optimized with target $\alpha_0 = 10$ (**b**) and $\alpha_0 = 50$ (c). Top panels show the resulting drives, and bottom panels show the semi-classical phase space trajectories at a large aspect ratio.

3.3.3 Fidelity model of a single ECD gate

The relative contribution of qubit and oscillator errors to the infidelity of each ECD operation depends on α_0 and $|\beta|$. Here we develop a simple model to study decoherence due to these effects, and our model could be used in future investigations to optimize the choice of these parameters. Suppose we perform an operation to create a cat state using a single ECD(β) gate, namely

$$\frac{1}{\sqrt{2}}\left(|g\rangle + |e\rangle\right)|0\rangle \rightarrow \frac{1}{\sqrt{2}}\left(|e\rangle|\beta/2\rangle + |g\rangle|-\beta/2\rangle\right), \tag{3.49}$$

with a gate time $T \approx \frac{|\beta|}{\chi\alpha_0}$. If a qubit error (bit-flip or phase-flip) occurs during the ECD gate, the joint state is left orthogonal to the target state above. The final state infidelity to the target state will be equal to the probability of such a qubit error occurring. With the ECD construction, this is given by $1 - \mathcal{F}_{\text{qubit}} \approx \gamma T \approx \gamma|\beta|/\chi\alpha_0$ where γ is the qubit error rate assumed to be small compared to the inverse gate time. For our system, $\gamma = \gamma_{2E}$. Post-selection after an ECD sequence on the target qubit state can help mitigate this error in the state-preparation case as is done in our experimental demonstrations.

Oscillator relaxation increases the state infidelity proportionally to $|\beta|^3$. Similar to the cat code, the rate of phase decoherence due to photon loss in a coherent state superposition will increase linearly with the number of photons in the cat [173], and the final density matrix will be approximately

$$\rho(T) \approx \frac{1}{2}\left[|-\beta/2\rangle\langle-\beta/2|\,|g\rangle\langle g| + |\beta/2\rangle\langle\beta/2|\,|e\rangle\langle e| + \right. \tag{3.50}$$

$$\left. \exp\left(-2\kappa\int_0^T \left|\frac{\beta(t)}{2}\right|^2 dt\right)\left(|-\beta/2\rangle\langle\beta/2|\,|g\rangle\langle e| + |\beta/2\rangle\langle-\beta/2|\,|e\rangle\langle g|\right)\right] \tag{3.51}$$

The integral can be approximated giving an infidelity

$$1 - \mathcal{F}_{\text{photon loss}} \approx (1/2)\left(1 - \exp\left(-\kappa|\beta|^2 T/4\right)\right) \approx \kappa|\beta|^3/(8\chi\alpha_0). \tag{3.52}$$

Oscillator dephasing will be enhanced by the large displacements during the ECD gates as discussed in section 3.2.1, resulting in an effective oscillator diffusion-like terms proportional to $2\kappa_\varphi|\alpha_0|^2$. The effect of these terms on the state fidelity will depend on the particular target state, however in the case of a single ECD gate we numerically find they result in an effective infidelity modeled well by $1-\mathcal{F}_{\text{dephasing}} \approx 2\kappa_\varphi \alpha_0^2 T \approx 2\kappa_\varphi|\beta|\alpha_0/\chi$. With this, the total state infidelity of a single ECD gate used for cat-state preparation is

$$1-\mathcal{F} \approx \frac{1}{\chi}\left(\gamma_{2E}|\beta|/\alpha_0 + \kappa\left|\beta\right|^3/\left(8\alpha_0\right) + 2\kappa_\varphi|\beta|\alpha_0\right). \tag{3.53}$$

The effective model here also effects tomography. In particular, the characteristic function tomography will have a radially-dependent reduction in contrast given by the scaling in the above equation. In [99], we explicitly measured this contrast reduction, and fit it to a heuristic model.

3.4 Measuring an oscillator in the weak-coupling regime

The goal of this section is to describe how the oscillator's state can be measured using an auxiliary transmon. A central development of this work is the characteristic function measurement in cQED, which can be used to measure the oscillator's state in a weak-coupling regime.

3.4.1 Phase estimation

To measure the state of a high-quality-factor oscillator in cQED, a circuit such as the one shown in fig. 3.7 is employed. This circuit is sometimes called a quantum phase-estimation circuit,[6] or a 'Hadamard-test'. First, the qubit is prepared in the $|+\rangle$ state. Next, a controlled-unitary of the form $U = e^{i\hat{O}/2}$ is performed, where $\hat{O}$ is a Hermitian operator

---

[6] since it can be used to measure the phase of $\langle e^{i\hat{O}}\rangle$

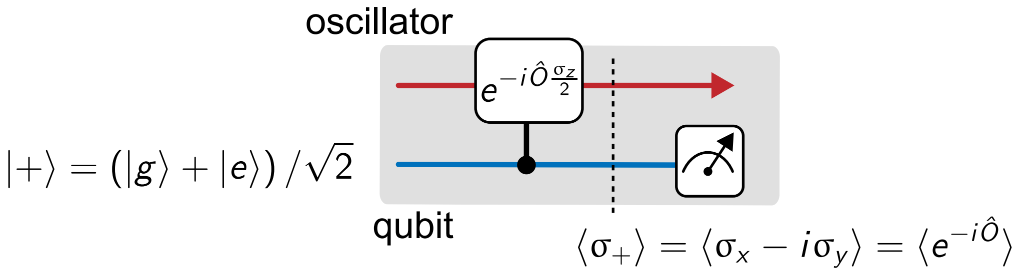

Figure 3.7: **The oscillator phase-estimation circuit.** This circuit is used to measure the expectation value of $U = e^{-i\hat{O}}$ where $\hat{O}$ is a Hermitian operator on the oscillator Hilbert space. The final qubit measurement is performed in a basis defined by a variable angle φ along the equatorial plane of the Bloch sphere be written as $|\pm\rangle_\varphi = (|g\rangle \pm e^{i\varphi}|e\rangle)$ ($\varphi = 0$ corresponds to a σ_x measurement while $\varphi = \pi/2$ corresponds to a σ_y measurement), usually performed by applying the appropriate $\pi/2$ rotation then measuring σ_z. In cases where U is unitary but not Hermitian, its eigenvalues will lie on the unit-circle in the complex plane, and a measurement of both σ_x and σ_y is required (hence the name 'phase-estimation'). When U is also Hermitian, the only possible eigenvalues are ± 1, and only σ_x is required. Note that when the oscillator is not in an eigenstate of U (which is most often the case, considering eigenstates of U can be non-normalizable), the magnitude of the expectation value will be less than unity. In this cases, both the phase and the magnitude can be extracted, however we often still call the circuit 'phase-estimation'.

on the oscillator. It can be easily shown that after this interaction, the expectation value of $\langle\sigma_+\rangle = \langle\sigma_x - i\sigma_y\rangle$ on the qubit is the same as the expectation value of $\langle e^{i\hat{O}}\rangle$ on the oscillator. From this, the real and imaginary part of $\langle e^{i\hat{O}}\rangle$ can be measured with a measurement of either σ_x or σ_y, respectively. These measurements can be carried out by applying the $R_{\pi/2}(\pi/2)$ or $R_0(\pi/2)$ gate to the auxiliary qubit and finally performing a σ_z measurement. By varying $\hat{O}$, different expectation values can be measured, and the oscillator's state can be reconstructed.

As an example, the Wigner function can be measured using a phase-estimation circuit of this type [173]. The Wigner function is related to the displaced-parity operator by $W(\alpha) = \langle D(\alpha)e^{i\pi a^\dagger a}D^\dagger(\alpha)\rangle$ [174]. A controlled-displaced-parity can be implemented from a controlled-parity operator (see section 2.4.3) by $D(\alpha)e^{i\pi a^\dagger a\sigma_z/2}D^\dagger(\alpha) = e^{i\pi D(\alpha)a^\dagger a D^\dagger(\alpha)\sigma_z/2}$. The displaced-parity operator is Hermitian and unitary, so the only two possible eigenvalues are real and ±1. The expectation value of σ_x while varying α can be used to measure the oscillator's Wigner function.

However, as discussed in section 2.4.3, the controlled-parity operation requires waiting for a time $T_{\text{parity}} = \pi/\chi$. In the weak-coupling regime, this can be prohibitively long, and the contrast of the measured data can be low due to transmon decay and dephasing during the measurement.

3.4.2 Characteristic function tomography

An alternative approach to measuring the oscillator's density matrix is to measure the Characteristic function, defined as $\mathcal{C} = \langle D(\alpha)\rangle$, with more details given in appendix A.3. The characteristic function is the Fourier transform of the Wigner function, and therefore defines the oscillator's reciprocal space.

The tomographic sequence used to measure the characteristic function after each ECD sequence is shown in fig. 3.8a. As shown in previous works ([26, 66, 175]), the oscillator's characteristic function defined as $\mathcal{C}(\beta) = \mathrm{Tr}\left(D(\beta)\rho\right)$ can be measured using a conditional displacement embedded within a qubit Ramsey sequence resulting in $\langle \sigma_x - i\sigma_y\rangle = \langle D(\beta)\rangle$ before the second $\pi/2$ pulse. By varying the phase of the second $\pi/2$ pulse, we can measure either the real or imaginary part of $\mathcal{C}(\beta)$ by measuring either $\langle\sigma_x\rangle$ or $\langle\sigma_y\rangle$ respectively. We also include a first measurement m_1 to disentangle the qubit and oscillator before the tomography, and post-select the results of the characteristic function (m_2) on $m_1 = |g\rangle$. We note that the pulses in this work are designed to realize state preparation sequences of the form $|0\rangle\,|g\rangle \to |\psi\rangle\,|g\rangle$ which disentangle the oscillator and qubit after the pulse. However, due to decoherence during the pulse, there is small residual entanglement between the oscillator and qubit, hence the need for m_1.

To simplify tomography, the ECD gate used to measure the characteristic function is realized using the optimization method in section 3.3.2 for $\beta = 1.0$ using $\alpha_0 = 2.0$. The amplitude and phase of this ECD gate is swept in experiment to sample the characteristic

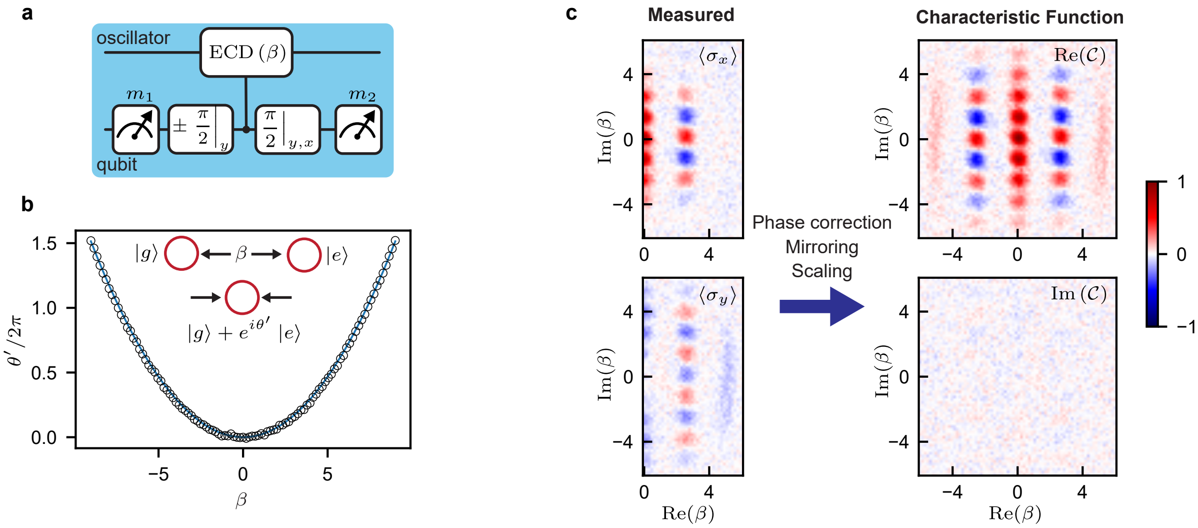

Figure 3.8: **Characteristic function tomography method. a.** Characteristic function measurement sequence **b.** Measured qubit phase accumulation (open circles) after the *cat-and-back* sequence (depicted in the inset). Data matches the phase predicted by eq. (3.44) (solid line). **c.** Example of characteristic function post-processing using the measured GKP $|+Z\rangle$ state.

function. This low α_0 is chosen so the second-order dispersive shift and Kerr have a negligible effect on the tomography, and the applied gate is well described by eq. (3.45). From this, the additional qubit phase θ' can be easily predicted and corrected in post-processing.

To verify the validity of eq. (3.41) in predicting this phase, we measure the phase θ' by using a *cat-and-back* ECD sequence depicted in the inset of fig. 3.8b: We prepare the qubit in $|+x\rangle = \frac{1}{\sqrt{2}}(|g\rangle + |e\rangle)$, then apply two conditional displacements: $\text{ECD}(\beta), \text{ECD}(-\beta)$, with a qubit π pulse between, after which the qubit phase is measured (by measuring $\langle\sigma_x\rangle$ and $\langle\sigma_y\rangle$). Here, the ECD gates are the same as those used for characteristic function tomography ($\alpha_0 = 2$ at $\beta = 1$, and amplitude is swept). The resulting phase θ' in fig. 3.8b shows excellent agreement with the prediction from eq. (3.41).

With this, the post-processing of the tomographic $\langle\sigma_x\rangle$ and $\langle\sigma_y\rangle$ is depicted in fig. 3.8c, using the measured data for the $|+Z\rangle_{\text{GKP}}$ state as an example. In experiment, we alternate between $\pm\pi/2$ for the first $\pi/2$ pulse to symmetrize the transmon's T_1 error channel during readout. Since the characteristic function obeys the property $\mathcal{C}(-\beta) = \mathcal{C}^*(\beta)$, we only measure half of the real and imaginary parts, then mirror about the $\mathrm{Re}(\beta) = 0$ axis. The characteristic function is found by applying a phase correction $\mathcal{C}(\beta) \to e^{i|\beta|^2\theta_0'}\mathcal{C}(\beta)$ where θ_0' is the phase predicted by eq. (3.41) for $\beta = 1$ using the ECD pulse optimized for tomography ($\alpha_0 = 2$). We note that this phase is slightly different than the phase found using the cat-and-back experiment described above, which is only verifying the validity of eq. (3.41). Finally, the data is scaled such that $\mathcal{C}(0) = 1$, effectively accounting for qubit decoherence (T_{2E}) during the tomography.

3.5 Speed limit of control

Finally, given the results of the characterization shown in this chapter, it is useful to analyze the fastest possible speed limit of universal oscillator control. For this, as an estimate, we will use the critical photon number in $|e\rangle$ as a rule-of-thumb for the maximum displacement of the oscillator. However, in practice, other effects such as two-level-systems and enhanced dephasing noise will limit the speed of gates. The latter of these is optimized explicitly in section 4.6.4.

Using the critical photon number given in eq. (3.13), the maximum conditional displacement rate is $g_{\text{eff}}^{\max} = \alpha_0^{\max}\chi \approx \sqrt{n_{\text{crit}}^{e}}\chi$ using the critical photon number for the first excited state of the transmon. From perturbation theory, the transmon-oscillator dispersive coupling is $\chi \approx (2g^2E_C)\,/\,(\Delta(\Delta - E_C))$ and the transmon anharmonicity is $K \approx E_C$ [34]. In the regime $\Delta \gg E_C$ we can approximate $\Delta - E_C \approx \Delta$ and combine the above expressions to find

$$g_{\text{eff}}^{\max} \approx \sqrt{\frac{\chi K}{6}} \tag{3.54}$$

We note other experiments using sideband three-wave-mixing interactions are similarly limited by a bound $\propto \sqrt{\chi K}$ [132,176,177]. This suggests that at a fixed dispersive shift, increasing transmon anharmonicity could lead to faster interaction rates, giving a path forward for engineering higher-fidelity gates with enhanced effective three-wave interactions.

Chapter 4

Demonstrating universal control of a nearly-linear oscillator

In this chapter, we combine results of the previous two chapters to work to answer the question: is it possible to control the quantum state of a nearly-linear oscillator? In particular, here we demonstrate the use of a weak-coupling architecture (chapter 3) with the phase-space universal gate set (section 2.4.5) to realize arbitrary control of the oscillator.

4.1 Summary of results

To introduce our demonstrations, recall that the full manipulation of a quantum system requires controlled evolution generated by strong nonlinear interactions. Such nonlinear control is most often coherent when the rate of nonlinearity is large compared with the rate of decoherence [106, 178]. As a result, engineered quantum systems typically rely on a bare nonlinearity much stronger than decoherence rates, and this hierarchy is usually assumed to be necessary.

Here we challenge this assumption by demonstrating the universal control of a quantum system where the rate of bare nonlinear interaction (quantified here by $\chi/2\pi$, the inverse of the typical gate time using previous methods [104]) is comparable to the fastest rate of decoherence (γ_2, the transmon dephasing rate). We do this by demonstrating a noise-resilient protocol - the phase-space instruction set architecture (section 2.4.5) using the Echoed Conditional Displacement (ECD) gate - for the universal quantum control of a nearly harmonic oscillator that takes advantage of an in situ enhanced nonlinearity instead of harnessing a bare nonlinearity, i.e., by using the Hamiltonian amplification ideas introduced in section 2.4.4.

Our demonstrations include the preparation of a single-photon state with high fidelity (section 4.3), the generation of squeezed vacuum with large intracavity squeezing (11.1 dB) (section 4.4), and measurement-free preparation of logical states for the binomial and Gottesman-Kitaev-Preskill quantum error-correcting codes (section 4.5). To the best of our knowledge, the squeezed state demonstrated here is the largest squeezing to date of a high-quality-oscillator in the microwave regime, demonstrating the power of our approach. The summary of results of these demonstrations is given in table 4.1, including the measured and simulated state preparation fidelities.

State	$\mathcal{F}_{\text{exp}}$ (%)	$\mathcal{F}_{\text{sim}}$ (%)	$\mathcal{F}_{\text{sim}}^{\kappa_\phi}$ (%)
$\lvert 1\rangle$	98	99	98
$\lvert 2\rangle$	92	97	94
$\lvert 3\rangle$	88	97	93
$\lvert 4\rangle$	87	97	92
$\lvert 5\rangle$	82	94	83
$\lvert +Z\rangle_{\text{bin}}$	92	98	95
$\lvert +X\rangle_{\text{bin}}$	89	97	94
$\lvert +Y\rangle_{\text{bin}}$	91	97	93
$\lvert +Z\rangle_{\text{GKP}}$	85	93	85
$\lvert +Y\rangle_{\text{GKP}}$	83	92	87
$\lvert -Z\rangle_{\text{GKP}}$	80	93	85

Table 4.1: **Measured and simulated state preparation fidelities.** $\mathcal{F}_{\text{exp}}$ is the measured fidelity found from density matrix reconstruction, $\mathcal{F}_{\text{sim}}$ is the simulated fidelity including all independently measured decoherence rates, and $\mathcal{F}_{\text{sim}}^{\kappa_\phi}$ is the simulated fidelity including additional cavity dephasing at a rate $\kappa_\phi = (150\,\text{ms})^{-1}$. Fidelity is defined as $\mathcal{F} = \langle\psi_t\rvert\,\rho_g\,\lvert\psi_t\rangle$ where ρ_g is the oscillator state after projecting the qubit in $\lvert g\rangle$ and $\lvert\psi_t\rangle$ is the oscillator target state. We estimate the quoted fidelities are accurate within 1% using bootstrapping. The average probability of measuring $\lvert g\rangle$ after the state preparation sequences are $\{0.96, 0.93, 0.96, 0.92\}$ for the Fock, squeezed, binomial, and GKP states respectively.

4.2 Experimental design

Our experiment consists of a high-quality-factor microwave cavity with weak dispersive coupling to a superconducting qubit with much lower quality. The details of modeling such a system are outlined in section 3.1.

The sample consists of two coaxial microwave cavities machined out of aluminum 6061 alloy anchored at the base stage of a dilution refrigerator operating at 20 mK. The lower-frequency cavity is used as a high-Q storage oscillator, while the other is overcoupled to a transmission line and used for readout of a fixed-frequency transmon qubit bridging the two cavities. The transmon includes a double-angle-evaporated Al/$\mathrm{AlO_x}$/Al Josephson-junction fabricated on a sapphire substrate. An FPGA system is used to control the transmon and cavity with a DAC sampling rate of 1 GS/s. The package and transmon used here is the same as was used in [26], with device parameters that have aged since that publication. We refer the reader to [26] and associated supplementary material for more details, as well as the wiring diagram, for which the only major difference here is the lowering of amplification power and addition of room-temperature microwave switches on the storage and readout line for better noise properties.

Single-shot readout is performed using a SNAIL parametric amplifier operating with 20 dB of gain in phase-preserving mode [109]. We use a square readout pulse of length 100 ns and acquire signal for 824 ns. With additional FPGA delays, the total readout time is 1.176 µs, leading to a readout fidelity greater than 98% as inferred by the measured average contrast of thresholded Rabi fringes. A measurement based feedback routine is used to prepare the transmon in $|g\rangle$ before each experimental iteration.

In equilibrium, the transmon's excited state population is $n_{\mathrm{th,q}} \sim 0.0092$, corresponding to a temperature of $\sim 68\,\mathrm{mK}$. We rely on a wait time longer than $5T_{1,c}$ between each experiment for the cavity to relax to near-equilibrium. As a conservative estimate, we assume the cavity mode is at the same temperature as the transmon when estimating error sources in section 4.6, corresponding to a cavity excited state population of $n_{\mathrm{th,c}} \sim 0.025$ before the start of each experiment.

4.2.1 System Hamiltonian and parameters

Given the range of displacements used in this work, our system is well described by the effective Hamiltonian $H_{\text{dispersive}}$ introduced in the previous chapter. To clarify our results, it is repeated here. In particular, the system dynamics are generated by the effective Hamiltonian [34, 143, 179]

$$\frac{H}{\hbar} = \tilde{\Delta} a^\dagger a - \chi a^\dagger a b^\dagger b - \chi' a^{\dagger 2} a^2 b^\dagger b - K_a a^{\dagger 2} a^2 - K_b b^{\dagger 2} b^2 + \varepsilon^*(t) a + \Omega^*(t) b + \text{h.c.} \tag{4.1}$$

where a (b) are bosonic annihilation operators for the hybridized oscillator-like (transmon-like) modes. $\Omega(t)$ and $\varepsilon(t)$ are complex-valued drives generated by IQ modulation, and we have ignored terms rotating at twice the drive frequencies. H is written in the co-rotating frame of the qubit and cavity drives, and in this work we use $\tilde{\Delta} = \chi/2$ when performing ECD gates, representing a cavity drive at frequency $(\omega_g + \omega_e)/2$, where ω_g (ω_e) is the cavity frequency with the transmon in the ground (excited) state. Under this choice, the Hamiltonian discussed in section 2.4.3 using a two-level system corresponds to projecting eq. (4.1) onto the ground and excited state transmon manifold using the mapping $\sigma_z = 1 - 2b^\dagger b$ and only keeping the dispersive interaction term. Hamiltonian parameters, as well as measured decoherence rates and mode frequencies, are given in table 4.2, and measurement techniques for these some of these values are described in the previous chapter, section 3.2.

Given these measured parameters, a two-step process is used to optimize control of the system. In the first step, outlined in section 2.6, the gate parameters $\left\{\vec{\beta}, \vec{\phi}, \vec{\theta}\right\}$ are optimized to realize a target unitary. This step is independent of the system parameters, allowing the same unitary ECD circuit to be performed on different experimental systems.

In the second optimization step, the cavity drive $\varepsilon(t)$ and qubit drive $H_q/\hbar = \Omega^*(t)\sigma^- + \Omega(t)\sigma^+$ are compiled from a set of ECD circuit parameters found in the first step. This

parameter	**value**
transmon g-e transition frequency	$\omega_{ge} = 2\pi \times 6.65\,\mathrm{GHz}$
transmon anharmonicity	$K = 2K_b = 2\pi \times 193\,\mathrm{MHz}$
transmon Ramsey coherence	$T_{2R,q} = 30\,\mu\mathrm{s}$
transmon echo coherence	$T_{2E,q} = 65\,\mu\mathrm{s}$
bare transmon relaxation	$T_{1,q} = 50\,\mu\mathrm{s}$
transmon relaxation with $\bar{n}_{\mathrm{cav}} = 900$	$\tilde{T}_{1,q} = 30\,\mu\mathrm{s}$
transmon equilibrium population	$n_{\mathrm{th}} = 0.0092$
readout frequency	$\omega_r = 2\pi \times 8.22\,\mathrm{GHz}$
readout dispersive shift	$\chi_{qr} = 2\pi \times 0.96\,\mathrm{MHz}$
readout relaxation rate	$\kappa_r = 1.7\,\mathrm{MHz}$
storage cavity frequency	$\omega_a = 2\pi \times 5.26\,\mathrm{GHz}$
storage dispersive shift	$\chi = 2\pi \times 32.8\,\mathrm{kHz}$
storage second-order dispersive shift	$\chi' = 2\pi \times 1.5\,\mathrm{Hz}$
storage cavity Kerr	$2K_a = 2\pi \times 1\,\mathrm{Hz}$
storage cavity relaxation	$T_{1,c} = 436\,\mu\mathrm{s}$
storage cavity Ramsey coherence	$T_{2R,c} < 2T_{1,c} = 872\,\mu\mathrm{s}$

Table 4.2: **Measured system parameters and loss rates**. Measurement of the dispersive shift, the second order dispersive shift, and Kerr is described in section 3.2.3. The Cavity relaxation time $T_{1,c}$ is measured by preparing a coherent state $\alpha_0 = 3.6$ and measuring $\langle \hat{a}^\dagger \hat{a} \rangle (t)$ using time-dependent transmon spectroscopy. The limit on the cavity Ramsey coherence time $T_{2,c}$ is inferred from the cavity relaxation time.

optimization is done with realistic constraints to realize the ECD sequence in the shortest time given bandwidth and amplitude limits.

A full ECD sequence specified by the parameters $\left\{\vec{\beta}, \vec{\phi}, \vec{\theta}\right\}$ is compiled into drives $\varepsilon(t)$ and $\Omega(t)$ by first optimizing the drives for each ECD gate given a target α_0. These are interleaved with qubit rotations, which are performed by modifying the phase and amplitude of fixed-length Gaussian pulses with $\sigma = 6\,\mathrm{ns}$ and total length $4\sigma = 24\,\mathrm{ns}$ independently calibrated in experiment. We note that pulse shaping techniques such as derivative reduction by adiabatic gate (DRAG) could also be incorporated to realize shorter transmon pulses [180,181]. Finally, the phase of each qubit pulse is updated to account for the additional phases associated with each ECD gate (θ') calculated by eq. (3.41). This correction is done by keeping track of the qubit frame given all preceding ECD gates and updating the phase φ of each qubit rotation gate accordingly. As an example, in fig. 4.8 we show the compiled ECD pulse sequence used to prepare $|+Z\rangle_{\mathrm{GKP}}$ in the cavity. Here, we use $\alpha_0 = 30$, however some ECD gates are performed at a smaller $\alpha_0' < \alpha_0$ resulting from the finite displacement pulse duration and the ECD optimization procedure described above.

4.2.2 Optimization of GRAPE and SNAP pulses

In this section, we outline numerical methods used to generate the GRAPE and SNAP pulses for comparison against the ECD pulses. For these examples, we optimize the fidelity of the quantum control problem $|0\rangle|g\rangle \to |n\rangle|g\rangle$ for the Fock states $n = 1$ through $n = 5$.

Optimization of GRAPE

We use the methods described in [101] to optimize GRAPE pulses for the cavity and qubit using our measured χ. The driven dispersive Hamiltonian is used with piecewise-constant pulses sampled every 33 ns and an oscillator Hilbert space truncation of $N = 50$. To find the numerical quantum speed limit (QSL) associated with each Fock state preparation, we sweep the length of the pulse and pick the shortest pulse with an optimized Fidelity $\mathcal{F} > 0.99$. We also employ typical bandwidth and amplitude constraints when optimizing these pulses. We note that the cavity drive amplitudes used in our ECD gates are over an order-of-magnitude larger than typical cavity drive amplitudes used in optimized GRAPE pulses [101]. Our results confirm that GRAPE pulses optimized in the usual way take a time greater than $2\pi/\chi$ as also observed in many state-of-the art bosonic control experiments [28,29,58,101,182–186].

Optimization of SNAP

The SNAP-displacement control sequence is parameterized as $D^\dagger(\alpha)\mathrm{SNAP}(\varphi)D(\alpha)$ as in [128]. For each target Fock state $|n\rangle$ with $n = 1...5$ and circuit depth $T = 1...5$, we optimize the parameters of this control sequence with reinforcement learning [99]. For each configuration (n, T), we repeat the training 10 times with different random initial seeds. The results show that to achieve fidelity $> 99\%$, the circuit depth has to be $T \geq 2$ for Fock states $n = 1, 2, 3$, and $T \geq 3$ for $n = 4, 5$. The best performing protocols are compared

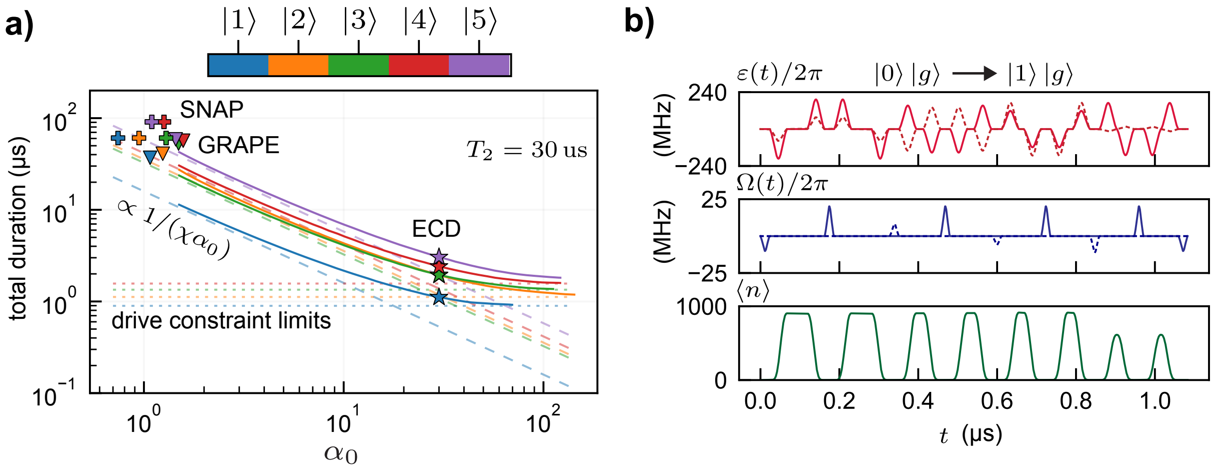

Figure 4.1: **Fock state preparation pulse duration comparison and optimized drives. a)** Total pulse sequence duration using the protocols from section 2.7.1 with minimum circuit depth such that $\mathcal{F} \geq 0.99$ (solid lines). Colored long-dashed lines are the instantaneous displacement scaling $T_{\text{total}} = (\chi\alpha_0)^{-1}\sum_{i=1}^{N}|\beta_i|$. Colored dotted lines are the drive constraint limits $T_{\text{total}} = 2Nt_q + 4Nt_D$. We use $\alpha_0 = 30$ in our experiment as indicated by the stars. Also included are durations for independently optimized GRAPE (triangles) and SNAP (crosses) protocols using our system parameters where the x-coordinate indicates the simulated largest displacement used ($\max|\langle a\rangle(t)|$). **b)** Cavity drive $\varepsilon(t)$ (upper panel) and transmon drive $\Omega(t)$ (middle panel) for preparation of Fock state $|1\rangle$ (real and imaginary parts shown in solid and dotted lines) and simulated average photon number during the sequence (lower panel).

against ECD control in fig. 4.1. For SNAP, we assume a gate time of $2\pi/\chi$, however SNAP is typically implemented with longer gate times [115].

4.3 Fock state preparation

Previously in section 2.7.1, I outlined the procedure for optimizing circuits using the phase-space ISA. Additionally, in section 3.3.2, I discussed how ECD gates can be optimized in an experiment. By combining these, we can compare the resulting pulse durations assuming our dispersive shift of $\chi/2\pi = 33\,\text{kHz}$ with pulses optimized using the Fock-space ISA (the SNAP and displacement gate) along with optimal control pulses.

The resulting sequence duration for preparation of Fock states $|1\rangle$ through $|5\rangle$ as a function of the displacement used during the ECD gates α_0 is shown in fig. 4.1a. For this plot, we use the circuits with the shortest depth such that the optimized fidelity from fig. 2.6a is greater than 99%. This choice represents an optimum fidelity in the presence of decoherence as verified by master equation simulations.

As shown in the figure, at intermediate values of α_0, the sequence duration follows the instantaneous-displacement limit $T_{\text{total}} \propto (\chi\alpha_0)^{-1}$. As α_0 increases, the amplitude and bandwidth constraints result in sequences limited by the total duration of the constituent pulses, $T_{\text{total}} = 2Nt_q + 4Nt_D$, where the duration of qubit rotation pulse and oscillator displacement pulses used in our experiment are $t_q = 24\,\text{ns}$ and $t_D = 44\,\text{ns}$. In our experimental demonstrations, we use $\alpha_0 = 30$ (as shown by the stars in fig. 4.1a) and operate close to the predicted maximum conditional displacement rate $g_{\text{eff}}^{\text{max}}/2\pi \approx 1\,\text{MHz}$. The shortest lifetime in our experiment is the transmon Ramsey coherence time $T_2 \approx 30\,\mu\text{s}$ realizing $\chi/2\pi \lesssim \Gamma_2 \ll g_{\text{eff}}/2\pi$ and allowing high-fidelity control in a regime where the bare nonlinearity is comparable to the fastest decoherence rate.

In fig. 4.1a, the duration of ECD pulse sequences are also compared to independently optimized GRAPE and SNAP sequences for Fock state preparation with our system parameters. Here, ECD sequences have over an order-of-magnitude enhancement in gate speed. Note that the GRAPE pulses used implement a typical Fock-space cutoff. The displaced-frame GRAPE method introduced in section 2.5.1 could instead be used to find fast protocols that make use of large displacements.

As an example of a full compiled pulse sequence, single-photon state preparation using $\alpha_0 = 30$ is shown in fig. 4.1b. This gate is realized about 30 times faster than $2\pi/\chi$, with compiled drives and simulated intracavity average photon number shown in fig. 4.1b, demonstrating the ability to utilize the oscillator's vast Hilbert space to enhance gate speed with a displaced-field of $\max|\alpha|^2 = 900$ photons during the gates.

We can also simulate the sensitivity of the compiled pulses for Fock prep to various coherent error channels, including a transmon detuning, oscillator detuning, drive amplitude miscalibration, and a miscalibration of the dispersive shift χ. The simulated sensitivities to

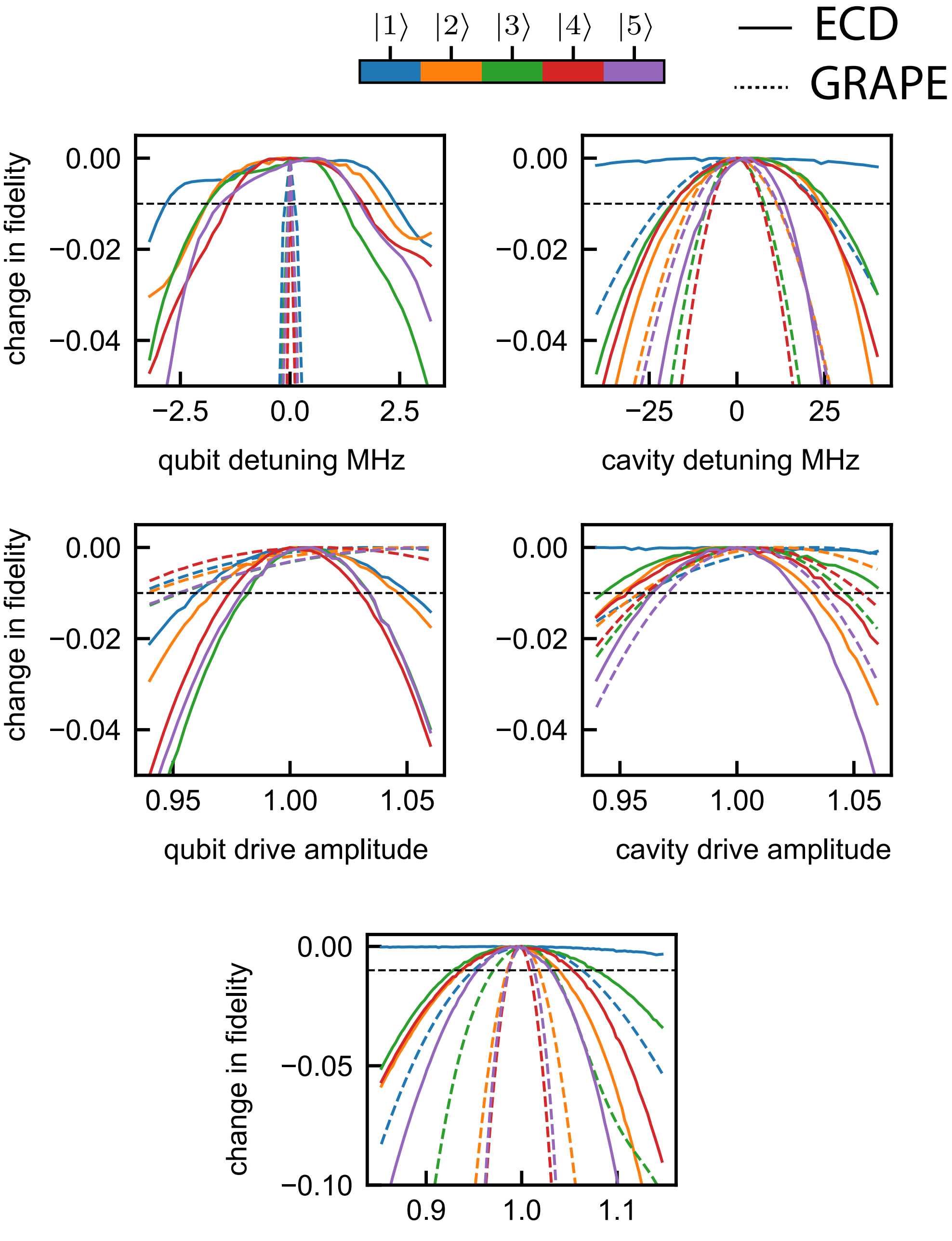

Figure 4.2: **Fock state preparation sensitivity to coherent errors**. Simulated drop in fidelity of Fock preparation sequences under different coherent error channels of qubit/oscillator detuning, drive amplitude miscalibration, and dispersive shift χ miscalibration. Dashed line indicates a drop of 1%. ECD control and GRAPE control are similar in their sensitivities, except for qubit detuning, where the dynamical decoupling built into ECD sequences decreases the sensitivity for ECD pulses.

these error channels are shown in fig. 4.2. In particular, the pulses are designed to be robust to low-frequency noise coupled to $b^\dagger b \propto \sigma_z$. As shown, simulation results for ECD Fock state preparation pulse sequences with an additional qubit detuning $H/\hbar = \delta\sigma_z/2$ show resilience at the level of $1 - \mathcal{F} \sim 0.01$ to static detuning on the order of $\delta/\hbar \sim 1\,\mathrm{MHz}$, indicating they are much more insensitive than the optimized GRAPE pulses.

In the experiment we measure the complex-valued characteristic function $\mathcal{C}(\beta) = \mathrm{Tr}\left(D(\beta)\rho\right)$ by using an ECD gate to perform phase estimation of the displacement operator $D(\beta)$ conditioned on a disentangling transmon measurement [26, 66, 175]. This method is outlined in section 3.4. Importantly, this tomography can be performed in a time much faster than $2\pi/\chi$ using large displacements (we note that direct Wigner tomography using typical circuit-QED parity measurements would be impractical, taking a time $\pi/\chi \approx 15\,\mu\mathrm{s}$.) The real parts of the measured characteristic functions for Fock states $|1\rangle$ through $|5\rangle$ are shown in fig. 4.3. From the real and imaginary parts (not shown) of the characteristic functions we reconstruct the density matrices using maximum likelihood estimation leading to the results summarized in table 4.1 and reaching a best fidelity of $\mathcal{F}_{\mathrm{exp}} = 0.98 \pm 0.01$ for Fock state $|1\rangle$.

The experimental fidelities in table 4.1 are compared to master equation simulations $\mathcal{F}_{\mathrm{sim}}$ including all independently measured decoherence mechanisms. Out of the measured decoherence sources, qubit relaxation during the ECD gates is the largest error contribution. The simulated fidelities are higher than the measured fidelity for most demonstrations, and a likely cause is additional coherent error sources arising from unknown microwave transfer functions, calibration drifts, and other forms of model bias. Closed-loop optimization strategies such as reinforcement learning could be used to mitigate these effects [99, 187], but in this work we did not perform such an optimization. An additional possible decoherence mechanism is pure oscillator dephasing that could arise from coupling to other uncontrolled modes such as two-level-systems [162]. Although we do not have an exact measurement of the pure oscillator dephasing rate in this experiment, we have simulated the influence of relatively slow pure oscillator dephasing at a rate $\kappa_\phi = (150\,\mathrm{ms})^{-1}$, resulting in sequences with

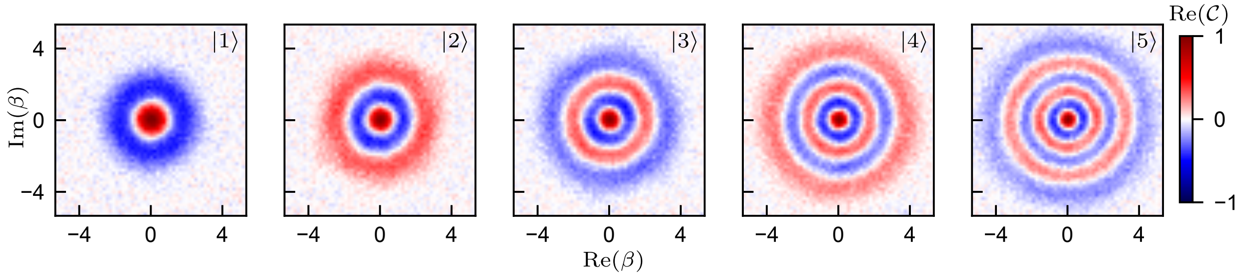

Figure 4.3: **Tomography of Fock states prepared with the phase-space ISA**. Measured real part of the characteristic functions for the first five excited Fock states in the cavity. The imaginary part is also measured (not shown) and used to reconstruct the density matrix (section 4.5.3). The resulting state fidelities are given in table 4.1, with a best fidelity of $\mathcal{F} = 98 \pm 1\%$ for Fock $|1\rangle$ preparation.

fidelities given by $\mathcal{F}^{\kappa_\phi}_{\text{sim}}$ in table 4.1. These results reveal that even a small pure dephasing rate of the oscillator can significantly lower the fidelity when using large displacements.

4.4 Squeezed state preparation

As a second demonstration, we prepare squeezed vacuum states $|\zeta\rangle = \exp\left(\frac{1}{2}(\zeta^* a^2 - \zeta a^{\dagger 2})\right)|0\rangle$ with a squeezing level in dB defined as $20\log_{10}\left(e^{|\zeta|}\right)$. Highly squeezed states of an oscillator can allow sensing beyond the standard quantum limit, as was recently used to enhance the search for dark matter axions [30]. However, the presence of a large oscillator self-Kerr degrades the quality by distorting the squeezed state and increasing the variance of the squeezed quadrature [188]. In our experiment, the small inherited oscillator self-Kerr of $\approx 1\,\text{Hz}$, over three orders of magnitude smaller than is typically used [101], minimizes the state distortion during preparation and idling periods.

In fig. 4.4a we show ECD optimization results for squeezed state preparation starting from vacuum. Plotted is the minimum circuit depth needed to reach a fidelity $\mathcal{F} \geq 99\%$. A related method for squeezed state creation was introduced in [189], and the protocols here have fewer conditional displacements, demonstrating the ability of our optimization method to find novel control circuits.

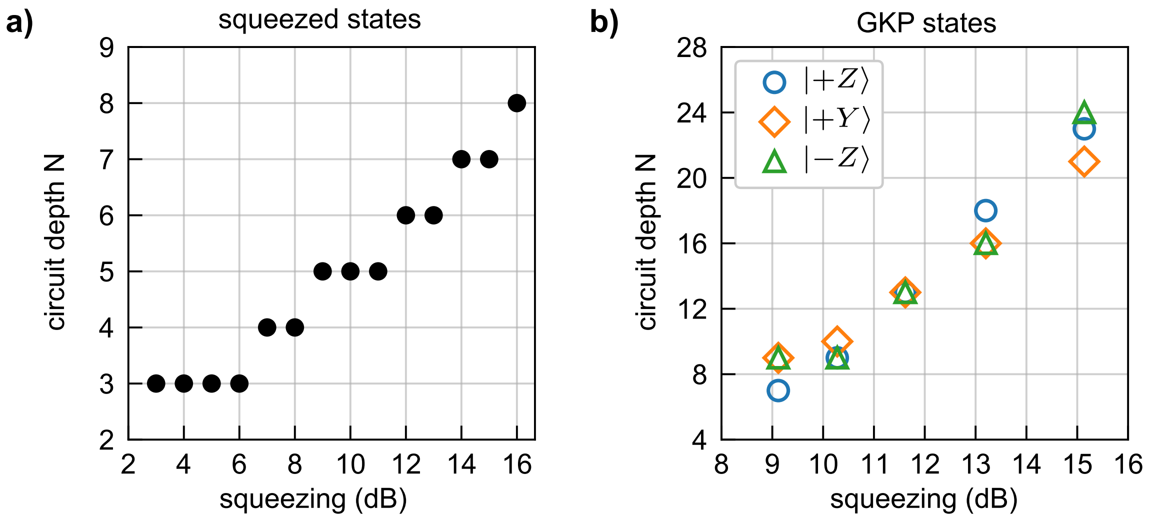

Figure 4.4: **Squeezed state and GKP state preparation optimization results.** Numerically optimized minimum circuit depth to reach state transfer fidelity $\mathcal{F} \geq 0.99$ for preparation of squeezed states (part **a**) and $\mathcal{F} \geq 0.98$ for preparation of logical GKP states (part **b**)

In our experiment, we apply the optimized squeezed state preparation ECD sequences for target squeezing levels of $\{6, 8, 10, 12, 14\}$ dB using a large displacement magnitude of $\alpha_0 = 30$. The measured characteristic functions are shown in fig. 4.5a, with achieved squeezing levels of $\{4.8, 6.7, 8.2, 9.8, 11.1\}$ dB calculated from a fit to the reconstructed probability distribution along the squeezed quadrature, shown in fig. 4.5b.

The reconstructed states show some non-Gaussian features as decoherence during the pulse causes distortion, similar to the Fock preparation case, leading to a lower effective squeezing. To the best of our knowledge, the measured squeezing of 11.1 dB demonstrated here is larger than any intraresonator squeezing demonstration in the microwave regime to date, with other demonstrations achieving steady-state intracavity squeezing at the level of 8.2 dB [188] and a post-selected state-preparation method demonstrating 5.7 dB [190]. The echoed conditional displacements realized here could also be used to sense small displacements of a squeezed state using phase estimation [191].

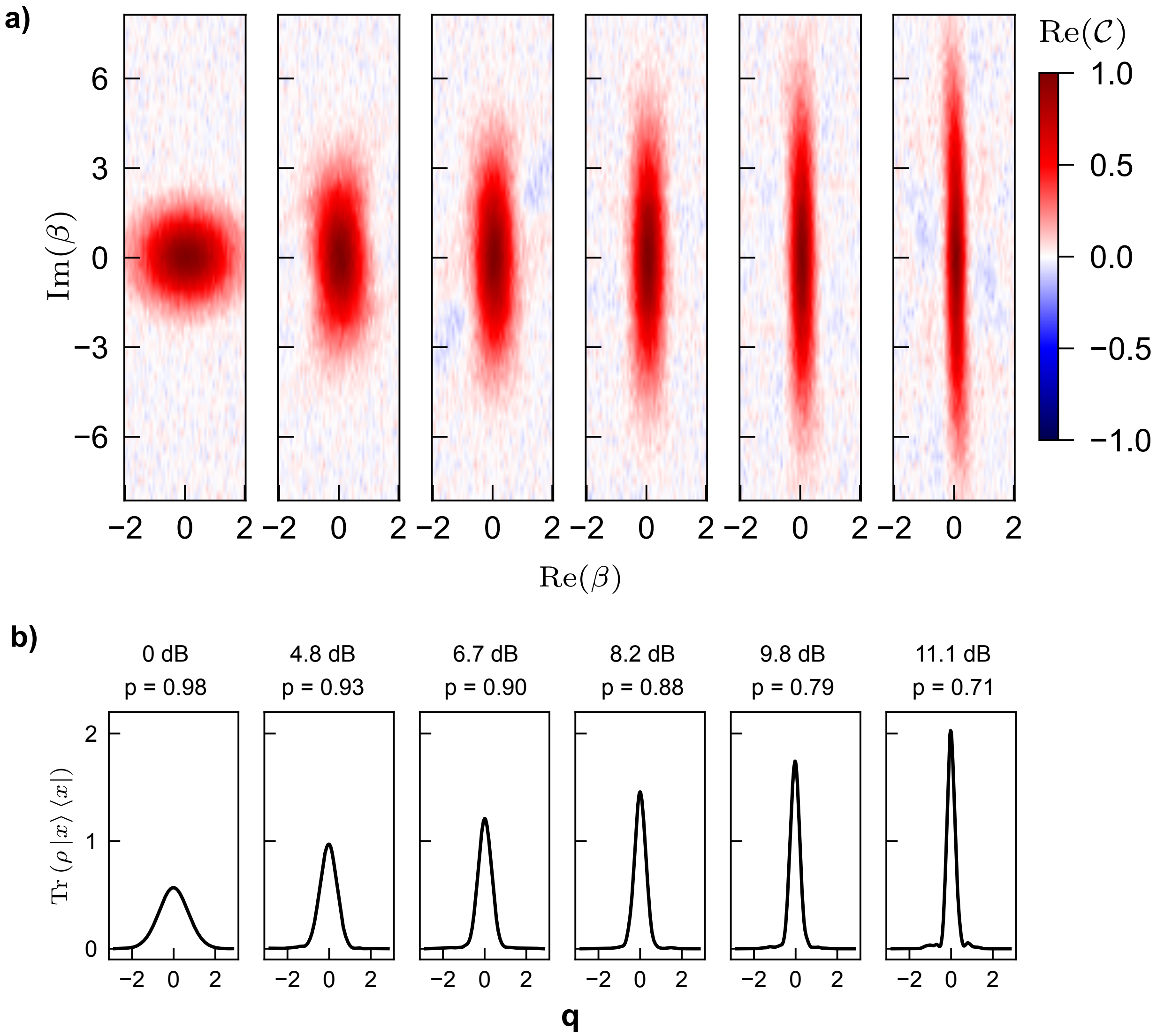

Figure 4.5: **Squeezed state tomography and reconstructed quadrature probability distributions. a)** Real part of measured characteristic functions for vacuum and squeezed states. Note that for characteristic functions, the squeezing corresponds to the elongation, not the width of the waist. **b)** Reconstructed position quadrature probability distributions and squeezing values found by a fit to Gaussian functions. Also shown are purities calculated as $p = \mathrm{Tr}(\rho^2)$.

4.4.1 Effective squeezing measurement

To find the effective squeezing of prepared states, the reconstructed density matrices are used to calculate the position quadrature probability distributions, $P(x) = \mathrm{Tr}\left(\rho \left|x\right\rangle \left\langle x\right|\right)$, with results shown in fig. 4.5b, including the measured cavity equilibrium thermal state for comparison. Here, a small rotation is applied to the reconstructed density matrices before calculating the probability distributions to align the squeezed quadrature. Also shown is the purity ($p = \mathrm{Tr}\left(\rho^2\right)$) of each reconstructed density matrix. These distributions are fit to Gaussian functions to extract the squeezing in each state. We compare these results to a calculation of the Fisher information using the full reconstructed probability distributions,

$$I_c = 2 \int dx \, \left(\partial_x \log P(x)\right)^2 P(x). \tag{4.2}$$

The Fisher information is a measure of the ability to sense small displacements along the position quadrature using the state with respect to homodyne detection [189,192]. For ideal squeezed states, $I_c = 2/\left\langle \Delta x^2 \right\rangle$. Although the calculated purity of the squeezed states decreases with larger target squeezing, the states can still be used to sense small displacements, since only the probability distribution $P(x) = \mathrm{Tr}\left(\rho \left|x\right\rangle \left\langle x\right|\right)$ enters into the Fisher information. In fig. 4.6, we compare the calculated I_C for each state to the target value. Finally, we also compare to $I_c = 2/\sigma_x^2$, where σ_x^2 is the variance of the Gaussian fit, indicating that the squeezed quadrature distributions are well approximated by a Gaussian, even though the full topographies show some non-Gaussian features.

4.5 Binomial and GKP code word preparation

To further characterize the method, we implement logical state preparation for two different quantum error correcting bosonic codes, the binomial code [193] and the square GKP code [1]. For the binomial code, we focus on the smallest code for which the loss of a single photon is

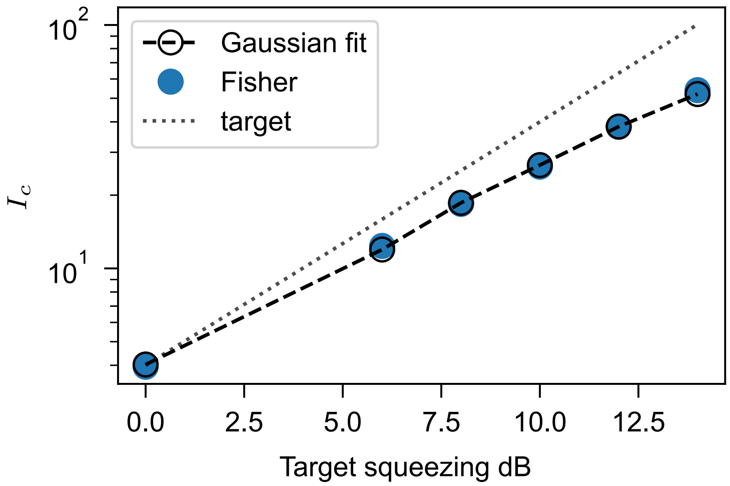

Figure 4.6: **Fisher information of measured squeezed states.** Calculated Fisher information from the probability distributions (orange), compared to that expected from a Gaussian fit (blue).

correctable, with code words $|+Z\rangle_{\text{bin}} = (|0\rangle + |4\rangle)/\sqrt{2}$ and $|-Z\rangle_{\text{bin}} = |2\rangle$. The GKP code, on the other hand, is defined as the mutual +1 eigenspace of the displacement stabilizers $S_p = D(\sqrt{2\pi})$ and $S_q = D(i\sqrt{2\pi})$ with logical operators given by $X = D(\sqrt{\pi/2})$ and $Z = D(i\sqrt{\pi/2})$. The ideal GKP code has infinite energy, and a finite energy code can be defined by modifying the stabilizers and logical operators using the envelope operator $E_\Delta = \exp\left\{-\Delta^2 a^\dagger a\right\}$ under the transformation $O_\Delta = E_\Delta O E_\Delta^{-1}$, leading to code states that are superpositions of squeezed states with squeezing parameter $\zeta = \ln \Delta$ [20, 64].

For the binomial code, previous experiments have demonstrated logical state preparation using GRAPE, relying on a large bare nonlinearity $\chi/2\pi$ compared to decoherence rates [29, 101, 182, 183, 185]. With ECD control, optimization results in protocols that prepare all cardinal points of the Bloch sphere to a fidelity $\mathcal{F} = 99\%$ with a circuit depth at most $N = 5$. Applying these circuits in experiment using $\alpha_0 = 30$ results in the measured characteristic functions shown in fig. 4.7 with fidelity given in table 4.1. The average pulse time for binomial state preparation is 3.27 µs - about 9 times faster than $2\pi/\chi$. In principle, fast logical operations, measurement, and stabilization of the binomial code could also be achieved using ECD control.

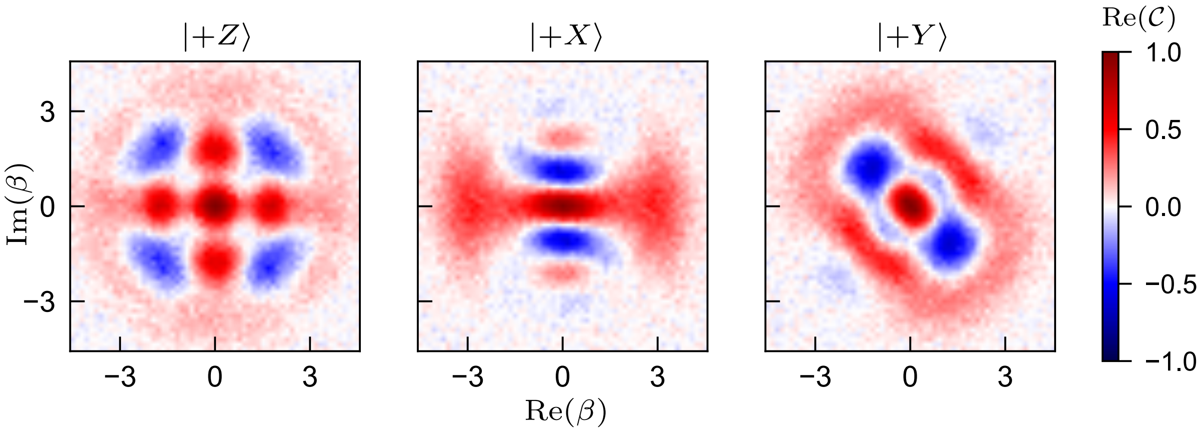

Figure 4.7: **Tomography of binomial code logical states.** Measured characteristic functions for logical state preparation of binomial code words, where the logical state $|-Z_L\rangle = |2\rangle$ is included in fig. 4.3. All other cardinal points on the Bloch sphere can be obtained by phase space rotations. Fidelities are given in table 4.1.

For GKP states, fig. 4.4b shows the circuit depth required for ECD protocols to prepare $|+Z\rangle_{\mathrm{GKP}}$, $|+Y\rangle_{\mathrm{GKP}}$, and $|-Z\rangle_{\mathrm{GKP}}$ optimized to a state transfer fidelity of $\mathcal{F} = 98\%$ at different squeezing levels. For a target squeezing of $\Delta_{\mathrm{target}} = 0.306$, the optimized phase-space ISA pulse for GKP $|+Z\rangle$ state preparation from vacuum is shown in fig. 4.8.

The protocols found here represent a unitary protocol for GKP state creation, as opposed to the non-unitary protocols recently demonstrated in both trapped ions [66] and superconducting circuits [26] that require multiple measurements with feedback or many rounds of dissipative pumping. A related measurement-free GKP state preparation protocol has been proposed [194] and implemented in trapped-ions [65], however it requires an initial squeezed state.

In fig. 4.9, we plot the measured characteristic functions found using these circuits with $\alpha_0 = 30$ achieving fidelities given in table 4.1. For the GKP states, we use a target squeezing level of 10.3 dB and experimentally achieve a squeezing level of 9.1 dB. Our pulse sequences are about 15 times faster than the state preparation method using measurements and feedback demonstrated in [26] with similar experimental parameters. This order-of-magnitude reduction in initialization time can reduce the hardware overhead of error correction pro-

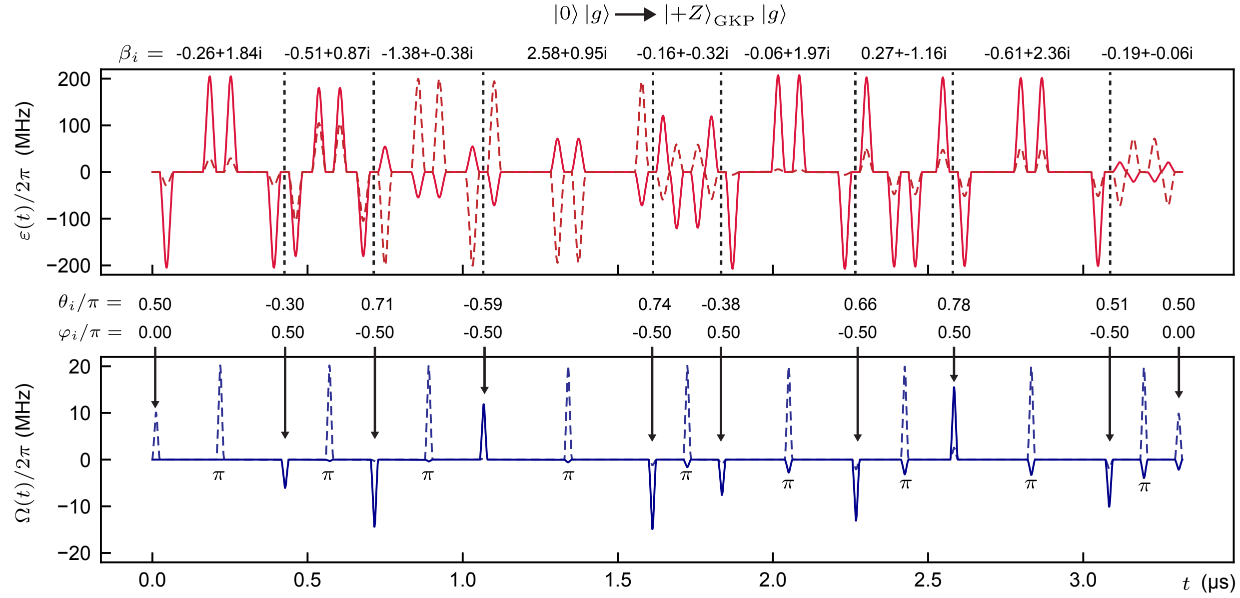

Figure 4.8: **GKP state preparation ECD pulse sequence** used to prepare $|{+Z}\rangle_{\mathrm{GKP}}$ in the cavity starting from vacuum using a circuit depth $N = 9$. Here, $\Delta_{\mathrm{target}} = 0.306$ as described in section 4.5.2 and the ECD control parameters $\left\{\vec{\beta}, \vec{\phi}, \vec{\theta}\right\}$ are found using the procedure described in section 3.3.2. $\varepsilon(t)$ is the cavity drive and $\Omega(t)$ is the transmon drive. Solid and dotted lines denote the real and imaginary parts of these drives, respectively.

tocols requiring GKP resource states, such as teleported error correction [23] or the GKP surface code [195, 196].

4.5.1 Binomial code analysis

The binomial *kitten code* is the smallest binomial code for which the loss of a single photon is correctable [23, 29, 183, 185, 193], with logical states given by $|{+Z}\rangle = (|0\rangle + |4\rangle)/\sqrt{2}$ and $|{-Z}\rangle = |2\rangle$. In table 4.3 we give the estimated expectation values of the logical Pauli operators of the prepared states found numerically using the reconstructed density matrices. We also quantify how errors in the prepared states could be corrected by ideal error correction, as some errors during the state preparation are in principle correctable. In particular, the correctable code space includes the normalized error states $|{+Z}\rangle_{\mathrm{e}} =$

$a\left|+Z\right\rangle/|\left\langle +Z|a^\dagger a|+Z\right\rangle|^2 = \left|3\right\rangle$ and $\left|-Z\right\rangle_{\mathrm{e}} = a\left|-Z\right\rangle/|\left\langle -Z|a^\dagger a|-Z\right\rangle|^2 = \left|1\right\rangle$. From these, we can define the logical operators corresponding to applying ideal error correction then performing a logical measurement, given by

$$\begin{aligned}
X_c &= \left|+Z\right\rangle\left\langle -Z\right| + \left|+Z\right\rangle_{\mathrm{e}}\left\langle -Z\right|_{\mathrm{e}} + \left|-Z\right\rangle\left\langle +Z\right| + \left|-Z\right\rangle_{e}\left\langle +Z\right|_{e} \\
Y_c &= i\left|-Z\right\rangle\left\langle +Z\right| + i\left|-Z\right\rangle_{e}\left\langle +Z\right|_{e} - i\left|+Z\right\rangle\left\langle -Z\right| - i\left|+Z\right\rangle_{e}\left\langle -Z\right|_{e} \\
Z_c &= \left|+Z\right\rangle\left\langle +Z\right| + \left|+Z\right\rangle_{\mathrm{e}}\left\langle +Z\right|_{\mathrm{e}} - \left|-Z\right\rangle\left\langle -Z\right| - \left|-Z\right\rangle_{e}\left\langle -Z\right|_{e} \\
I_c &= \left|+Z\right\rangle\left\langle +Z\right| + \left|+Z\right\rangle_{\mathrm{e}}\left\langle +Z\right|_{\mathrm{e}} + \left|-Z\right\rangle\left\langle -Z\right| + \left|-Z\right\rangle_{e}\left\langle -Z\right|_{e}.
\end{aligned} \tag{4.3}$$

The expectation values of these operators quantify the logical information encoded in the prepared states after ideal error correction assuming a photon loss error channel. We calculate these expectation values using the reconstructed density matrices with results shown in table 4.3. If these prepared states were to be used in an error correction setting, the error decoding model should instead be adapted to fit the actual errors encountered during state preparation.

State	$\langle I\rangle$	$\langle X\rangle$	$\langle Y\rangle$	$\langle Z\rangle$	$\langle I_c\rangle$	$\langle X_c\rangle$	$\langle Y_c\rangle$	$\langle Z_c\rangle$
$\left\|+X\right\rangle_{\mathrm{bin}}$	0.90	0.98	0.08	-0.05	0.95	0.92	0.09	-0.08
$\left\|+Y\right\rangle_{\mathrm{bin}}$	0.92	-0.06	0.90	-0.10	0.98	-0.06	0.96	-0.13
$\left\|+Z\right\rangle_{\mathrm{bin}}$	0.92	0.03	-0.05	0.92	0.97	0.04	-0.04	0.96
$\left\|-Z\right\rangle_{\mathrm{bin}}$	0.93	-0.01	-0.10	-0.93	0.99	-0.02	-0.10	-0.98

Table 4.3: **Binomial code Pauli expectation values** found numerically using the reconstructed density matrices.

4.5.2 GKP code analysis

The finite energy square GKP code stabilizers and logical Pauli operators are defined as [1,15,20,23,64,197]

$$S_{q,\Delta} = e^{-\Delta^2 a^\dagger a} D\left(i\sqrt{2\pi}\right) e^{\Delta^2 a^\dagger a} \qquad S_{p,\Delta} = e^{-\Delta^2 a^\dagger a} D\left(\sqrt{2\pi}\right) e^{\Delta^2 a^\dagger a} \tag{4.4}$$

$$X_\Delta = e^{-\Delta^2 a^\dagger a} D\left(\sqrt{\pi/2}\right) e^{\Delta^2 a^\dagger a} \qquad Z_\Delta = e^{-\Delta^2 a^\dagger a} D\left(i\sqrt{\pi/2}\right) e^{\Delta^2 a^\dagger a} \tag{4.5}$$

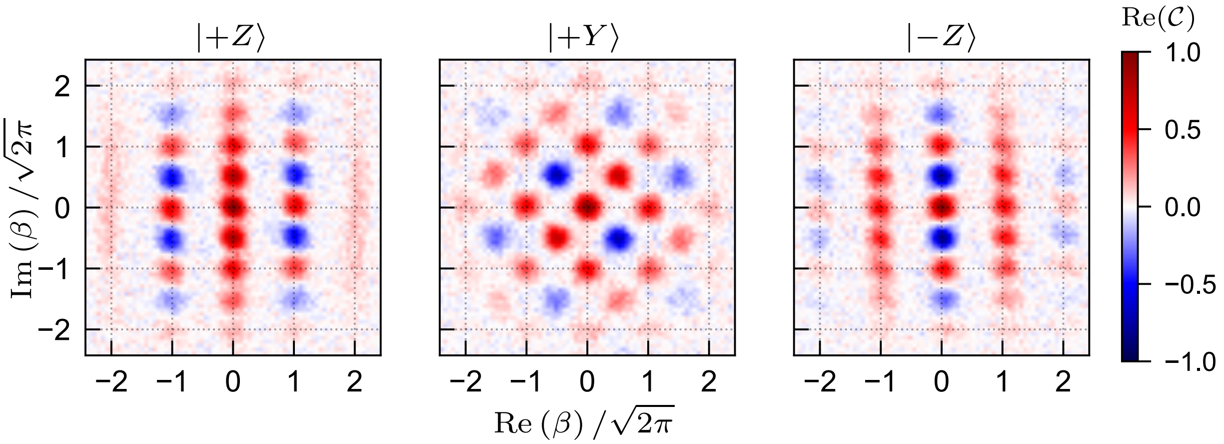

Figure 4.9: **Tomography of GKP code words using measurement-free preparation.** Measured characteristic functions for logical state preparation of the GKP code. All other cardinal points on the Bloch sphere can be obtained by phase space rotations. Fidelities are given in table 4.1.

with $Y_\Delta = iX_\Delta Z_\Delta$. The target GKP states are found numerically by letting $|+Z_\Delta\rangle$ be the ground state of a fictitious Hamiltonian $H = -S_{q,\Delta} - S_{p,\Delta} - Z_\Delta$, then by applying the appropriate finite energy logical operators and normalizing. The GKP Hamiltonian method described in appendix G can also be used to define these states.

Here, we use a target state squeezing of $\Delta_{\text{target}} = 0.306$ (10.3 dB). To estimate the effective squeezing of the prepared GKP states in experiment, we find the value of Δ that maximizes the expectation value of the projector onto the finite-energy code space $P_\Delta = |+Z_\Delta\rangle\langle +Z_\Delta| + |-Z_\Delta\rangle\langle -Z_\Delta|$ using the reconstructed density matrices. We find a squeezing of $\Delta_{\text{exp}} = 0.35$ (9.1 dB) for all prepared states within the precision of the reconstruction. In addition to the fidelities given in table 4.1, we quantify the quality of the prepared states here by numerically estimating the expectation values of the finite-energy Pauli operators and stabilizers with results given in table 4.4.

In addition, we quantify the prepared GKP states by the logical expectation values that would result from an ideal homodyne detection. In fig. 4.10, we plot the reconstructed marginal probability distributions for the prepared GKP states along the generalized quadrature coordinate $x_\theta = \left(e^{i\theta}a^\dagger + e^{-i\theta}a\right)/\sqrt{2}$ with $\theta = \{0, \pi/2, \pi/4\}$ ($x_0 = x$ and $x_{\frac{\pi}{2}} = p$). From

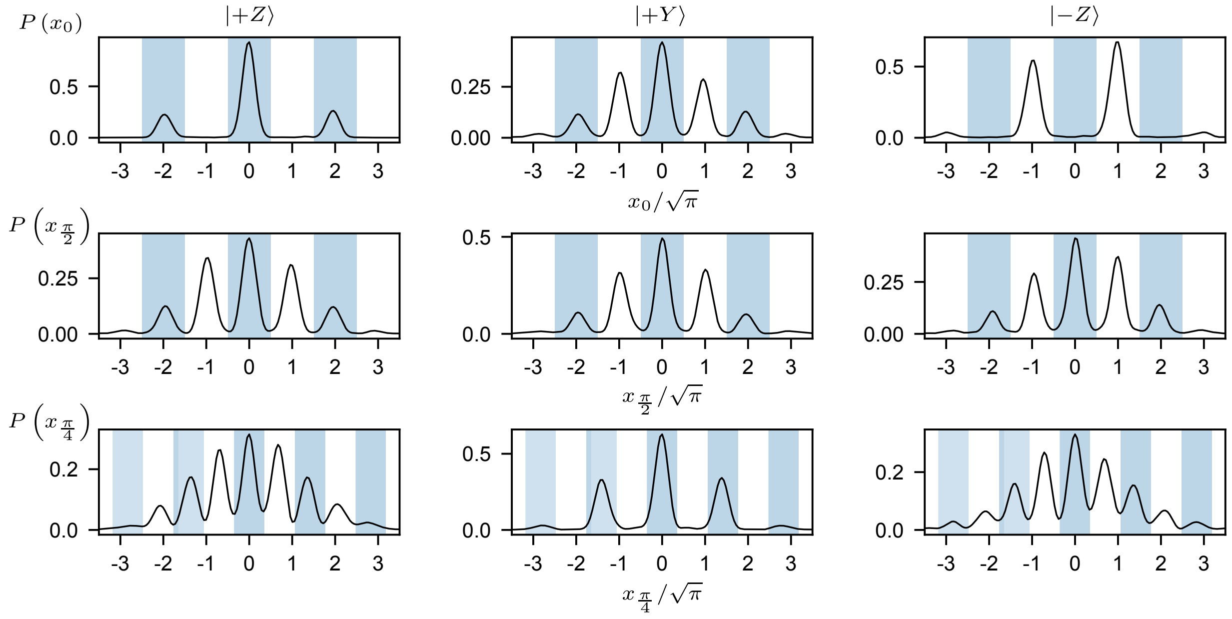

Figure 4.10: **Reconstructed GKP state marginal probability distributions.** Blue and white bins represent the integration zones corresponding to assigning the associated logical Pauli operator ±1 respectively.

these, we can define the corresponding homodyne expectation values (X_H, Y_H, and Z_H) resulting from integrating the probability distributions and assigning a logical value. These are given by the total probability of finding a homodyne measurement result in sectors closest to $x_0 \mod 2\sqrt{\pi} = 0$ or $x_0 \mod 2\sqrt{\pi} = \sqrt{\pi}$ for $Z_H = \pm 1$, with analogous definitions for X_H and Y_H [1]. The results are given in table 4.4.

State	$\mathrm{Re}\left(\langle S_{q,\Delta}\rangle\right)$	$\mathrm{Re}\left(\langle S_{p,\Delta}\rangle\right)$	$\mathrm{Re}\left(\langle X_{\Delta}\rangle\right)$	$\mathrm{Re}\left(\langle Y_{\Delta}\rangle\right)$	$\mathrm{Re}\left(\langle Z_{\Delta}\rangle\right)$	$\langle X_{\mathrm{H}}\rangle$	$\langle Y_{\mathrm{H}}\rangle$	$\langle Z_{\mathrm{H}}\rangle$
$\lvert +Z\rangle_{\mathrm{GKP}}$	0.75	0.88	0.01	-0.02	0.94	0.00	-0.01	0.94
$\lvert +Y\rangle_{\mathrm{GKP}}$	0.78	0.78	0.02	0.87	0.05	0.01	0.87	0.06
$\lvert -Z\rangle_{\mathrm{GKP}}$	0.81	0.71	0.02	0.03	-0.85	0.02	0.02	-0.91

Table 4.4: **GKP code stabilizer and Pauli expectation values**. For the finite energy stabilizers and Pauli operators, we use $\Delta = \Delta_{\mathrm{exp}} = 0.35$.

Finally, we note that the ECD gate set is designed to be well suited in the weak-χ regime since it requires fast unselective qubit rotations, an important operation that can become challenging at large dispersive shifts. With independent experiments on a different sample not presented in this work, we have confirmed the validity of the ECD approach for $\chi/2\pi \sim 200\,\mathrm{kHz}$. To realize faster gates using a larger dispersive shift on the order of $\chi/2\pi \gtrsim 1\,\mathrm{MHz}$, the gate set could be modified to take the partially selective nature of the finite-bandwidth qubit rotations into account, or GRAPE based techniques could be incorporated.

4.5.3 Density matrix reconstruction

To estimate the fidelity and purity of the oscillator state in experiment, we employ density matrix reconstruction using maximum likelihood estimation. For this, we use the measured real and imaginary parts of the characteristic functions, taken with 1,280 averages per point and use a numerical, iterative, convex optimization algorithm. For all demonstrations, the measured imaginary parts are close to zero, as is expected for states with symmetric Wigner functions. Any small deviations away from zero in the imaginary part are captured by the reconstruction.

For the Fock states, binomial states, and GKP states, the reconstruction is done in the Fock basis. For the squeezed states, reconstruction is performed in the squeezed-Fock basis $|n\rangle_\zeta = S(\zeta)\,|n\rangle$ with a basis squeezing ζ equal to the target squeezing to reduce the computer memory needed. The reconstruction Hilbert space size is swept, and a Hilbert space truncation is chosen such that increasing or decreasing the truncation does not change the fidelity or purity within the quoted error bars. For the binomial,GKP, and squeezed states, some states display a small phase-space rotation in the tomography. For these, a small inverse rotation is applied to the reconstructed density matrix. The maximum change in fidelity from this rotation is 1(%) for the $|-Z\rangle_{\mathrm{GKP}}$ state.

4.6 Sources of infidelity

In this section, we use simulations to estimate the sources of infidelity for the Fock state, binomial state, and GKP state preparation.

4.6.1 Decoherence-free error budget

First, we estimate how accurately our pulse compilation procedure, described in section 3.3.2, can realize ideal ECD control unitaries, U_{ECD} in eq. (2.52), especially in the presence of Kerr and the second-order dispersive shift. In the open red circles of fig. 4.11, we show simulated oscillator state preparation fidelities of the ideal ECD unitaries, defined as $\mathcal{F}_g = |\langle\psi_{\text{target}}|\psi_g\rangle|^2$ where $|\psi_g\rangle$ is the oscillator's state after post-selecting the qubit in $|g\rangle$.

Next, we use the pulse compilation procedure described in section 3.3.2 with our system parameters, except we set $K_s = 0$ and $\chi' = 0$ to construct oscillator and qubit pulses which realize the ECD sequences without these higher order nonlinearities. These pulses are simulated with $K_s = 0$ and $\chi' = 0$, and the resulting fidelities are shown by the blue triangles in fig. 4.11. These fidelities are close to the ideal unitary fidelities, demonstrating our ability to realize ECD sequences with the ideal dispersive Hamiltonian. These pulses are then simulated using eq. (3.22) with all nonlinear terms included using the measured system parameters, and the results are shown by the green crosses in fig. 4.11. These infidelities are significantly higher, demonstrating the need to account for higher order nonlinearities in the pulse construction.

In addition, we include the measured values of K_c and χ' in the pulse construction, following the procedure outlined in section 3.3.2 which corrects for the linear contributions of Kerr and the second-order dispersive shift in the displaced frame. The resulting pulses are simulated with the full Hamiltonian, resulting in the infidelities given by purple diamonds in fig. 4.11. These infidelities are close to the pulses optimized and simulated with $K = 0$ and $\chi' = 0$, indicating that correcting for the linear contributions of these terms is enough to significantly reduce their deleterious impact on the overall gate fidelity.

Additional coherent sources of infidelity can arise from unknown microwave distortions and drifts of calibrations during the measurements. In our experiment, drive strengths and phases are first independently calibrated, and we do not use in-situ optimization of these parameters since a fast, direct measurement of fidelity is not easily available. However, in future implementations the characteristic function can be efficiently sampled to estimate the fidelity, and this could be used with with a Nelder-Mead or reinforcement learning approach for in-situ parameter optimization [99].

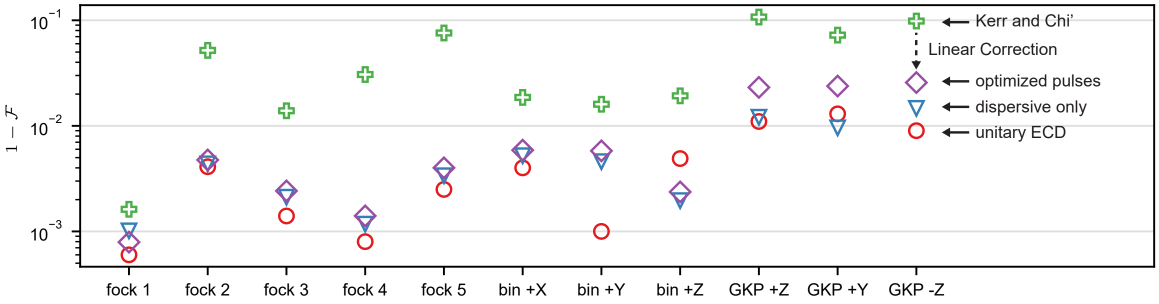

Figure 4.11: **Decoherence free error budget.** Simulated fidelity of constructed ECD sequences under different conditions. Red circles: result from unitary ECD parameter optimization. Blue triangles: pulses constructed and simulated with $K = \chi' = 0$. Green crosses: pulses optimized with $K = \chi' = 0$ and simulated with measured K and χ' (nonzero). Purple diamonds: pulses optimized and simulated with measured K and χ' (nonzero)f.

4.6.2 Impact of decoherence

Next, we study the impact of transmon and cavity decoherence on the state preparation fidelity. In particular, we perform master equation simulations in the time-dependent displaced frame. Under a unitary frame transformation $\rho \to \tilde{\rho} = U\rho U^\dagger$, the master equation $\partial_t \rho = -(i/\hbar)[H,\rho] + \sum_i \mathcal{D}[L_i]\rho$ becomes $\partial_t\tilde{\rho} = -(i/\hbar)\left[\tilde{H},\rho\right] + \sum_i \mathcal{D}[UL_iU^\dagger]\tilde{\rho}$ with $\tilde{H} = UHU^\dagger + i\hbar(\partial_t U)$. Using the time-dependent displaced frame in section 3.2.2, we evolve the joint transmon-cavity density matrix according to

$$\begin{aligned}\partial_t\tilde{\rho} = -\frac{i}{\hbar}\left[\tilde{H}(t),\tilde{\rho}\right] + \gamma_\downarrow\mathcal{D}[q]\tilde{\rho} + \gamma_\uparrow\mathcal{D}[q^\dagger]\tilde{\rho} + 2\gamma_\phi\mathcal{D}[q^\dagger q]\tilde{\rho} \\ + \kappa_\downarrow\mathcal{D}[a]\tilde{\rho} + \kappa_\uparrow\mathcal{D}[a^\dagger + \alpha^*(t)]\tilde{\rho} + 2\kappa_\phi\mathcal{D}[(a^\dagger + \alpha^*(t))(a+\alpha(t))]\tilde{\rho}\end{aligned} \tag{4.6}$$

where $\tilde{H}(t)$ is the displaced frame Hamiltonian in eq. (3.22) and $\alpha(t)$ is the nonlinear response to the drive given by solving eq. (3.23). By simulating in the displaced frame which tracks the

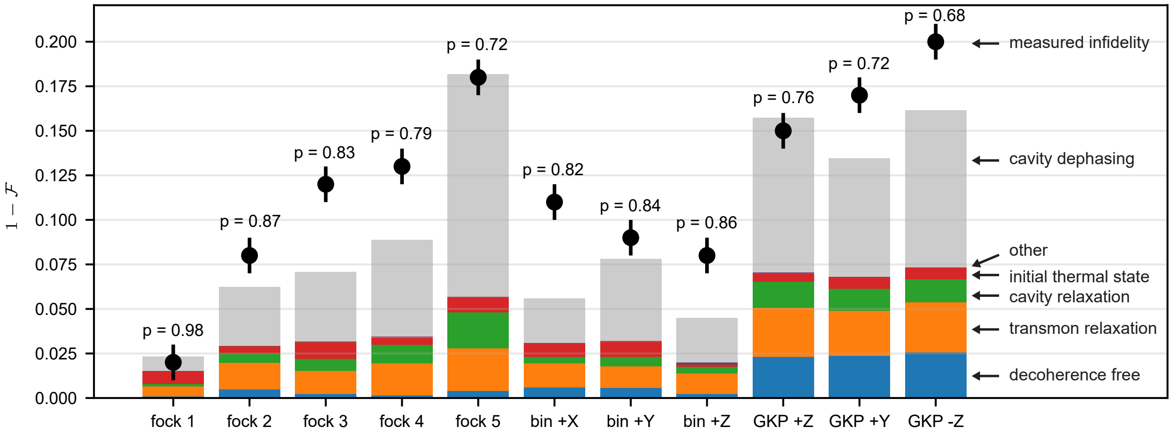

Figure 4.12: **Full error budget compared to measured fidelities and purities.** For each state preparation example, black dots indicate infidelities found from maximum likelihood reconstruction using the measured characteristic functions after post-selecting the transmon in $|g\rangle$. Also shown is the purity of the reconstructed states $p = \mathrm{Tr}\,(\rho^2)$. For each state, we include the baseline infidelity (labeled *decoherence-free*) which is equivalent to the purple diamonds in fig. 4.11. On top of this baseline, contributions to the total simulated infidelity using the measured decoherence rates are shown by the colored bars. Here, *other* (bars not visible) includes contributions from transmon dephasing, transmon heating, and cavity heating at the quoted rates. Also included is simulated contribution due to intrinsic cavity dephasing at a rate $\kappa_\phi = (150\,\mathrm{ms})^{-1}$.

classical trajectory of the state's center-of-probability in phase space, we reduce the Hilbert space truncation required to accurately capture the dynamics. This is especially important considering our pulses drive the oscillator to photon numbers of $\sim 10^3$.

We first simulate the impact of transmon relaxation, heating, and dephasing, as well as cavity relaxation and heating, given the measured rates in table 4.2. When simulating transmon relaxation, we use the averaged measured relaxation rate with $\langle n\rangle_{\mathrm{cav}} = 900$ photons in the cavity $\tilde{T}_{1,q} \approx 30\,\mu\mathrm{s}$, however we note this changes with time as shown in fig. 3.2, and the contribution from this error channel is also expected to change depending on the particular $\tilde{T}_{1,q}$ at the time of averaging. In addition, we approximate the qubit dephasing rate to be $\gamma_\phi = \gamma_{2E} - \gamma_1/2$, which assumes the echoing of low-frequency noise during the ECD gates results in an effective white noise dephasing.

The results are summarized by the colored bars in fig. 4.12, where each contribution to the error budget is simulated by only including a single decoherence mechanism. Also included is infidelity associated to an initial cavity thermal state ($n_{\text{th}} = 0.025$) since we do not employ active cavity cooling before each experiment. Independent simulations have verified that adding the infidelities of individual error channels is a good predictor of the total infidelity when simulating with all error channels combined. Out of these error channels, transmon relaxation has the biggest overall impact on the infidelity as ancilla relaxation during the conditional displacements can result in large oscillator displacements [26].

4.6.3 Error budget discussion

As shown in fig. 4.12, these decoherence mechanisms alone under-predict the infidelity found in experiment. Possible additional sources of infidelity include unknown transfer functions [198–200], drifts in parameters and calibrations, additional cavity heating due to the strong drives, and cavity dephasing. Out of these mechanisms, we simulate the effect of cavity dephasing using the displaced-frame dephasing term in eq. (4.6).

In this experiment, we do not have a direct measurement of the small intrinsic cavity dephasing rate, and such a measurement is an ongoing topic of investigation. We instead use master equation simulations to study the impact of cavity dephasing. In fig. 4.12 we include a contribution to the infidelity by simulating the pulses with a cavity dephasing rate of $\kappa_\phi = (150\,\text{ms})^{-1}$, shown by the light grey bars. For some state preparation experiments, such as Fock $|5\rangle$ and GKP $|+Z\rangle$, this rate roughly matches the measured infidelity. This is evidence that the dephasing rate is likely smaller than $1\,\text{Hz}$.

The simulated infidelities with all error contributions do not exactly follow the trend of measured infidelities. This is likely due to the fluctuating relaxation rate of the transmon as shown in fig. 3.4. All data was taken over the time span of about a week, and each measurement over the time span of a few hours, during which time the relaxation rate of the transmon with photons in the oscillator fluctuates, making the exact error budget difficult to establish.

4.6.4 Dephasing and gate speed trade-off

Large displacements increase gate speed to reduce the impact of transmon errors and oscillator relaxation. However they amplify oscillator dephasing, resulting in decoherence scaling with photon number. Here, we use a simple model verified numerically to investigate this trade-off.

If a single transmon error (bit-flip or phase-flip) spoils the fidelity of a state-preparation sequence of duration $T = \sum_i |\beta|_i/\chi\alpha_0$, the infidelity will scale as $1 - \mathcal{F} \propto \gamma_{2E}T \propto \gamma_{2E}/\alpha_0$. If a single oscillator photon loss spoils the fidelity, it will scale as $1-\mathcal{F} \propto \langle n \rangle \kappa T \propto \langle n \rangle \kappa/\alpha_0$ where $\langle n \rangle$ is the average photon number in the displaced frame during the gate sequence. Oscillator dephasing will cause errors at a rate $1 - \mathcal{F} \propto \kappa_\phi \alpha_0^2 T \propto \kappa_\phi \alpha_0$, amplified by the photon number during ECD gates. Together, these rates suggest the optimal choice in α_0 will be $\alpha_0^{\text{optimal}} = c(\kappa_\phi)^{-1/2}$ with a proportionality factor c that can be found numerically and depends on $\gamma_{2E}, \kappa, \langle n \rangle$, drive constraints, and higher-order nonlinearities. As an example, in fig. 4.13 we simulate state preparation with our experimental parameters while varying κ_ϕ and α_0.

4.7 Discussion of experimental results

With these proof-of-principle results, we demonstrate the counter-intuitive result that high-fidelity universal control can be carried out in a regime where the relevant rate of bare nonlinear evolution is comparable to the fastest decoherence rate. In particular, a large on-off ratio between the rate of control and the bare oscillator-qubit hybridization can be achieved without the need for additional hardware such as a tunable coupler. Importantly, the approach still requires a large ancilla qubit nonlinearity K, reflected by the enhanced interaction speed limit $\propto \sqrt{\chi K}$.

Although our examples are specific to the oscillator and qubit system, similar displaced-field type control schemes could be designed and performed in other bosonic systems with

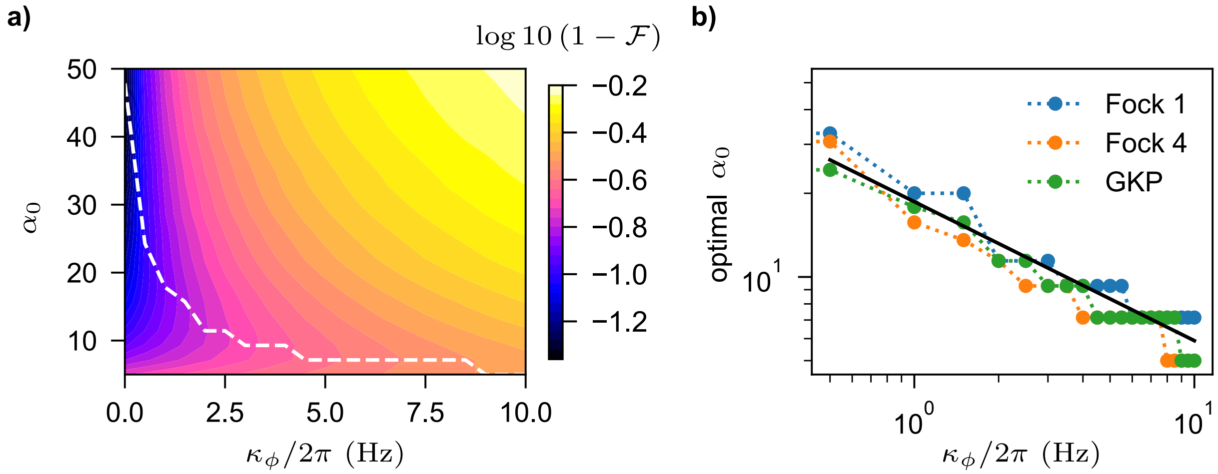

Figure 4.13: **Optimal ECD displacement with oscillator dephasing included.** a.) Simulated infidelity of $|+Z\rangle_{\text{GKP}}$ state preparation with oscillator and transmon decoherence at different α_0 and κ_φ. Dotted white line indicates the optimal α_0. b.) Optimal α_0 for state preparation of $|1\rangle, |4\rangle, |+Z\rangle_{\text{GKP}}$. Although these states have different $\langle n\rangle$, they have a similar prediction for the optimal α_0. Solid line is a fit to $\alpha_0^{\text{optimal}} = c(\kappa_\phi)^{-1/2}$ with $c = 46.75$.

bare nonlinearity of fourth order or greater, such as the recently proposed scheme to enhance the rate of Fock state preparation in a Kerr oscillator [201]. The phase-space ISA and parameter optimizations shown in this work could also be applied to realize universal control of the motional state of a trapped-ion. In such systems, spin-dependent forces can be used to realize a conditional displacement [202], and circuits similar to those presented here have been demonstrated for application-specific control [65, 66].

Finally, a weak bare nonlinearity has many benefits in the context of quantum information processing - for example, by sufficiently reducing the dispersive coupling χ, oscillator nonlinearity and loss inherited from the qubit can be minimized while retaining controllability, realizing a modular architecture where the qubit and oscillator can be more independently optimized. This is important in applications where these spurious couplings can cause decoherence and distortion of encoded states, especially during idling periods [19]. Also, the approach could allow for control of oscillators with measured relaxation times on the order of seconds [55] without reducing their lifetimes from the coupling to a lossy qubit through the Purcell effect [34].

It is worth noting that the ECD control method is designed for the weak-dispersive setting and performs best in this limit. At larger values of χ, the fidelity will be limited by higher order nonlinearities (such as Kerr) and the inability to perform unselective qubit rotations due to the limited bandwidth of qubit pulses. The point at which these effects become important will depend on the particular ECD sequence, transmon anharmonicity, and drive constraints. As an estimate of these effects, we simulated ECD pulse sequences for state preparation while increasing χ and higher-order nonlinearities as expected [142] using $\alpha_0 = \sqrt{n^e_{\text{crit}}} = \sqrt{K/(6\chi)}$ and keeping all other parameters fixed to match our experiment. We find that for $\chi/2\pi > 200\,\text{kHz}$, the total pulse duration saturates to the lower bound set by our drive constraints. At larger dispersive shifts on the order of $\chi/2\pi \gtrsim 500\,\text{kHz}$, the additional infidelity due to higher-order nonlinearities and finite-bandwidth effects becomes important relative to other decoherence mechanisms. These effects could be mitigated by using more complex pulse sequences optimized to account for higher order nonlinearity and finite-bandwidth effects while still maintaining the speed enhancement of large displacements. Finally, when the ECD method fails, the controlled parity gadget given in section 2.4.5 can instead be used to realize conditional displacements with a large dispersive coupling.

Chapter 5

Error correction of grid states encoded in an oscillator

5.1 A brief introduction to bosonic quantum error correction

Physical qubits and oscillators are engineered to minimize noise such as unwanted couplings with the environment, cross talk, and control distortion. However, realistic levels of physical noise are too large for reliable quantum computation, even with an optimistic outlook. For example, in a quantum circuit with G independent operations, each with failure probability p_{fail}, the success probability of the full circuit in the worst case is $(1-p_{\text{fail}})^G$ - exponentially small - so a quantum circuit with G gates will require a per-gate error rate of roughly $p_{\text{fail}} <\sim 1/G$. It is estimated that on the order of 10^7 two-qubit gates will be needed to realize a quantum advantage, with much longer circuits (orders-of-magnitude longer) needed for factoring [7]. This should be compared with the best physical two-qubit gate error rates, currently on the order of 10^{-3} for multi-qubit processors [6]. Clearly, error correction is needed to bridge this large gap, as it is unlikely that physical qubits will reach these error rates in the near-term.

To overcome such noise, in quantum error correcting codes, *logical* quantum information (the information on which a quantum computation is performed) is encoded redundantly as non-local correlations in the large state space of a many-level *physical* quantum system, often comprised itself of many distinct physical units. This encoding is done such that operations on the logical information (including the identity operation in the case of a quantum memory) are unaffected by small local perturbations. Furthermore, these small local perturbations can be measured and corrected (in some cases autonomously) before they build up enough to cause a logical error.

The first theoretical proposals for quantum error correcting codes use many-qubit approach to encode quantum information non-locally came around 1996 [8, 10, 11, 203–208], and these were also the first class of codes realized in superconducting circuits in 2012 [60]. Today, topological quantum error correcting codes such as the surface code [12–14, 90, 209] are the leading candidates for realizing FTQC, and recent experiments have shown that scaling these codes can lead to a decrease in error rates [6]. These error correcting codes can be thought of as the realization of an artificial phase of matter that has intrinsic topological protection against local perturbations. This is made explicit by the connection with lattice gauge theories [210]. I will not cover multi-qubit QEC here, and I refer the reader to one of the many great reviews or textbooks on the subject [2, 13, 14, 90, 211], and the online *error correction zoo* is also a wonderful resource.

Although the many-qubits approach is promising, it is likely that using oscillators for realizing FTQC will lead to an advantage in resource efficiency. This is the domain of bosonic quantum error correction, in which logical qubits are encoded into one or many oscillators. There are a number of bosonic codes that have been proposed and realized; I refer the reader to the many current reviews on the subject for a more in-depth introduction [18, 19, 22, 41, 43, 212–214].

One of these bosonic codes, the Gottesman-Kitaev-Preskill (GKP) code, is the focus of this PhD work and was introduced in section 1.2.2; For the GKP code, there has been a recent surge of interest in understanding the properties and performance of multimode GKP qubit codes [215–219]. Intuitively, we anticipate that a multimode GKP qubit code will outperform a single-mode GKP qubit simply due to "diffusion" of logical information across a larger space—the $2N$-dimensional phase of N bosonic modes—as opposed to the smaller 2-dimensional phase space for single mode codes. Of course, it is also important to consider the trade-offs associated with multimode encoding, such as the potential increase in susceptibility to certain types of errors, e.g., cross-talk between neighboring modes. See our recent review [22] for an in-depth discussion.

It is important to emphasize that the multi-mode GKP encoding is the ultimate goal of our research. However, in our current work, we first realize the single-oscillator GKP QEC code as a quantum memory, and this should be seen as a stepping stone towards an eventual multi-mode or concatenated encoding, such as a GKP surface code [41, 196, 220]. Our realization is a fundamental module in a future multi-mode code, requiring additional engineering and more advancements to scale up.

In this chapter, I will focus on the experimental realization of the single-mode GKP code. First in section 5.1.1, I will give a brief technical introduction to quantum error correction by reviewing the Knill-Laflamme conditions, specifying the requirements for any QEC code. Next, in section 5.1.2, I will introduce the finite-energy GKP code as a modification to the infinite-energy GKP code that was already introduced. Following this, in section 5.2.2 and section 5.2.3, I will discuss the QEC protocols we used to stabilize the single-mode GKP code. Finally, in section 5.3 and section 5.4, I will review and compare our 2020 [26] and our 2023 [99] quantum error correction experiments, ultimately leading to a demonstration of an error-corrected quantum memory beyond break-even.

5.1.1 The Knill-Laflamme Conditions

A d-dimensional error correcting code can be specified by its logical code words, $\{|\mu_L\rangle\}_{\{\mu=0,1,\ldots,d-1\}}$, forming a subspace of some larger Hilbert space $\mathcal{H}$. These code words define a projector onto the code space, given by $\Pi_c = \sum_\mu |\mu_L\rangle \langle\mu_L|$.

Given a QEC code, the Knill-Laflamme conditions (introduced in [221]) can be used to determine if a set of errors, $\{E_k\}$, is correctable [14]. Typically, these errors are the Kraus operators of a quantum channel, acting as

$$\rho \to \sum_k E_k \rho E_k^\dagger \tag{5.1}$$

under the condition $\sum_k E_k^\dagger E_k = 1$.

Explicitly, the Knill-Laflamme error correcting conditions are

$$\Pi_c E_k^\dagger E_{k'} \Pi_c = \alpha_{kk'} \Pi_c \tag{5.2}$$

for all k, k', where $\alpha_{k,k'}$ are the elements of a complex Hermitian matrix.

The conditions can also be written as

$$\langle\mu_L| E_k^\dagger E_{k'} |v_L\rangle = \alpha_{kk'} \delta_{\mu v} \tag{5.3}$$

for all k, k', μ, v where $|\mu_L\rangle, |v_L\rangle$ are code words.

For many codes, including most bosonic codes, the Knill-Laflamme conditions are only satisfied approximately (see for example, the calculation for the binomial code given in [193]). They are part of a class of codes known as approximate error correcting codes [222].

For the GKP code, the Knill-Laflamme conditions can be difficult to calculate; such a calculation requires evaluating the errors in the displacement basis (the characteristic function, see appendix A.3), however error operators such as $\hat{a}$ are unbounded and hence do not have a valid characteristic function. However, by applying the conditions instead to the Kraus operators of the photon-loss channel, the conditions for the finite-energy code have been calculated approximately by Albert *et al.* [18, 19, 43].

Alternatively, an intuitive approach can also be taken to understand the GKP code's protection to photon loss. As discussed in table A.1, the photon loss channel at rate $\kappa_\downarrow$ acting for a time t applies a very simple transformation to the characteristic function of the oscillator. In the case of pure photon loss (no photon gain $\kappa_\uparrow = 0$) after a time t, an initial characteristic function $\mathcal{C}(\alpha)$ is transformed into a new characteristic function $\mathcal{C}(\alpha, t)$ according to

$$\mathcal{C}\left(\alpha, t\right) = \mathcal{C}(\alpha e^{-\kappa_\downarrow t/2}) \exp\left(\left(e^{-\kappa_\downarrow t} - 1\right)\frac{|\alpha|^2}{2}\right) \overset{\kappa_\downarrow t \ll 1}{\approx} \mathcal{C}\left(\alpha\left(1 - \kappa_\downarrow t/2\right)\right)\exp\left(-\kappa_\downarrow t \frac{|\alpha|^2}{2}\right). \tag{5.4}$$

Equation (5.4) shows that photon loss causes the characteristic function to grow and a Gaussian filter is applied. In the limit of small $\kappa_\downarrow t$, the variance of the Gaussian filter is $(\kappa_\downarrow t)^{-1}$. This should be interpreted as high-frequency correlations of the Wigner function being filtered out under photon loss, along with a directional diffusion term, evident from the stochastic Fokker-Planck equation under photon loss.

With this in mind, the GKP logical information is stored as low-frequency correlations in phase space. Explicitly, the logical operators are points in the reciprocal space (the characteristic function) that are as close to the origin as is allowed by the commutation law for displacement operators, while still satisfying the required commutation laws for a qubit stabilizer code (eq. (1.21)). As long as error correction is carried out quickly relative to the rate of photon loss, this information is only marginally affected by the Gaussian filter applied to the characteristic function.

5.1.2 The finite-energy GKP code

The single-mode infinite-energy GKP code was introduced in section 1.2.2; readers should become familiar with that introduction before proceeding. Here, I will discuss the finite-energy GKP code.

As introduced in [20, 24, 64, 223], the finite-energy GKP code can be defined as a modification of the infinite energy GKP code by using the (non-unitary) envelope operator, defined as

$$E_\Delta = \exp\left(-\Delta^2 a^\dagger a\right). \tag{5.5}$$

The finite-energy GKP code words are given by applying the envelope operator to the infinite-energy code words

$$\left|\pm Z\right\rangle_\Delta = \mathcal{N}_\Delta E_\Delta \left|\pm Z\right\rangle \tag{5.6}$$

where $\mathcal{N}_\Delta$ is a normalization factor [64]. This formalism is powerful, as it allows us to define finite-energy logical operators: any infinite-energy logical operator, $\hat{O}$, can be transformed into the finite-energy version $\hat{O}_\Delta$ using the similarity transformation, $\hat{O}_\Delta = E_\Delta \hat{O} E_\Delta^{-1}$. As shown in [64], this applies the following transformations to the oscillator position and momentum operators,

$$E_\Delta \hat{q} E_\Delta^{-1} = \cosh\left(\Delta^2\right)\hat{q} + i\sinh\left(\Delta^2\right)\hat{p} \tag{5.7}$$

$$E_\Delta \hat{p} E_\Delta^{-1} = \cosh\left(\Delta^2\right)\hat{p} - i\sinh\left(\Delta^2\right)\hat{q}. \tag{5.8}$$

From these relations, in the limit of small Δ such that $\cosh\left(\Delta^2\right) \approx 1$ and $\sinh\left(\Delta^2\right) \approx \Delta^2$, the finite energy logical operators and stabilizers can be written as

$$S_{q,\Delta} \approx \exp\left(i2\sqrt{\pi}\hat{q} - 2\sqrt{\pi}\Delta^2\hat{p}\right) \qquad Z_\Delta \approx \exp\left(i\sqrt{\pi}\hat{q} - \sqrt{\pi}\Delta^2\hat{p}\right) \tag{5.9}$$

$$S_{p,\Delta} \approx \exp\left(-i2\sqrt{\pi}\hat{p} - 2\sqrt{\pi}\Delta^2\hat{q}\right) \qquad X_\Delta \approx \exp\left(-i\sqrt{\pi}\hat{p} - \sqrt{\pi}\Delta^2\hat{q}\right) \tag{5.10}$$

The finite-energy GKP states are the +1 eigenstates of the finite-energy stabilizers. These finite energy logical states have a finite-overlap. However, in practice, this overlap is negligible given current measurement capabilities; for a squeezing of 9 dB, the overlap of finite-energy logical states is on the order of 10^{-6} [224].

An alternative approach to define the finite-energy GKP states is to diagonalize the

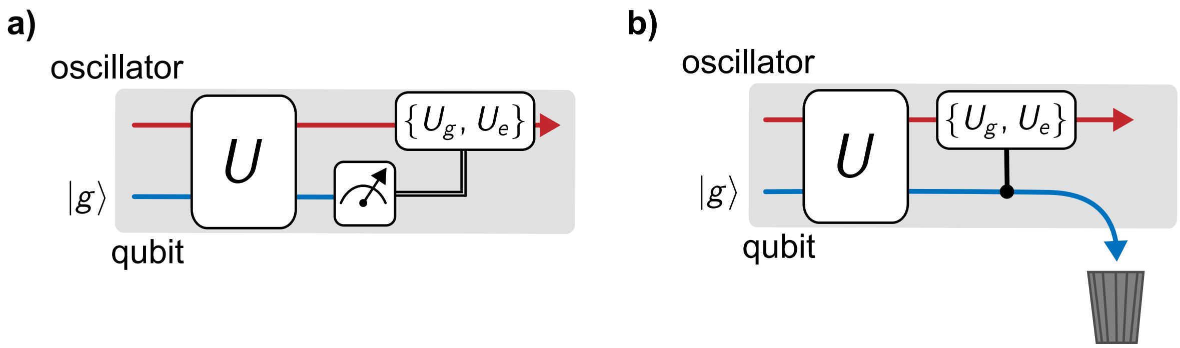

Figure 5.1: **Quantum error correction circuits: a.) feedback vs b.) autonomous.** In the ensemble sense, these two circuits enact the same channel on the oscillator. The 'trash can' symbol represents the partial trace over the qubit mode. In reality, the circuit in **b** is usually followed by a qubit reset, however this is not strictly necessary to write the Kraus map.

confined GKP Hamiltonian, given by

$$H_{\mathrm{GKP},\Delta} = \frac{\omega_0}{2}\left(\hat{p}^2 + \hat{q}^2\right) - E_p \cos\left(\frac{\sqrt{2\pi d}}{\eta}\,\hat{p}\right) - E_q \cos\left(\eta\sqrt{2\pi d}\,\hat{q}\right). \tag{5.11}$$

The finite-energy GKP manifold is given as the quasi degenerate +1 eigenstates of $H_{\mathrm{GKP},\Delta}$. I cover this method in depth in appendix G and also in [22], along with the related Zak basis in appendix F. The Hamiltonian approach will be a powerful tool for future Floquet-engineering approaches to realizing the GKP code [39, 40, 225–227].

5.2 Stabilization of the finite-energy GKP code using an auxiliary qubit

In this section, I will review methods to perform quantum error correction of a single-mode GKP encoding using an auxiliary qubit.

5.2.1 The Kraus operator approach

The circuits we use for stabilization of finite-energy GKP states are all of the same type shown in fig. 5.1. Before discussing the details of GKP error correction, I will introduce the approach to understanding these circuits using the Kraus formalism. Importantly, I will show that the transformation applied by the circuit in fig. 5.1a using classical feedback is equivalent to the circuit on the right, using a 'quantum-controlled' unitary, where the equivalence is taken in the ensemble sense.

Let us first focus in the circuit shown in fig. 5.1a. Here, the auxiliary qubit is prepared in pure state $|g\rangle$, it interacts with the oscillator via a unitary U, and is then measured in the σ_z basis. Finally, the information used for classical feedback, and the unitary U_g or U_e is applied to the oscillator conditioned on the measurement result.

The initial state in the circuit is given by $\rho = \rho_o \otimes |g\rangle\langle g|$, where ρ_o is the initial oscillator density matrix. After the entangling unitary U is applied, but before the classical feedback is applied, the state of the oscillator is given by the partial trace,

$$\begin{aligned}
\tilde{\rho_o} &= \mathrm{Tr}_q\left(U\left(\rho_o \otimes |g\rangle\langle g|\right)U^\dagger\right) && (5.12)\\
&= \langle g| U\left(\rho_o \otimes |g\rangle\langle g|\right)U^\dagger |g\rangle + \langle e| U\left(\rho_o \otimes |g\rangle\langle g|\right)U^\dagger |e\rangle && (5.13)\\
&= \langle g|U|g\rangle\, \rho_o\, \langle g|U^\dagger|g\rangle + \langle e|U|g\rangle\, \rho_o\, \langle g|U^\dagger|e\rangle && (5.14)\\
&= K_g\rho_o K_g^\dagger + K_e\rho_o K_e^\dagger. && (5.15)
\end{aligned}$$

Here $K_g = \langle g|U|g\rangle$ and $K_e = \langle e|U|g\rangle$ are called the Kraus operators of the quantum channel associated with the circuit (before the feedback is applied). They satisfy $\sum_n K_n^\dagger K_n = 1$, and any quantum channel can be written as $\rho \to \sum_n K_n \rho K_n^\dagger$. The action of these Kraus operators on the oscillator is also called the 'back-action' of the circuit.

When the measurement is applied, the oscillator density matrix after the measurement result is given by the POVM (positive operator-valued measure) formalism [2]. Written in terms of the Kraus operators,

$$\rho_g = \frac{K_g \rho_o K_g^\dagger}{p_g} \tag{5.16}$$

$$\rho_e = \frac{K_e \rho_o K_e^\dagger}{p_e} \tag{5.17}$$

$$p_g = \mathrm{Tr}\left(K_g \rho_o K_g^\dagger\right) \tag{5.18}$$

$$p_e = \mathrm{Tr}\left(K_e \rho_o K_e^\dagger\right) \tag{5.19}$$

where p_g and p_e are the probabilities of measuring $|g\rangle$ and $|e\rangle$. The classical feedback can then be applied, resulting in the final density matrices of the circuit $\rho_{g,f} = U_g \rho_g U_g^\dagger$ and $\rho_{e,f} = U_e \rho_e U_e^\dagger$, where the f here stands for 'final'.

The measurement results can tell us which feedback was applied. However, we can also take an ensemble approach to the circuit. If we don't record the measurement, the ensemble result of the circuit will be given by

$$\rho_f = p_g \rho_{g,f} + p_e \rho_{e,f} \tag{5.20}$$

$$= U_g K_g \rho_o K_g^\dagger U_g^\dagger + U_e K_e \rho_o K_e^\dagger U_e^\dagger \tag{5.21}$$

$$= \tilde{K}_g \rho_o \tilde{K}_g^\dagger + \tilde{K}_e \rho_o \tilde{K}_e^\dagger \tag{5.22}$$

where $\tilde{K}_g = \langle g|U_g U|g\rangle$ and $\tilde{K}_e = \langle e|U_e U|g\rangle$.

We can now examine the autonomous circuit, shown in fig. 5.1b. Here, the start of the circuit is the same. However, instead of a measurement and classical feedback, a qubit-controlled unitary $U_g |g\rangle \langle g| + U_e |e\rangle \langle e|$ is performed. Finally, the 'trash can' symbol indicates that we ignore the qubit after this gate - it is traced out. In practice, another circuit will follow this one, and the qubit will be reset.

The Kraus operators of the autonomous circuit can also be computed using the method shown above, considering that U_g and U_e act on the oscillator alone. Interestingly, the Kraus operators for this circuit are $\tilde{K}_g$ and $\tilde{K}_e$ - exactly the same as the circuit with classical feedback when the measurement was ignored! From this result, circuits discussed in this chapter can be realized either using classical feedback or 'quantum' feedback, by replacing the classically-conditioned unitary with a qubit-controlled unitary. If desired, the qubit in the autonomous circuit can be measured after the circuit, and the result of such a measurement will reveal which error was corrected (in the language of quantum trajectories, which trajectory was taken).

5.2.2 Stabilization of finite energy GKP states with the sharpen-trim protocol

As shown by Terhal and Weigand in 2016 [59], phase estimation circuits of the type introduced in section 3.4 can be used to prepare and measure GKP states. Here, we now derive a QEC protocol called the sharpen-trim protocol, based on the ideas in [59], but importantly modified to stabilize the finite-energy code.

The sharpen-trim protocol is shown in fig. 5.2b. It employs the phase space ISA described in section 2.4.5 and chapter 4 to protect finite-energy grid states. This protocol was derived in [26] and was used for the first demonstration of QEC for GKP states. Here, we describe the protocol using the language of Kraus operators derived in the previous section. Later, in section 5.2.3, we review the work of Royer *et al.* [64], where the sharpen-trim protocol was further explained using the language of engineered dissipation, and additional stabilization protocols were introduced.

Both the sharpen and trim steps use the same circuit, with different parameter values. This circuit was first introduced in section 3.4, where the goal was to measure the $\langle D(\alpha)\rangle$ (the characteristic function of the oscillator) using phase estimation. Here, it is no surprise the circuits are similar; given the GKP stabilizers and logical operators are displacement operators. However, in this case, the goal is to use the back-action on the oscillator to stabilize a manifold of grid states.

First, note that there exists an optimal width of the envelope Δ, resulting from a trade-

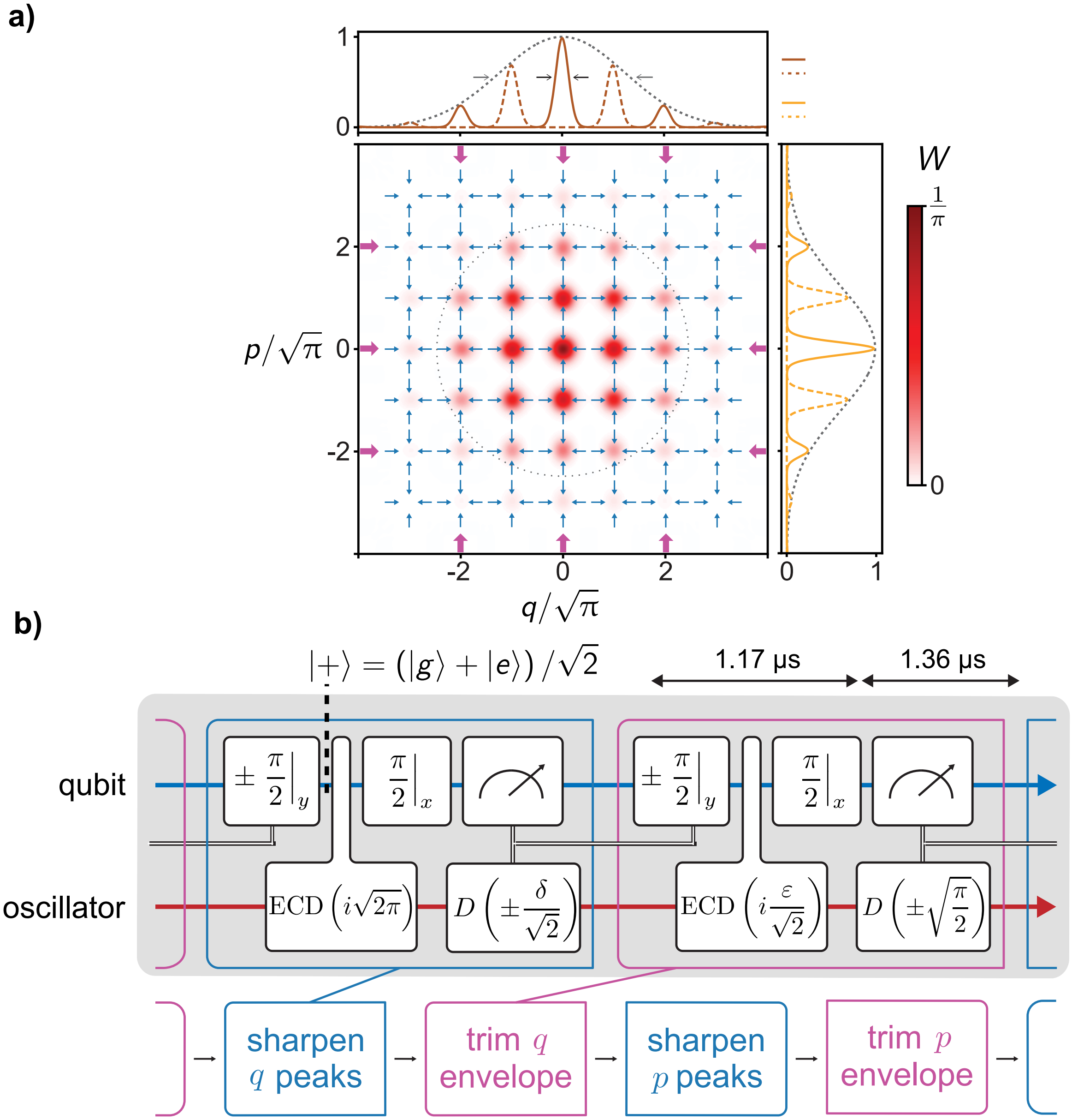

Figure 5.2: **GKP sharpen-trim error correction protocol from [26]. a)** Wigner representation of engineered dissipation for stabilizing the finite-energy GKP code, here shown as acting on the maximally-mixed state in the code. The protocol has two goals: first, to stabilize the grid (blue arrows, the 'sharpen' step), and second, to stabilize the envelope (purple arrows, the 'trim' step). **b)** The sharpen trim circuit, with timings shown as realized in [26]. The qubit feedback is such that the qubit is prepared in $|+\rangle$ before each ECD gate.

off: more extended grid states have better resolved peaks and are thus more robust against shifts, but are more sensitive to dissipation. Therefore, our protocol is designed with two objectives in mind:

- **Sharpen** first, to keep the oscillator state probability distribution peaked in phase-space at $q,\ p = 0 \bmod \sqrt{\pi},\ \sqrt{\pi}$. Shown by the blue arrows in fig. 5.2a.
- **Trim** second, to prevent the overall envelope from drifting or expanding more than necessary. Shown by the purple arrows in fig. 5.2a.

Let us first re-examine the general phase-estimation circuit shown in fig. 3.7. To remind the reader, the qubit is initialized in the $|+\rangle$ state. Next, a conditional displacement of β is applied. Finally, the qubit can be measured in some basis at angle φ along the $\sigma_x - \sigma_y$ equatorial plane of the Bloch sphere (by applying the appropriate $\pi/2$ qubit rotation before a σ_z measurement). Let us examine this circuit, but now using the Kraus operator approach to examine the back-action on the oscillator.

Let the measurement basis of the qubit at angle φ along the equatorial plane of the Bloch sphere be written as $|\pm\rangle_\varphi = (|g\rangle \pm e^{i\varphi}|e\rangle)$ ($\varphi = 0$ corresponds to a σ_x measurement while $\varphi = \pi/2$ corresponds to a σ_y measurement). The Kraus operators are evaluated to be

$$
\begin{aligned}
K_{\pm}^{(\varphi)} &= {}_{\varphi}\langle\pm| \left(D\left(\frac{\beta}{2}\right)|g\rangle\langle g| + D\left(\frac{-\beta}{2}\right)|e\rangle\langle e|\right)|+\rangle_0 &(5.23)\\
&= \frac{1}{2}\left(\left(\langle g| \pm e^{-i\varphi}\langle e|\right)\left(D\left(\frac{\beta}{2}\right)|g\rangle\langle g| + D(\frac{-\beta}{2})|e\rangle\langle e|\right)(|g\rangle + |e\rangle)\right) &(5.24)\\
&= \frac{1}{2}\left(D\left(\frac{\beta}{2}\right) \pm e^{-i\varphi}D(\frac{-\beta}{2})\right) &(5.25)\\
&= \exp\left(-\frac{i}{2}\left(\varphi + \frac{\pi}{2} \mp \frac{\pi}{2}\right)\right)\cos\left(\frac{1}{2}\left(-\sqrt{2}|\beta|\hat{q}_\perp + \varphi + \frac{\pi}{2} \mp \frac{\pi}{2}\right)\right), &(5.26)
\end{aligned}
$$

where we have defined the perpendicular quadrature $q_\perp = \cos(\Theta)\hat{p} - \sin(\Theta)\hat{q}$ with $\Theta = \text{angle}\,(\beta)$ (see appendix A.1).

It is useful to examine the specific case of a conditional displacement along either the momentum direction $\beta = ib$ or position direction $\beta = b$ and a measurement in the σ_y basis ($\varphi = \pi/2$). The σ_y basis is chosen using the intuition introduced in the introduction section 1.2.2: a measurement of σ_y corresponds to a measurement of the imaginary part of the displacement operator, which is more sensitive to small displacements than the real part if we expect the displacement to be small. The Kraus map can be written in the basis of $\hat{q}_\perp$ to show the probability distribution $P(q_\perp)$ is transformed according to

$$P(q_\perp) \to P(q_\perp) \cos^2\left(\frac{1}{2}\left(-\sqrt{2}|\beta|q_\perp \mp \frac{\pi}{2}\right)\right). \tag{5.27}$$

With this transformation, the back-action acts by multiplication, transforming the probability distribution by multiplication with a squared cosine function with period $2\pi/\sqrt{2}|\beta|$. The cosine is shifted to the left or right corresponding to the measurement result. With this description, we can now examine the sharpen and trim circuits shown in fig. 5.2b.

We first examine the sharpen circuit. Here, $\beta = \sqrt{2\pi}$, corresponding to a stabilizer. In fig. 5.3, I show the action of the Kraus operator back-action on the oscillator q probability distribution for a q sharpen round. In the left panel, the initial probability distribution is shown, which has been broadened due to dissipation acting since the previous sharpen round. Such a broadening can be understood as a diffusion in phase space, or equivalently, as the multiplication of the characteristic function by a Gaussian filter (given in eq. (5.4)).

The result of the sharpen circuit when measuring either $|\pm y\rangle$ is shown in the upper and lower right panel of fig. 5.3. The initial distribution (black) is multiplied by a shifted cosine (dotted line) corresponding to the measurement result. The result of such a multiplication is shown as the solid colored lines. Clearly, the peaks are sharpened! However, they are slightly shifted to the right or left, depending on the measurement outcome. This is where the classical feedback comes into play: by applying a small 'kick' in position, depending on the measurement result, the resulting distribution can be centered. The net result of

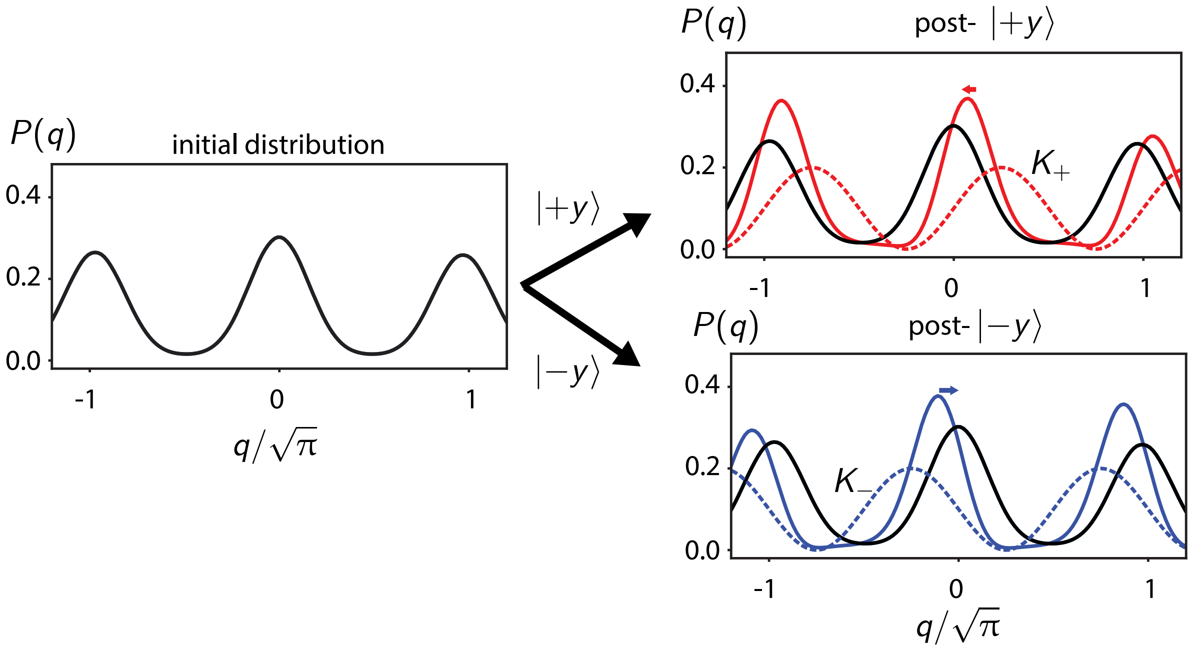

Figure 5.3: **Back-action of the sharpen circuit.** Modified and reproduced from the supplement of [26]. **Left:** an initial GKP probability distribution that has been broadened. **Right:** Conditioned on the measurement result, multiplication by the shifted cosines (dotted) results in sharpened distributions. These distributions are centered after the measurement with small kicks using low-latency classical feedback.

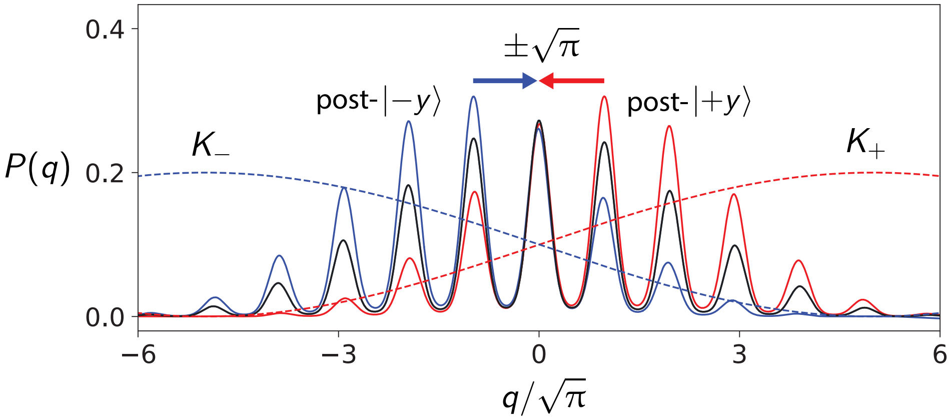

Figure 5.4: **Back-action of trim circuit**, reproduced from [26]. Back action associated with a trimming step in position. The initial position probability distribution (black line) is multiplied by the shifted cosine. The resulting distributions are trimmed but not centered. A feedback displacement conditioned on the measurement result is then used to center the envelope,

the sharpen circuit, when averaged over both Kraus operators as discussed in the previous section (the measurement probabilities are roughly $p_+ = p_- = 0.5$ under photon loss), results in a centered and sharpened distribution. This circuit is applied along both position and momentum to sharpen peaks in both directions.

However, if only the sharpen circuit were applied, the envelope would not be properly contained; each sharpen round adds energy to the oscillator through the conditional displacement, resulting in a broader envelope. Given typical loss rates, photon loss alone is not enough to contain the state from growing.

To solve this problem, we introduced the trim round in [26]. The trim circuit, shown in fig. 5.2, uses the same sequence of gates as the sharpen circuit, however with different values for the conditional displacement and feedback. For these trimming rounds, a small conditional displacement of size $|\beta| = \varepsilon/\sqrt{2}$ is applied. As shown in fig. 5.4, the back-action applied to the oscillator probability distribution is the same: multiplication by a shifted cosine squared. However, here the cosine with has a much larger period of $2\pi/\sqrt{2}\varepsilon$, resulting in a trimmed envelope and shifted envelope; after measurement of $|\pm y\rangle$, the envelope is centered at $\pm\sqrt{\pi}$. To recenter the envelope, a feedback kick of $\pm\sqrt{\pi}$ is applied to the state, conditioned on the result of the measurement.

The full protocol, shown in fig. 5.2b, consists of 4 alternating rounds: sharpen position, trim position, sharpen momentum, trim momentum. Finally, the sharpen-trim circuit can also be performed autonomously by replacing the final measurement, feedback, and classical displacements with a conditional displacement followed by a qubit reset, as shown in fig. 5.9 and discussed in the previous section.

5.2.3 The engineered dissipation approach

In Royer *et al.*, [64] the sharpen-trim circuit was further examined using an engineered dissipation approach, and other stabilization circuits were derived. Here, I will briefly review their method, with more details given in [64].

An alternative to measuring the stabilizers of the quantum codes is engineering a system-bath interaction,

$$H = \sqrt{\Gamma}(\hat{d}\hat{b}(t)^\dagger + \hat{d}^\dagger \hat{b}(t)), \tag{5.28}$$

which relaxes the system to states satisfying $\hat{d}\,|\psi\rangle = 0$, where $\hat{d}$ is known as the dissipator. Any excitation in the system due to $\hat{d}^\dagger$ are transferred to the zero-temperature bath, autonomously cooling the system to the desired state $|\psi\rangle$. A Markovian model of dissipation is realized by the above Hamiltonian where the field operators (bath) obey $[\hat{b}(t), \hat{b}(t')^\dagger] = \delta(t - t')$, with $\delta(t)$ being the Dirac-delta distribution.

There are multiple ways to design dissipators into the codespace. In Ref. [64], the authors defined dissipators to the GKP codespace as the natural logarithm of the finite-energy stabilizers S, since $\ln S_\Delta\,|\psi\rangle = 0.$[1]. The two finite-energy stabilizers $S_{q,\Delta}$ and $S_{p,\Delta}$ (approximations given in eq. (5.9)) define two target dissipators, $\hat{d}_x = \ln S_{q,\Delta}$ and $\hat{d}_p = \ln S_{p,\Delta}$. Given this, after tracing out the Markovian bath (assuming a zero-temperature bath), the system bath interaction in eq. (5.28) under system bath coupling rates $\sqrt{\Gamma_q}$ and $\sqrt{\Gamma_p}$ gives results

---

[1] We note an alternative definition of the dissipators was introduced in Ref. [39]

in the master equation

$$\partial_t \rho = \Gamma_q \mathcal{D}[\hat{d}_q]\rho + \Gamma_p \mathcal{D}[\hat{d}_p]\rho, \tag{5.29}$$

where $\mathcal{D}[O]\rho = O\rho O^\dagger - \{O^\dagger O, \rho\}/2$ is the standard dissipation superoperator.

However, actually realizing a system bath coupling of this type would be challenging, involving many high-weight, non-local couplings [39]. Instead, we can make use of repeated interactions with the qubit, each followed by a qubit reset, in order to effectively realize the master equation of eq. (5.29) in a 'stroboscopic' approach.

With details shown in [64], this stroboscopic approach gives rise to a few different finite-energy GKP stabilization protocols, including the exact sharpen-trim method discussed in section 5.2.2 and derived using different considerations!. Furthermore, the effective stabilization rate and envelope size can now be derived from the effective dissipation rate (assuming no additional loss; oscillator photon loss can modify the stabilized envelope size.)

Two additional protocols were derived in [64], each using a second-order trotter approximation to the effective unitary interaction needed to realize the master equation eq. (4.6) with repeated qubit interactions. These two protocols, named the 'small-Big-small' protocol and 'Big-small-Big' protocol after the relative magnitude of conditional displacements used, combine the sharpen and trim step into one circuit. The small-Big-small circuit is less sensitive to ancilla errors than the Big-small-Big circuit, and it is shown in fig. 5.5. This is the circuit used as a seed in the 2023 GKP QEC experiment, as discussed in section 5.4.

5.3 Realizing quantum error correction of the GKP code

In this section, I review our results from year 2020 demonstrating quantum error correction of the GKP code for the first time [26]. The weak-coupling architecture, as introduced in chapter 3, was used for this realization, with explicit experimental parameters given in

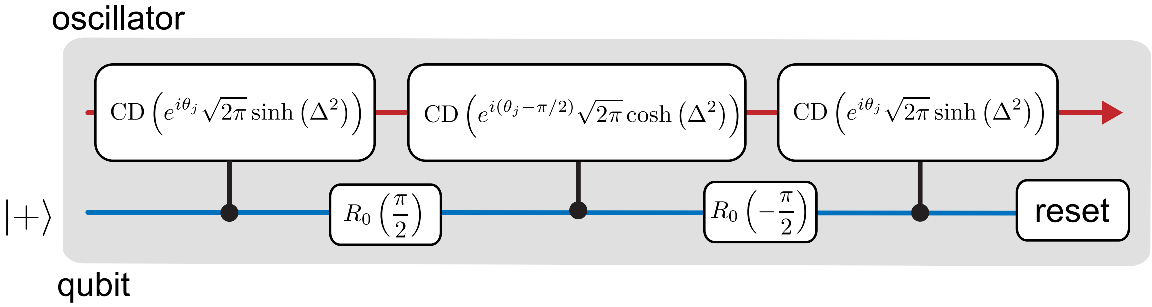

Figure 5.5: **small-Big-small circuit** for the single-mode square GKP qubit, from [64] and independently introduced in [65]. Here, written explicitly in terms of the envelope size Δ. The angle θ_j is varied as $\theta_j = \{0, \pi/2, \pi, 3\pi/2\}$ to make a symmetric protocol, stabilizing along position and momentum.

Storage oscillator single-photon lifetime	T_s	245 µs
Storage oscillator frequency	$\omega_s/2\pi$	5.26 GHz
Storage oscillator Kerr anharmonicity	$K_s/2\pi$	1 Hz
Transmon energy lifetime	T_1	50 µs
Transmon coherence lifetime (echo)	T_{2E}	60 µs
Transmon coherence lifetime (Ramsey)	T_{2R}	8 µs
Transmon resonance frequency	$\omega_t/2\pi$	6.71 GHz
Transmon anharmonicity	$K_t/2\pi$	193 MHz
Readout oscillator single-photon lifetime	T_r	65 ns
Readout oscillator frequency	$\omega_r/2\pi$	8.2 GHz
Storage-transmon dispersive shift	$\chi/2\pi$	28 kHz
Readout-transmon dispersive shift	$\chi_r/2pi$	1 MHz
Jump rate to higher transmon levels during error-correction	$\Gamma_{\rightarrow f}$	3 ms^{-1}

Table 5.1: **Measured system parameters for the 2020 GKP experiment**

table 5.1.

In this experiment, we used the measurement-based sharpen-trim protocol introduced in section 5.2.2. This circuit implements engineered dissipation to the GKP code manifold as discussed in the previous section. By utilizing fast FPGA electronics with a latency on the order of 200 ns, the transmon was measured and fast feedback displacements were employed to correct for small shift errors in real time in a four-round QEC cycle. As a verification experiment, the QEC cycle was repeated starting from the vacuum state of the oscillator, and the expectation values of stabilizers were measured after each step. The results of this experiment are shown in Figure 5.6a, with a convergence to the quasi-steady state after about 20 rounds (here, a round is defined as a single sharpen or trim step). The pattern in the measured stabilizers is clear: during each four round cycle, the measured position (or momentum) stabilizer value increases after the corresponding sharpen round, and slightly decreases during the next 3 rounds, matching simulation. Also shown in Fig. 5.6b is the convergence of the oscillator to a mixed state in the code manifold after 200 rounds of stabilization, longer than the decay constant of logical information.

To measure the performance of the quantum error correction protocol, Pauli eigenstates of the GKP code were prepared with a measurement-based protocol [26,66]. In this protocol, the code is first stabilized to an arbitrary (mixed) state in the code manifold by many rounds of stabilization. Next, the GKP code is projected into one of the $|\pm Z\rangle$ logical eigenstates by an infinite-energy Z logical measurement. For this measurement, the transmon is initialized in the $|+x\rangle$ state, a conditional displacement corresponding to a Z logical Pauli is applied, and the transmon is measured in the x basis. A real-time feedback displacement conditioned on the measurement result was then applied to prepare the desired logical state. The same procedure was used to prepare X and Y logical states by measuring the corresponding logical displacements. The measured characteristic functions resulting from this state preparation method is shown in fig. 5.7b. It is interesting to note that visually, these states are of higher quality than the states prepared using a full unitary approach in section 4.5.

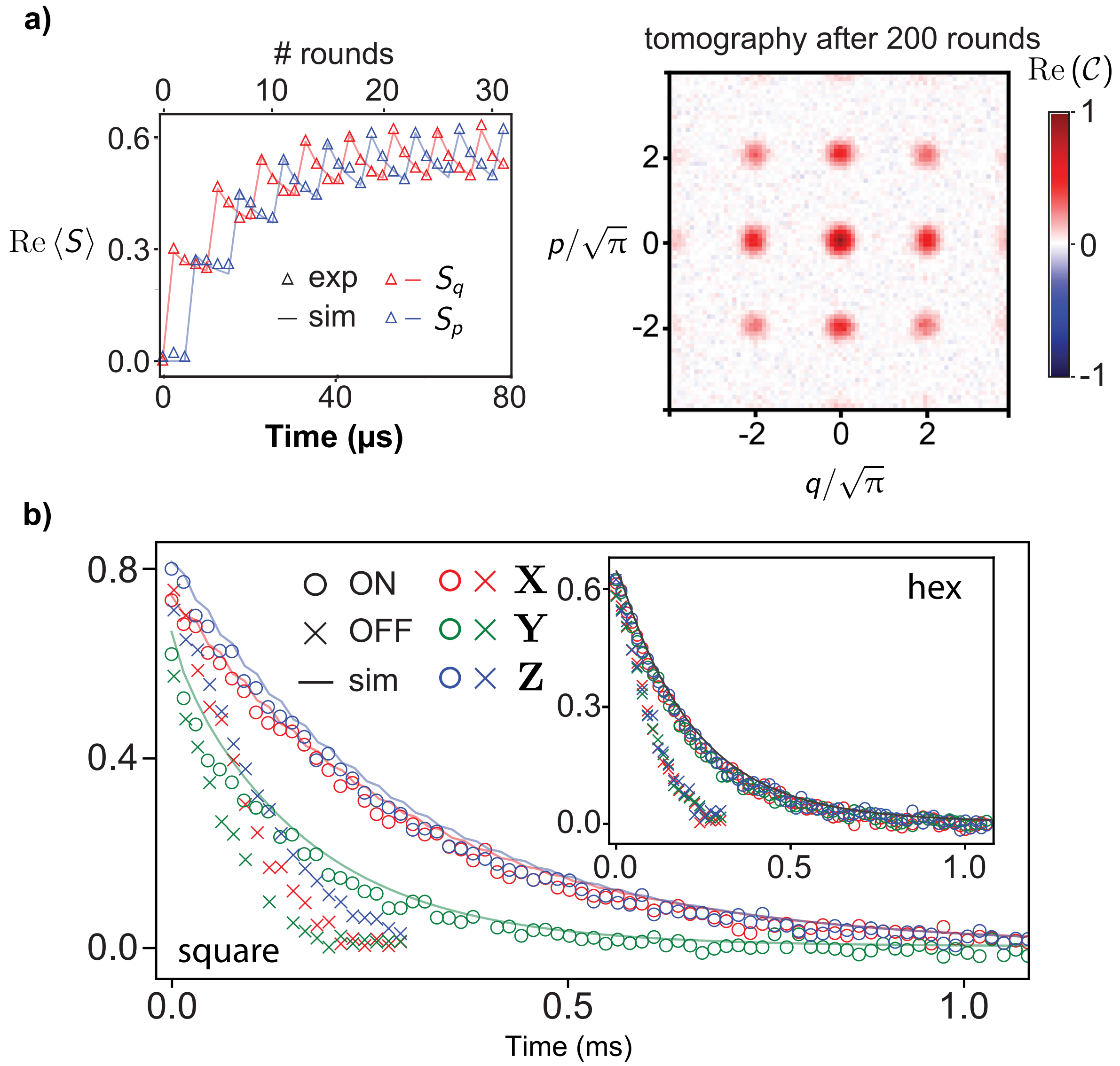

Figure 5.6: **Measured and simulated results for measurement and feedback based error correction of the single mode square GKP code.** a) Measurement based sharpen-trim protocol. b) Left: Evolution of the square-code position and momentum stabilizers under repeated QEC cycles starting from vacuum. Right: Measured characteristic function after 200 rounds. c) Lifetimes of the uncorrected (crosses) and corrected (circles) square GKP qubit. Inset: Hexagonal lifetimes.

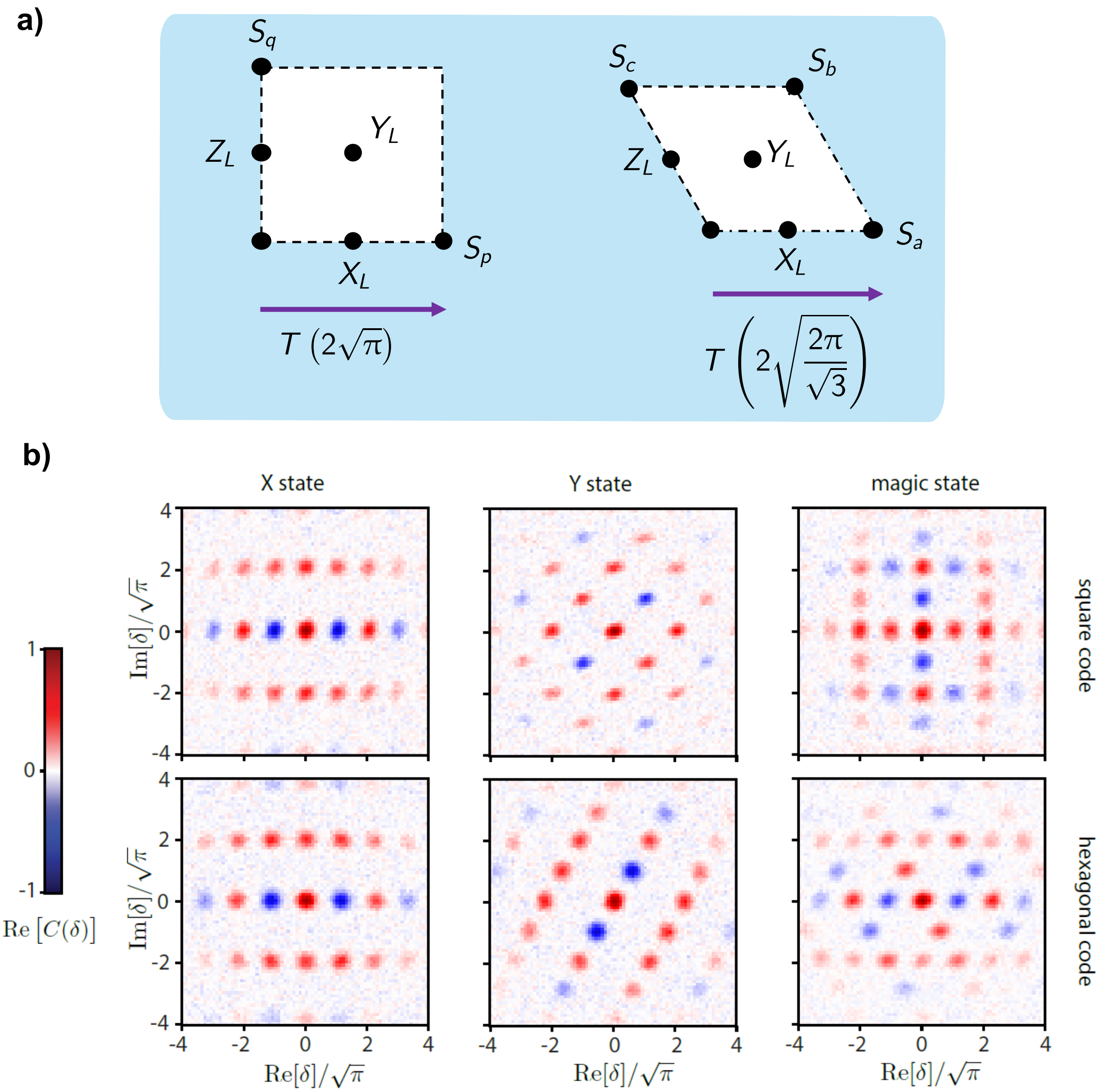

Figure 5.7: **Tomography of measurement-based GKP logical state preparation.a.)** Unit cell in characteristic function space for the square (left) and hexagonal (right) single-mode GKP code GKP code. **b.)** Measured characteristic functions for state-preparation of X logical states, Y logical states, and the logical $\pi/8$ state, given by $|\psi\rangle = \cos\left(\frac{\pi}{8}\right)|+X\rangle - \sin\left(\frac{\pi}{8}\right)|-X\rangle$. The $\pi/8$ state was prepared using a gate-teleportation protocol, see [26]. Top row: square code. Bottom row: hexagonal code.

After state preparation, decay of the Pauli expectation values are measured in two cases: during free evolution and with repeated QEC cycles applied via the sharpen-trim protocol. The results for the square GKP code are shown in Figure 5.6b. The lifetime of the error-corrected GKP Pauli expectation values is longer than the unstabilized counterparts by about a factor of two. As shown by the characteristic function unit cells in fig. 5.7a, the square code has a natural noise bias: Because the displacement corresponding to the Y logical stabilizer is $\sqrt{2}$ times larger in phase-space than the X and Z stabilizers (see section 1.2.2), the code distance along the Y direction is reduced, leading to a reduction in the lifetime of Y eigenstates.

To realize a logical qubit with a depolarizing error channel, a similar 6-round sharpen-trim protocol was used to stabilize the hexagonal GKP code, with details given in Ref. [26] and results shown in the inset of Figure 5.6b. As expected, for the hexagonal code, the lifetimes of X, Y and Z are equal, due to the equal lengths of each displacement stabilizer (and hence equal code distance) as shown by the unit cell in fig. 5.7a. Finally, arbitrary rotations within the code manifold can be performed by a measurement-based gate teleportation protocol [26, 66]. With details given in Ref. [26], the gate-teleportation protocol is similar to the logical measurement protocol, except the transmon is prepared in an arbitrary state on the $x - y$ plane of the Bloch sphere to perform a logical rotation within the manifold. This procedure was used to prepare Hadamard eigenstates in both the square and hexagonal codes, as shown in Figure 5.6d.

Although we realized stabilized GKP states with lifetimes longer than their unstabilized counterparts in [26], the experiment did not realize error correction beyond *break-even*. In particular, for a quantum channel $\mathcal{E} : \rho \rightarrow \mathcal{E}(\rho)$, we can define the average channel fidelity relative to a target unitary channel $U : \rho \rightarrow U\rho U^\dagger$ given by $\bar{\mathcal{F}} = \int d\psi \, \langle\psi| \, U^\dagger \mathcal{E} \left(|\psi\rangle \langle\psi|\right) U \, |\psi\rangle$ where the integral is over the uniform measure in state space. Using the Pauli transfer matrix approach, the experimental decay of Pauli expectation values can be used to compute the channel fidelity to the target identity channel $U = \mathcal{I}$ [228]. At small times δt, this fidelity can be expanded as $\bar{\mathcal{F}}\left(\delta t\right) = 1 - \frac{1}{2}\Gamma\delta t$, allowing the short-time decay rate of different qubits and channels (which generally have non-exponential decay curves) to be compared through a single decay rate, Γ [27]. With this, the *quantum error correction gain* is defined as

$$G = \frac{\Gamma_{\text{physical}}}{\Gamma_{\text{logical}}} \tag{5.30}$$

where Γ_{physical} is the fidelity decay constant of the best physical qubit in an experiment and Γ_{logical} is the decay constant of the error-corrected logical qubit. $G = 1$ corresponds to the break-even point. To the best of our knowledge, only three experiments to date have achieved beyond break-even QEC ($G > 1$) of a quantum memory given this metric, all using bosonic codes [27, 58, 229]. We note that this definition is in the context of a *quantum memory* experiment, where a long-lived stabilized manifold is the target application, i.e. the identity is the target unitary $U = \mathcal{I}$. A more careful definition involving SPAM (state preparation and measurement) errors as well as logical gate errors will be needed in future works to compare error-corrected logical qubits for use in quantum computation.

Using these definitions, for the 2020 GKP error correction experiment [26], the average channel lifetimes of the stabilized logical qubits were $\Gamma^{-1}_{\text{square, 2020}} = 222\,\mu\text{s}$ for the square encoding and $\Gamma^{-1}_{\text{hex, 2020}} = 205\,\mu\text{s}$ for the hexagonal. This should be compared to the the best physical qubit in the system, the $\{\left|0\right\rangle, \left|1\right\rangle\}$ Fock encoding of the high quality-factor microwave cavity, with decay constant $\Gamma^{-1}_{\text{Fock, 2020}} = 368\,\mu\text{s}$ (for the cavity, $T_1 = 245\,\mu\text{s}$, and we are assuming here that $T_2 = 2T_1$, as the measured cavity intrinsic dephasing rate was negligible). From this, the realized QEC gain was $G_{\text{square, 2020}} = 0.6$ and $G_{\text{hex, 2020}} = 0.56$. As confirmed by master equation simulations, a limiting factor in realizing a larger gain was bit flips of the auxiliary transmon during the large conditional displacements. Since bit flips do not commute with the interaction Hamiltonian eq. (3.22), they can lead to large displacement errors of the GKP state, causing logical errors. The stabilization rounds were spaced optimally in time so the contribution from auxiliary qubit errors was on par with the contribution from cavity errors.

5.4 Optimizing QEC to realize an error corrected quantum memory beyond break-even

In a more recent 2023 experiment [27], we made advancements to reach quantum error correction beyond break-even. In this section, I will briefly review our results of this experiment; a more detailed overview can be found in the PhD dissertation of Volodymyr Sivak [44].

The incorporation of three main innovations led to this improvement in gain compared to the 2020 experiment. First, by using recently development fabrication techniques for realizing a 3D transmon with tantalum pads [230], a relatively long-lived auxiliary transmon was used with an average lifetime of $T_1 = 280\,\mu\mathrm{s}$, close to a six-time improvement over the auxiliary transmon used in 2020 [26]. Secondly, the measurement-based sharpen trim protocol used in 2020 was replaced with a *semi-autonomous* version of the small-Big-small (sBs) protocol, as introduced in section 5.2.3 and shown in fig. 5.5. Here, we call the protocol semi-autonomous since the final oscillator displacement in each sBs round is performed with a conditional displacement, however the auxiliary qubit and oscillator phase was still reset between QEC rounds using measurement and feedback (now incorporating reset of the $|f\rangle$ transmon state). The reset could be replaced with an autonomous transmon reset to make the protocol fully autonomous. The third major advancement was incorporating online optimization of the QEC protocol using model-free reinforcement learning [99]. This sBs protocol was used as an ansatz for the QEC cycle, and a proximal policy optimization (PPO) reinforcement learning algorithm was used to train 45 real-valued parameters of the QEC cycle *in-situ* to optimize the lifetime. Such training was essential to realizing the large QEC gain.

Together, these improvements led to the square GKP code logical decay curves shown in Figure 5.8a, with logical lifetimes of $T_{X,\,2023} = T_{Z,\,2023} = 2.20\,\mathrm{ms}$ and $T_{Y,\,2023} = 1.36\,\mathrm{ms}$

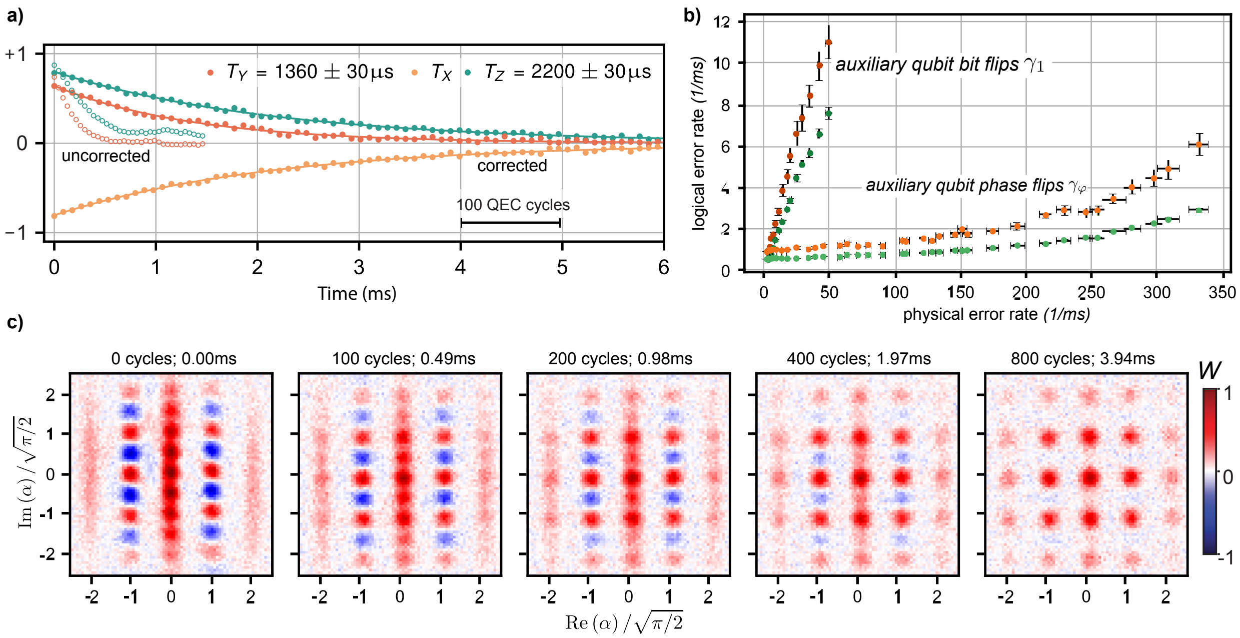

Figure 5.8: **Demonstrating an error corrected quantum memory beyond break-even.** Figures reproduced from [27]. **a)** Lifetimes of the uncorrected (open circles) and corrected (filled circles) square GKP code. **b)** Measured logical error rate sensitivity to increasing auxiliary qubit bit-flip or phase-flip rate. **c)** Measured Wigner functions of an error corrected $|+Z\rangle$ logical state, taken as snapshots after varying number of rounds.

with decay time constant of the average channel fidelity of $1/\Gamma_{\text{square, 2023}} = 1.82\,\text{ms}$. In contrast with the 2020 experiment, here the GKP states were prepared using ECD control [25] following the methods outlined in section 4.5. Given the Fock encoding $\{|0\rangle, |1\rangle\}$ lifetime of $\Gamma_{\{|0\rangle,|1\rangle\},2023} = 0.8\,\text{ms}$, the achieved QEC gain was $G_{\text{square, 2023}} = \Gamma_{\{|0\rangle,|1\rangle\},2023}/\Gamma_{\text{square, 2023}} = 2.27 \pm 0.07$, well beyond break-even. Snapshots of the Wigner functions at different points in the logical decay curve with QEC starting from $|+Z\rangle$ is shown in Figure 5.8c, indicating the decay of the logical information encoded in the interference fringes. Finally, we note that the logical Pauli measurements used in Refs. [27] and [26] were the infinite-energy versions, which lowers the contrast of the decay curves. In future applications, these measurements could be replaced with measurements of the finite-energy Pauli operators, as discussed in [64, 224], to increase the contrast.

In [99] we also experimentally studied the stabilized GKP qubit's sensitivity to auxiliary qubit noise. For this, they injected noise to selectively increase the auxiliary qubit's bit-flip rate γ_1 or phase-flip rate γ_φ. The results of this experiment are shown in Figure 5.8b. Fitting these slopes in the low physical error rate regime, the authors found that the QEC logical error rate is 65-times more sensitive to auxiliary qubit bit flips than auxiliary phase flip.

To better understand the error correction protocol, we analyzed the Kraus maps for the small-Big-small protocol, with more detail to be found in Volodymyr Sivak's thesis [99]. In particular, the sBs protocol repeatedly implements a composite channel $\mathcal{R}_\Delta(\rho) = \left(\mathcal{R}^Z_\Delta \circ \mathcal{R}^X_\Delta\right)(\rho)$ where ρ is the oscillator's density matrix and $\left\{\mathcal{R}^X_\Delta, \mathcal{R}^Z_\Delta\right\}$ are the rank-2 channels associated with sBs rounds in the position and momentum directions. These channels can be written as Kraus maps, $\mathcal{R}^X_\Delta(\rho) = \sum_{i=\{g,e\}} K^{X\dagger}_i \rho K^X_i$ where $\sum_i K^{X\dagger}_i K^X_i = \mathcal{I}$ and a similar definition for Z. Here, $K^X_{\{g,e\}}$ are the Kraus operators corresponding to measuring the auxiliary qubit in $\{\left|g\right\rangle, \left|e\right\rangle\}$, explicitly given by

$$K^X_g = \left\langle g\right| U^X_{sBs} \left|g\right\rangle \tag{5.31}$$

$$K^X_e = \left\langle e\right| U^X_{sBs} \left|g\right\rangle, \tag{5.32}$$

where U^X_{sBs} is the unitary corresponding to an X- sBs round.

To understand these Kraus maps, the authors of Ref. [27] analyzed the four Kraus operators for the composite channel $\mathcal{R}_\Delta$ given by $K_{gg} = K^Z_g K^X_g$, $K_{ge} = K^Z_g K^X_e$, $K_{ef} = K^Z_e K^X_g$, and $K_{ee} = K^Z_e K^X_e$ corresponding to the two auxiliary qubit measurement outcomes of each full QEC cycle consisting of X and Z QEC rounds. For $\Delta = 0.34$, these Kraus operators are plotted as matrices in the truncated eigenbasis of $K^\dagger_{gg} K_{gg}$ in Figure 5.9. The eigenbasis splits into pairs of states $\mathcal{C}_i$ that define the various error spaces and are each orthogonal to the code space $\mathcal{C}_0$. These matrices shed a new light onto the sBs protocol by revealing a *trickle-down* approach to error correction: measuring $\left|e\right\rangle$ in either the X or Y sBs round signals that an error has been corrected, and the corresponding Kraus matrix applied shifts the state down to the next lower error space. Similar code and error spaces can be defined as the quasi-degenerate pairs of eigenstates of the confined GKP Hamiltonian discussed in

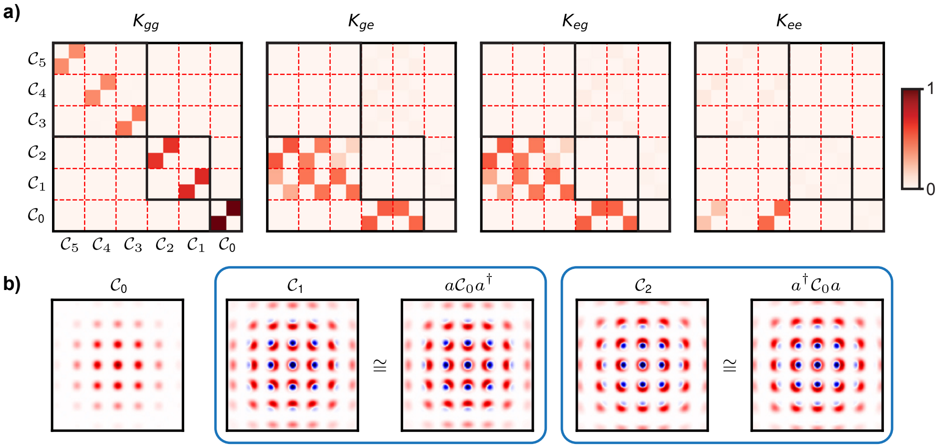

Figure 5.9: **Kraus map of the two-round sBs protocol.** Figures reproduced from [27]. **a)** Kraus operators for the composite QEC channel, plotted in the basis for which $K_{gg}^\dagger K_{gg}$ is diagonal (absolute values of matrix entries is shown). The code and error spaces are labeled, each consisting of two states forming a logical Bloch sphere. **b)** Wigner functions of projectors onto the code and error spaces, along with comparisons to a single photon loss or gain error applied to $\mathcal{C}_0$.

appendix G.

The authors of Ref. [27] also plotted these spaces explicitly, as reproduced in Figure 5.9b, displaying the Wigner functions of the projectors Π_0, Π_1, and Π_2 onto the codespace and first two error spaces. As shown in the figure, the first two error spaces are well approximated by $\Pi_1 \approx a\Pi_0 a^\dagger$ and $\Pi_2 \approx a^\dagger \Pi_0 a$, indicating that the hierarchy closely resembles photon loss a and photon gain $a^\dagger$ type errors. The higher error spaces can also be studied this way, with more details in Ref. [27]. The Kraus operators can also be written in the position or momentum basis, as done in Ref. [26] for the case of the sharpen-trim protocol.

Besides the approaches to mitigate auxiliary qubit noise discussed in section 6.1, using the error corrected GKP qubits for quantum computation and other applications will require high-fidelity single-qubit and multi-qubit gates. For realistic GKP qubits, the gates must be engineered to suppress leakage out of the finite energy manifold. For Clifford gates, one simple approach is to apply the infinite-energy version of the gate (a Gaussian unitary) followed by many cycles of finite-energy QEC to project the states back onto the finite-energy manifold. An alternative is to engineer gates that directly respect the finite-energy condition, with one approach proposed in [231]. In superconducting circuits, purpose-built couplers must be used to achieve these Gaussian operations without introducing spurious nonlinearities, as discussed in section 6.1. Some promising approaches include using Kerr-free parametric three-wave mixing with a SNAIL (Superconducting Nonlinear Asymmetric Inductive eLement) mixer [109, 232, 233] or other couplers that could be engineered in a Kerr-free regime [234–236].

Chapter 6

Outlook and conclusion

6.1 Outlook

Below, I give a list of some near-term research directions that I believe would be beneficial for scaling up the GKP code and demonstrating useful applications.

Finite-energy readout

The observant reader will notice that the measured decay of the logical Pauli operators, shown in fig. 5.6 and fig. 5.8, have a low contrast; the initial measured $\langle Z \rangle$ point is around 0.8 for these experiments. Although part of this contrast reduction is due to auxiliary qubit errors during the measurement circuit, and part is due to the finite-fidelity state preparation, a large portion comes from our use of an infinite-energy measurement circuit (phase estimation shown in fig. 3.7) on the finite-energy code.

In [64, 224], a circuit for realizing readout of the finite-energy GKP logical operators was introduced. This circuit is similar to the sBs circuit, and could be easily implemented in our hardware. Once implemented, the finite-energy logicals can be used in the cost function for model-free optimization.

A better conditional displacement

As discussed in section 3.2.1 and section 4.6.4, large displacements amplify dephasing noise, causing effective diffusion-like noise at rate $\kappa_\phi |\alpha|^2$, where $|\alpha|$ is the size of the displacement.

This type of noise, however, can be avoided. In particular, an alternative style of conditional displacement for readout was shown in [132]. In this protocol, the qubit is driven at the oscillator frequency to resonantly activate an $ab^\dagger b + \text{h.c.}$ interaction term, where a is the oscillator annihilation operator and b is the transmon annihilation operator. However, if only this drive is applied, the cavity would displace due to leakage of the drive to the cavity field. This effect can be avoided by employing a cancellation drive on the cavity pin, to cancel the net displacement of the oscillator while maintaining the conditional displacement term. The same idea has been employed to realizing qubit 'cloaking', where the conditional drive was instead tuned to cancel the conditional displacement [237].

However, the technique in [132] was developed for readout, and needs modification if it is employed for realizing conditional displacements of a high-quality-factor oscillator. In particular, the always-on dispersive interaction $\chi a^\dagger a b^\dagger b$, must still be echoed out, similar to the ECD gate. This can be achieved, however, by using drives inspired by the ECD gate: by driving the transmon at the oscillator frequency for a time T with amplitude ξ, applying an echo π pulse, then driving the transmon with amplitude $-\xi$ for a time T, the dispersive interaction and Stark-shift can be echoed out while realizing a conditional displacement. While driving the transmon, a cancellation drive can be applied to the oscillator (also flipping its phase after a time T) in order to avoid displacement of the mean-field. The gate should still allow faster-than-χ interactions, with an interaction speed limit scaling as $\propto \sqrt{\chi E_C}$.

Surprisingly, the protocol I propose here is very similar to the echoed-cross-resonance gate commonly employed by IBM to realize qubit-qubit interactions [238]. In this sense, the 'ECD with cancellation' proposed above is equivalent to an echoed-cross-resonance gate between a qubit and an oscillator. Note that other effects, such as nonlinear resonances and the Stark-shifting of the transmon into two-level systems (discussed in chapter 3) will, unfortunately, likely remain when using the ECD with cancellation gate. For this reason, the main purpose of the gate is to avoid amplified dephasing noise of the oscillator.

Flagging transmon errors

An alternative conditional displacement (that could be combined with the ideas of the previous paragraphs) is to displace the oscillator conditioned on the $|g\rangle, |f\rangle$ levels of the transmon. Such a gate could be performed by driving the usual ECD gate on resonance with the oscillator $|e\rangle$ frequency. With this, similar to the gates developed in [239,240], decay from the $|f\rangle$ state can be flagged by the $|e\rangle$ state. However, this will need to be analyzed in more detail to see if it is beneficial in a more broad context, such as in a GKP surface code, similar to the recent work that has been done for the dual-rail surface code [240].

Squeezing for control of noise bias

The GKP code has a nice property: inherent 'compatibility with squeezing'. Using the squeezing transformation described in section 2.4.4, the quadratures can be transformed according to

$$S^\dagger(r)\hat{q}S(r) = qe^{-r} \tag{6.1}$$

$$S^\dagger(r)\hat{p}S(r) = qe^{r}, \tag{6.2}$$

allowing the code distance along one axis of the Bloch sphere to increase, at the expense of decreasing the distance along the orthogonal axis, in a reversible way. This should be contrasted with (single-mode) rotationally symmetric bosonic codes [23], which do not have this property, given that phase-preserving amplification cannot be performed without adding noise [241,242]. Applying squeezing to the GKP code has many possible uses. For example, the squeezed GKP codes have been considered for concatenation using repetition codes and XZZX surface codes [243,244]. Squeezing can also be used as a way to realize a noise-biased

GKP ancilla to stabilize a target GKP qubit, as proposed in [245].

However, there are a few applications of squeezing that I believe have not yet been explored fully. Namely, if such squeezing is done with a Kerr-free mixer (such as a SNAIL (Superconducting Nonlinear Asymmetric eLement) or JRM (Josephson Ring Modulator) [99, 109, 236]), it can occur while the auxiliary qubit(s) are in the ground state, and hence be resistant to qubit errors. With this in mind, squeezing can be combined with GKP logical gates and stabilization protocols in order to better avoid the propagation of auxiliary qubit errors. For example, by squeezing before and de-squeezing after each QEC round (sharpen trim or sBs), the conditional displacements needed to map the stabilizer to the auxiliary qubit can be made much faster through Hamiltonian amplification. Although the 'small' conditional displacements will be slower, they will not cause uncorrectable errors. In this way, a periodic code deformation can be performed to the GKP code during stabilization to achieve a higher QEC gain.

Such periodic squeezing can also be applied in Floquet-engineering protocols that are proposed in [39, 40, 227]. In these protocols, a high-impedance superconducting circuit is needed with impedance greater than twice the superconducting resistance quantum; this is the main limitation to their realization. However, if parametric squeezing is employed before and after each stabilization round, it could effectively 'shorten' phase-space, and lower the impedance requirements by a significant enough margin to make these circuits feasible. With this, I think the main application of squeezing is to lower the impedance requirements of Floquet-engineered GKP codes.

Finally, squeezing can be combined with GKP gates in interesting ways. For example, the realization of finite-energy gates (discussed below in section 6.1) will likely require the use of an auxiliary qubit, and be sensitive to these errors. However, if the modes interacting were squeezed and de-squeezed before each interaction, the gates could be done more quickly as a result of Hamiltonian amplification. This should be seen as a general application of the fact that a GKP lattice (such as a square lattice) can be continuously deformed into another lattice (such as a hexagonal lattice) using Gaussian operations. It will be interesting to see how this can be optimized for various tasks moving forward.

GKP qudit codes and qudit surface codes

The techniques developed in this thesis can easily be extended to realize a qudit encoded in an oscillator. A $d-$ dimensional qudit has an algebra that follows the 'clock-shift' operators,

$$X\left|j\right\rangle = \left|j+1\,(\mathrm{mod}\;d)\right\rangle, \tag{6.3}$$

$$Z\left|j\right\rangle = \omega^{j}\left|j\right\rangle \tag{6.4}$$

$$ZX = \omega XZ = \omega Y. \tag{6.5}$$

As introduced in [1], this can be realized as a grid code in phase space (of a single oscillator) by stabilizer translations that enclose an area of $2\pi n$ in phase-space, for example,

$$S_q = e^{i\sqrt{d2\pi}q} = T(i\sqrt{d2\pi}) \tag{6.6}$$

$$S_p = e^{-i\sqrt{d2\pi}p} = T(\sqrt{d2\pi}) \tag{6.7}$$

$$Z = (S_q)^{1/d} = e^{i\sqrt{2\pi/d}q} = T(i\sqrt{2\pi/d}) \tag{6.8}$$

$$X = (S_p)^{1/d} = e^{-i\sqrt{2\pi/d}p} = T(i\sqrt{2\pi/d}). \tag{6.9}$$

It should first be noted that the qudit codes have a decreased code distance; shifts in q of $|\Delta q| < \sqrt{\pi/2d}$ and shifts in p of $|\Delta p| < \sqrt{\pi/2d}$ are correctable. As expected, there is diminishing returns when encoding a d level state space in the oscillator. However, such codes could be used for many interesting applications, such as error-detection within a single oscillator used in an erasure surface code [246].

One of the most promising applications of oscillator qudits encoded as GKP codes is using them to construct a qudit-surface code [247–251] and other realizations of lattice gauge theories that are not easily implemented with a lattice of qubits.

A better ancilla

As shown in [26, 99] and discussed in chapter 5, the GKP error correction protocols are limited by errors of the auxiliary qubit, and the protocol is much more sensitive to auxiliary bit-flips than phase-flips. As suggested in [252] (and a similar idea in [253]), a biased-noise qubit could instead be used as an ancilla. Good potential candidates for this are the Kerr-cat bosonic qubit [114, 254], the heavy-fluxonium qubit [255], a biased-GKP / squeezed cat qubit [245], or other pumped approaches.

Envelope-preserving non-Clifford gate

In [216], it was shown that a non-Clifford $\sqrt{\text{Had}}$ (square-root-Hadamard) gate on the GKP code can be realized with a Kerr interaction. For the single-mode square GKP code,

$$\sqrt{\text{Had}} = \exp\left(i\frac{\pi}{8}\left(a^\dagger a\right)^2\right), \tag{6.10}$$

This gate is similar to the 'Kerr-refocusing' gate for cat codes first demonstrated in [256]; interestingly the GKP code also refocuses under Kerr to realize a non-Clifford gate.

Because $[\sqrt{\text{Had}}, E_\Delta] = 0$, the envelope is preserved under the action of the gate, and no finite-energy modification is required[1]. For this reason, the gate is an interesting resource to explore, however, a Kerr interaction with fast control and a large ON/OFF ratio will be needed. This could potentially be implemented by fast flux-tuning a nonlinear mode near-resonance with the GKP oscillator.

Finite-energy gates

The logical gates derived in [1] for the infinite-energy GKP code must be modified for the finite-energy GKP code. This can be done using the envelope operator as discussed in section 5.1.2. For example, a modification of the CNOT gate to its finite-energy version was

---

[1] This is the case for all gates that commute with the number operator.

discussed in [231]. The finite-energy gates modified this way are non-Hermitian, requiring an auxiliary mode (such as a qubit) for their realization. However, there may be unitary alternatives.

Hamiltonian engineering

The Hamiltonian approach to GKP is discussed in appendix G. The Hamiltonian approach has not yet been fully analyzed. In particular, GKP codes can be described in terms of a gapped spectrum, and by using the Zak basis techniques (see appendix F), this spectrum and the energy splittings can be well understood. Other lattices in phase space can be realized, such as Moiré lattices similar to the magic-angle ideas used in bi-layer graphene, to construct Hamiltonians with non-trivial gapped spectrums[2]. Such Hamiltonians could be be realized though Floquet engineering, similar to the Kerr-cat.

In addition, it will be interesting to construct gates for finite-energy GKP codes using a Hamiltonian approach. For example, by modifying the impedance of the GKP Hamiltonian adiabatically with respect to the gap, finite-energy gates can be performed. These ideas could be extended to multiple modes for two-qubit gates.

Quantum sensing and communication

In 2017, Duivenvoorden *et al.* showed the sensing capabilities of the single-mode GKP code [191]. By measuring both modular position and modular momentum, small displacements can be sensed without prior knowledge of the phase (in contrast to a squeezed-state sensor, where the squeezing must align with the signal to be measured). The finite-energy error correction we performed can also be seen as a realization of these ideas. By combining error correction with sensing, the record of measurements could be used to reconstruct a signal.

The GKP code will also be useful in quantum communication. For example, error-

---

[2] The sharpen-trim protocol (and sBs protocol) can be seen as a stabilization of two lattices that don't quite commute, giving rise to a gapped Hamiltonian spectrum.

correctable quantum repeaters can be used in a quantum network along with GKP codes to correct for loss along a communication channel [257]. More ideas are discussed in-depth in [22].

Concatenated GKP codes

Finally, more research is needed to investigate the technical aspects of a hybrid concatenated code architecture in superconducting circuits. For example, linear oscillators with GKP states can be employed as the data qubits, while the measure qubits can be of a different variety, perhaps transmons or Kerr-cats. More analysis is needed to investigate noise propagation and thresholds for these hybrid architectures, as they are a promising path forward in the near term. This was suggested in Ref. [42], however to the best of my knowledge, a full analysis of noise in such a hybrid concatenated code architecture has not yet been published.

Additionally, it was shown in Ref. [27] that post-selection on outcome strings in sBs type error correction significantly increased the lifetime of the stabilized quantum memory, at the cost of a lower success probability. We anticipate that some classical post-processing on these output strings of sBs could yield better lifetimes even without post-selection. Furthermore, it would be intriguing to explore whether these measurement strings could be effectively employed for erasure conversions of GKP data qubit errors when combined with DV(discrete-variable) codes (e.g., surface codes), which then could be used to leverage the improved threshold with erasure noise. This feature has already been put to use for resource reduction of fault-tolerant quantum computing with surface code architectures realized in neutral atoms, trapped ions and superconducting circuits (via transmon and dual-rail codes) [240, 258–262].

6.2 Conclusion

In this dissertation, I have comprehensively introduced theoretical and experimental advances carried out as part of my PhD work in bosonic quantum control and quantum error correction using GKP codes, with a focus on the weak-coupling architecture. With the development of quantum engineering in such microwave cQED systems, multimode GKP qubit codes and GKP oscillators-to-oscillators codes provide many opportunities in quantum information processing such quantum computing, communication, and sensing. Yet many research directions have yet to be fully explored and open problems remain, as outlined in the previous section.

Bosonic QEC opens up a wide array of application spaces beyond the goal of fault-tolerant quantum computing, with quantum communication and sensing being prominent examples. Additionally, universal unitary engineering using near-linear oscillators with the phase-space ISA holds the potential to open up opportunities in quantum simulation, offering a pathway to tackle fundamental problems crucial to condensed matter and high-energy physics.

In order to fully leverage the capabilities of bosonic QEC with GKP codes, it is essential to address the open problems outlined earlier and actively search for new challenges to overcome. As research continues in this rapidly evolving field, I anticipate unforeseen breakthroughs that will not only enhance our understanding of quantum error correction but also lead to the practical realization of quantum information processing applications.

Appendices

Appendix A

Quantum harmonic oscillators: selected topics

A.1 The displacement and translation operators

The displacement operator is defined as

$$D(\alpha) = \exp\left(\alpha a^\dagger - \alpha^* a\right) = \exp\left(\sqrt{2}\left(-i\mathrm{Re}(\alpha)\hat{p} + i\mathrm{Im}(\alpha)\hat{q}\right)\right) \tag{A.1}$$

$$= \exp\left(-i\sqrt{2}|\beta|\hat{q}_\perp\right) \tag{A.2}$$

where $\alpha \in \mathbb{C}$. In the last relation we have defined the perpendicular quadrature $q_\perp = \cos(\Theta)\hat{p} - \sin(\Theta)\hat{q}$ with $\Theta = \mathrm{angle}\,(\beta)$. The displacement operator $D\left(\alpha = \mathrm{Re}\,(\alpha) + i\mathrm{Im}\,(\alpha)\right)$ can be thought of as 'moving a state around' in optical phase-space (Wigner units) by $\mathrm{Re}\,(\alpha)$ along the $\langle a + a^\dagger\rangle/2$ axis (parallel to position) and an amount $\mathrm{Im}\,(\alpha)$ along the $-i\langle a - a^\dagger\rangle/2$ axis (parallel to momentum) as shown in fig. A.1. In other words, for any state ρ with mean value $\mathrm{Tr}\,(\rho a) = \alpha_0$, the displacement operator will transform the mean value of a to $\mathrm{Tr}\left(D(\alpha)\rho D^\dagger(\alpha)a\right) = \alpha_0 + \alpha$, without changing any higher-order central-moments of a (such as the variance)! Besides the action of moving a state's phase-space distribution around, the

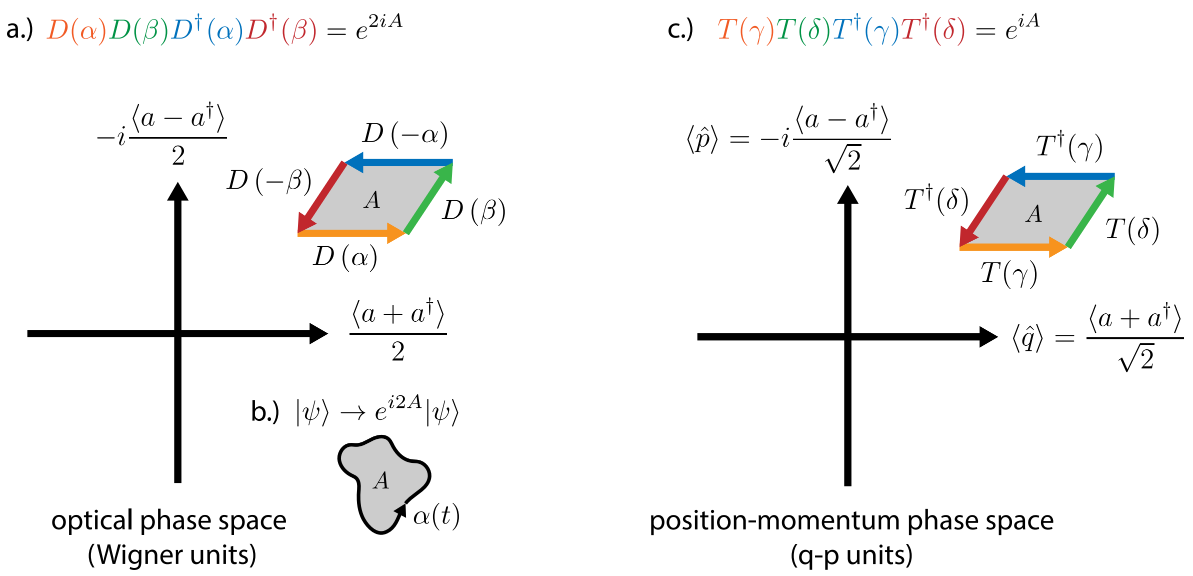

Figure A.1: **Geometric phase from a displacement trajectory.** a.) The group commutation relation for displacements. b.) A trajectory in phase space will cause any oscillator state $|\psi\rangle$ to pick up a geometric phase.

displacement is also associated with a geometric phase, as discussed later in this section.

Displacement operators are orthogonal,

$$\mathrm{Tr}\left(D(\alpha)D^\dagger(\beta)\right) = \pi\delta^{(2)}(\alpha - \beta), \tag{A.3}$$

and using the Baker-Campbell-Hausdorff (BCH) relation can be written using normal and anti-normal order as

$$D(\alpha) = e^{-\frac{|\alpha|^2}{2}} e^{\alpha a^\dagger} e^{-\alpha^* a} = e^{\frac{|\alpha|^2}{2}} e^{-\alpha^* a} e^{\alpha a^\dagger}, \tag{A.4}$$

or, in terms of position and momentum,

$$D(\alpha) = e^{i\mathrm{Re}(\alpha)\mathrm{Im}(\alpha)} e^{-i\sqrt{2}\mathrm{Re}(\alpha)\hat{p}} e^{i\sqrt{2}\mathrm{Im}(\alpha)\hat{q}} = e^{-i\mathrm{Re}(\alpha)\mathrm{Im}(\alpha)} e^{i\sqrt{2}\mathrm{Im}(\alpha)\hat{q}} e^{-i\sqrt{2}\mathrm{Re}(\alpha)\hat{p}}. \tag{A.5}$$

An important use case of eq. (A.4) is calculating the derivative of the displacement operator with respect to α and α^*,[1]

$$\partial_\alpha D(\alpha) = \left(a^\dagger - \frac{\alpha^*}{2}\right) D(\alpha) = D(\alpha)\left(a^\dagger + \frac{\alpha^*}{2}\right), \tag{A.6}$$

$$\partial_{\alpha^*} D(\alpha) = \left(-a + \frac{\alpha}{2}\right) D(\alpha) = D(\alpha)\left(-a - \frac{\alpha}{2}\right), \tag{A.7}$$

$$\partial_\alpha D^\dagger(\alpha) = \left(-a^\dagger - \frac{\alpha^*}{2}\right) D^\dagger(\alpha) = D^\dagger(\alpha)\left(-a^\dagger + \frac{\alpha^*}{2}\right), \tag{A.8}$$

$$\partial_{\alpha^*} D^\dagger(\alpha) = \left(a + \frac{\alpha}{2}\right) D^\dagger(\alpha) = D^\dagger(\alpha)\left(a - \frac{\alpha}{2}\right). \tag{A.9}$$

These will be used for calculating the time-dependent displaced frame transformation in section C.2.1. They also imply

$$D^\dagger(\alpha) a D(\alpha) = a + \alpha, \tag{A.10}$$

$$D^\dagger(\alpha) a^\dagger D(\alpha) = a^\dagger + \alpha^*. \tag{A.11}$$

As can be shown with the BCH relation, displacement operators satisfy the group commutation and composition relations

$$D(\alpha)D(\beta) = e^{(\alpha\beta^* - \alpha^*\beta)} D(\beta)D(\alpha) = e^{i2A} D(\beta)D(\alpha), \tag{A.12}$$

$$D(\alpha)D(\beta) = e^{(\alpha\beta^* - \alpha^*\beta)/2} D(\alpha+\beta) = e^{iA} D(\alpha+\beta), \tag{A.13}$$

where $A = -i(\alpha^*\beta - \beta^*\alpha)/2 = \mathrm{Im}\,(\alpha^*\beta)$ is the signed area of the parallelogram enclosed by the vectors α and β in optical phase-space (with counter-clockwise transversal being a positive area). This is the geometric (Berry) phase factor associated with linear displacements as shown in fig. A.1a. As derived in section C.2.1, a geometric phase can also arise from a general smooth trajectory through phase space $\alpha(t)$, as shown in fig. A.1b.

The factor of 2 in eq. (A.12) can be annoying to work with. It is for this reason that we often work with a scaled version of the displacement operator, called the *translation operator*,

---

[1] Here, derivative with respect to a complex number is using the notation of *Wirtinger derivatives.*

which moves a state around in position-momentum space (with axes $\langle\hat{q}\rangle = \langle a + a^\dagger\rangle/\sqrt{2}$ and $\langle\hat{p}\rangle = -i\langle a - a^\dagger\rangle/\sqrt{2}$) space, defined as

$$T(\alpha) = D\left(\frac{\alpha}{\sqrt{2}}\right) = \exp\left(\frac{1}{\sqrt{2}}\left(\alpha a^\dagger - \alpha^* a\right)\right) = \exp\left(-i\mathrm{Re}(\alpha)\hat{p} + i\mathrm{Im}(\alpha)\hat{q}\right) \tag{A.14}$$

$$= \exp\left(-i|\alpha|\hat{q}_\perp\right), \tag{A.15}$$

along with group commutation and composition rules

$$T(\gamma)T(\delta) = e^{(\gamma\delta^* - \gamma^*\delta)/2}T(\delta)T(\gamma) = e^{iA}T(\delta)T(\gamma), \tag{A.16}$$

$$T(\gamma)T(\delta) = e^{(\gamma\delta^* - \gamma^*\delta)/4}D(\gamma+\delta) = e^{iA/2}T(\gamma+\delta), \tag{A.17}$$

where A is the signed area in position-momentum phase space as shown in fig. A.1c. They also have a modified orthogonality relation,

$$\mathrm{Tr}\left(T(\gamma)T^\dagger(\delta)\right) = 2\pi\delta^{(2)}\left(\gamma - \delta\right), \tag{A.18}$$

which will modify the unit element of area in complex phase space from $d^2\alpha/\pi$ for displacement operators to $d^2\beta/2\pi$ for translation operators in all integrals over operator space. I use translation operators when discussing GKP states in section 1.2.2. All relations and equations using displacement operators can be cast into translation operators with the appropriate rescaling.

Finally, I note that the matrix elements of the displacement operator in the Fock (number) basis can be written as

$$\langle m|D(\alpha)|n\rangle = e^{\frac{-|\alpha|^2}{2}}\left(\frac{n!}{m!}\right)^{1/2}\alpha^{m-n}L_n^{(m-n)}\left(|\alpha|^2\right), \tag{A.19}$$

where $L_q^{(p)}(x)$ is an associated Laguerre polynomial [263]. This form can be useful for simulations.

A.2 Coherent states

Coherent states are defined using the displacement operator,

$$|\alpha\rangle = D(\alpha)\,|0\rangle \tag{A.20}$$

where $|0\rangle$ is the vacuum (zero-photon) state with $a\,|0\rangle = 0$. Coherent states are eigenstates of the annihilation operator,

$$a\,|\alpha\rangle = \alpha\,|\alpha\rangle \tag{A.21}$$

with overlap

$$\langle\beta|\alpha\rangle = \exp\left(-\frac{|\alpha|^2}{2} - \frac{|\beta|^2}{2} + \beta^*\alpha\right) \tag{A.22}$$

and Fock state representation

$$|\alpha\rangle = e^{-\frac{|\alpha|^2}{2}} \sum_{n=0}^{\infty} \frac{\alpha^n}{\sqrt{n!}}\,|n\rangle \tag{A.23}$$

leading to a Poissonian Fock-state probability distribution $P(n) = e^{\langle n\rangle}\left(\frac{\langle n\rangle^n}{n!}\right)$ with average photon number $\langle n\rangle = |\alpha|^2$ and variance $|\alpha|^2$.[2]

From eq. (A.12), the action of a displacement operator on a coherent state includes an important geometric phase,

$$D(\beta)\,|\alpha\rangle = e^{(\alpha\beta^* - \alpha^*\beta)/2}\,|\alpha + \beta\rangle\,. \tag{A.24}$$

From eq. (A.22), the coherent state basis is overcomplete. The resolution of the identity is given by[3]

$$I = \frac{1}{\pi}\int d^2\alpha\;|\alpha\rangle\,\langle\alpha|\,. \tag{A.25}$$

---

[2] It is for this reason that Optical phase-space (Wigner units) is so useful: the radius squared in optical phase-space represents the average photon number of a coherent state at position α.

[3] integrals written without bounds are over all space

From this, states and operators (including the density matrix operator) can be represented in the coherent state basis as

$$|\psi\rangle = \frac{1}{\pi}\int d^2\alpha \ |\alpha\rangle \langle\alpha|\psi\rangle \tag{A.26}$$

$$\hat{O} = \frac{1}{\pi^2}\int d^2\alpha \, d^2\beta \ |\alpha\rangle \langle\beta| \langle\alpha|\hat{O}|\beta\rangle \tag{A.27}$$

The coherent state basis is related to the displacement operator basis (and characteristic function) and useful for calculating characteristic functions as discussed in the next section. It can also be helpful in some cases to calculate the trace of an operator in the coherent state basis, $\mathrm{Tr}\left(\hat{O}\right) = (\pi)^{-1}\int d^2\alpha \ \langle\alpha|\hat{O}|\alpha\rangle$.

A.3 Reciprocal Phase-Space: The displacement operator basis and the Characteristic Function

As shown in [263], the displacement operator basis forms a complete basis for operators, in the sense that and bounded operator $\hat{O}$ can be represented as

$$\hat{O} = \frac{1}{\pi}\int d^2\beta \, \mathcal{C}\left(\beta\right) D^{\dagger}(\beta), \tag{A.28}$$

where the function $\mathcal{C}\left(\beta\right) = \mathrm{Tr}\left(\hat{O}D(\beta)\right) \in \mathbb{C}$ is called the *characteristic function* of $\hat{O}$.[4] When needed, I will use the notation $\mathcal{C}^{[\hat{O}]}\left(\beta\right)$ to indicate the characteristic function is of the operator $\hat{O}$. For GKP states, it is often more convenient to use the translation operator, so I will denote the *characteristic function in translation units* as $\mathcal{C}_T(\beta) = \mathrm{Tr}\left(\hat{O}T(\beta)\right) = \mathcal{C}\left(\frac{\beta}{\sqrt{2}}\right)$

---

[4] In particular, these are the symmetric-ordered characteristic function, which I will use throughout this thesis. Other characteristic functions exist, and that is beyond the scope of this work.

with modified operator representation

$$\hat{O} = \frac{1}{2\pi} \int d^2\beta \, \mathcal{C}_T(\beta) \, T^\dagger(\beta). \tag{A.29}$$

Characteristic functions have a few nice properties that are easy to show. To start, if a bounded, operator-valued function only depends on position or momentum, then the characteristic function is the (one-dimensional) physicist's Fourier transform,

$$\hat{O} = f(\hat{q}) \leftrightarrow \mathcal{C}_T(\beta) = \int dq \, f(q) e^{i\mathrm{Im}(\beta) q}, \tag{A.30}$$

$$\hat{O} = f(\hat{p}) \leftrightarrow \mathcal{C}_T(\beta) = \int dp \, f(p) e^{-i\mathrm{Re}(\beta) p}. \tag{A.31}$$

Proof. Calculating the trace in the position basis, using the cyclic property of the trace, and using eq. (A.5),

$$\mathcal{C}_T(\beta) = \mathrm{Tr}\left(f(\hat{q}) T(\beta)\right) \tag{A.32}$$

$$= \int dq \, \langle q | T(\beta) f(\hat{q}) | q \rangle \tag{A.33}$$

$$= \int dq \, \langle q | e^{i\mathrm{Re}(\beta)\mathrm{Im}(\beta)/2} e^{-i\mathrm{Re}(\beta)\hat{p}} e^{i\mathrm{Im}(\beta)\hat{q}} f(\hat{q}) | q \rangle \tag{A.34}$$

$$= \int dq \, f(q) e^{i\mathrm{Im}(\beta) q} e^{i\mathrm{Re}(\beta)\mathrm{Im}(\beta)/2} \langle q | q + \mathrm{Re}(\beta) \rangle \tag{A.35}$$

$$= \delta^{(2)}\left(\mathrm{Re}(\beta)\right) \int dq \, f(q) e^{i\mathrm{Im}(\beta) q}. \tag{A.36}$$

A similar proof holds when $\hat{O} = f(\hat{p})$. □

This property is quite powerful. Since the trace is linear, we can use it to easily calculate characteristic functions of operators that are linear combinations of functions of $\hat{q}$ and $\hat{p}$. The following table includes some of these characteristic functions.

As shown in [264],the action of photon loss at rate $\kappa_\downarrow$ and photon gain at rate $\kappa_\uparrow$ after a

Name	definition	characteristic function equation
characteristic function	$\mathcal{C}\left(\beta\right)$	$\mathrm{Tr}\left(\hat{O}D(\beta)\right)$
bounded operator	$\hat{O}$	$\frac{1}{\pi}\int\, d^2\beta\,\mathcal{C}\left(\beta\right)D^{\dagger}(\beta)$
linear superposition	$\hat{O}=a\hat{A}+b\hat{B}$	$\mathcal{C}^{\left[\hat{O}\right]}\left(\beta\right)=a\mathcal{C}^{\left[\hat{A}\right]}\left(\beta\right)+b\mathcal{C}^{\left[\hat{B}\right]}\left(\beta\right)$
Frobenius norm	$\lVert\hat{O}\rVert_{\mathrm{F}}=\sqrt{\mathrm{Tr}\left(O^{\dagger}O\right)}$	$\left(\frac{1}{\pi}\int\, d^2\beta\,\lvert\mathcal{C}(\beta)\rvert^2\right)^{1/2}$
trace	$\mathrm{Tr}\,\hat{O}$	$\mathcal{C}\left(0\right)$
trace overlap	$\mathrm{Tr}\left(\hat{A}\hat{B}\right)$	$\frac{1}{\pi}\int\, d^2\beta\,\mathcal{C}^{[\hat{A}]}\left(\beta\right)\mathcal{C}^{[\hat{B}]}\left(-\beta\right)$
purity	$\mathrm{Tr}\left(\rho^2\right)$	$\frac{1}{\pi}\int\, d^2\beta\,\lvert\mathcal{C}\left(\beta\right)\rvert^2$
Fidelity (to pure state)	$\langle\psi\rvert\rho\lvert\psi\rangle$	$\frac{1}{\pi}\int\, d^2\beta\,\mathcal{C}^{[\hat{\rho}]}\left(\beta\right)\mathcal{C}^{[\lvert\psi\rangle\langle\psi\rvert]}\left(-\beta\right)$
position function	$\hat{O}=f(\hat{q})$	$\mathcal{C}\left(\beta\right)=\delta^{(2)}\left(\mathrm{Re}\left(\beta\right)\right)\int\, dq\, f(q)e^{i\sqrt{2}\mathrm{Im}(\beta)q}$
momentum function	$\hat{O}=f(\hat{p})$	$\mathcal{C}\left(\beta\right)=\delta^{(2)}\left(\mathrm{Im}\left(\beta\right)\right)\int\, dp\, f(p)e^{-i\sqrt{2}\mathrm{Re}(\beta)p}$
translated operator (or state)	$D(\alpha)\hat{O}D^{\dagger}(\alpha)$	$\mathcal{C}^{\left[D(\alpha)\hat{O}D^{\dagger}(\alpha)\right]}\left(\beta\right)=e^{\alpha^*\beta-\alpha\beta^*}\mathcal{C}^{\left[\hat{O}\right]}\left(\beta\right)$
hermitian conjugate	$\hat{O}^{\dagger}$	$\mathcal{C}^{\left[\hat{O}^{\dagger}\right]}\left(\beta\right)=\left(\mathcal{C}^{\left[\hat{O}\right]}\left(-\beta\right)\right)^*$

Table A.1: **Transformations and properties of characteristic functions**. Any equations using ρ are assuming ρ is a valid density matrix (positive semi-definite, Hermitian, and trace unity.)

Name	Definition	Characteristic function $C(\beta)$
identity	$\mathcal{I}$	$\pi\delta^{(2)}(\beta)$
vacuum	$\lvert 0\rangle\langle 0\rvert$	$e^{-\frac{\lvert\beta\rvert^2}{2}}$
thermal state	ρ_{th}	$e^{-\left(n_{\mathrm{th}}+\frac{1}{2}\right)\lvert\beta\rvert^2}$
displacement	$D(\alpha)$	$\pi\delta^{(2)}\left(\alpha+\beta\right)$
cosine	$\cos\left(a\hat{q}\right)$	$\frac{\pi}{2}\left(\delta^{(2)}\left(\beta+\frac{ia}{\sqrt{2}}\right)+\delta^{(2)}\left(\beta-\frac{ia}{\sqrt{2}}\right)\right)$

Table A.2: **Characteristic function pairs**. Note that the translation property from table A.1 can be used to easily calculate translated versions of each state.

time t applies the following transformation to the characteristic function,

$$C\left(\alpha,t\right) = C(\alpha\sqrt{\eta},0)\exp\left(\frac{\kappa_{\downarrow}+\kappa_{\uparrow}}{\kappa_{\downarrow}-\kappa_{\uparrow}}\left(\eta-1\right)\frac{|\alpha|^2}{2}\right), \tag{A.37}$$

$$\eta = \exp\left(\left(\kappa_{\uparrow}-\kappa_{\downarrow}\right)t\right). \tag{A.38}$$

It is useful to analyze this equation in a few limiting cases.

Photon loss

In the case of pure photon loss ($\kappa_{\uparrow} = 0$),

$$C\left(\alpha,t\right) = C(\alpha e^{-\kappa_{\downarrow}t/2})\exp\left(\left(e^{-\kappa_{\downarrow}t}-1\right)\frac{|\alpha|^2}{2}\right) \overset{\kappa_{\downarrow}t\ll 1}{\approx} C\left(\alpha\left(1-\kappa_{\downarrow}t/2\right)\right)\exp\left(-\kappa_{\downarrow}t\frac{|\alpha|^2}{2}\right). \tag{A.39}$$

Equation (A.39) shows that photon loss causes the characteristic function to *grow* and a Gaussian filter is applied. In the limit of small $\kappa_{\downarrow}t$, the variance of the Gaussian filter is $(\kappa t)^{-1}$. This should be interpreted as high-frequency correlations of the Wigner function being filtered out under photon loss, along with a directional diffusion due to the Fockker-Planck equation.

Additive Gaussian Noise (diffusion)

In the limit of additive Gaussian noise (pure diffusion), $\kappa_{\downarrow} = \kappa_{\uparrow} = \kappa$. In this case, the characteristic function is updated according to

$$C(\alpha,t) = C(\alpha)\exp(-\kappa t|\alpha|^2). \tag{A.40}$$

That is, a Gaussian filter is applied with variance $(2\kappa t)^{-1}$, half the variance for pure photon loss or pure photon gain. However, unlike the case of photon loss or gain, the characteristic function does not grow or shrink.

Appendix B

Derivation of the Selective-Qubit-Rotation (SQR) gate

Starting from the driven-dispersive Hamiltonian in the co-rotating frame of the oscillator and qubit,

$$H = \chi a^\dagger a \sigma_z + \Omega^*(t)\sigma_- + \Omega(t)\sigma_+, \tag{B.1}$$

we =perform a unitary frame transformation (see appendix C.2) to eliminate the dynamics of the dispersive term [103] by using the dispersive unitary $U_\chi = \exp\left(-i\chi t a^\dagger a \sigma_z/2\right)$. This transforms the σ_- and $\sigma_+ = \sigma_-^\dagger$ operators according to

$$U_\chi^\dagger \sigma_- U_\chi = e^{i\chi t a^\dagger a \sigma_z/2}\sigma_- e^{-i\chi t a^\dagger a \sigma_z/2} \tag{B.2}$$

$$= e^{i\chi t n a^\dagger a \sigma_z/2}\sum_{n=0}^{\infty} |n\rangle\langle n| \sigma_- e^{-i\chi t a^\dagger a \sigma_z/2} \tag{B.3}$$

$$= \sum_{n=0}^{\infty} |n\rangle\langle n| e^{i\chi n t \sigma_z/2}\sigma_- e^{-i\chi n t \sigma_z/2} \tag{B.4}$$

$$= \sum_{n=0}^{\infty} |n\rangle\langle n| \sigma_- e^{i\chi n t}. \tag{B.5}$$

From this, the transformed Hamiltonian $\tilde{H} = U_\chi^\dagger H U_\chi + i\left(\partial_t U_\chi^\dagger\right) U_\chi$ is

$$\tilde{H} = \sum_{n=0}^{\infty} |n\rangle\langle n| \left(\Omega^*(t)\sigma_- e^{i\chi n t} + \Omega(t)\sigma_+ e^{-i\chi n t}\right) \tag{B.6}$$

For the SQR gate up to Fock state N, we drive the qubit resonant with each number-shifted transition. This drive takes the form $\Omega(t) = \sum_{k=0}^{N-1} \Omega_k(t) e^{ik\chi t}$ where $\Omega_k(t)$ are complex-valued envelopes. With this drive, the Hamiltonian becomes

$$\tilde{H} = \sum_{n=0}^{\infty} |n\rangle\langle n| \sum_{k=0}^{N} \left(\Omega_k^*(t)\sigma_- e^{i\chi(n-k)t} + \Omega_k(t)\sigma_+ e^{-i\chi(n-k)t}\right). \tag{B.7}$$

Under the condition of slow pulses (total time $T_{\text{gate}} > 2\pi/\chi$) with a small bandwidth compared to χ, the first-order rotating-wave-approximation can be invoked, and rotating terms can be dropped. The implications of this approximation, along with mitigation techniques for faster pulses, are discussed in [103]. The RWA results in

$$\tilde{H}_{\text{RWA}} = \sum_{n=0}^{N} |n\rangle\langle n| \left(\Omega_n^*(t)\sigma_- + \Omega_n(t)\sigma_+\right). \tag{B.8}$$

To realize SQR, we pick $\Omega_n(t) = s(t)\theta_n e^{i\varphi_n}$ where $s(t)$ is a real-valued envelope function with $\int_0^{T_{\text{gate}}} s(\tau)d\tau = 1$. By transforming the operator back to the initial frame, the total unitary after time T_{gate} is

$$U = U_\chi \mathcal{T} \exp\left(-i\int_0^{T_{\text{gate}}} \tilde{H}_{\text{RWA}} dt\right) U_\chi^\dagger = \text{CR}\left(\chi T_{\text{gate}}\right) \text{SQR}\left(\vec{\theta}, \vec{\varphi}\right) \text{CR}\left(-\chi T_{\text{gate}}\right) \tag{B.9}$$

where $\text{SQR}(\vec{\theta}, \vec{\varphi}) = \sum_n R_{\varphi_n}(\theta_n) \otimes |n\rangle\langle n|$ as defined in section 2.4.3. As indicated, the full gate includes additional conditional rotations, which account for the cavity's pull on the qubit during the gate. However, this can be accounted for by picking the correct phase of drive for each Fock state.

Appendix C

Quantum dynamics: selected topics

C.1 derivatives of exponential operators

Calculating derivatives of exponential operators can be useful for gradient-based optimization, and in other settings. Let $\hat{A}(x)$ be an operator that depends on x Then,

$$\partial_x e^{\hat{A}} = \left(\int_0^1 ds\, e^{s\hat{A}} \left(\partial_x \hat{A}\right) e^{-s\hat{A}}\right) e^{\hat{A}}. \tag{C.1}$$

Implying[1]

$$\left[\partial_x \hat{A}, \hat{A}\right] = 0 \longleftrightarrow \partial_x e^{\hat{A}} = \left(\partial_x \hat{A}\right) e^{\hat{A}}. \tag{C.2}$$

C.2 Time-dependent frame transformations

A time-dependent unitary frame transformation is applied using

---

[1] This is also easily seen from the Taylor series definition of $e^{\hat{A}}$

$$\begin{aligned}
&\tilde{H} = U^\dagger H U + i\hbar(\partial_t U^\dagger)U, \\
&|\tilde{\psi}\rangle = U^\dagger |\psi\rangle , \\
&i\hbar\partial_t |\psi\rangle = H|\psi\rangle \rightarrow i\hbar\partial_t |\tilde{\psi}\rangle = \tilde{H}|\tilde{\psi}\rangle , \\
&O(t) \rightarrow \tilde{O}(t) = U^\dagger(t)O(t)U(t).
\end{aligned}$$

C.2.1 Time-dependent displaced frame

Note the following derivative:

$$\partial_t D(\alpha) = \partial_\alpha D(\alpha)\partial_t\alpha + \partial_{\alpha^*} D(\alpha)\partial_t\alpha^* \tag{C.3}$$

$$\rightarrow \partial_t D(\alpha) = \left[\left(a^\dagger - \frac{\alpha^*}{2}\right)\partial_t\alpha + \left(-a + \frac{\alpha}{2}\right)\partial_t\alpha^*\right] D(\alpha) \tag{C.4}$$

With this, we have

$$U(t) = D(\alpha(t)) \tag{C.5}$$

$$H\left(a, a^\dagger\right) \rightarrow \tilde{H} = U^\dagger H U + i(\partial_t U^\dagger)U \tag{C.6}$$

$$\tilde{H} = H\left(a + \alpha(t), a^\dagger + \alpha^*(t)\right) + i\left[\left(-a^\dagger - \frac{\alpha^*}{2}\right)\partial_t\alpha + \left(a + \frac{\alpha}{2}\right)\partial_t\alpha^*\right] \tag{C.7}$$

As an example, we can apply these formulas to a driven oscillator to calculate the generalized geometric phase associated with an oscillator trajectory.

Example: Driven oscillator

Let

$$H(t) = \varepsilon^*(t)a + \varepsilon(t)a^\dagger. \tag{C.8}$$

The displaced frame Hamiltonian is

$$\tilde{H}(t) = \varepsilon^*(t)\left(a + \alpha(t)\right) + \varepsilon(t)\left(a^\dagger + \alpha^*(t)\right) + i\left(\left(-a^\dagger - \frac{\alpha^*}{2}\right)\partial_t\alpha + \left(a + \frac{\alpha}{2}\right)\partial_t\alpha^*\right) \tag{C.9}$$

$$= \left(\varepsilon(t) - i\partial_t\alpha(t)\right)a^\dagger + \text{h.c.} + \alpha(t)\left(\varepsilon^*(t) + \frac{i}{2}\partial_t\alpha^*(t)\right) + \text{c.c.} \tag{C.10}$$

We can choose $\alpha(t)$ to be anything, making this transformation quite powerful to cancel classical dynamics. One convenient choice, especially when performing numerical simulations, is to cancel the terms linear in a and $a^\dagger$ in $\tilde{H}(t)$ by picking

$$i\partial_t\alpha(t) = \varepsilon(t) \tag{C.11}$$

$$\alpha(t_0) = \alpha_0 \tag{C.12}$$

with typical initial condition $\alpha_0 = 0$. With this choice, the Hamiltonian only contains terms proportional to the identity. These terms are often ignored. However, they can be important in multi-oscillator systems or hybrid oscillator qubit systems. In particular, with the choice of $\alpha(t)$ in eq. (C.11), the displaced frame Hamiltonian becomes

$$\tilde{H} = \frac{i}{2}\alpha^*(t)\partial_t\alpha(t) + \text{c.c.} = -\text{Im}\left(\alpha^*(t)\partial_t\alpha(t)\right) \tag{C.13}$$

The unitary associated with this displaced frame Hamiltonian is

$$\tilde{U}(t) = \exp\left(i\int_0^T \text{Im}\left(\alpha^*(t)\partial_t\alpha(t)\right)\right) = \exp\left(i2A(t)\right) \tag{C.14}$$

where A is the signed area enclosed by the $\alpha(t)$ trajectory in phase space, with trajectories traversed counterclockwise being positive (as with the usual Green's theorem).[2] In particular, if the trajectory is closed $\alpha(t_0) = \alpha(T)$, then the oscillator's state picks up a geometric phase

---

[2] For a complex-valued parameterized trajectory $z(t) = x(t) + iy(t)$ in x, y Cartesian space, the area enclosed is given by $A(t) = \frac{1}{2}\int_0^t \text{Im}\left(z^*(\tau)\partial_\tau z(\tau)\right)$.

(Berry phase) factor

$$|\psi(T)\rangle = e^{i2A}\,|\psi(t_0)\rangle \tag{C.15}$$

where A is the phase-space area enclosed by the trajectory as shown in fig. A.1.

Appendix D

Microwave drive IQ modulation

IQ mixing using a carrier at drive frequency ω_d results in a classical voltage signal $\varepsilon_{\text{lab}}(t) = \varepsilon_{\text{I}}(t)\cos(\omega_d t) + \varepsilon_{\text{Q}}(t)\sin(\omega_d t)$. We can define a complex-valued drive $\varepsilon(t) = \varepsilon_{\text{I}}(t) + i\varepsilon_{\text{Q}}(t)$, and write the classical-valued drive as $\varepsilon_{\text{lab}}(t) = \varepsilon^*(t)e^{i\omega_d t} + \varepsilon(t)e^{-i\omega_d t}$. With this, the voltage driven oscillator Hamiltonian takes the form

$$\frac{H}{\hbar} = \omega_a a^\dagger a + \varepsilon_{\text{lab}}(t)(a + a^\dagger) = \omega_a a^\dagger a + \left(\varepsilon^*(t)e^{i\omega_d t} + \varepsilon(t)e^{-i\omega_d t}\right)\left(a + a^\dagger\right) \tag{D.1}$$

Denoting the oscillator-drive detuning to be $\Delta_{ad} = \omega_a - \omega_d$, The Hamiltonian can be moved into the frame rotating at the drive frequency ω_d to find

$$\begin{aligned}\frac{\tilde{H}}{\hbar} &= \Delta_{ad} a^\dagger a + \left(\varepsilon^*(t)e^{i\omega_d t} + \varepsilon(t)e^{-i\omega_d t}\right)\left(a e^{-i\omega_d t} + a^\dagger e^{i\omega_d t}\right) &\text{(D.2)}\\ &= \Delta_{ad} a^\dagger a + \left(\varepsilon^*(t)a + \varepsilon(t)a^\dagger\right) + \left(\varepsilon(t)a e^{-2\omega_d t} + \varepsilon^*(t)a^\dagger e^{2\omega_d t}\right). &\text{(D.3)}\end{aligned}$$

In the regime where $2\omega_d \gg |\varepsilon(t)|, \Delta_{ad}$, the rotating wave approximation can be invoked, and the final term in parentheses can be dropped, leading to the final drive-frame Hamiltonian

$$\frac{\tilde{H}_{\text{RWA}}}{\hbar} = \Delta_{ad} a^\dagger a + \left(\varepsilon^*(t)a + \varepsilon(t)a^\dagger\right). \tag{D.4}$$

Appendix E

Universality proofs

E.1 Law and Eberly

The Law and Eberly gate set (section 2.4.1) is

$$L.E. = \{\mathrm{JC}\left(\theta, \varphi\right), R_{\varphi}\left(\theta\right)\} \tag{E.1}$$

with generators $\left\{\left(a^{\dagger}\sigma_{-} + a\sigma_{+}\right), i\left(a^{\dagger}\sigma_{-} - a\sigma_{+}\right), \left(\sigma_{+} + \sigma_{-}\right), i\left(\sigma_{+} - \sigma_{-}\right)\right\}$. The generator of conditional displacements can be found in the first level of commutators,

$$\left[a^{\dagger}\sigma_{-} + a\sigma_{+}, \sigma_{+} + \sigma_{-}\right] = (a^{\dagger} - a)\sigma_{z}, \tag{E.2}$$

$$\left[-i\left(a^{\dagger}\sigma_{-} - a\sigma_{+}\right), \sigma_{+} + \sigma_{-}\right] = (a^{\dagger} + a)\sigma_{z}. \tag{E.3}$$

Because the conditional displacement gate set is universal (as shown in appendix E.3), and the Law and Eberly generates the conditional displacement algebra, the Law and Eberly gateset is universal.

E.2 Dispersive gate set

The dispersive gate set is $\mathcal{D} = \{\mathrm{CR}\left(\theta\right), D(\alpha), R_\varphi(\theta)\}$.

Since

$$\left[a + a^\dagger, a^\dagger a \sigma_z\right] = (a - a^\dagger)\sigma_z \tag{E.4}$$

$$\left[-i(a - a^\dagger), a^\dagger a \sigma_z\right] = i(a + a^\dagger)\sigma_z, \tag{E.5}$$

the dispersive gate set can simulate the conditional displacement gate set, and is thus universal.

E.3 Conditional Displacement (ECD)

Starting with the set of generators for $\mathrm{ECD}(\beta)$ and $R_\varphi(\theta)$, $\{q\sigma_z, p\sigma_z, \sigma_x, \sigma_y\}$, commutators such as $[q\sigma_z, \sigma_x] \propto q\sigma_y$ and $[\sigma_x, \sigma_y] \propto \sigma_z$ can be used to expand the set to $\{\sigma_i, q\sigma_i, p\sigma_i\}$ where $i \in \{x, y, z\}$. This shows that effectively, by rotating the qubit between conditional displacements, the ECD gate set can create more general Rabi type interactions between the oscillator and qubit, where qubit-mediated nonlinear gates have been proposed [265, 266].

By using commutators similar to $[q\sigma_x, q\sigma_y] \propto q^2\sigma_z$, our set can further be expanded to all quadratic polynomials of $q\sigma_i$ and $p\sigma_i$. This process can be iterated in order to generate any $q^j p^k \sigma_i$ product, where $i \in \{x, y, z\}$. Terms which do not contain a Pauli operator such as $q^j p^k$ can be generated from commutators such as $\left[q^{j+1}p^k\sigma_z, p\sigma_z\right] \propto q^j p^k$. With this, the full Lie algebra for polynomial operators on the qubit and oscillator Hilbert space is generated.

Appendix F

Modular variables and the Zak basis

In this section we discuss one final approach for the representation of GKP states and operators, called the modular variables formalism or the Zak basis [267–274], which is useful for representing oscillator wavefunctions and operators on a restricted domain of two variables instead of an unrestricted domain of one variable. In particular, the modular wavefunction serves as an efficient basis for representing (and simulating) GKP-like states, or more generally, oscillator states that are close to periodic such as finite-energy GKP states. The formalism has been used in various other contexts in physics, such as in the analysis of spatial interference patterns and in quantum-Hall-effect literature.

The (single-mode) Zak basis has been used extensively in GKP literature, with applications in analysis of the GKP Hamiltonian (see appendix G), engineering superconducting circuits for realizing passive or active error correction (see chapter 5), and an understanding of GKP error correction through the lens of a modular variable subsystem decomposition [273, 274]. In this decomposition, the oscillator's Hilbert space is divided into two subsystems: one that stores logical qubit information and a second continuous-variable gauge subsystem that carries no logical information. In this subsection, we will briefly review the single-mode Zak basis and the Zak transform, using the notation and conventions from Ref. [274].

Given a position periodicity a (in GKP, typically chosen to be the length of a stabilizer translation), the Zak kets form a complete single-mode basis and are given in the position and momentum representation by

$$|u, v\rangle := \sqrt{\frac{a}{2\pi}} \sum_{m\in\mathbb{Z}} e^{iamv} |u + am\rangle_q = \sqrt{\frac{1}{a}} e^{-iuv} \sum_{m\in\mathbb{Z}} e^{-i2\pi mu/a} |v + 2\pi m/a\rangle_p . \tag{F.1}$$

They are orthonormal in the Dirac-comb sense,

$$\langle u, v| |u', v'\rangle = \sum_m \delta(u - u' + am) \sum_n \delta(v - v' + (2\pi/a)n) . \tag{F.2}$$

The Zak kets are eigenstates of displacement operators,

$$e^{-ia\hat{p}} |u, v\rangle = e^{-iav} |u, v\rangle \text{ and } e^{i\frac{2\pi}{a}\hat{q}} |u, v\rangle = e^{i\frac{2\pi}{a}u} |u, v\rangle , \tag{F.3}$$

with quasi-periodicity in the first variable and periodicity in the second, satisfying

$$e^{-it\hat{p}} |u, v\rangle = |u + t, v\rangle , \qquad |u + a, v\rangle = e^{-iav} |u, v\rangle , \tag{F.4}$$

$$e^{it\hat{q}} |u, v\rangle = e^{iut} |u, v + t\rangle , \qquad |u, v + 2\pi/a\rangle = |u, v\rangle . \tag{F.5}$$

This leads to a restricted domain for u (of width a) and v (of width $2\pi/a$), giving a total of domain of area of 2π called Zak patch $\mathcal{P}$ with a center that we are free to choose. One choice of domain that is convenient for representing computational GKP states is $u \in [-a/4, 3a/4)$ and $v \in [-\pi/a, \pi/a)$. For example, using $a = 2\sqrt{\pi}$, the (single-mode) infinite-energy square GKP computational states are represented as $|+Z\rangle = |0, 0\rangle$ and $|-Z\rangle = |a/2, 0\rangle$. Arbitrary oscillator states can be represented in the basis of modular wavefunctions living on a torus $|\psi\rangle = \int_{\mathcal{P}} dudv\, \psi(u, v) |u, v\rangle$ with boundary conditions $\psi(u + a, v) = e^{iav}\psi(u, v)$, $\psi(u, v + 2\pi/a) = \psi(u, v)$.

The power of the Zak basis is that square-integrable wavefunctions of an unbounded variable (such as position q) can be mapped onto quasi-periodic modular wavefunctions of two real variables with a bounded domain. This mapping is given by the Zak transform [267, 274, 275]

$$(Z\psi)(u,v) = \sqrt{\frac{a}{2\pi}} \sum_{m\in\mathbb{Z}} e^{-iamv} \psi(u+am). \tag{F.6}$$

Finally, operators can also be described in the context of the Zak basis and modular wavefunctions. Explicitly, the position and momentum operators can be broken up into a modular part and a remainder part,

$$\hat{q} = \hat{u} + a\hat{m} \qquad\qquad \hat{p} = \hat{v} + \frac{2\pi}{a}\hat{n} \tag{F.7}$$

where $\hat{n}$ ($\hat{m}$) have integer eigenvalues (interpreted as the "which-bin" information), and $\hat{u} = (\hat{q}+c_q)\mathrm{mod}\,[a] - c_q$ ($\hat{v} = (\hat{p}+c_p)\mathrm{mod}\,[2\pi/a] - c_p$) are the modular position (momentum) operators (interpreted as the relative position or momentum within the specified bin). Here, c_q (c_p) are constants used to center the Zak patch [269]. In the modular wavefunction representation these variables have a differential form,

$$\langle u,v|\,\hat{u} = u\,\langle u,v| \qquad\qquad \langle u,v|\,\hat{v} = v\,\langle u,v| \tag{F.8}$$

$$\langle u,v|\,a\hat{m} = i\frac{\partial}{\partial v}\,\langle u,v| \qquad\qquad \langle u,v|\,\frac{2\pi}{a}\hat{n} = -\left(i\frac{\partial}{\partial u} + v\right)\langle u,v|\,, \tag{F.9}$$

giving a differential form for the oscillator position and momentum variables,

$$\langle u,v|\,\hat{q} = \left(u + i\frac{\partial}{\partial v}\right)\langle u,v| \qquad\qquad \langle u,v|\,\hat{p} = -i\frac{\partial}{\partial u}\,\langle u,v| \tag{F.10}$$

used to analyze the action of operators and Hamiltonians on modular wavefunctions [276], as is done in appendix G. Also, a multimode Zak basis and modular variable approach could be useful in the development of error correction strategies for multi-oscillator GKP codes [273].

Appendix G

A Hamiltonian description of the GKP code

As defined in chapter 1, $\hat{q} = \left(a + a^{\dagger}\right)/\sqrt{2}$ and $\hat{p} = -i\left(a - a^{\dagger}\right)/\sqrt{2}$ are the position and momentum operators of a quantum harmonic oscillator with $\left[a, a^{\dagger}\right] = 1$ (unit is chosen as $\hbar = 1$). The infinite-energy GKP Hamiltonian for a single-mode rectangular-lattice can be written as [1]

$$H_{\mathrm{GKP}} = -E_p \cos\left(\frac{\sqrt{2\pi d}}{\eta}\,\hat{p}\right) - E_q \cos\left(\eta\sqrt{2\pi d}\,\hat{q}\right). \tag{G.1}$$

H_{GKP} has a d-fold degenerate ground state manifold encoding the infinite-energy rectangular d-dimensional GKP code where η sets the lattice aspect ratio in phase space; here d is the code dimension of the single-mode GKP code.[1] Analogous Hamiltonians exist for other lattices, such as the hexagonal lattice. The spectrum of H_{GKP} is continuous with eigenstates given by Zak basis states [226,267,274,276–278] (see appendix F) and E_q/E_p can be used to tune the relative dispersion along the q and p directions. We note that the GKP Hamiltonian is closely related to Harper's equation [279], which is a tight binding model for motional dynamics of noninteracting electrons in the presence of a 2D periodic potential and uniform

---

[1] In this section, we often restrict to the qubit ($d = 2$ case) and use the nomenclature "2D GKP" state, Hamiltonian etc. to refer to a *single-mode* GKP with $d = 2$ code dimension.

magnetic field, as discussed more below [1, 226, 278, 280].

The usual argument behind passive QEC is to construct a Hamiltonian for which the codespace is the degenerate ground state manifold, protected by an energy gap [12]. However, passive QEC for continuous-variable systems is different than in multi-qubit systems such as the toric or surface code. In both cases, the protection Hamiltonian is of the form $H = -\sum_k E_k S_k$, where $\{S_k\}$ are the stabilizer generators and E_k are the energy scales which should be positive and very large compared with typical couplings to the bath. For multi-qubit codes, the discrete spectrum of Pauli stabilizers gives rise to a spectral gap. For the infinite-energy GKP code, the spectrum of displacement stabilizers is continuous, rendering H_{GKP} gapless. As a result, the perturbation theory argument relying on a gap, such that local perturbations of the Hamiltonain give rise to small variations in energy, does not apply to H_{GKP} directly [226, 281].

Depending on the physical realization of H_{GKP}, it is unclear if a continuous spectrum is really an issue, as proper thermalization to a cold bath could still prevent uncorrectable errors; this is highly context dependent and an active topic of research. Nonetheless, a gapped spectrum can be engineered by including a weak confinement potential, giving rise to the finite-energy GKP Hamiltonian $H_{\mathrm{GKP},\Delta}$ [1, 226, 276, 281]. The most straightforward is a harmonic confinement[2],

$$H_{\mathrm{GKP},\Delta} = \frac{\omega_0}{2}\left(\hat{p}^2 + \hat{q}^2\right) - E_p \cos\left(\frac{\sqrt{2\pi d}}{\eta}\,\hat{p}\right) - E_q \cos\left(\eta\sqrt{2\pi d}\,\hat{q}\right). \tag{G.2}$$

The Δ notation here indicates the quasi-degenerate ground states are now finite-energy GKP states. The ground state manifold of the $H_{\mathrm{GKP},\Delta}$ serves as an alternative definition to the single-mode finite-energy code manifold. We anticipate this definition can be extended to multimode GKP encodings.

---

[2] A general harmonic confinement of $H = \hat{p}^2/2m + k\hat{q}^2/2$ can cast into the form of eq. (G.2) by scaling position and momentum as $\hat{q} \to \hat{q}/\sqrt{Z}, \hat{p} \to \hat{p}\sqrt{Z}$, where $Z = 1/\sqrt{km}$ is the impedance of the harmonic confinement

To analyze the Hamiltonian, the Zak basis introduced in appendix F can be used [276]. In particular, using a Zak basis period of $a = \sqrt{2\pi d}/\eta$ and a Zak patch[3] of $\mathcal{P} = u \in [-a/2d, a(2d-1)/2d)$, $v \in [-\pi/a, \pi/a)$, the Hamiltonian can be written as a differential operator in the Zak-wavefunction basis $H\,|\psi\rangle = \int_{\mathcal{P}} dudv\, H(u,v)\psi(u,v)\,|u,v\rangle$ using eq. (F.10) as

$$H_{\text{GKP},\Delta}(u,v) = \frac{\omega_0}{2}\left(p_u^2 + (u-p_v)^2\right) - E_p \cos\left(\frac{\sqrt{2\pi d}}{\eta}v\right) - E_q \cos\left(\eta\sqrt{2\pi d}\,u\right) \tag{G.3}$$

where we have defined effective momenta in the u, v directions as $p_u = -i\frac{\partial}{\partial u}$ and $p_v = -i\frac{\partial}{\partial v}$ [276]. From this, the finite-energy GKP Hamiltonian $H_{\text{GKP},\Delta}$ can be thought of as describing a particle of mass $1/\omega_0$ on a torus parameterized by u, v, coupled to a vector potential and two cosine potentials.

In the limit of weak harmonic confinement, $E_q, E_p \gg \omega_0$, the tunneling between cosine minima is suppressed. In this regime, $H_{\text{GKP},\Delta}$ has a set of d nearly degenerate ground states, each localized in different minima at positions $(u,v) = (an/d, 0)$ with $n = 0, 1, ..., d-1$. The cosine terms can be expanded to quadratic order around a minima, leading to a local effective Hamiltonian that is well approximated by two uncoupled harmonic oscillators with frequencies $\omega_u = \left(\eta\sqrt{2\pi d}\right)\left(\sqrt{\omega_0 E_q}\right)$ and $\omega_v = \left(\sqrt{2\pi d}/\eta\right)\left(\sqrt{\omega_0 E_p}\right)$ and a spectral gap between the quasi-degenerate ground state manifold and the first excited states of approximately $E \approx \min(\omega_u, \omega_v)$.

Expanding the cosine potentials in eq. (G.3) to quadratic order can also be used to estimate the GKP squeezing parameters. GKP states can have different squeezings along the position and momentum directions in cases where $\eta \neq 1$ or $E_q \neq E_p$, and these can be estimated from the zero-point motion associated with the effective oscillator impedances of u and v, given by $Z_u = \left(\eta\sqrt{2\pi d}\right)^{-1}\sqrt{\omega_0/E_q}$ and $Z_v = \left(\sqrt{2\pi d}/\eta\right)^{-1}\sqrt{\omega_0/E_p}$. The zero-point motion leads to GKP squeezing parameters of $\Delta_q \approx 1/\sqrt{Z_u}$ and $\Delta_p \approx 1/\sqrt{Z_p}$. Other

---

[3] Any patch of of width a in u and $2\pi/a$ in v will do, however we find this patch to be the most convenient for representing GKP qudit states

quantities, such as the tunnel splitting of the ground state manifold, can be estimated by applying different perturbation techniques to the Zak-basis Hamiltonian, see for example Refs. [226, 276].

In the case of a square lattice with equal energy scales in q and p ($\eta = 1, E_q = E_p$), the ground states are well approximated by the finite-energy Hadamard eigenstates

$$\psi_{H+}(q) \approx \cos\left(\frac{\pi}{8}\right)\psi_{\Delta,0}(q) + \sin(\pi/8)\,\psi_{\Delta,1}(q)\,, \tag{G.4}$$

$$\psi_{H-}(q) \approx -\sin\left(\frac{\pi}{8}\right)\psi_{\Delta,0}(q) + \cos(\pi/8)\,\psi_{\Delta,1}(q)\,, \tag{G.5}$$

where $\psi_{\Delta,\substack{1\\0}}(q)$ are the wavefunctions for the finite-energy 0 and 1 logical states. This can be seen from the Hamiltonian's invariance with respect to the Fourier transform (a $\pi/2$ rotation in phase space). As an example, in Ref. [226], the numerically obtained lowest-energy eigenstates are shown. Modifying the impedance of the confinement potential can break this symmetry and lead to other ground state manifolds. Varying from one confinement potential to another could be used to engineer transformations of the finite-energy GKP states [281].

The GKP Hamiltonian can also arise as the low-energy Hamiltonian of a single electron confined to a two-dimensional plane with a periodic potential and a perpendicular magnetic field [1, 226]. Although this system is likely not practical to implement, requiring unrealistically large magnetic fields, it is useful for a theoretical understanding of the GKP code. In Ref. [226], the authors show that the effective low energy Hamiltonian [the lowest Landau level (LLL) Hamiltonian] for this system in the weak Landau-level coupling limit is

$$H_{\mathrm{LLL}} = -V_0\left[\cos\left(2\sqrt{\pi}\hat{q}\right) + \cos\left(\frac{t}{s}\sqrt{\pi}\hat{p}\right)\right]. \tag{G.6}$$

Here $\{t, s\}$ are coprime natural numbers describing the rational multiple of flux quantum contained in a loop enclosed by magnetic translation operators, $\Phi = (s/t)\,\Phi_0$ where Φ_0 is the (non-superconducting) flux quantum. The eigenvalue equation associated with H_{LLL} is the

Harper equation, resulting in an energy spectrum in the form of a Hofstadter butterfly [280]. In [226], the spectrum is plotted as a function of t/s (also see [278]). This spectrum has s bands that are t-fold degenerate, and the two-dimensional GKP code space corresponds to the ground state manifold at $s/t = 1/2$ (equivalently $t/s = 2$) as shown by the red star in the figure. In Ref. [278], the authors discuss this model in the context of topological order and introduce the notion of a phase-space interaction potential, connecting to the dynamics of some many-body systems.

Bibliography

[1] D. Gottesman, A. Kitaev, J. Preskill, Encoding a qubit in an oscillator, Phys. Rev. A 64 (1) (2001) 012310. doi:10.1103/PhysRevA.64.012310.

[2] M. A. Nielsen, I. L. Chuang, Quantum Computation and Quantum Information: 10th Anniversary Edition, Cambridge University Press, 2010. doi:10.1017/cbo9780511976667.

[3] R. P. Feynman, Simulating physics with computers, International Journal of Theoretical Physics 21 (6) (1982) 467–488.

[4] P. Shor, Polynomial-Time Algorithms for Prime Factorization and Discrete Logarithms on a Quantum Computer, SIAM J. Comput. 26 (1997) 1484–1509. doi:10.1137/s0097539795293172.

[5] B. Schroeder, E. Pinheiro, W.-D. Weber, Dram errors in the wild: A large-scale field study, in: Sigmetrics, 2009.

[6] R. Acharya, I. Aleiner, R. Allen, T. I. Andersen, M. Ansmann, F. Arute, K. Arya, A. Asfaw, J. Atalaya, R. Babbush, et al., Suppressing quantum errors by scaling a surface code logical qubit, Nature 614 (7949) (2023) 676–681. doi:10.1038/s41586-022-05434-1.

[7] S. Bravyi, O. Dial, J. M. Gambetta, D. Gil, Z. Nazario, The future of quantum computing with superconducting qubits, Journal of Applied Physics 132 (16) (2022) 160902.

[8] P. W. Shor, Scheme for reducing decoherence in quantum computer memory, Phys. Rev. A 52 (1995) R2493–r2496. doi:10.1103/PhysRevA.52.R2493.

[9] E. T. Campbell, B. M. Terhal, C. Vuillot, Roads towards fault-tolerant universal quantum computation, Nature 549 (7671) (2017) 172–179.

[10] D. Gottesman, An introduction to quantum error correction and fault-tolerant quantum computation (2009). arXiv:0904.2557.

[11] D. Gottesman, Stabilizer codes and quantum error correction (1997). arXiv:quant-ph/9705052.

[12] A. Kitaev, Fault-tolerant quantum computation by anyons, Annals of Physics 303 (1) (2003) 2–30. doi:10.1016/s0003-4916(02)00018-0.

[13] A. G. Fowler, M. Mariantoni, J. M. Martinis, A. N. Cleland, Surface codes: Towards practical large-scale quantum computation, Phys. Rev. A 86 (2012) 032324. doi:10.1103/PhysRevA.86.032324.

[14] B. M. Terhal, Quantum error correction for quantum memories, Rev. Mod. Phys. 87 (2) (2015) 307–346. doi:10.1103/RevModPhys.87.307.

[15] B. M. Terhal, J. Conrad, C. Vuillot, Towards scalable bosonic quantum error correction, Quantum Sci. Technol. 5 (4) (2020) 043001. doi:10.1088/2058-9565/ab98a5.

[16] S. Ganjam, Y. Wang, Y. Lu, A. Banerjee, C. U. Lei, L. Krayzman, K. Kisslinger, C. Zhou, R. Li, Y. Jia, M. Liu, L. Frunzio, R. J. Schoelkopf, Surpassing millisecond coherence times in on-chip superconducting quantum memories by optimizing materials, processes, and circuit design (2023). arXiv:2308.15539.

[17] M. Reagor, W. Pfaff, C. Axline, R. W. Heeres, N. Ofek, K. Sliwa, E. Holland, C. Wang, J. Blumoff, K. Chou, et al., Quantum memory with millisecond coherence in circuit QED, Phys. Rev. B 94 (1) (2016) 014506. doi:10.1103/PhysRevB.94.014506.

[18] V. V. Albert, Bosonic coding: introduction and use cases (2022). arXiv:2211.05714.

[19] V. V. Albert, K. Noh, K. Duivenvoorden, D. J. Young, R. T. Brierley, P. Reinhold, C. Vuillot, L. Li, C. Shen, S. M. Girvin, et al., Performance and structure of single-mode bosonic codes, Phys. Rev. A 97 (3) (2018) 032346. doi:10.1103/PhysRevA.97.032346.

[20] K. Noh, V. V. Albert, L. Jiang, Quantum Capacity Bounds of Gaussian Thermal Loss Channels and Achievable Rates With Gottesman-Kitaev-Preskill Codes, IEEE Trans. Inf. Theory 65 (4) (2019) 2563–2582. doi:10.1109/tit.2018.2873764.

[21] P. Leviant, Q. Xu, L. Jiang, S. Rosenblum, Quantum capacity and codes for the bosonic loss-dephasing channel, Quantum 6 (2022) 821. doi:10.22331/q-2022-09-29-821.

[22] A. J. Brady, A. Eickbusch, S. Singh, J. Wu, Q. Zhuang, Advances in bosonic quantum error correction with gottesman–kitaev–preskill codes: Theory, engineering and applications, Progress in Quantum Electronics (2024) 100496doi:10.1016/j.pquantelec.2023.100496.

[23] A. L. Grimsmo, J. Combes, B. Q. Baragiola, Quantum Computing with Rotation-Symmetric Bosonic Codes, Phys. Rev. X 10 (1) (2020) 011058. doi:10.1103/PhysRevX.10.011058.

[24] K. Noh, C. Chamberland, Fault-tolerant bosonic quantum error correction with the surface–Gottesman-Kitaev-Preskill code, Phys. Rev. A 101 (2020) 012316. doi:10.1103/PhysRevA.101.012316.

[25] A. Eickbusch, V. Sivak, A. Z. Ding, S. S. Elder, S. R. Jha, J. Venkatraman, B. Royer, S. Girvin, R. J. Schoelkopf, M. H. Devoret, Fast universal control of an oscillator with weak dispersive coupling to a qubit, Nat. Phys. 18 (12) (2022) 1464–1469. doi:10.1038/s41567-022-01776-9.

[26] P. Campagne-Ibarcq, A. Eickbusch, S. Touzard, E. Zalys-Geller, N. E. Frattini, V. V. Sivak, P. Reinhold, S. Puri, S. Shankar, R. J. Schoelkopf, et al., Quantum error correction of a qubit encoded in grid states of an oscillator, Nature 584 (7821) (2020) 368–372. doi:10.1038/s41586-020-2603-3.

[27] V. V. Sivak, A. Eickbusch, B. Royer, S. Singh, I. Tsioutsios, S. Ganjam, A. Miano, B. L. Brock, A. Z. Ding, L. Frunzio, S. M. Girvin, R. J. Schoelkopf, M. H. Devoret, Real-time quantum error correction beyond break-even, Nature 616 (7955) (2023) 50–55. doi:10.1038/s41586-023-05782-6.

[28] C. S. Wang, J. C. Curtis, B. J. Lester, Y. Zhang, Y. Y. Gao, J. Freeze, V. S. Batista, P. H. Vaccaro, I. L. Chuang, L. Frunzio, et al., Efficient Multiphoton Sampling of Molecular Vibronic Spectra on a Superconducting Bosonic Processor, Phys. Rev. X 10 (2) (2020) 021060. doi:10.1103/PhysRevX.10.021060.

[29] L. D. Burkhart, J. D. Teoh, Y. Zhang, C. J. Axline, L. Frunzio, M. Devoret, L. Jiang, S. Girvin, R. Schoelkopf, Error-Detected State Transfer and Entanglement in a Superconducting Quantum Network, PRX Quantum 2 (3) (2021) 030321. doi:10.1103/PRXQuantum.2.030321.

[30] K. M. Backes, D. A. Palken, S. A. Kenany, B. M. Brubaker, S. Cahn, A. Droster, G. C. Hilton, S. Ghosh, H. Jackson, S. K. Lamoreaux, et al., A quantum enhanced search for dark matter axions, Nature 590 (7845) (2021) 238–242. doi:10.1038/s41586-021-03226-7.

[31] U. Vool, M. Devoret, Introduction to quantum electromagnetic circuits, International Journal of Circuit Theory and Applications 45 (7) (2017) 897–934. doi:10.1002/cta.2359.

[32] D. Griffiths, Introduction to Quantum Mechanics, Cambridge University Press, 2017.

[33] S. M. Girvin, R. J. Schoelkopf, Circuit qed: Superconducting qubits coupled to microwave photons, Oxford University Press, 2015.

[34] A. Blais, A. L. Grimsmo, S. M. Girvin, A. Wallraff, Circuit quantum electrodynamics, Rev. Mod. Phys. 93 (2) (2021) 025005. `doi:10.1103/RevModPhys.93.025005`.

[35] H. Weyl, The Theory of Groups and Quantum Mechanics, Dover Books on Mathematics, Dover Publications, 1950.

[36] T. L. Curtright, D. B. Fairlie, C. K. Zachos, A Concise Treatise on Quantum Mechanics in Phase Space, World Scientific, 2014. `doi:10.1142/8870`.

[37] E. Cohen, H. Larocque, F. Bouchard, F. Nejadsattari, Y. Gefen, E. Karimi, Geometric phase from aharonov–bohm to pancharatnam–berry and beyond, Nature Reviews Physics 1 (7) (2019) 437–449.

[38] U. Leonhardt, Essential Quantum Optics: From Quantum Measurements to Black Holes, Cambridge University Press, 2010.

[39] L.-A. Sellem, A. Sarlette, Z. Leghtas, M. Mirrahimi, P. Rouchon, P. Campagne-Ibarcq, A GKP qubit protected by dissipation in a high-impedance superconducting circuit driven by a microwave frequency comb (2023). `arXiv:2304.01425`.

[40] L.-A. Sellem, R. Robin, P. Campagne-Ibarcq, P. Rouchon, Stability and decoherence rates of a GKP qubit protected by dissipation (2023). `arXiv:2304.03806`.

[41] B. Terhal, L. Pryadko, D. Weigand, Y. Wang, H. Asasi, C. Vuillot, Scalable quantum error correction with the bosonic GKP code, in: APS March Meeting Abstracts, Vol. 2019, 2019, pp. F62–004.

[42] A. L. Grimsmo, S. Puri, Quantum Error Correction with the Gottesman-Kitaev-Preskill Code, PRX Quantum 2 (2) (2021) 020101. `doi:10.1103/PRXQuantum.2.020101`.

[43] K. Noh, Quantum computation and communication in bosonic systems (2021). arXiv:2103.09445.

[44] V. Sivak, Quantum error correction beyond break-even, Phd thesis, Yale University (2023).

[45] S. Touzard, Stabilization of bosonic codes in superconducting circuits, Phd thesis, Yale University (2019).

[46] G. J. Dolan, Offset masks for lift-off photoprocessing, Applied Physics Letters 31 (5) (1977) 337–339.

[47] D. E. Chang, V. Vuletić, M. D. Lukin, Quantum nonlinear optics —photon by photon, Nature Photonics 8 (9) (2014) 685–694.

[48] S. Konno, W. Asavanant, F. Hanamura, H. Nagayoshi, K. Fukui, A. Sakaguchi, R. Ide, F. China, M. Yabuno, S. Miki, H. Terai, K. Takase, M. Endo, P. Marek, R. Filip, P. van Loock, A. Furusawa, Propagating gottesman-kitaev-preskill states encoded in an optical oscillator (2023). arXiv:2309.02306.

[49] O. Instruments, Principles of dilution refrigeration.

[50] M. Tinkham, Introduction to Superconductivity, Dover Books on Physics Series, Dover Publications, 2004.

[51] J. Koch, T. M. Yu, J. Gambetta, A. A. Houck, D. I. Schuster, J. Majer, A. Blais, M. H. Devoret, S. M. Girvin, R. J. Schoelkopf, Charge-insensitive qubit design derived from the Cooper pair box, Phys. Rev. A 76 (4) (2007) 042319. doi:10.1103/PhysRevA.76.042319.

[52] H. Paik, D. I. Schuster, L. S. Bishop, G. Kirchmair, G. Catelani, A. P. Sears, B. R. Johnson, M. J. Reagor, L. Frunzio, L. I. Glazman, et al., Observation of High Coherence in Josephson Junction Qubits Measured in a Three-Dimensional Circuit QED

Architecture, Phys. Rev. Lett. 107 (24) (2011) 240501. doi:10.1103/PhysRevLett.107.240501.

[53] D. Pozar, Microwave Engineering, 4th Edition, Wiley, 2011.

[54] O. Milul, B. Guttel, U. Goldblatt, S. Hazanov, L. M. Joshi, D. Chausovsky, N. Kahn, E. Çiftyürek, F. Lafont, S. Rosenblum, A superconducting quantum memory with tens of milliseconds coherence time (2023). arXiv:2302.06442.

[55] A. Romanenko, R. Pilipenko, S. Zorzetti, D. Frolov, M. Awida, S. Belomestnykh, S. Posen, A. Grassellino, Three-Dimensional Superconducting Resonators at $T = 20$ mK with Photon Lifetimes up to $\tau = 2$ s, Phys. Rev. Appl. 13 (3) (2020) 034032. doi:10.1103/PhysRevApplied.13.034032.

[56] A. Wallraff, D. I. Schuster, A. Blais, L. Frunzio, R. S. Huang, J. Majer, S. Kumar, S. M. Girvin, R. J. Schoelkopf, Strong coupling of a single photon to a superconducting qubit using circuit quantum electrodynamics, Nature 431 (7005) (2004) 162–167.

[57] A. Blais, R.-S. Huang, A. Wallraff, S. M. Girvin, R. J. Schoelkopf, Cavity quantum electrodynamics for superconducting electrical circuits: An architecture for quantum computation, Phys. Rev. A 69 (6) (2004) 062320. doi:10.1103/PhysRevA.69.062320.

[58] N. Ofek, A. Petrenko, R. Heeres, P. Reinhold, Z. Leghtas, B. Vlastakis, Y. Liu, L. Frunzio, S. Girvin, L. Jiang, et al., Extending the lifetime of a quantum bit with error correction in superconducting circuits, Nature 536 (7617) (2016) 441–445. doi:10.1038/nature18949.

[59] B. M. Terhal, D. Weigand, Encoding a qubit into a cavity mode in circuit QED using phase estimation, Phys. Rev. A 93 (1) (2016) 012315. doi:10.1103/PhysRevA.93.012315.

[60] M. D. Reed, L. DiCarlo, S. E. Nigg, L. Sun, L. Frunzio, S. M. Girvin, R. J. Schoelkopf, Realization of three-qubit quantum error correction with superconducting circuits, Nature 482 (7385) (2012) 382–385.

[61] D. Sank, Z. Chen, M. Khezri, J. Kelly, R. Barends, B. Campbell, Y. Chen, B. Chiaro, A. Dunsworth, A. Fowler, E. Jeffrey, E. Lucero, A. Megrant, J. Mutus, M. Neeley, C. Neill, P. J. J. O'Malley, C. Quintana, P. Roushan, A. Vainsencher, T. White, J. Wenner, A. N. Korotkov, J. M. Martinis, Measurement-Induced State Transitions in a Superconducting Qubit: Beyond the Rotating Wave Approximation, Physical Review Letters 117 (19) (2016) 190503. `doi:10.1103/PhysRevLett.117.190503`.

[62] R. Lescanne, L. Verney, Q. Ficheux, M. H. Devoret, B. Huard, M. Mirrahimi, Z. Leghtas, Escape of a Driven Quantum Josephson Circuit into Unconfined States, Physical Review Applied 11 (1) (2019) 014030. `doi:10.1103/PhysRevApplied.11.014030`.

[63] M. Khezri, A. Opremcak, Z. Chen, A. Bengtsson, T. White, O. Naaman, R. Acharya, K. Anderson, M. Ansmann, F. Arute, K. Arya, A. Asfaw, J. C. Bardin, A. Bourassa, J. Bovaird, L. Brill, B. B. Buckley, D. A. Buell, T. Burger, B. Burkett, N. Bushnell, J. Campero, B. Chiaro, R. Collins, A. L. Crook, B. Curtin, S. Demura, A. Dunsworth, C. Erickson, R. Fatemi, V. S. Ferreira, L. F. Burgos, E. Forati, B. Foxen, G. Garcia, W. Giang, M. Giustina, R. Gosula, A. G. Dau, M. C. Hamilton, S. D. Harrington, P. Heu, J. Hilton, M. R. Hoffmann, S. Hong, T. Huang, A. Huff, J. Iveland, E. Jeffrey, J. Kelly, S. Kim, P. V. Klimov, F. Kostritsa, J. M. Kreikebaum, D. Landhuis, P. Laptev, L. Laws, K. Lee, B. J. Lester, A. T. Lill, W. Liu, A. Locharla, E. Lucero, S. Martin, M. McEwen, A. Megrant, X. Mi, K. C. Miao, S. Montazeri, A. Morvan, M. Neeley, C. Neill, A. Nersisyan, J. H. Ng, A. Nguyen, M. Nguyen, R. Potter, C. Quintana, C. Rocque, P. Roushan, K. Sankaragomathi, K. J. Satzinger, C. Schuster, M. J. Shearn, A. Shorter, V. Shvarts, J. Skruzny, W. C. Smith, G. Sterling, M. Szalay, D. Thor, A. Torres, B. W. K. Woo, Z. J. Yao, P. Yeh, J. Yoo, G. Young, N. Zhu,

N. Zobrist, D. Sank, A. Korotkov, Y. Chen, V. Smelyanskiy, Measurement-induced state transitions in a superconducting qubit: Within the rotating wave approximation (2022). arXiv:2212.05097.

[64] B. Royer, S. Singh, S. M. Girvin, Stabilization of Finite-Energy Gottesman-Kitaev-Preskill States, Phys. Rev. Lett. 125 (26) (2020) 260509. doi:10.1103/PhysRevLett.125.260509.

[65] B. de Neeve, T. L. Nguyen, T. Behrle, J. Home, Error correction of a logical grid state qubit by dissipative pumping, arXiv:2010.09681 [quant-ph] (Oct. 2020).

[66] C. Flühmann, T. L. Nguyen, M. Marinelli, V. Negnevitsky, K. Mehta, J. P. Home, Encoding a qubit in a trapped-ion mechanical oscillator, Nature 566 (7745) (2019) 513–517. doi:10.1038/s41586-019-0960-6.

[67] M. A. Nielsen, A simple formula for the average gate fidelity of a quantum dynamical operation, Physics Letters A 303 (4) (2002) 249–252. doi:10.1016/s0375-9601(02)01272-0.

[68] C. E. Shannon, The synthesis of two-terminal switching circuits, The Bell System Technical Journal 28 (1) (1949) 59–98. doi:10.1002/j.1538-7305.1949.tb03624.x.

[69] C. H. Bennett, Logical reversibility of computation, IBM Journal of Research and Development 17 (6) (1973) 525–532. doi:10.1147/rd.176.0525.

[70] R. Landauer, Irreversibility and heat generation in the computing process, IBM Journal of Research and Development 5 (3) (1961) 183–191. doi:10.1147/rd.53.0183.

[71] M. A. Nielsen, Neural Networks and Deep Learning, Determination Press, 2015.

[72] A. M. Childs, Y. Su, M. C. Tran, N. Wiebe, S. Zhu, Theory of trotter error with commutator scaling, Phys. Rev. X 11 (2021) 011020. doi:10.1103/PhysRevX.11.011020.

[73] S. L. Braunstein, P. van Loock, Quantum information with continuous variables, Rev. Mod. Phys. 77 (2) (2005) 513–577. `doi:10.1103/RevModPhys.77.513`.

[74] S. Lloyd, Universal quantum simulators, Science 273 (5278) (1996) 1073–1078. `doi:10.1126/science.273.5278.1073`.

[75] K. J. Ferris, A. J. Rasmusson, N. T. Bronn, O. Lanes, Quantum simulation on noisy superconducting quantum computers (2022). `arXiv:2209.02795`.

[76] P. Krantz, M. Kjaergaard, F. Yan, T. P. Orlando, S. Gustavsson, W. D. Oliver, A Quantum Engineer's Guide to Superconducting Qubits, Applied Physics Reviews 6 (2) (06 2019). `doi:10.1063/1.5089550`.

[77] D. D'Alessandro, Introduction to Quantum Control and Dynamics, CRC Press, 2008. `doi:10.1201/9781003051268`.

[78] N. Margolus, L. B. Levitin, The maximum speed of dynamical evolution, Physica D: Nonlinear Phenomena 120 (1) (1998) 188–195.

[79] T. Caneva, M. Murphy, T. Calarco, R. Fazio, S. Montangero, V. Giovannetti, G. E. Santoro, Optimal control at the quantum speed limit, Phys. Rev. Lett. 103 (2009) 240501. `doi:10.1103/PhysRevLett.103.240501`.

[80] S. Lloyd, S. Montangero, Information theoretical analysis of quantum optimal control, Phys. Rev. Lett. 113 (2014) 010502. `doi:10.1103/PhysRevLett.113.010502`.

[81] J. J. W. H. Sørensen, M. K. Pedersen, M. Munch, P. Haikka, J. H. Jensen, T. Planke, M. G. Andreasen, M. Gajdacz, K. Mølmer, A. Lieberoth, J. F. Sherson, Exploring the quantum speed limit with computer games, Nature 532 (7598) (2016) 210–213.

[82] D. E. Deutsch, Quantum computational networks, Proc. R. Soc. Lond. A 425 (1989) 73–90. `doi:10.1098/rspa.1989.0099`.

[83] D. P. DiVincenzo, Two-bit gates are universal for quantum computation, Phys. Rev. A 51 (1995) 1015–1022. doi:10.1103/PhysRevA.51.1015.

[84] A. Barenco, C. H. Bennett, R. Cleve, D. P. DiVincenzo, N. Margolus, P. Shor, T. Sleator, J. A. Smolin, H. Weinfurter, Elementary gates for quantum computation, Phys. Rev. A 52 (1995) 3457–3467. doi:10.1103/PhysRevA.52.3457.

[85] S. Lloyd, Almost any quantum logic gate is universal, Phys. Rev. Lett. 75 (1995) 346–349. doi:10.1103/PhysRevLett.75.346.

[86] D. E. Deutsch, A. Barenco, A. Ekert, Universality in quantum computation, Proc. R. Soc. Lond. A 449 (1995) 669–677. doi:0.1098/rspa.1995.0065.

[87] E. Bernstein, U. Vazirani, Quantum complexity theory, SIAM Journal on Computing 26 (5) (1997) 1411–1473.

[88] D. Gottesman, The heisenberg representation of quantum computers (Jun. 1998).

[89] S. Aaronson, D. Gottesman, Improved simulation of stabilizer circuits, Phys. Rev. A 70 (2004) 052328. doi:10.1103/PhysRevA.70.052328.

[90] D. Litinski, A game of surface codes: Large-scale quantum computing with lattice surgery, Quantum 3 (2019) 128. doi:10.22331/q-2019-03-05-128.

[91] A. Y. Kitaev, Quantum computations: algorithms and error correction, Russian Mathematical Surveys 52 (6) (1997) 1191. doi:10.1070/RM1997v052n06ABEH002155.

[92] C. M. Dawson, M. A. Nielsen, The solovay-kitaev algorithm, Quantum Info. Comput. 6 (1) (2006) 81–95.

[93] S. Aaronson, Introduction to quantum information science lecture notes (Fall 2018).

[94] A. M. Dalzell, S. McArdle, M. Berta, P. Bienias, C.-F. Chen, A. Gilyén, C. T. Hann, M. J. Kastoryano, E. T. Khabiboulline, A. Kubica, G. Salton, S. Wang, F. G. S. L. B.

ao, Quantum algorithms: A survey of applications and end-to-end complexities (2023). arXiv:2310.03011.

[95] I. Chuang, E. Crane, A. Eickbusch, S. M. Girvin, R. Li, Y. Liu, J. M. Martyn, J. Sinanan-Singh, S. Singh, K. C. Smith, M. B. Soley, N. Wiebe, Hybrid oscillator-qubit quantum processors: Instruction set architectures, abstract machine models, and applications, In Prep. (2024).

[96] S. Lloyd, S. L. Braunstein, Quantum Computation over Continuous Variables, Phys. Rev. Lett. 82 (8) (1999) 1784. doi:10.1103/PhysRevLett.82.1784.

[97] S. Krastanov, V. V. Albert, C. Shen, C.-L. Zou, R. W. Heeres, B. Vlastakis, R. J. Schoelkopf, L. Jiang, Universal control of an oscillator with dispersive coupling to a qubit, Phys. Rev. A 92 (4) (2015) 040303. doi:10.1103/PhysRevA.92.040303.

[98] J. Chen, J. L. Habif, Z. Dutton, R. Lazarus, S. Guha, Optical codeword demodulation with error rates below the standard quantum limit using a conditional nulling receiver, Nat. Photon. 6 (6) (2012) 374–379.

[99] V. V. Sivak, A. Eickbusch, H. Liu, B. Royer, I. Tsioutsios, M. H. Devoret, Model-Free Quantum Control with Reinforcement Learning, Phys. Rev. X 12 (2022) 011059. doi:10.1103/PhysRevX.12.011059.

[100] N. Khaneja, T. Reiss, C. Kehlet, T. Schulte-Herbrüggen, S. J. Glaser, Optimal control of coupled spin dynamics: Design of NMR pulse sequences by gradient ascent algorithms, Journal of Magnetic Resonance 172 (2) (2005) 296–305. doi:10.1016/j.jmr.2004.11.004.

[101] R. W. Heeres, P. Reinhold, N. Ofek, L. Frunzio, L. Jiang, M. H. Devoret, R. J. Schoelkopf, Implementing a universal gate set on a logical qubit encoded in an oscillator, Nat. Commun. 8 (1) (2017) 1–7. doi:10.1038/s41467-017-00045-1.

[102] P. Reinhold, Controlling error-correctable bosonic qubits, Phd thesis, Yale University (2019).

[103] V. V. Sivak, GKP machine learning, in prep (2021).

[104] W.-L. Ma, S. Puri, R. J. Schoelkopf, M. H. Devoret, S. Girvin, L. Jiang, Quantum control of bosonic modes with superconducting circuits, Science Bulletin 66 (17) (2021) 1789–1805. doi:10.1016/j.scib.2021.05.024.

[105] H. Ball, M. Biercuk, A. Carvalho, J. Chen, M. R. Hush, L. A. de Castro, L. Li, P. J. Liebermann, H. Slatyer, C. Edmunds, V. Frey, C. Hempel, A. Milne, Software tools for quantum control: Improving quantum computer performance through noise and error suppression, Quantum Science and Technology (2021). doi:10.1088/2058-9565/abdca6.

[106] W. H. Zurek, Decoherence, einselection, and the quantum origins of the classical, Reviews of Modern Physics 75 (3) (2003) 715–775. doi:10.1103/RevModPhys.75.715.

[107] C. Weedbrook, S. Pirandola, R. García-Patrón, N. J. Cerf, T. C. Ralph, J. H. Shapiro, S. Lloyd, Gaussian quantum information, Rev. Mod. Phys. 84 (2012) 621–669. doi:10.1103/RevModPhys.84.621.

[108] T. Tsunoda, J. D. Teoh, W. D. Kalfus, S. J. de Graaf, B. J. Chapman, J. C. Curtis, N. Thakur, S. M. Girvin, R. J. Schoelkopf, Error-detectable bosonic entangling gates with a noisy ancilla, PRX Quantum 4 (2023) 020354. doi:10.1103/PRXQuantum.4.020354.

[109] N. E. Frattini, V. V. Sivak, A. Lingenfelter, S. Shankar, M. H. Devoret, Optimizing the Nonlinearity and Dissipation of a SNAIL Parametric Amplifier for Dynamic Range, Phys. Rev. Appl. 10 (5) (2018) 054020. doi:10.1103/PhysRevApplied.10.054020.

[110] T. Hillmann, F. Quijandría, G. Johansson, A. Ferraro, S. Gasparinetti, G. Ferrini, Universal Gate Set for Continuous-Variable Quantum Computation with Microwave Circuits, Phys. Rev. Lett. 125 (16) (2020) 160501. doi:10.1103/PhysRevLett.125.160501.

[111] A. M. Eriksson, T. Sépulcre, M. Kervinen, T. Hillmann, M. Kudra, S. Dupouy, Y. Lu, M. Khanahmadi, J. Yang, C. C. Moreno, P. Delsing, S. Gasparinetti, Universal control of a bosonic mode via drive-activated native cubic interactions (2023). arXiv:2308.15320.

[112] C. Flühmann, V. Negnevitsky, M. Marinelli, J. P. Home, Sequential Modular Position and Momentum Measurements of a Trapped Ion Mechanical Oscillator, Phys. Rev. X 8 (2018) 021001. doi:10.1103/PhysRevX.8.021001.

[113] Q. Xie, H. Zhong, M. T. Batchelor, C. Lee, The quantum rabi model: solution and dynamics, Journal of Physics A: Mathematical and Theoretical 50 (11) (2017) 113001.

[114] A. Grimm, N. E. Frattini, S. Puri, S. O. Mundhada, S. Touzard, M. Mirrahimi, S. M. Girvin, S. Shankar, M. H. Devoret, Stabilization and operation of a Kerr-cat qubit, Nature 584 (7820) (2020) 205–209. doi:10.1038/s41586-020-2587-z.

[115] R. W. Heeres, B. Vlastakis, E. Holland, S. Krastanov, V. V. Albert, L. Frunzio, L. Jiang, R. J. Schoelkopf, Cavity State Manipulation Using Photon-Number Selective Phase Gates, Physical Review Letters 115 (13) (2015) 137002. doi:10.1103/PhysRevLett.115.137002.

[116] A. A. Houck, D. I. Schuster, J. M. Gambetta, J. A. Schreier, B. R. Johnson, J. M. Chow, L. Frunzio, J. Majer, M. H. Devoret, S. M. Girvin, R. J. Schoelkopf, Generating single microwave photons in a circuit, Nature 449 (7160) (2007) 328–331.

[117] Z. Wang, A. H. Safavi-Naeini, Quantum control and noise protection of a Floquet $0-\pi$ qubit (2023). arXiv:2304.05601.

[118] Z. Leghtas, G. Kirchmair, B. Vlastakis, M. H. Devoret, R. J. Schoelkopf, M. Mirrahimi, Deterministic protocol for mapping a qubit to coherent state superpositions in a cavity, Physical Review A 87 (4) (2013) 042315. doi:10.1103/PhysRevA.87.042315.

[119] C. Shen, K. Noh, V. V. Albert, S. Krastanov, M. H. Devoret, R. J. Schoelkopf, S. M. Girvin, L. Jiang, Quantum channel construction with circuit quantum electrodynamics, Phys. Rev. B 95 (2017) 134501. doi:10.1103/PhysRevB.95.134501.

[120] C. K. Law, J. H. Eberly, Arbitrary control of a quantum electromagnetic field, Phys. Rev. Lett. 76 (7) (1996) 1055–1058. doi:10.1103/PhysRevLett.76.1055.

[121] Y. Y. Gao, B. J. Lester, Y. Zhang, C. Wang, S. Rosenblum, L. Frunzio, L. Jiang, S. M. Girvin, R. J. Schoelkopf, Programmable interference between two microwave quantum memories, Phys. Rev. X 8 (2018) 021073. doi:10.1103/PhysRevX.8.021073.

[122] B. J. Chapman, S. J. de Graaf, S. H. Xue, Y. Zhang, J. Teoh, J. C. Curtis, T. Tsunoda, A. Eickbusch, A. P. Read, A. Koottandavida, S. O. Mundhada, L. Frunzio, M. Devoret, S. Girvin, R. Schoelkopf, High-on-off-ratio beam-splitter interaction for gates on bosonically encoded qubits, PRX Quantum 4 (2023) 020355. doi:10.1103/PRXQuantum.4.020355.

[123] K. W. Murch, U. Vool, D. Zhou, S. J. Weber, S. M. Girvin, I. Siddiqi, Cavity-Assisted Quantum Bath Engineering, Physical Review Letters 109 (18) (2012) 183602. doi:10.1103/PhysRevLett.109.183602.

[124] C. S. Wang, N. E. Frattini, B. J. Chapman, S. Puri, S. M. Girvin, M. H. Devoret, R. J. Schoelkopf, Observation of wave-packet branching through an engineered conical intersection, Phys. Rev. X 13 (2023) 011008. doi:10.1103/PhysRevX.13.011008.

[125] M. Hofheinz, H. Wang, M. Ansmann, R. C. Bialczak, E. Lucero, M. Neeley, A. D. O'Connell, D. Sank, J. Wenner, J. M. Martinis, A. N. Cleland, Synthesizing arbitrary

quantum states in a superconducting resonator, Nature 459 (7246) (2009) 546–549. doi:10.1038/nature08005.

[126] L. Sun, A. Petrenko, Z. Leghtas, B. Vlastakis, G. Kirchmair, K. M. Sliwa, A. Narla, M. Hatridge, S. Shankar, J. Blumoff, L. Frunzio, M. Mirrahimi, M. H. Devoret, R. J. Schoelkopf, Tracking photon jumps with repeated quantum non-demolition parity measurements, Nature 511 (7510) (2014) 444–448.

[127] N. Ezzell, B. Pokharel, L. Tewala, G. Quiroz, D. A. Lidar, Dynamical decoupling for superconducting qubits: a performance survey (2023). arXiv:2207.03670.

[128] T. Fösel, S. Krastanov, F. Marquardt, L. Jiang, Efficient cavity control with SNAP gates, arXiv:2004.14256 [quant-ph] (Apr. 2020).

[129] M. Kudra, M. Kervinen, I. Strandberg, S. Ahmed, M. Scigliuzzo, A. Osman, D. P. Lozano, M. O. Tholén, R. Borgani, D. B. Haviland, et al., Robust Preparation of Wigner-Negative States with Optimized SNAP-Displacement Sequences, PRX Quantum 3 (2022) 030301. doi:10.1103/PRXQuantum.3.030301.

[130] C. Arenz, D. I. Bondar, D. Burgarth, C. Cormick, H. Rabitz, Amplification of quadratic hamiltonians, Quantum 4 (2020) 271. doi:10.22331/q-2020-05-25-271.

[131] B. J. Chapman, E. I. Rosenthal, J. Kerckhoff, B. A. Moores, L. R. Vale, J. A. B. Mates, G. C. Hilton, K. Lalumière, A. Blais, K. W. Lehnert, Widely Tunable On-Chip Microwave Circulator for Superconducting Quantum Circuits, Phys. Rev. X 7 (2017) 041043. doi:10.1103/PhysRevX.7.041043.

[132] S. Touzard, A. Kou, N. E. Frattini, V. V. Sivak, S. Puri, A. Grimm, L. Frunzio, S. Shankar, M. H. Devoret, Gated Conditional Displacement Readout of Superconducting Qubits, Physical Review Letters 122 (8) (2019) 080502. doi:10.1103/PhysRevLett.122.080502.

[133] J. Tilly, H. Chen, S. Cao, D. Picozzi, K. Setia, Y. Li, E. Grant, L. Wossnig, I. Rungger, G. H. Booth, J. Tennyson, The variational quantum eigensolver: A review of methods and best practices, Physics Reports 986 (2022) 1–128.

[134] B. Zhang, Q. Zhuang, Energy-dependent barren plateau in bosonic variational quantum circuits (2023). `arXiv:2305.01799`.

[135] D. P. Kingma, J. Ba, Adam: A Method for Stochastic Optimization, arXiv:1412.6980 [cs] (Jan. 2017).

[136] Y. Ma, Y. Xu, X. Mu, W. Cai, L. Hu, W. Wang, X. Pan, H. Wang, Y. P. Song, C.-L. Zou, L. Sun, Error-transparent operations on a logical qubit protected by quantum error correction, Nature Physics 16 (8) (2020) 827–831. `doi:10.1038/s41567-020-0893-x`.

[137] M. Boissonneault, J. M. Gambetta, A. Blais, Improved superconducting qubit readout by qubit-induced nonlinearities, Phys. Rev. Lett. 105 (2010) 100504. `doi:10.1103/PhysRevLett.105.100504`.

[138] M. Boissonneault, J. M. Gambetta, A. Blais, Dispersive regime of circuit QED: Photon-dependent qubit dephasing and relaxation rates, Physical Review A 79 (1) (2009) 013819. `doi:10.1103/PhysRevA.79.013819`.

[139] E. M. Purcell, Spontaneous Emission Probabilities at Radio Frequencies, Physical Review 69 (1946) 681. `doi:10.1103/PhysRev.69.674.2`.

[140] E. Jeffrey, D. Sank, J. Y. Mutus, T. C. White, J. Kelly, R. Barends, Y. Chen, Z. Chen, B. Chiaro, A. Dunsworth, A. Megrant, P. J. J. O'Malley, C. Neill, P. Roushan, A. Vainsencher, J. Wenner, A. N. Cleland, J. M. Martinis, Fast accurate state measurement with superconducting qubits, Phys. Rev. Lett. 112 (2014) 190504. `doi:10.1103/PhysRevLett.112.190504`.

[141] E. A. Sete, J. M. Martinis, A. N. Korotkov, Quantum theory of a bandpass purcell filter for qubit readout, Phys. Rev. A 92 (2015) 012325. doi:10.1103/PhysRevA.92.012325.

[142] Z. K. Minev, Z. Leghtas, S. O. Mundhada, L. Christakis, I. M. Pop, M. H. Devoret, Energy-participation quantization of Josephson circuits, arXiv:2010.00620 [cond-mat, physics:quant-ph] (Feb. 2021).

[143] S. E. Nigg, H. Paik, B. Vlastakis, G. Kirchmair, S. Shankar, L. Frunzio, M. H. Devoret, R. J. Schoelkopf, S. M. Girvin, Black-Box Superconducting Circuit Quantization, Physical Review Letters 108 (24) (2012) 240502. doi:10.1103/PhysRevLett.108.240502.

[144] K. Serniak, M. Hays, G. de Lange, S. Diamond, S. Shankar, L. D. Burkhart, L. Frunzio, M. Houzet, M. H. Devoret, Hot nonequilibrium quasiparticles in transmon qubits, Phys. Rev. Lett. 121 (2018) 157701. doi:10.1103/PhysRevLett.121.157701.

[145] S. Diamond, V. Fatemi, M. Hays, H. Nho, P. D. Kurilovich, T. Connolly, V. R. Joshi, K. Serniak, L. Frunzio, L. I. Glazman, M. H. Devoret, Distinguishing parity-switching mechanisms in a superconducting qubit, PRX Quantum 3 (2022) 040304. doi:10.1103/PRXQuantum.3.040304.

[146] C.-H. Liu, D. C. Harrison, S. Patel, C. D. Wilen, O. Rafferty, A. Shearrow, A. Ballard, V. Iaia, J. Ku, B. L. T. Plourde, R. McDermott, Quasiparticle poisoning of superconducting qubits from resonant absorption of pair-breaking photons (2022). arXiv:2203.06577.

[147] D. H. Slichter, R. Vijay, S. J. Weber, S. Boutin, M. Boissonneault, J. M. Gambetta, A. Blais, I. Siddiqi, Measurement-induced qubit state mixing in circuit qed from up-converted dephasing noise, Phys. Rev. Lett. 109 (2012) 153601. doi:10.1103/PhysRevLett.109.153601.

[148] Z. Wang, S. Shankar, Z. Minev, P. Campagne-Ibarcq, A. Narla, M. Devoret, Cavity Attenuators for Superconducting Qubits, Physical Review Applied 11 (1) (2019) 014031. `doi:10.1103/PhysRevApplied.11.014031`.

[149] M. D. Reed, L. DiCarlo, B. R. Johnson, L. Sun, D. I. Schuster, L. Frunzio, R. J. Schoelkopf, High-Fidelity Readout in Circuit Quantum Electrodynamics Using the Jaynes-Cummings Nonlinearity, Physical Review Letters 105 (17) (2010) 173601. `doi:10.1103/PhysRevLett.105.173601`.

[150] R. Shillito, A. Petrescu, J. Cohen, J. Beall, M. Hauru, M. Ganahl, A. G. Lewis, G. Vidal, A. Blais, Dynamics of transmon ionization, Phys. Rev. Appl. 18 (2022) 034031. `doi:10.1103/PhysRevApplied.18.034031`.

[151] L. Verney, R. Lescanne, M. H. Devoret, Z. Leghtas, M. Mirrahimi, Structural Instability of Driven Josephson Circuits Prevented by an Inductive Shunt, Physical Review Applied 11 (2) (2019) 024003. `doi:10.1103/PhysRevApplied.11.024003`.

[152] J. Gao, The physics of superconducting microwave resonators, Phd thesis, California Institute of Technology (2008).

[153] J. M. Martinis, K. B. Cooper, R. McDermott, M. Steffen, M. Ansmann, K. D. Osborn, K. Cicak, S. Oh, D. P. Pappas, R. W. Simmonds, C. C. Yu, Decoherence in josephson qubits from dielectric loss, Phys. Rev. Lett. 95 (2005) 210503. `doi:10.1103/PhysRevLett.95.210503`.

[154] J. M. Martinis, Surface loss calculations and design of a superconducting transmon qubit with tapered wiring, npj Quantum Information 8 (1) (2022) 26.

[155] W. A. Phillips, Tunneling states in amorphous solids, Journal of Low Temperature Physics 7 (3) (1972) 351–360.

[156] B. I. H. P. w. Anderson, c. M. Varma, Anomalous low-temperature thermal properties of glasses and spin glasses, The Philosophical Magazine: A Journal of Theoretical Experimental and Applied Physics 25 (1) (1972) 1–9.

[157] L. Faoro, L. B. Ioffe, Internal loss of superconducting resonators induced by interacting two-level systems, Phys. Rev. Lett. 109 (2012) 157005. `doi:10.1103/PhysRevLett.109.157005`.

[158] L. Faoro, L. B. Ioffe, Interacting tunneling model for two-level systems in amorphous materials and its predictions for their dephasing and noise in superconducting microresonators, Phys. Rev. B 91 (2015) 014201. `doi:10.1103/PhysRevB.91.014201`.

[159] I. Siddiqi, Engineering high-coherence superconducting qubits, Nature Reviews Materials 6 (10) (2021) 875–891.

[160] P. V. Klimov, J. Kelly, Z. Chen, M. Neeley, A. Megrant, B. Burkett, R. Barends, K. Arya, B. Chiaro, Y. Chen, A. Dunsworth, A. Fowler, B. Foxen, C. Gidney, M. Giustina, R. Graff, T. Huang, E. Jeffrey, E. Lucero, J. Y. Mutus, O. Naaman, C. Neill, C. Quintana, P. Roushan, D. Sank, A. Vainsencher, J. Wenner, T. C. White, S. Boixo, R. Babbush, V. N. Smelyanskiy, H. Neven, J. M. Martinis, Fluctuations of Energy-Relaxation Times in Superconducting Qubits, Physical Review Letters 121 (9) (2018) 090502. `doi:10.1103/PhysRevLett.121.090502`.

[161] T. Thorbeck, A. Eddins, I. Lauer, D. T. McClure, M. Carroll, Two-level-system dynamics in a superconducting qubit due to background ionizing radiation, PRX Quantum 4 (2023) 020356. `doi:10.1103/PRXQuantum.4.020356`.

[162] D. Niepce, J. J. Burnett, M. Kudra, J. H. Cole, J. Bylander, Stability of superconducting resonators: Motional narrowing and the role of Landau-Zener driving of two-level defects, Sci. Adv. 7 (39) (2021) eabh0462. `doi:10.1126/sciadv.abh0462`.

[163] J. Cohen, A. Petrescu, R. Shillito, A. Blais, Reminiscence of classical chaos in driven transmons, PRX Quantum 4 (2023) 020312. `doi:10.1103/PRXQuantum.4.020312`.

[164] J. Venkatraman, X. Xiao, R. G. Cortiñas, A. Eickbusch, M. H. Devoret, Static effective hamiltonian of a rapidly driven nonlinear system, Physical Review Letters 129 (10) (Aug. 2022). `doi:10.1103/physrevlett.129.100601`.

[165] C. Smith, Design of protected superconducting qubits, Phd thesis, Yale University (2019).

[166] Z. K. Minev, S. O. Mundhada, S. Shankar, P. Reinhold, R. Gutiérrez-Jáuregui, R. J. Schoelkopf, M. Mirrahimi, H. J. Carmichael, M. H. Devoret, To catch and reverse a quantum jump mid-flight, Nature 570 (7760) (2019) 200–204. `doi:10.1038/s41586-019-1287-z`.

[167] J. J. Burnett, A. Bengtsson, M. Scigliuzzo, D. Niepce, M. Kudra, P. Delsing, J. Bylander, Decoherence benchmarking of superconducting qubits, npj Quantum Information 5 (1) (2019) 1–8. `doi:10.1038/s41534-019-0168-5`.

[168] M. Carroll, S. Rosenblatt, P. Jurcevic, I. Lauer, A. Kandala, Dynamics of superconducting qubit relaxation times, arXiv:2105.15201 [cond-mat, physics:quant-ph] (May 2021).

[169] S. Chaturvedi, M. S. Sriram, V. Srinivasan, Berry's phase for coherent states, Journal of Physics A: Mathematical and General 20 (16) (1987) L1071–l1075. `doi:10.1088/0305-4470/20/16/007`.

[170] G. Vacanti, R. Fazio, M. S. Kim, G. M. Palma, M. Paternostro, V. Vedral, Geometric-phase backaction in a mesoscopic qubit-oscillator system, Physical Review A 85 (2) (2012) 022129. `doi:10.1103/PhysRevA.85.022129`.

[171] M. Pechal, S. Berger, A. A. Abdumalikov, J. M. Fink, J. A. Mlynek, L. Steffen, A. Wallraff, S. Filipp, Geometric Phase and Nonadiabatic Effects in an Electronic Harmonic Oscillator, Physical Review Letters 108 (17) (2012) 170401. `doi:10.1103/PhysRevLett.108.170401`.

[172] C. Song, S.-B. Zheng, P. Zhang, K. Xu, L. Zhang, Q. Guo, W. Liu, D. Xu, H. Deng, K. Huang, D. Zheng, X. Zhu, H. Wang, Continuous-variable geometric phase and its manipulation for quantum computation in a superconducting circuit, Nature Communications 8 (1) (2017) 1061. `doi:10.1038/s41467-017-01156-5`.

[173] S. Haroche, J. Raimond, Exploring the Quantum: Atoms, Cavities, and Photons, Oxford Graduate Texts, OUP Oxford, 2013.

[174] L. G. Lutterbach, L. Davidovich, Method for direct measurement of the wigner function in cavity qed and ion traps, Phys. Rev. Lett. 78 (1997) 2547–2550. `doi:10.1103/PhysRevLett.78.2547`.

[175] C. Flühmann, J. P. Home, Direct Characteristic-Function Tomography of Quantum States of the Trapped-Ion Motional Oscillator, Physical Review Letters 125 (4) (2020) 043602. `doi:10.1103/PhysRevLett.125.043602`.

[176] M. Pechal, L. Huthmacher, C. Eichler, S. Zeytinoğlu, A. A. Abdumalikov, S. Berger, A. Wallraff, S. Filipp, Microwave-Controlled Generation of Shaped Single Photons in Circuit Quantum Electrodynamics, Physical Review X 4 (4) (2014) 041010. `doi:10.1103/PhysRevX.4.041010`.

[177] S. Rosenblum, Y. Y. Gao, P. Reinhold, C. Wang, C. J. Axline, L. Frunzio, S. M. Girvin, L. Jiang, M. Mirrahimi, M. H. Devoret, R. J. Schoelkopf, A CNOT gate between multiphoton qubits encoded in two cavities, Nature Communications 9 (1) (2018) 652. `doi:10.1038/s41467-018-03059-5`.

[178] W. H. Zurek, J. P. Paz, Decoherence, chaos, and the second law, Physical Review Letters 72 (16) (1994) 2508–2511. doi:10.1103/PhysRevLett.72.2508.

[179] Z. K. Minev, Z. Leghtas, S. O. Mundhada, L. Christakis, I. M. Pop, M. H. Devoret, Energy-participation quantization of Josephson circuits, npj Quantum Information 7 (1) (2021) 1–11. doi:10.1038/s41534-021-00461-8.

[180] F. Motzoi, J. M. Gambetta, P. Rebentrost, F. K. Wilhelm, Simple pulses for elimination of leakage in weakly nonlinear qubits, Phys. Rev. Lett. 103 (11) (2009) 110501. doi:10.1103/PhysRevLett.103.110501.

[181] Z. Chen, J. Kelly, C. Quintana, R. Barends, B. Campbell, Y. Chen, B. Chiaro, A. Dunsworth, A. G. Fowler, E. Lucero, E. Jeffrey, A. Megrant, J. Mutus, M. Neeley, C. Neill, P. J. J. O'Malley, P. Roushan, D. Sank, A. Vainsencher, J. Wenner, T. C. White, A. N. Korotkov, J. M. Martinis, Measuring and suppressing quantum state leakage in a superconducting qubit, Phys. Rev. Lett. 116 (2) (2016) 020501. doi:10.1103/PhysRevLett.116.020501.

[182] C. J. Axline, L. D. Burkhart, W. Pfaff, M. Zhang, K. Chou, P. Campagne-Ibarcq, P. Reinhold, L. Frunzio, S. M. Girvin, L. Jiang, M. H. Devoret, R. J. Schoelkopf, On-demand quantum state transfer and entanglement between remote microwave cavity memories, Nature Physics 14 (7) (2018) 705–710. doi:10.1038/s41567-018-0115-y.

[183] L. Hu, Y. Ma, W. Cai, X. Mu, Y. Xu, W. Wang, Y. Wu, H. Wang, Y. P. Song, C. L. Zou, et al., Quantum error correction and universal gate set operation on a binomial bosonic logical qubit, Nat. Phys. 15 (5) (2019) 503–508. doi:10.1038/s41567-018-0414-3.

[184] W. Wang, Y. Wu, Y. Ma, W. Cai, L. Hu, X. Mu, Y. Xu, Z.-J. Chen, H. Wang, Y. P. Song, H. Yuan, C.-L. Zou, L.-M. Duan, L. Sun, Heisenberg-limited single-mode quantum metrology in a superconducting circuit, Nature Communications 10 (1) (2019) 4382. doi:10.1038/s41467-019-12290-7.

[185] J. M. Gertler, B. Baker, J. Li, S. Shirol, J. Koch, C. Wang, Protecting a bosonic qubit with autonomous quantum error correction, Nature 590 (7845) (2021) 243–248. doi:10.1038/s41586-021-03257-0.

[186] J. C. Curtis, C. T. Hann, S. S. Elder, C. S. Wang, L. Frunzio, L. Jiang, R. J. Schoelkopf, Single-shot number-resolved detection of microwave photons with error mitigation, Physical Review A 103 (2) (2021) 023705. doi:10.1103/PhysRevA.103.023705.

[187] Y. Baum, M. Amico, S. Howell, M. Hush, M. Liuzzi, P. Mundada, T. Merkh, A. R. Carvalho, M. J. Biercuk, Experimental Deep Reinforcement Learning for Error-Robust Gate-Set Design on a Superconducting Quantum Computer, PRX Quantum 2 (4) (2021) 040324. doi:10.1103/PRXQuantum.2.040324.

[188] R. Dassonneville, R. Assouly, T. Peronnin, A. Clerk, A. Bienfait, B. Huard, Dissipative Stabilization of Squeezing Beyond 3 dB in a Microwave Mode, PRX Quantum 2 (2) (2021) 020323. doi:10.1103/PRXQuantum.2.020323.

[189] J. Hastrup, K. Park, R. Filip, U. L. Andersen, Unconditional Preparation of Squeezed Vacuum from Rabi Interactions, Physical Review Letters 126 (15) (2021) 153602. doi:10.1103/PhysRevLett.126.153602.

[190] W. Wang, L. Hu, Y. Xu, K. Liu, Y. Ma, S.-B. Zheng, R. Vijay, Y. P. Song, L.-M. Duan, L. Sun, Converting Quasiclassical States into Arbitrary Fock State Superpositions in a Superconducting Circuit, Physical Review Letters 118 (22) (2017) 223604. doi:10.1103/PhysRevLett.118.223604.

[191] K. Duivenvoorden, B. M. Terhal, D. Weigand, Single-mode displacement sensor, Phys. Rev. A 95 (1) (2017) 012305. doi:10.1103/PhysRevA.95.012305.

[192] M. Paris, J. Rehacek, Quantum State Estimation, Springer Science & Business Media, 2004.

[193] M. H. Michael, M. Silveri, R. T. Brierley, V. V. Albert, J. Salmilehto, L. Jiang, S. M. Girvin, New Class of Quantum Error-Correcting Codes for a Bosonic Mode, Physical Review X 6 (3) (2016) 031006. `doi:10.1103/PhysRevX.6.031006`.

[194] J. Hastrup, K. Park, J. B. Brask, R. Filip, U. L. Andersen, Measurement-free preparation of grid states, npj Quantum Information 7 (1) (2021) 17. `doi:10.1038/s41534-020-00353-3`.

[195] C. Vuillot, H. Asasi, Y. Wang, L. P. Pryadko, B. M. Terhal, Quantum error correction with the toric Gottesman-Kitaev-Preskill code, Phys. Rev. A 99 (3) (2019) 032344. `doi:10.1103/PhysRevA.99.032344`.

[196] K. Noh, C. Chamberland, F. G. Brandão, Low-overhead fault-tolerant quantum error correction with the surface-GKP code, PRX Quantum 3 (1) (2022) 010315. `doi:10.1103/PRXQuantum.3.010315`.

[197] N. C. Menicucci, Fault-Tolerant Measurement-Based Quantum Computing with Continuous-Variable Cluster States, Physical Review Letters 112 (12) (2014) 120504. `doi:10.1103/PhysRevLett.112.120504`.

[198] S. Gustavsson, O. Zwier, J. Bylander, F. Yan, F. Yoshihara, Y. Nakamura, T. P. Orlando, W. D. Oliver, Improving quantum gate fidelities by using a qubit to measure microwave pulse distortions, Phys. Rev. Lett. 110 (4) (2013) 040502. `doi:10.1103/PhysRevLett.110.040502`.

[199] M. A. Rol, C. C. Bultink, T. E. O'Brien, S. R. de Jong, L. S. Theis, X. Fu, F. Luthi, R. F. L. Vermeulen, J. C. de Sterke, A. Bruno, D. Deurloo, R. N. Schouten, F. K. Wilhelm, L. DiCarlo, Restless Tuneup of High-Fidelity Qubit Gates, Physical Review Applied 7 (4) (2017) 041001. `doi:10.1103/PhysRevApplied.7.041001`.

[200] M. Jerger, A. Kulikov, Z. Vasselin, A. Fedorov, *In Situ* Characterization of Qubit Control Lines: A Qubit as a Vector Network Analyzer, Physical Review Letters 123 (15) (2019) 150501. doi:10.1103/PhysRevLett.123.150501.

[201] A. Lingenfelter, D. Roberts, A. A. Clerk, Unconditional Fock state generation using arbitrarily weak photonic nonlinearities, Science Advances 7 (48) (2021) eabj1916. doi:10.1126/sciadv.abj1916.

[202] P. C. Haljan, K.-A. Brickman, L. Deslauriers, P. J. Lee, C. Monroe, Spin-Dependent Forces on Trapped Ions for Phase-Stable Quantum Gates and Entangled States of Spin and Motion, Physical Review Letters 94 (15) (2005) 153602. doi:10.1103/PhysRevLett.94.153602.

[203] A. R. Calderbank, P. W. Shor, Good quantum error-correcting codes exist, Phys. Rev. A 54 (1996) 1098–1105. doi:10.1103/PhysRevA.54.1098.

[204] C. H. Bennett, D. P. DiVincenzo, J. A. Smolin, W. K. Wootters, Mixed-state entanglement and quantum error correction, Phys. Rev. A 54 (1996) 3824–3851. doi:10.1103/PhysRevA.54.3824.

[205] R. Laflamme, C. Miquel, J. P. Paz, W. H. Zurek, Perfect quantum error correcting code, Phys. Rev. Lett. 77 (1996) 198–201. doi:10.1103/PhysRevLett.77.198.

[206] A. M. Steane, Error correcting codes in quantum theory, Phys. Rev. Lett. 77 (1996) 793–797. doi:10.1103/PhysRevLett.77.793.

[207] A. M. Steane, Multiple-particle interference and quantum error correction, Proc. R. Soc. Lond. A. 452 (1996) 2551–2577. doi:http://doi.org/10.1098/rspa.1996.0136.

[208] D. Gottesman, Class of quantum error-correcting codes saturating the quantum hamming bound, Phys. Rev. A 54 (1996) 1862–1868. doi:10.1103/PhysRevA.54.1862.

[209] S. B. Bravyi, A. Y. Kitaev, Quantum codes on a lattice with boundary (1998). arXiv:quant-ph/9811052.

[210] Y. D. Lensky, K. Kechedzhi, I. Aleiner, E.-A. Kim, Graph gauge theory of mobile non-abelian anyons in a qubit stabilizer code, Annals of Physics 452 (2023) 169286.

[211] D. Lidar, T. Brun, Quantum Error Correction, Cambridge University Press, 2013.

[212] S. M. Girvin, Introduction to quantum error correction and fault tolerance, SciPost Phys. Lect. Notes (2023) 70doi:10.21468/SciPostPhysLectNotes.70.

[213] A. Joshi, K. Noh, Y. Y. Gao, Quantum information processing with bosonic qubits in circuit QED, Quantum Sci. Technol. 6 (3) (2021) 033001. doi:10.1088/2058-9565/abe989.

[214] W. Cai, Y. Ma, W. Wang, C.-L. Zou, L. Sun, Bosonic quantum error correction codes in superconducting quantum circuits, Fundamental Research 1 (1) (2021) 50–67. doi:10.1016/j.fmre.2020.12.006.

[215] J. Harrington, J. Preskill, Achievable rates for the Gaussian quantum channel, Phys. Rev. A 64 (6) (2001) 062301. doi:10.1103/PhysRevA.64.062301.

[216] B. Royer, S. Singh, S. Girvin, Encoding Qubits in Multimode Grid States, PRX Quantum 3 (2022) 010335. doi:10.1103/PRXQuantum.3.010335.

[217] J. Conrad, J. Eisert, F. Arzani, Gottesman-Kitaev-Preskill codes: A lattice perspective, Quantum 6 (2022) 648. doi:10.22331/q-2022-02-10-648.

[218] J. Conrad, J. Eisert, J.-P. Seifert, Good Gottesman-Kitaev-Preskill codes from the NTRU cryptosystem (2023). arXiv:2303.02432.

[219] M. Lin, C. Chamberland, K. Noh, Closest lattice point decoding for multimode Gottesman-Kitaev-Preskill codes (2023). arXiv:2303.04702.

[220] K. Noh, C. Chamberland, F. G. S. L. Brandão, Low overhead fault-tolerant quantum error correction with the surface-GKP code, arXiv:2103.06994 [quant-ph] (Mar. 2021).

[221] E. Knill, R. Laflamme, Theory of quantum error-correcting codes, Phys. Rev. A 55 (1997) 900–911. doi:10.1103/PhysRevA.55.900.

[222] D. W. Leung, M. A. Nielsen, I. L. Chuang, Y. Yamamoto, Approximate quantum error correction can lead to better codes, Phys. Rev. A 56 (1997) 2567–2573. doi:10.1103/PhysRevA.56.2567.

[223] K. Noh, S. M. Girvin, L. Jiang, Encoding an Oscillator into Many Oscillators, Phys. Rev. Lett. 125 (2020) 080503. doi:10.1103/PhysRevLett.125.080503.

[224] J. Hastrup, U. L. Andersen, Improved readout of qubit-coupled Gottesman–Kitaev–Preskill states, Quantum Sci. Technol. 6 (3) (2021) 035016. doi:10.1088/2058-9565/ac070d.

[225] J. Conrad, Twirling and Hamiltonian engineering via dynamical decoupling for Gottesman-Kitaev-Preskill quantum computing, Phys. Rev. A 103 (2) (2021) 022404. doi:10.1103/PhysRevA.103.022404.

[226] M. Rymarz, S. Bosco, A. Ciani, D. P. DiVincenzo, Hardware-Encoding Grid States in a Nonreciprocal Superconducting Circuit, Phys. Rev. X 11 (2021) 011032. doi:10.1103/PhysRevX.11.011032.

[227] X. C. Kolesnikow, R. W. Bomantara, A. C. Doherty, A. L. Grimsmo, Gottesman-Kitaev-Preskill state preparation using periodic driving (2023). arXiv:2303.03541.

[228] M. A. Nielsen, A simple formula for the average gate fidelity of a quantum dynamical operation, Phys. Lett. A 303 (4) (2002) 249–252. doi:10.1016/s0375-9601\%2802\%2901272-0.

[229] Z. Ni, S. Li, X. Deng, Y. Cai, L. Zhang, W. Wang, Z.-B. Yang, H. Yu, F. Yan, S. Liu, et al., Beating the break-even point with a discrete-variable-encoded logical qubit, Nature 616 (7955) (2023) 56–60. doi:10.1038/s41586-023-05784-4.

[230] A. P. M. Place, L. V. H. Rodgers, P. Mundada, B. M. Smitham, M. Fitzpatrick, Z. Leng, A. Premkumar, J. Bryon, A. Vrajitoarea, S. Sussman, et al., New material platform for superconducting transmon qubits with coherence times exceeding 0.3 milliseconds, Nat. Commun. 12 (1) (2021) 1779. doi:10.1038/s41467-021-22030-5.

[231] I. Rojkov, P. M. Röggla, M. Wagener, M. Fontboté-Schmidt, S. Welte, J. Home, F. Reiter, Two-qubit operations for finite-energy Gottesman-Kitaev-Preskill encodings (2023). arXiv:2305.05262.

[232] V. Sivak, N. Frattini, V. Joshi, A. Lingenfelter, S. Shankar, M. Devoret, Kerr-Free Three-Wave Mixing in Superconducting Quantum Circuits, Phys. Rev. Appl. 11 (2019) 054060. doi:10.1103/PhysRevApplied.11.054060.

[233] B. J. Chapman, S. J. de Graaf, S. H. Xue, Y. Zhang, J. Teoh, J. C. Curtis, T. Tsunoda, A. Eickbusch, A. P. Read, A. Koottandavida, et al., A high on-off ratio beamsplitter interaction for gates on bosonically encoded qubits (2022). arXiv:2212.11929.

[234] Y. Lu, A. Maiti, J. W. O. Garmon, S. Ganjam, Y. Zhang, J. Claes, L. Frunzio, S. M. Girvin, R. J. Schoelkopf, A high-fidelity microwave beamsplitter with a parity-protected converter (2023). arXiv:2303.00959.

[235] Y. Ye, K. Peng, M. Naghiloo, G. Cunningham, K. P. O'Brien, Engineering Purely Nonlinear Coupling between Superconducting Qubits Using a Quarton, Phys. Rev. Lett. 127 (2021) 050502. doi:10.1103/PhysRevLett.127.050502.

[236] T.-C. Chien, O. Lanes, C. Liu, X. Cao, P. Lu, S. Motz, G. Liu, D. Pekker, M. Hatridge, Multiparametric amplification and qubit measurement with a Kerr-free Josephson ring modulator, Phys. Rev. A 101 (2020) 042336. doi:10.1103/PhysRevA.101.042336.

[237] C. Lledó, R. Dassonneville, A. Moulinas, J. Cohen, R. Shillito, A. Bienfait, B. Huard, A. Blais, Cloaking a qubit in a cavity, Nature Communications 14 (1) (2023) 6313.

[238] S. Sheldon, E. Magesan, J. M. Chow, J. M. Gambetta, Procedure for systematically tuning up cross-talk in the cross-resonance gate, Phys. Rev. A 93 (2016) 060302. doi:10.1103/PhysRevA.93.060302.

[239] S. Rosenblum, P. Reinhold, M. Mirrahimi, L. Jiang, L. Frunzio, R. J. Schoelkopf, Fault-tolerant detection of a quantum error, Science 361 (6399) (2018) 266–270. doi:10.1126/science.aat3996.

[240] J. D. Teoh, P. Winkel, H. K. Babla, B. J. Chapman, J. Claes, S. J. de Graaf, J. W. O. Garmon, W. D. Kalfus, Y. Lu, A. Maiti, K. Sahay, N. Thakur, T. Tsunoda, S. H. Xue, L. Frunzio, S. M. Girvin, S. Puri, R. J. Schoelkopf, Dual-rail encoding with superconducting cavities (2022). arXiv:2212.12077.

[241] C. M. Caves, Quantum limits on noise in linear amplifiers, Phys. Rev. D 26 (1982) 1817–1839. doi:10.1103/PhysRevD.26.1817.

[242] A. A. Clerk, D. W. Utami, Using a qubit to measure photon-number statistics of a driven thermal oscillator, Physical Review A 75 (4) (2007) 042302. doi:10.1103/PhysRevA.75.042302.

[243] Z. Li, D. Su, Correcting biased noise using gottesman-kitaev-preskill repetition code with noisy ancilla (2023). arXiv:2308.01549.

[244] J. Zhang, Y.-C. Wu, G.-P. Guo, Concatenation of the Gottesman-Kitaev-Preskill code with the XZZX surface code, Phys. Rev. A 107 (2023) 062408. doi:10.1103/PhysRevA.107.062408.

[245] C. Siegele, P. Campagne-Ibarcq, Robust suppression of noise propagation in GKP error-correction (2023). arXiv:2302.12088.

[246] J. Teoh, Error detected operations for bosonic quantum information processing, Phd thesis, Yale university (2023).

[247] S. S. Bullock, G. K. Brennen, Qudit surface codes and gauge theory with finite cyclic groups, Journal of Physics A: Mathematical and Theoretical 40 (13) (2007) 3481.

[248] H. Watanabe, M. Cheng, Y. Fuji, Ground state degeneracy on torus in a family of ZN toric code, Journal of Mathematical Physics 64 (5) (2023) 051901.

[249] H. Anwar, B. J. Brown, E. T. Campbell, D. E. Browne, Fast decoders for qudit topological codes, New Journal of Physics 16 (6) (2014) 063038.

[250] M. H. Freedman, D. A. Meyer, Projective plane and planar quantum codes (1998). arXiv:quant-ph/9810055.

[251] T. D. Ellison, Y.-A. Chen, A. Dua, W. Shirley, N. Tantivasadakarn, D. J. Williamson, Pauli topological subsystem codes from abelian anyon theories, Quantum 7 (2023) 1137. doi:10.22331/q-2023-10-12-1137.

[252] S. Puri, A. Grimm, P. Campagne-Ibarcq, A. Eickbusch, K. Noh, G. Roberts, L. Jiang, M. Mirrahimi, M. H. Devoret, S. M. Girvin, Stabilized Cat in a Driven Nonlinear Cavity: A Fault-Tolerant Error Syndrome Detector, Phys. Rev. X 9 (4) (2019) 041009. doi:10.1103/PhysRevX.9.041009.

[253] Y. Shi, C. Chamberland, A. Cross, Fault-tolerant preparation of approximate GKP states, New Journal of Physics 21 (9) (2019) 093007. doi:10.1088/1367-2630/ab3a62.

[254] S. Puri, S. Boutin, A. Blais, Engineering the quantum states of light in a Kerr-nonlinear resonator by two-photon driving, npj Quantum Inf. 3 (1) (2017) 18. doi:10.1038/s41534-017-0019-1.

[255] V. E. Manucharyan, J. Koch, L. I. Glazman, M. H. Devoret, Fluxonium: Single Cooper-Pair Circuit Free of Charge Offsets, Science 326 (5949) (2009) 113–116. arXiv:https://www.science.org/doi/pdf/10.1126/science.1175552, doi:10.1126/science.1175552.

[256] G. Kirchmair, B. Vlastakis, Z. Leghtas, S. E. Nigg, H. Paik, E. Ginossar, M. Mirrahimi, L. Frunzio, S. M. Girvin, R. J. Schoelkopf, Observation of quantum state collapse and revival due to the single-photon kerr effect, Nature 495 (7440) (2013) 205–209. doi:10.1038/nature11902.

[257] F. Schmidt, D. Miller, P. van Loock, Error-corrected quantum repeaters with GKP qudits (2023). arXiv:2303.16034.

[258] Y. Wu, S. Kolkowitz, S. Puri, J. D. Thompson, Erasure conversion for fault-tolerant quantum computing in alkaline earth Rydberg atom arrays, Nat. Commun. 13 (1) (2022) 4657. doi:10.1038/s41467-022-32094-6.

[259] P. Scholl, A. L. Shaw, R. B.-S. Tsai, R. Finkelstein, J. Choi, M. Endres, Erasure conversion in a high-fidelity Rydberg quantum simulator (2023). arXiv:2305.03406.

[260] M. Kang, W. C. Campbell, K. R. Brown, Quantum Error Correction with Metastable States of Trapped Ions Using Erasure Conversion, PRX Quantum 4 (2023) 020358. doi:10.1103/PRXQuantum.4.020358.

[261] A. Kubica, A. Haim, Y. Vaknin, F. B. ao, A. Retzker, Erasure qubits: Overcoming the T_1 limit in superconducting circuits (2022). arXiv:2208.05461.

[262] H. Levine, A. Haim, J. S. C. Hung, N. Alidoust, M. Kalaee, L. DeLorenzo, E. A. Wollack, P. A. Arriola, A. Khalajhedayati, R. Sanil, Y. Vaknin, A. Kubica, A. A. Clerk, D. Hover, F. B. ao, A. Retzker, O. Painter, Demonstrating a long-coherence dual-rail erasure qubit using tunable transmons (2023). arXiv:2307.08737.

[263] K. E. Cahill, R. J. Glauber, Ordered expansions in boson amplitude operators, Phys. Rev. 177 (5) (1969) 1857–1881. doi:10.1103/PhysRev.177.1857.

[264] U. Leonhardt, Entanglement, Cambridge University Press, 2010. doi:10.1017/cbo9780511806117.007.

[265] K. Park, P. Marek, R. Filip, Qubit-mediated deterministic nonlinear gates for quantum oscillators, Scientific Reports 7 (1) (2017) 11536. doi:10.1038/s41598-017-11353-3.

[266] K. Park, P. Marek, R. Filip, Deterministic nonlinear phase gates induced by a single qubit, New Journal of Physics 20 (5) (2018) 053022. doi:10.1088/1367-2630/aabb86.

[267] J. Zak, Finite Translations in Solid-State Physics, Phys. Rev. Lett. 19 (1967) 1385–1387. doi:10.1103/PhysRevLett.19.1385.

[268] Y. Aharonov, H. Pendleton, A. Petersen, Modular variables in quantum theory, International Journal of Theoretical Physics 2 (3) (1969) 213–230. doi:10.1007/bf00670008.

[269] A. Ketterer, A. Keller, S. P. Walborn, T. Coudreau, P. Milman, Quantum information processing in phase space: A modular variables approach, Phys. Rev. A 94 (2016) 022325. doi:10.1103/PhysRevA.94.022325.

[270] G. Pantaleoni, B. Q. Baragiola, N. C. Menicucci, Modular bosonic subsystem codes, Phys. Rev. Lett. 125 (2020) 040501. doi:10.1103/PhysRevLett.125.040501.

[271] G. Pantaleoni, B. Q. Baragiola, N. C. Menicucci, Subsystem analysis of continuous-variable resource states, Phys. Rev. A 104 (2021) 012430. doi:10.1103/PhysRevA.104.012430.

[272] L. J. Mensen, B. Q. Baragiola, N. C. Menicucci, Phase-space methods for representing, manipulating, and correcting gottesman-kitaev-preskill qubits, Phys. Rev. A 104 (2021) 022408. doi:10.1103/PhysRevA.104.022408.

[273] M. H. Shaw, A. C. Doherty, A. L. Grimsmo, Stabilizer subsystem decompositions for single- and multi-mode gottesman-kitaev-preskill codes (2022). `arXiv:2210.14919`.

[274] G. Pantaleoni, B. Q. Baragiola, N. C. Menicucci, The Zak transform: a framework for quantum computation with the Gottesman-Kitaev-Preskill code (2023). `arXiv:2210.09494`.

[275] J. Zak, The Kq-Representation in the Dynamics of Electrons in Solids 27 (1972) 1–62. `doi:10.1016/s0081-1947(08)60236-2`.

[276] S. Ganeshan, M. Levin, Formalism for the solution of quadratic Hamiltonians with large cosine terms, Phys. Rev. B 93 (2016) 075118. `doi:10.1103/PhysRevB.93.075118`.

[277] D. T. Le, A. Grimsmo, C. Müller, T. M. Stace, Doubly nonlinear superconducting qubit, Phys. Rev. A 100 (2019) 062321. `doi:10.1103/PhysRevA.100.062321`.

[278] P. Liang, M. Marthaler, L. Guo, Floquet many-body engineering: topology and many-body physics in phase space lattices, New J. Phys. 20 (2) (2018) 023043. `doi:10.1088/1367-2630/aaa7c3`.

[279] P. G. Harper, The General Motion of Conduction Electrons in a Uniform Magnetic Field, with Application to the Diamagnetism of Metals, Proc. Phys. Soc. A 68 (10) (1955) 879. `doi:10.1088/0370-1298/68/10/305`.

[280] D. R. Hofstadter, Energy levels and wave functions of Bloch electrons in rational and irrational magnetic fields, Phys. Rev. B 14 (1976) 2239–2249. `doi:10.1103/PhysRevB.14.2239`.

[281] B. Douçot, L. B. Ioffe, Physical implementation of protected qubits, Reports on Progress in Physics 75 (7) (2012) 072001. `doi:10.1088/0034-4885/75/7/072001`.